Space-time topology optimization for multi-axis additive manufacturing

Wu, K.

DOI
10.4233/uuid:3be97b56-f03e-4d07-b182-b1427f249db5

Publication date
2025

Document Version
Final published version

Citation (APA)
Wu, K. (2025). *Space-time topology optimization for multi-axis additive manufacturing*. [Dissertation (TU Delft), Delft University of Technology]. https://doi.org/10.4233/uuid:3be97b56-f03e-4d07-b182-b1427f249db5

SPACE-TIME TOPOLOGY OPTIMIZATION FOR MULTI-AXIS ADDITIVE MANUFACTURING

Kai Wu

SPACE-TIME TOPOLOGY OPTIMIZATION FOR MULTI-AXIS ADDITIVE MANUFACTURING

SPACE-TIME TOPOLOGY OPTIMIZATION FOR MULTI-AXIS ADDITIVE MANUFACTURING

Dissertation

for the purpose of obtaining the degree of doctor
at Delft University of Technology
by the authority of the Rector Magnificus, prof. dr. ir. T.H.J.J. van der Hagen,
chair of the Board for Doctorates
to be defended publicly on
Wednesday 11 June 2025 at 10:00 o'clock

by

Kai WU

Master of Science in Mechanics, Tsinghua University, China
born in Jiangsu, China

This dissertation has been approved by the promotors.

Composition of the doctoral committee:

Rector Magnificus,	chairperson
Prof. dr. ir. A. van Keulen,	Delft University of Technology, *promotor*
Dr. J. Wu,	Delft University of Technology, *promotor*
Independent members:	
Prof. dr. ir. M. Langelaar	Delft University of Technology
Dr. ir. M.J.M. Hermans	Delft University of Technology
Prof. dr. I. Gibson	University of Twente
Prof. dr. C.C.L. Wang	The University of Manchester, United Kingdom
Prof. dr. ir. K.M.B. Jansen	Delft University of Technology, reserve member

Keywords: Design for additive manufacturing, multi-axis additive manufacturing, wire arc additive manufacturing, topology optimization, process planning, space-time topology optimization, fabrication sequence optimization, layer geometry control, curved slicing, residual stress, process-induced distortion, anisotropic material

Printed by: ProefschriftMaken

Cover by: Kai & Stefanie van den Herik & AI, inspired by the cliffs of Étretat
– *When science shapes form, it sometimes echoes the rhythms of nature, like cliffs sculpted across space, like topologies carved by code, yet reminiscent of wind, wave, and time.*

ISBN 978-94-6510-665-6

An electronic copy of this dissertation is available at
https://repository.tudelft.nl/.

To my wife Jingyi, and the wonderful journey of life we share.

Kai

CONTENTS

SUMMARY

Multi-axis additive manufacturing is a set of advanced technologies that leverage robotic systems capable of rotational and translational motion in additive manufacturing processes. These systems enable dynamic adjustments to the build direction and deposition plane, offering ultimate flexibility for fabricating intricate structures using curved layers. Such systems are well-suited for processes such as fused deposition modeling (FDM) for polymers and wire arc additive manufacturing (WAAM) for metals.

In this dissertation, an optimization framework is developed for multi-axis additive manufacturing, with a particular emphasis on WAAM. The framework aims to address key challenges, such as residual stress and thermal-induced distortion, by investigating two critical aspects for additive manufacturing: structural design and process planning.

At the core of the framework is the concept of space-time topology optimization. Unlike conventional workflows that treat the above two aspects as separate steps, this framework enables concurrent optimization of the structural layout and the fabrication sequence. It incorporates a pseudo-density field to represent the structural layout and a pseudo-time field to encode the fabrication sequence. This dual-field optimization provides comprehensive information about the structural geometry and the layer-by-layer manufacturing process. In addition, the framework can also be adapted for pure fabrication sequence optimization when the structural layout is set as fixed.

To better align with manufacturing realities, the space-time topology optimization is first regularized using a heat equation. The monotonic additive manufacturing process is conceptualized as a heat conduction process starting from the surface upon which a component is constructed layer by layer in a forward progression. Instead of being optimized explicitly, the pseudo-time field is derived implicitly by solving the heat equation. Due to the physics it resembles, the regularized pseudo-time field is continuous and free of local minima, which complies with manufacturing principles.

On this basis, a layer geometry control scheme is further developed to improve the uniformity of layer thickness within each layer and to ensure that every layer's thickness remains within a feasible range. The method also promotes convex layer curvatures locally, reducing the risk of collisions during manufacturing. It monitors and adjusts layer shapes by leveraging both the gradient and the Hessian matrix of the pseudo-time field. The method is validated within the space-time optimization framework and is focused solely on fabrication sequence optimization. These improvements in geometric consistency further contribute to ensuring the manufacturability.

Furthermore, we demonstrate the feasibility of reducing residual stresses and distortions in WAAM through both pure fabrication sequence planning and the concurrent optimization of the structural layout and sequence. The inherent strain method is adopted as a simplified process simulation model to predict stresses and distortions accumulated during manufacturing. To address these challenges, local residual stresses are ag-

gregated using a p-norm function, which is integrated as a constraint into the distortion minimization framework. Numerical examples demonstrate that the optimized non-planar fabrication strategies can significantly reduce these thermal-induced issues.

Last but not least, we further explore the possibility of incorporating additional characteristics of multi-axis additive manufacturing into the framework. In WAAM, material anisotropy arises from the deposition process. To integrate this into space-time topology optimization, the material deposition direction is directly derived from the pseudo-time field, where the local material orientation is perpendicular to its gradient. Numerical examples demonstrate that the optimized fabrication sequences rationally align deposition orientations to take advantage of the stiffer direction of materials, thereby improving mechanical performances.

In summary, this dissertation advances the space-time topology optimization framework to improve its compatibility with practical manufacturing scenarios. It inspires the exploration and utilization of the innovative potential offered by multi-axis manufacturing strategies.

SAMENVATTING

Meerassig 3D printen is een groep van geavanceerde productie technologieën, die in het 3D printproces gebruik maken van robot systemen, met de capaciteit om roterende en translerende bewegingen te maken. Deze systemen maken dynamische aanpassingen aan de printrichting en het afzettingsvlak mogelijk, wat ultieme flexibiliteit biedt in het fabriceren van complexe structuren. Dit soort systemen zijn zeer geschikt voor processen als fused deposition modelling (FDM) voor polymeren en wire arc additive manufacturing (WAAM) voor metalen.

In dit proefschrift wordt een optimalisatiemethode kader voor meerassig 3D printen ontwikkeld, met een specifieke nadruk op WAAM. Het kader is gericht op het aanpakken van belangrijke uitdagingen, zoals restspanningen en thermische vervormingen, door twee cruciale aspecten van additieve fabricage te onderzoeken: structureel ontwerp en procesplanning.

De kern van het kader is het concept van ruimte-tijd topologie-optimalisatie. In tegenstelling tot conventionele werkwijzen, waarin deze twee aspecten als afzonderlijke stappen worden behandeld, maakt dit kader het mogelijk om tegelijkertijd de fabricagevolgorde alsook het structurele ontwerp te optimaliseren. Het gebruikt daarvoor een pseudo-dichtheidsveld om het structurele ontwerp te beschrijven en een pseudo-tijdsveld om de fabricagevolgorde te coderen. Dit twee-velden optimalisatieproces biedt uitgebreide informatie over de structurele geometrie en het laagsgewijze fabricageproces. Deze methode kan ook vereenvoudigd worden om alleen de fabricagevolgorde te optimaliseren als het structurele ontwerp al bekend is.

Om beter aan te sluiten bij de praktische realiteit van het fabricageproces, wordt de ruimte-tijd topologie optimalisatie eerst geregulariseerd door middel van een hitte vergelijking. Het monotone 3D printproces wordt gemodelleerd als een warmtegeleidingsproces dat begint bij het vlak waarop de component laagsgewijs gebouwd wordt in een voorwaartse richting. In plaats van dat deze expliciet wordt geoptimaliseerd, wordt het pseudo-tijd veld impliciet afgeleid door het oplossen van de warmtevergelijking. Door het fysische proces dat gemodelleerd wordt, is het geregulariseerde pseudo-tijd veld continu en zonder lokale minima, wat voldoet aan de fabricageprincipes.

Op basis hiervan is een methode voor controle over de laaggeometrie verder ontwikkeld om de gelijkmatigheid van de laagdiktes in elke laag te verbeteren en om te verzekeren dat de laagdiktes binnen een uitvoerbaar bereik blijven. Deze methode bevordert ook lokaal convexe laagkrommingen, waardoor het risico op botsingen tijdens de productie wordt verminderd. De methode bewaakt en past de laagvormen door gebruik te maken van zowel de gradiënt als de Hessiaanse matrix van het pseudo-tijdveld. De methode is gevalideerd binnen het ruimte-tijdoptimalisatiekader en is uitsluitend gericht op de optimalisatie van de fabricagesequentie. Deze verbeteringen in geometrische consistentie dragen verder bij aan de productiemogelijkheden.

Verder demonstreren we de haalbaarheid van het verminderen van restspanningen en vervormingen in WAAM door én alleen planning van de fabricagevolgorde én het tegelijkertijd optimaliseren van het structurele ontwerp en de fabricagevolgorde. De inherente-rekmethode wordt gebruikt als een gesimplificeerde simulatie van het proces om spanningen en vervormingen te voorspellen die accumuleren tijdens fabricage. Om rekening te houden met restspanningen, worden deze samengevoegd door middel van een p-norm functie, die de basis vormt voor de formulatie van een numerieke methode voor de optimalisatie. Numerieke voorbeelden demonstreren dat de geoptimaliseerde en niet vlakke fabricagestrategieën deze thermisch veroorzaakte problemen sterk kunnen verminderen.

Ten slotte onderzoeken we de mogelijkheid om aanvullende karakteristieken van meerassig 3D printen op te nemen in het kader. In WAAM komt materiële anisotropie voort uit het depositieproces. Om dit te integreren in ruimte-tijd topologie-optimalisatie wordt de materiaaldepositierichting direct afgeleid van het pseudo-tijdveld, waarbij de lokale materiaaloriëntatie loodrecht staat op de gradiënt ervan. Numerieke voorbeelden demonstreren dat de geoptimaliseerde fabricagevolgordes rationeel de materiaaldepositierichtingen uitlijnen om te profiteren van de stijvere richting van het materiaal, waardoor de mechanische prestaties verbeteren.

Samengevat bevordert dit proefschrift het ruimte-tijd topologie optimalisatie kader door de comptabiliteit met praktische fabricagescenario's te verbeteren. Het inspireert het verkennen en gebruiken van de innovatieve mogelijkheden die geboden wordt door meerassig fabricage strategieën.

1

INTRODUCTION

This research focuses on addressing challenges in additive manufacturing from a design perspective. Its primary scope encompasses structural design and process planning for multi-axis additive manufacturing. This chapter provides an overview of the research background and the key challenges, followed by an outline of the thesis structure.

1

1.1. RESEARCH BACKGROUD

1.1.1. MULTI-AXIS ADDITIVE MANUFACTURING

ADDITIVE manufacturing, commonly referred to as 3D printing, is a transformative technology that redefines conventional notions of how structures can be built or manufactured. In contrast to conventional subtractive manufacturing methods that involve intensive material removal, additive manufacturing constructs components layer by layer directly from digital models, promoting more sustainable production practices. It also offers greater design and manufacturing flexibility, enabling the fabrication of complex geometries that would be difficult or even impossible to achieve using conventional techniques.

An emerging advancement in additive manufacturing is multi-axis additive manufacturing [155]. In traditional additive manufacturing, the process follows a fixed build direction: the printer head moves horizontally to create each planar layer, then raises to form the next layer, a technique often referred to as 2.5D printing. In contrast, multi-axis additive manufacturing uses either a rotating build plate or a flexible printing head, allowing the material deposition direction to be dynamically adjusted throughout the manufacturing process. This can provide greater fabrication flexibility. Multi-axis techniques have been developed for both metal [44, 71, 135, 171] and polymer fabrication [38, 198]. As shown in Fig. 1.1, multi-axis setups are available for processes like direct energy deposition (DED), including wire arc additive manufacturing (WAAM), and material extrusion, including fused deposition modeling (FDM).

WAAM is the main application scenario for the research conducted in this dissertation. WAAM uses an electric welding arc as the heat source and a metal wire as feedstock. The desired object is manufactured by stacking welding beads layer-by-layer with the aid of a welding robot [44, 71, 135, 171]. It is particularly effective for manufacturing large metallic components, making it ideal for applications across various industries, as can be seen in Fig. 1.2.

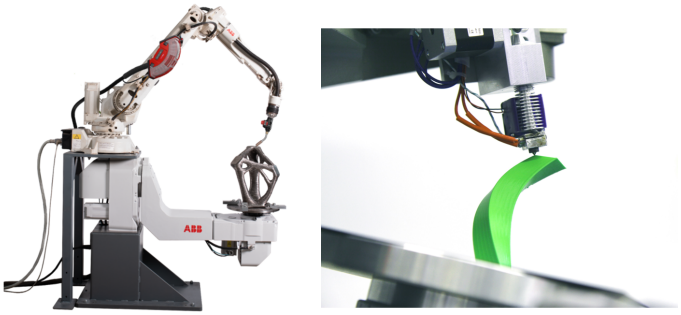

(a) (b)

Figure 1.1.: Multi-axis additive manufacturing setups. (a) Wire arc additive manufacturing (Courtesy MX3D). (b) Fused deposition modeling (Courtesy ISM Universität Stuttgart [35]).

Figure 1.2.: Components manufactured using WAAM. Top left: A WAAM produced engineering component (Courtesy MIGAL). Top right: World's first metal additively manufactured bridge [59, 82] (Courtesy MX3D). Bottom left: A marine propeller is under construction using WAAM (Courtesy RAMLAB). Bottom right: Artistic illustration of a self-support robotic manufacturing bridge (Courtesy MX3D).

However, there are several challenges that remain to be solved for multi-axis additive manufacturing, which mainly result from the complex manufacturing process. For instance, effective slicing and toolpath planning strategies need to be developed to prevent collisions and manage process-dependent loads [54, 188, 189, 200]. Additionally, material anisotropy should be accounted for, as the manufacturing process inherently exhibits anisotropic and heterogeneous characteristics [14, 66, 74, 78, 80, 93, 172, 208]. In metal-based techniques, issues such as residual stress and distortion arise due to the significant energy input [27, 172, 181]. This research aims to address multiple process-specific challenges in multi-axis additive manufacturing from a design perspective, as will be elaborated later.

1.1.2. DESIGN FOR ADDITIVE MANUFACTURING

Additive manufacturing has revolutionized the construction of complex systems, necessitating updates in design methodologies to fully exploit its new possibilities and opportunities [106, 156]. This section examines two critical aspects of designing for additive manufacturing: structural optimization and process planning.

A typical workflow for additive manufacturing can be seen in Fig. 1.3. In this workflow, structural design is followed by process planning, carried out in a sequential manner. The component is then fabricated, with post-processing steps performed subsequently to prepare the part for its intended application. While this linear approach is widely adopted, the advanced fabrication flexibility of multi-axis additive manufacturing offers new possibilities, allowing engineers to innovate in both structural design and manufacturing processes.

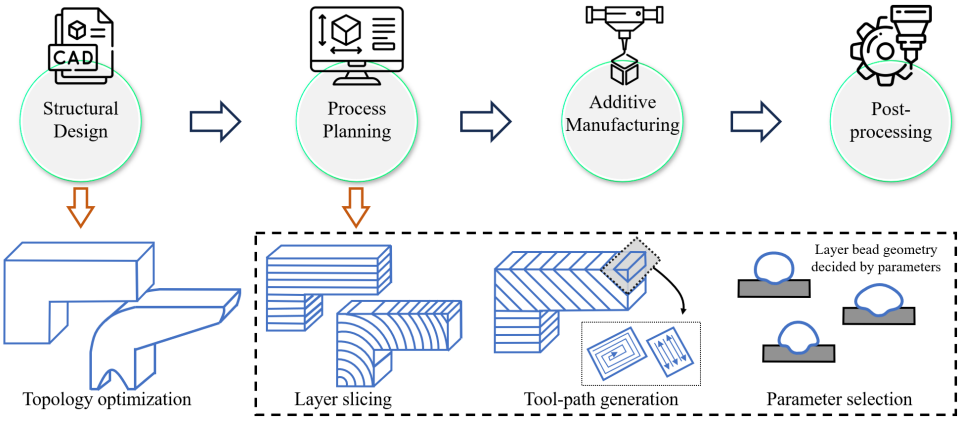

Figure 1.3.: Workflow of multi-axis additive manufacturing.

STRUCTURAL DESIGN THROUGH TOPOLOGY OPTIMIZATION

Structural design is an important aspect of design for additive manufacturing. The fabrication flexibility of additive manufacturing makes it ideal for creating intricate structures, such as multi-scale design [176], multi-material components [121], and geometries with high complexity [1], offering a vast design space for innovation.

Topology optimization is one of the most advanced structural design methods, which has been developed rapidly during the last few decades [12, 13]. What sets topology optimization apart from other structural optimization techniques is its ability to generate entirely new topological configurations. Various approaches have been developed for topology optimization [146], including density-based approaches [11, 147], level-set approaches [6, 161, 167], geometry projection methods [65, 123], discrete approaches [186], and others. Topology optimization has been extensively employed to design optimal structures tailored for additive manufacturing [100, 101, 207]. The ultimate design freedom offered by topology optimization complements the capabilities of additive manufacturing, which eliminates many geometric constraints through its layer-by-layer material deposition or solidification processes.

A wide range of topics has been discussed regarding the integration of topology optimization and additive manufacturing [100, 207]. Most of them can be divided into two categories: one is to design cost-effective multiscale / hierarchy structures that are suitable to be additively manufactured, such as porous infill [105, 174, 175, 177] and functionally graded material [31]. The other is to take manufacturing constraints into account in topology optimization to achieve product design and manufacturing integration. For example, to handle overhang structures in topology optimization, support slimming or overhang-free topology optimization [86, 87, 158–160] has been developed. Methods like the virtual temperature method [95, 104, 108] have been proposed for the restriction of enclosed voids in additive manufacturing. Besides, the feature sizes of the design should be ensured to be compatible with the manufacturing technique [57, 58, 90]. In addition to geometric

considerations, the structural design process can also account for several key physical phenomena in additive manufacturing [9], such as local overheating [133], residual stresses [5, 190] and distortion [113], and microstructure evolution [112].

For multi-axis additive manufacturing, some of the challenges mentioned above become less significant. For example, multi-axis additive manufacturing is able to deposit overhang features by changing the build direction. This inherent advantage mitigates the need for support structures, which is a major consideration in traditional additive manufacturing. Consequently, a fundamental rethinking of structural design approaches is required to fully leverage the unique capabilities and increased fabrication freedom offered by multi-axis additive manufacturing.

MANUFACTURING PROCESS PLANNING

Manufacturing process planning is another important aspect of design for additive manufacturing, encompassing all the necessary steps to convert a digital CAD model into a physical part. It spans a broad spectrum of tasks, including build orientation selection, slicing into layers, toolpath planning, and the selection of process parameters [41]. Each of these decisions plays a vital role in ensuring the quality, efficiency, and reliability of the final product.

Slicing is the procedure of dividing the component into a series of 2D layers to be manufactured sequentially [114, 188]. Conventional additive manufacturing commonly employs a planar layer-by-layer strategy, often referred to as 2.5D printing. In this method, the slicing pattern is determined by the selected build orientation and layer thickness. Minor adjustments, such as adaptive variations in the layer thickness, can be applied to enhance the surface quality. Therefore, selecting an appropriate build orientation becomes a critical preliminary step for planar slicing, as it helps reduce the need for support structures while improving printing efficiency and quality.

In contrast, multi-axis additive manufacturing enables the use of more sophisticated and efficient slicing techniques, such as multi-directional slicing [45, 68, 148] or free-form slicing [54, 55, 76, 97, 137, 185, 202]. These techniques go beyond the traditional planar slicing used in conventional AM systems. In particular, free-form slicing enables the generation of curved layers, fully leveraging the fabrication flexibility of multi-axis systems. This brings multiple benefits, including enhanced mechanical performance, improved manufacturing quality, and the elimination of support structures. However, this also presents new challenges, such as increased complexity in process planning, the need for effective collision avoidance strategies, and the requirement for precise control over the manufacturing process.

After slicing, a series of toolpaths need to be generated on each sliced 2D plane to guide the movement of the 3D printer. Toolpath planning governs the finer details of how the material is deposited. It plays a critical role in determining the final part quality and structural integrity. Various path-planning algorithms have been developed to improve manufacturing quality [15, 42, 43, 46, 97, 206]. These algorithms generally address two primary aspects: geometrically, they aim to avoid collisions, ensure smooth tool movement, and align anisotropic materials with the load paths; physically, they seek to minimize process-dependent loads or thermal

effects through rational planning. Through such strategies, toolpath planning acts as a bridge between slicing and physical printing, directly impacting both the efficiency and quality of the printed component.

In addition, the selection of process parameters is also important, as they are closely related to the layer bead geometry, energy input, and resulting mechanical performances. Taking WAAM as an example, the geometric dimensions of its layer are dependent on various process parameters, including the wire feed rate, travel speed, arc discharge time, and others [3, 85, 163]. Besides, variations in these parameters lead to different thermal histories, which significantly influence the accumulation of residual stresses [24] as well as the formation of microstructures [112].

It is important to note that these process planning procedures above are often interdependent, with each step potentially influencing the others, making iterative design and refinement difficult to avoid. Aside from the procedures mentioned above, post-processing steps such as surface polishing and heat treatment should also be planned ahead of time to improve the manufacturing quality.

In summary, optimizing process planning that provides efficient and defect-free deposition is key for additive manufacturing. This dissertation focuses on a critical aspect of process planning: the fabrication sequence planning, aimed at addressing several process-induced challenges. The potential integration of other aspects of process planning will be discussed in the outlook.

1.1.3. SPACE-TIME TOPOLOGY OPTIMIZATION

Although Structural design and process planning are commonly dealt with as two separate tasks when designing for additive manufacturing, they are in fact deeply interconnected. Process planning needs to be tailored to the geometric features of the component, while structural design should be compatible with the constraints and capabilities of the manufacturing process. Addressing these two aspects in a sequential manner [77, 136] fails to capture the coupled interactions between them, potentially leading to suboptimal outcomes.

Recognizing this interdependence, recent research is increasingly shifting towards integrating manufacturing process planning directly into the structural design phase [9]. This enables a comprehensive consideration of both geometric and physics-based manufacturing constraints, leading to more robust and feasible designs. For example, topology optimization combined with toolpath planning has been studied to enhance structural performances by making use of anisotropic material properties [102, 103, 191, 192], to control temperature during manufacturing [16], and to mitigate residual stress and distortion [26].

A systematic approach known as space-time topology optimization has been introduced to unify structural design and process planning into a single optimization process [168]. This method was initially motivated by the need to account for process-dependent loads, such as the self-weight of intermediate structures and thermomechanical loads, within the structural design phase [7, 22, 67, 77]. In space-time topology optimization, the spatial and temporal distributions of materials are optimized simultaneously, allowing designers to determine not only where but also when material should be deposited throughout the manufacturing process. As

illustrated in the upper left part of Fig. 1.4, the structural layout is described using a pseudo-density field, following the principles of classical density-based topology optimization. In parallel, a pseudo-time field is introduced to encode the fabrication sequence. Layer divisions can be derived by combining the two fields, enabling a numerical representation of the entire manufacturing process.

The versatility of space-time topology optimization has been demonstrated across various application scenarios [168], addressing the self-weight of the intermediate structures, process-dependent loads from an attached moving manufacturing platform, and time-dependent material properties. Additionally, a pure fabrication sequence optimization aimed at minimizing thermal distortion in the WAAM process has also been studied [169] within the same framework. It is important to highlight that multi-axis additive manufacturing allows full freedom for the planning of the fabrication process in contrast to conventional 2.5D additive manufacturing methods, making it well-suited for the implementation of space-time topology optimization.

1.2. CHALLENGES AND RESEARCH SCOPE

The main content of this dissertation is summarized in Fig. 1.4, including the development of the space-time topology optimization framework tailored for compatibility with additive manufacturing, the integration of manufacturing features such as material anisotropy into the framework, and the application of this framework to tackle challenges associated with WAAM.

Space-time topology optimization has shown significant potential in improving the quality of multi-axis additive manufacturing processes. However, the original method exhibits several critical limitations that often lead to impractical or unmanufacturable results. One major issue lies in the generation of local extrema in the pseudo-time field, which leads to unrealistic fabrication sequences, as can be seen in the bottom

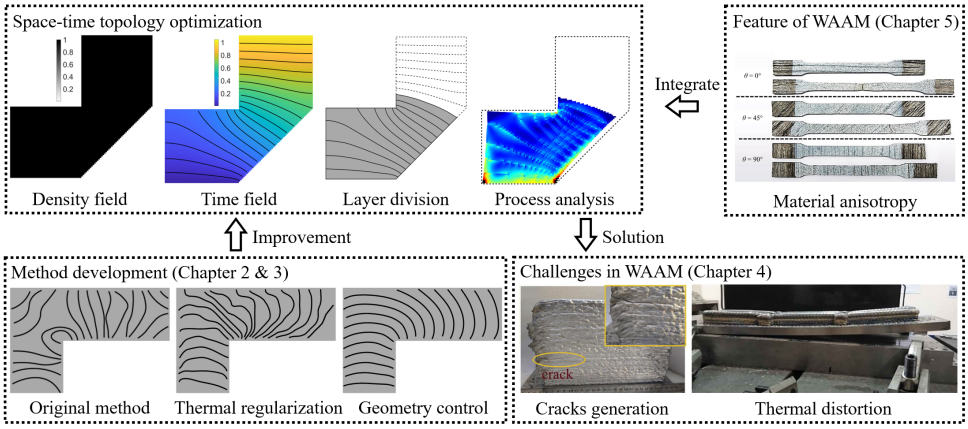

Figure 1.4.: Illustration of the main content of this dissertation. Courtesy: material anisotropy (Kyvelou et al. 2020 [83]), cracks generation (Chen et al. 2022 [28]), thermal distortion (Xu et al. 2018 [187]).

left part of Fig. 1.4. Specifically, local minima in the time field correspond to isolated parts that lack sufficient support from previous layers. These results can not be manufactured unless additional supports are added, which is not favored by multi-axis additive manufacturing. On the other hand, local maxima compel the manufacturing process to backtrack to earlier layers, which is often infeasible in the context of three-dimensional fabrication.

Another significant limitation is the lack of uniformity in the geometric dimensions of the resulting layers. Considerable variations in layer thickness are observed both within individual layers and across successive layers in the original method. These inconsistencies present major manufacturing challenges, as they require continuous adjustment of process parameters during fabrication. For practical application, it is essential that each layer maintains a relatively consistent thickness, remaining within the operational limits of the chosen manufacturing technique. Moreover, concave layer shapes are undesirable, as they increase the risk of collisions between the end effector and the structure. Addressing these issues is critical for bridging the gap between numerical optimization and practical implementation, thereby enabling the effective use of space-time topology optimization in real-world scenarios.

Afterwards, the space-time topology optimization framework is employed to address the specific challenges associated with the WAAM process. The direct energy deposition process of WAAM undergoes steep temperature gradients, as the material is melted and deposited layer by layer to create a component. The complex thermal conditions result in uneven expansion and contraction, along with frequent phase transformations, which in turn cause substantial residual stresses and distortions in the fabricated parts. Such issues have a pronounced impact on both the structural integrity and the dimensional accuracy of the final product, as illustrated in the bottom right part of Fig. 1.4. Although residual stresses and distortions can be alleviated to some extent using treatments such as preheating, interpass cooling, and annealing [27, 135], this dissertation approaches the problem from a design perspective. Specifically, we explore the possibility of mitigating residual stress and distortion through fabrication sequence planning and its combination with structural design. The space-time topology optimization framework is adopted as the basis of the numerical methodology.

In addition, some multi-axis additive manufacturing techniques, such as WAAM and FDM, exhibit anisotropic material behavior, particularly in mechanical properties like elastic modulus and tensile strength. This anisotropy originates from the layer-by-layer deposition process inherent to these techniques, resulting in notable differences in material performance along the deposition direction versus across layers. Recognizing and accounting for material anisotropy opens up opportunities to tailor material properties through process planning and to incorporate direction-dependent behavior into computational design frameworks for improved performance and reliability of the final product. Given that these anisotropic properties are inherently linked to the fabrication sequence, they are naturally associated with the time field in space-time topology optimization. This provides an important opportunity to explore the potential integration of process-induced material anisotropy into the optimization framework.

In summary, the main research objective of this PhD dissertation is to further develop the space-time topology optimization framework for multi-axis additive manufacturing, with a particular focus on WAAM. This framework aims to integrate structural design and process planning, either concurrently or in a decoupled manner, while considering various manufacturing-related requirements.

The main research questions that will be addressed in this dissertation are:

(i) What are the flaws and limitations of the original space-time topology optimization? How to get rid of them efficiently in the numerical algorithm?

(ii) Is it possible to reduce residual stress and thermal distortion simultaneously in WAAM through fabrication sequence planning? Does the concurrent optimization of structural layout and fabrication sequence outperform a decoupled sequential optimization strategy?

(iii) How can space-time topology optimization account for process-induced material anisotropy? What are the advantages does this offer?

1.3. OUTLINE

This dissertation builds upon multiple peer-reviewed journal papers, with each chapter designed to be read independently. Minor adjustments have been made to mathematical notations and layouts to ensure consistency across chapters. Consequently, some introductory content and mathematical formulations may be repeated. The outline of this dissertation is as follows:

Chapter 2 introduces a regularization scheme based on the heat equation to address the local minima problem in space-time topology optimization. We conceptualize the monotonic additive manufacturing process as a virtual heat conduction process starting from the surface upon which a component is constructed layer by layer. In this new formulation, we use local virtual heat conductivity coefficients as optimization variables to steer the temperature field and, consequently, the fabrication sequence. The inherent smoothness of the virtual temperature field, driven by its physical analogy, mitigates local minima issues. The physical implications of fabrication sequences on manufacturing-induced distortions are explored in depth. This chapter lays the groundwork for the enhanced methods developed in subsequent chapters.

Building on this basis, **Chapter** 3 further advances the space-time optimization framework by including a layer geometry control scheme to ensure manufacturability. This approach maintains nearly constant layer thickness, reducing the need for frequent and abrupt adjustments to processing parameters such as move speed. In addition, a curvature control scheme is introduced to mitigate the formation of concave layers that may be inaccessible during manufacturing due to collision risks. Numerically, the layer thickness is approximated by the gradient of the pseudo-time field, while the curvature is computed from its Hessian matrix. Integrating the geometry control scheme into the fabrication sequence optimization yields more uniform layers while still effectively suppressing manufacturing-induced distortion.

In **Chapter** 4, we demonstrate the feasibility of reducing residual stresses and thermal-induced distortion simultaneously in WAAM through space-time topology optimization. Local residual stresses are aggregated using a p-norm function, which is integrated as a constraint into the distortion minimization problem. Numerical examples demonstrate that optimizing the time field alone can effectively reduce both residual stresses and distortions through fabrication sequence planning. Furthermore, space-time topology optimization facilitates the design of complex components with restricted residual stresses and thermal-induced distortion by concurrently optimizing the structure and fabrication sequence. A comparative study of optimizing these factors concurrently versus sequentially is also conducted, highlighting the interplay between structural and sequence optimization.

In **Chapter** 5, we extend the framework to address manufacturing-induced material anisotropy in multi-axis additive manufacturing. In order to model process-induced material anisotropy within the space-time topology optimization framework, we derive the material deposition direction from the gradient of the pseudo-time field according to an orthogonal relationship. This integration enables the effective utilization of material anisotropy to enhance the performance of intermediate structures during fabrication and the final structural properties. By aligning material properties with fabrication sequences, this chapter broadens the applicability of space-time topology optimization to handle manufacturing-induced material anisotropy.

Finally, **Chapter** 6 concludes the key findings of the dissertation, providing a comprehensive summary of the PhD project. It also discusses common themes across chapters, linking the methods and insights into a cohesive framework. Future research directions are recommended, offering a perspective on the potential extensions and broader applications of the proposed methodologies.

2

REGULARIZATION IN SPACE-TIME TOPOLOGY OPTIMIZATION

In additive manufacturing, the fabrication sequence has a large influence on the quality of manufactured components. While planning of the fabrication sequence is typically performed after the component has been designed, recent developments have demonstrated the possibility and benefits of simultaneous optimization of both the structural layout and the corresponding fabrication sequence. This is particularly relevant in multi-axis additive manufacturing, where rotational motion offers enhanced flexibility compared to planar fabrication. The simultaneous optimization approach, called space-time topology optimization, introduces a pseudo-time field to encode the manufacturing process order, alongside a pseudo-density field representing the structural layout. To comply with manufacturing principles, the pseudo-time field needs to be monotonic, i.e., free of local minima. However, explicitly formulated constraints proposed in prior work are not always effective, particularly for complex structural layouts that commonly result from topology optimization.

In this chapter, we introduce a novel method to regularize the pseudo-time field in space-time topology optimization. We conceptualize the monotonic additive manufacturing process as a virtual heat conduction process starting from the surface upon which a component is constructed layer by layer. The virtual temperature field, which shall not be confused with the actual temperature field during manufacturing, serves as an analogy for encoding the fabrication sequence. In this new formulation, we use local virtual heat conductivity coefficients as optimization variables to steer the temperature field and, consequently, the fabrication sequence. The virtual temperature field is inherently free of local minima due to the physics it resembles.

Parts of this chapter have been published in *Computer Methods in Applied Mechanics and Engineering* **431**, 117202 (2024) authored by Weiming Wang, Kai Wu, Fred van Keulen and Jun Wu, under the title *Regularization in Space-Time Topology Optimization for Multi-Axis Additive Manufacturing.* Author statement of Kai Wu: Writing – original draft, Methodology, Funding acquisition.

2.1. INTRODUCTION

THE past few years have seen tremendous progress in computational design for additive manufacturing [64] and topology optimization approaches in particular [18, 195]. In topology optimization, structural design is formulated as an optimization problem of distributing a limited amount of material in a design domain to maximize its performance, for example, load-bearing capacity. The highly optimized designs often have complex geometry, which makes them difficult to produce. While the flexibility of additive manufacturing makes it possible to produce geometrically complex components, it is not without challenges. In the past decade, a focus in topology optimization has been on the incorporation of additive manufacturability, to avoid optimized designs that cannot be 3D printed directly or need costly post-processing [100]. The additive manufacturability is commonly characterized by geometric features such as the overhang angle [60, 86, 130, 158] and enclosed voids [49, 104].

A recent development in topology optimization for additive manufacturing has been on the integration of the physics involved in the layer-by-layer additive process into design optimization [9]. This means simulating the physics, such as self-weight and thermomechanical loads, acting on intermediate structures during the fabrication process. Allaire et al. [4] proposed one of the first approaches in this emerging direction, addressing overhang constraints, which had typically been treated as a geometric criterion [60, 86, 130, 158]. By restricting the deformation of intermediate structures due to their self-weight, the final optimized structure exhibits fewer overhanging features, reducing the need for auxiliary supports during fabrication. The self-weight of intermediate structures was considered similarly by Amir and Mass [7], Bruggi et al. [22], and Haveroth et al. [67]. Starting from self-weight, more sophisticated and computationally demanding physics in the fabrication process has been incorporated in topology optimization, particularly for mitigating undesired effects due to thermomechanical loads [5, 110, 113, 128]. These process-informed topology optimization approaches, by incorporating a model of the layer-by-layer manufacturing process in design optimization, provide a more detailed level of quality control compared to focusing on geometric (and topological) features of optimized designs.

In the aforementioned topology optimization approaches, the structural layout is optimized to generate high-performance components. In addition to structural design, the fabrication sequence, according to which the component is produced line-by-line and layer-by-layer, significantly influences the manufacturability and the quality of the fabricated components. In wire and arc additive manufacturing (WAAM), for example, substantial distortion may occur during fabrication as well as after cutting off the build plate [171]. The distortion is largely influenced by the fabrication sequence. Typically, the fabrication sequence is planned after the structural layout has been designed. This sequential workflow results in a gap between the quality of digital designs and their physical counterparts. Earlier work tackled this problem by assuming a prescribed fabrication sequence, e.g., considering factors like material anisotropy due to a prescribed toolpath strategy in the optimization of the structural layout [39, 102]. More recent efforts have started

optimizing the toolpath for powder bed fusion [15, 16] and layers for multi-axis additive manufacturing [168, 169]. Boissier et al. [15, 16] represented the toolpath as a continuous curve, formulating it as a shape optimization problem.

Our work is motivated by emerging robotic-assisted multi-axis additive manufacturing (e.g., WAAM), where the rotation of robotic arms offers more flexibility than traditional 3D printing, allowing not only translational but also rotational motion. Rotation facilitates the creation of non-planar layers. This brings benefits such as turning an overhanging feature into a self-supporting one, by appropriately rotating the build plate [38]. In the recently proposed space-time topology optimization framework [168, 169], the fabrication sequence was encoded by a pseudo-time field, where a larger pseudo-time indicates that the corresponding location is to be materialized later in the fabrication process. Iso-contours of the pseudo-time field segment the structural layout into (curved) layers. This parameterization is akin to density-based topology optimization in the sense that each location in the design domain carries an optimization variable, opening up the solution space of fabrication sequences. This parameterization also enables the simultaneous optimization of the structural layout and the fabrication sequence, i.e., by optimizing the density and time field concurrently.

Although parameterizing the fabrication process by a pseudo-time field opens up a huge solution space, the sequence represented by the iso-contours of the pseudo-time field is not guaranteed to be manufacturable. It is thus necessary to regularize the pseudo-time field to ensure that the optimized fabrication sequence meets manufacturing requirements. A critical requirement that we focus on in this chapter is the continuity of fabrication: material can only be deposited on the already produced portion of the part, besides directly on the build plate. In the pseudo-time field, the violation of this requirement can be characterized by local minima, i.e., the surrounding points are associated with larger time values, and thus have not been materialized yet. A local minimum may present inside the domain or on the boundary of the domain. Both are undesirable, except it is adjacent to the build plate. An illustration of these violations is illustrated in Fig. 2.1.

In the prior work [168, 169], these violations have been addressed by introducing explicitly formulated constraints. While these constraints function well in most cases, their effectiveness depends on the initialization of the pseudo-time field. In this chapter, we present a novel regularization method to implicitly handle these constraints. Our starting point is to initiate the pseudo-time field using geodesic distances. Unlike Euclidean distances, geodesic distances are dependent on the structural layout and free of local minima. This initialization strategy works for fixed structural layouts, but is not directly applicable to space-time topology optimization, where the structural layout and the fabrication sequence are optimized concurrently. As the structural layout evolves over iterations, and is not well defined during optimization, i.e., grey elements as encountered in density-based topology optimization. To solve these problems, we reformulate this initialization strategy using a partial differential equation, a heat equation in particular. This equation enables us to encode intermediate densities and evolving structural layouts in its parameters.

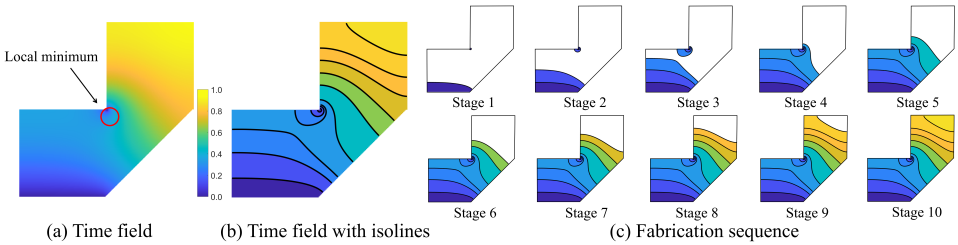

Figure 2.1.: (a) Illustration of a component and a pseudo-time field, with a smaller value indicating that the corresponding point is materialized earlier in fabrication. (b) The isolines of the pseudo-time field segment the part into a set of consecutive layers. (c) A series of intermediate structural layouts during the fabrication process. Note that, in stages 1 to 3, a patch of material, corresponding to a local minimum in the pseudo-time field, is in isolation from the rest of the component. This renders the fabrication sequence infeasible.

The remainder of this chapter is organized as follows. In Section 2.2, we present a simplified setup of space-time topology optimization where the structural layout is fixed. This problem is solved by initializing the fabrication sequence based on geodesic distances. In Section 2.3, this solution to the simplified problem setup is extended to address problems in space-time topology optimization where the structural layout and the fabrication sequence are optimized concurrently. The effectiveness of the proposed approach is evaluated in Section 2.4 for design optimization in 2D and 3D under process-dependent self-weight and thermomechanical loads. In Section 2.5, we conclude the chapter with some ideas for future work.

2.2. FABRICATION SEQUENCE OPTIMIZATION

In this section, we consider a simplified version of space-time topology optimization. Here, the structural layout is prescribed, and we optimize the fabrication sequence to produce it. This reduced problem is intended to illustrate the problem of local minima, demonstrate the effects of the initial sequence in optimization, and highlight the efficacy of a novel initialization strategy. These insights inspire our approach to solving the problem in the full space-time topology optimization.

2.2.1. SEQUENCE PARAMETERIZATION

We parameterize the fabrication sequence to produce a component using a pseudo-time field defined over the domain of the component. The component is discretized using a Cartesian grid, resulting in quadrilateral elements in 2D and hexahedral elements in 3D. To mimic the additive manufacturing process, each element e is associated with a scalar value t_e, indicating the pseudo-time at which the material associated with the element is added to the structure. Thus, an element with a larger pseudo-time indicates that this element is materialized later than an

element with a smaller one. For simplicity, we also refer to the pseudo-time field as the time field.

The time field $\boldsymbol{t}$ serves as design variables in sequence optimization. It is bounded to be between 0 and 1. The iso-contours by $\tau_j = \frac{j}{N}$, with $j = 0, ..., N$, thus partition the component into N layers. The partition is illustrated in Fig. 2.2. Each layer consists of elements whose time value belongs to the corresponding time interval. For instance, the j-th layer is denoted as

$$\boldsymbol{\eta}^{\{j\}} = \begin{cases} \{e | t_e \in [\tau_{j-1}, \tau_j)\}, & j = 1, 2, ..., N-1, \\ \{e | t_e \in [\tau_{N-1}, 1]\}, & j = N. \end{cases} \tag{2.1}$$

We note that the time field is a continuous scalar field, mimicking the progressive additive manufacturing process. The iso-contours of the time field, and the resulting layers between two consecutive iso-contours, are not restricted to be planar but can be curved.

We describe the intermediate structures during fabrication by a series of pseudo-density fields (or density fields, for simplicity), $\boldsymbol{\rho}^{\{j\}}$, with $j = 0, 1, ..., N$. Two successive intermediate structures are illustrated in Fig. 2.2. The superscript $\{j\}$ indicates the j-th stage during fabrication, i.e., layers from the first up to the j-th have been fabricated. $j = 0$ refers to the start of fabrication, $\rho_e^{\{0\}} = 0$, $\forall e$, while $j = N$ refers to the completion of fabrication, $\rho_e^{\{N\}} = 1$, $\forall e$.

The evolving intermediate structure is derived from the time field. Let $\mathbf{1}$ denote the density field of a prescribed, solid component. Assuming that the density field and time field are discretized using the same Cartesian grid, the intermediate structure at the j-th stage is described by an entry-wise multiplication between the density and the time field,

$$\boldsymbol{\rho}^{\{j\}}(\boldsymbol{t}) = \mathbf{1} \circ \bar{\boldsymbol{t}}^{\{\tau_j\}}, \quad j = 1, ..., N. \tag{2.2}$$

Here $\bar{\boldsymbol{t}}^{\{\tau\}}$ is a function of the time field $\boldsymbol{t}$. It converts time values less than τ to 1 and time values greater than τ to 0, in a differentiable manner. It is implemented using a smoothed Heaviside function, a commonly employed approach in density-based

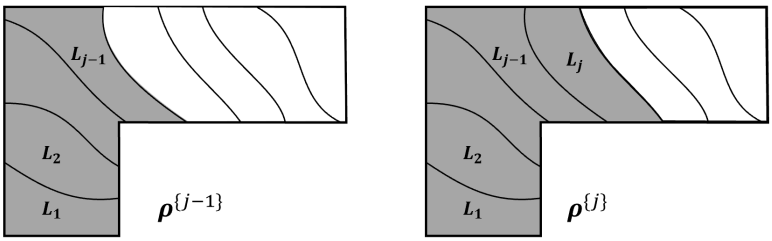

Figure 2.2.: Schematic of curved layers for fabricating an L-shaped component. Two successive intermediate structures during fabrication are illustrated on the left and right.

topology optimization [166],

$$\bar{t}^{\{\tau\}} = 1 - \frac{\tanh\big(\beta_t \tau\big) + \tanh\big(\beta_t (t-\tau)\big)}{\tanh\big(\beta_t \tau\big) + \tanh\big(\beta_t (1-\tau)\big)}, \tag{2.3}$$

where β_t is a positive number to control the projection sharpness. A continuation scheme is applied to increase this sharpness parameter after a certain number of iterations.

2.2.2. SEQUENCE OPTIMIZATION

The sequence optimization is generically formulated as

$$\underset{\boldsymbol{t}}{\text{minimize}}: \quad c(\boldsymbol{t}) = f(\boldsymbol{\rho}^{\{1\}}(\boldsymbol{t}), ..., \boldsymbol{\rho}^{\{j\}}(\boldsymbol{t}), ..., \boldsymbol{\rho}^{\{N\}}(\boldsymbol{t})), \tag{2.4}$$

$$\text{subject to}: \quad t_e \geq \min\{t_i | i \in \mathbb{N}_e\}, \forall e \in \mathscr{M} \backslash \Gamma_0, \tag{2.5}$$

$$t_e \leq \max\{t_i | i \in \mathbb{N}_e\}, \forall e \in \mathscr{M} \backslash \Gamma, \tag{2.6}$$

$$t_e \in [0,1], \forall e. \tag{2.7}$$

The objective concerns the evolving structure during fabrication $\boldsymbol{\rho}^{\{j\}}$, which is a function of the time field (cf. Eq. 2.2). In Eq. 2.5 and Eq. 2.6, $\mathbb{N}_e$ denotes the set of elements adjacent to element e. Eq. 2.5 requests the time value of each element to be larger than the minimum among its adjacent elements. This requirement applies to all elements in the component ($\mathscr{M}$), except those designated as the start region for fabrication ($\Gamma_0 = \{e | t_e = 0\}$), i.e., on the build plate. An element where this condition is violated indicates that the element needs to be materialized in midair, i.e., before any of its adjacent elements have been produced. Similarly, Eq. 2.6 requests the time value of each element to be smaller than the maximum among its adjacent elements. This requirement applies to all elements in the component ($\mathscr{M}$), except those on the boundary of the component (Γ). An element where this condition is violated indicates that the element needs to be materialized within an enclosed region, i.e., all of its adjacent elements have been produced. Both Eq. 2.5 and Eq. 2.6 are essential for the validity of a fabrication sequence.

The challenges to solving this formulation are twofold. Firstly, the constraints (Eq. 2.5 and Eq. 2.6) involve min and max functions, which are non-differential. Secondly, the number of constraints is large, since both Eq. 2.5 and Eq. 2.6 apply to all elements in the component. In previous work [168, 169], these constraints were reformulated using approximation and aggregation schemes. For instance,

$$\frac{1}{n(\mathscr{M})} \sum_{e \in \mathscr{M}} ||t_e - \text{mean}_{i \in \mathbb{N}_e}(t_i)||^2 \leq \epsilon, \tag{2.8}$$

where n denotes the number of elements in a set. The mean function calculates the average of time values of adjacent elements, i.e., $\text{mean}_{i \in \mathbb{N}_e}(t_i) = \frac{1}{n(\mathbb{N}_e)} \sum_{i \in \mathbb{N}_e} t_i$. ϵ is a small constant for numerical stability (e.g., $\epsilon = 10^{-6}$). While this approximation works well in most cases, its efficacy depends on the initialization of the fabrication sequence.

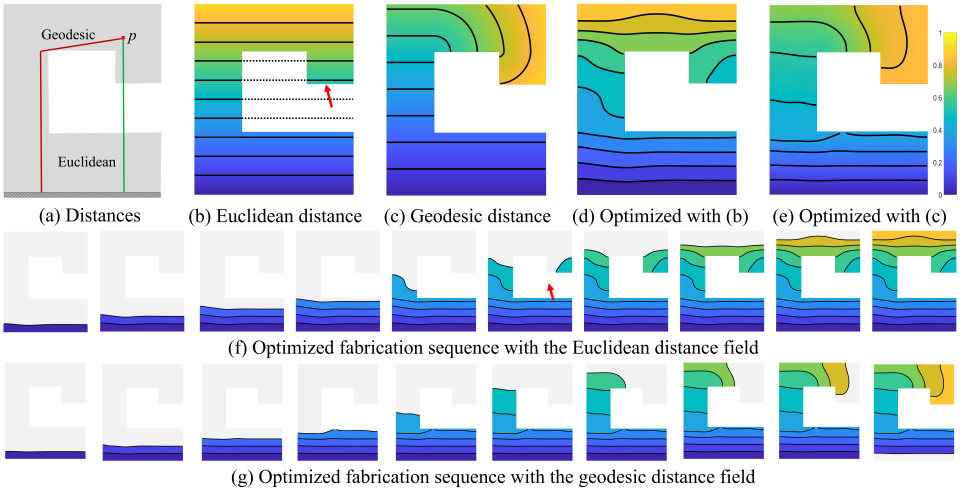

(a) Distances (b) Euclidean distance (c) Geodesic distance (d) Optimized with (b) (e) Optimized with (c)

(f) Optimized fabrication sequence with the Euclidean distance field

(g) Optimized fabrication sequence with the geodesic distance field

Figure 2.3.: Comparison of the Euclidean and the geodesic distance field as the initialization of the time field for fabrication sequence optimization. (a) A 2D component. The Euclidean distance and the geodesic distance from location p to the build plate at the bottom are shown by the green line and the black polyline, respectively. (b) The Euclidean distance field. (c) The geodesic distance field. (d) The optimized time field using (b) as initialization. (e) The optimized time field using (c) as initialization. The sequences corresponding to the time fields in (d) and (e) are shown in (f) and (g), respectively.

2.2.3. INITIALIZATION OF FABRICATION SEQUENCE

The initialization of the fabrication sequence greatly influences the validity of optimized sequences, especially when the structural layout is complex. Distance fields serve as a good option for initialization as they can mimic the progression of additive manufacturing. A distance field is a scalar field, representing the minimal distance from each point in the domain to a certain shape, i.e., the build plate. Depending on the distance metric, the distance field has quite different features. Fig. 2.3 compares the effects of two distance metrics as initialization for sequence optimization. The component is illustrated in Fig. 2.3(a), where a horizontal build plate is located at the bottom[1]. The two distance metrics under comparison are the Euclidean distance and geodesic distance. The Euclidean distance measures the shortest path (i.e., a straight line) between a point and the build plate. The Euclidean distance is irrespective of the shape of the component. In contrast, the geodesic distance measures the shortest path, within the component, from a point to the build plate. The shortest Euclidean path and geodesic path for a single point are illustrated in Fig. 2.3(a). The corresponding distance fields, together with iso-contours, are visualized in Fig. 2.3(b) and (c). Both distance fields are normalized by dividing the distance values over the corresponding largest distance. In Fig. 2.3(b),

[1] In multi-axis additive manufacturing, the build plate is not necessarily flat nor located at the bottom.

the iso-contours of the Euclidean distance field are planar. On the right-hand side of the domain, there is an overhanging feature, and there the iso-contours are separated by the void region. In contrast, in Fig. 2.3(c), the geodesic distance field is free of local minima. The iso-contours of the geodesic distance field in the top-right of the component are curved. The optimized fabrication sequences starting from these two initial sequences are shown in Fig. 2.3(d) and (e), while the corresponding layered fabrication processes are shown in (f) and (g), respectively. It can be seen in Fig. 2.3(f) that during fabrication, an isolated layer appears at stage 6. This shows that the optimization is incapable of eliminating the local minimum inherited from the initial field. While this violates the constraint in Eq. 2.5, it numerically satisfies the approximated version (Eq. 2.8). Setting a smaller threshold (ϵ) proves to be ineffective. Even though the approximated constraint is not precisely satisfied, the optimization is incapable of steering the location of the local minimum such that it disappears. This experiment shows the importance of a valid initial sequence that can mimic the progression of additive manufacturing and is free of local minima. The geodesic distance field fulfills these requirements.

The geodesic distance field is free of local minima. This can be explained as follows: consider an arbitrary point in the component that is not on the build plate. The geodesic distance field represents the shortest path from this arbitrary point (denoted by A) to the build plate (denoted by B). Any point on this shortest path, known as the geodesic path, is by definition within the component. As a point moves along the shortest path from A to B, its geodesic distance to B decreases monotonically. Therefore, in the vicinity of point A, there always exists a point on the geodesic path from A to B with a geodesic distance smaller than that of A. Consequently, any point A does not represent a local minimum in the geodesic distance field.

2.3. REGULARIZATION OF SPACE-TIME TOPOLOGY OPTIMIZATION

As discussed in the previous section, using the geodesic distance field to initialize the time field is promising for optimizing the fabrication sequence when the structural layout is fixed. However, it is not directly applicable to space-time topology optimization, where the structural layout, including its topology, evolves during the optimization process.

In this section, we present a novel approach to regularize the time field in order to avoid the occurrence of local minima in the context of space-time topology optimization. Specifically, we relate the time field to the solution of a heat equation, i.e., a temperature field. The temperature field is monotonic along its propagating direction and free of local minima. Furthermore, the heat equation is defined on the structural layout, and the resulting temperature field is sensible to changes in the structural layout. The monotonicity and the sensibility to shape changes are essential features of the geodesic distance field. Furthermore, by adapting the parameters in the heat equation we can accommodate intermediate density values as encountered during optimization. Our adoption of the heat equation is inspired by advancements

in computer graphics, where research has demonstrated that the heat equation offers a computationally efficient means for calculating an approximate geodesic distance field [36]. In topology optimization for additive manufacturing, heat equations were previously used for identifying enclosed voids and consequently avoiding them [104, 108].

2.3.1. OPTIMIZATION WORKFLOW

The workflow of space-time topology optimization using heat equations for regularizing the time field is illustrated in Fig. 2.4. We employ a density field ($\boldsymbol{\rho}$, $\rho_e \in [0,1]$) to represent the complete structure and a time field ($\boldsymbol{t}$, $t_e \in [0,1]$) to encode the fabrication sequence. While the density field eventually converges to either 0 or 1, the time field is continuous. The product of $\boldsymbol{\rho}$ and $\boldsymbol{t}$ is projected into a series of intermediate structures, using increasing threshold values $\tau_j = \frac{j}{N}$, with $j = 0, ..., N$ and N being the prescribed number of layers. Rather than taking $\boldsymbol{\rho}$ and $\boldsymbol{t}$ as design variables, we introduce two auxiliary fields, $\boldsymbol{\phi}$ and $\boldsymbol{\mu}$. The density field $\boldsymbol{\rho}$ is computed from design field $\boldsymbol{\phi}$, following a density filter ($\tilde{\boldsymbol{\phi}}$) and a smoothed Heaviside projection ($\bar{\tilde{\boldsymbol{\phi}}}$). This process ($\boldsymbol{\phi} \rightarrow \tilde{\boldsymbol{\phi}} \rightarrow \boldsymbol{\rho} = \bar{\tilde{\boldsymbol{\phi}}}$) is commonly used in density-based topology optimization, and thus not included in the workflow illustration.

The novel element in the workflow is the transformation from $\boldsymbol{\mu}$ and $\boldsymbol{\rho}$, through $\boldsymbol{T}$, to $\boldsymbol{t}$. We use a heat equation to obtain a monotonic time field defined on an evolving structural layout $\boldsymbol{\rho}$ with heterogeneous thermal diffusivity $\boldsymbol{\mu}$. The solution of the heat equation is a virtual temperature field $\boldsymbol{T}$. It is important to note that this virtual temperature field shall not be confused with the temperature field coming from the thermal process involved in metal additive manufacturing. Here the heat equation is meant to create a monotonic field, rather than predicting the actual temperature distribution during fabrication. Conceptually, it works as follows. An artificial heat source is placed on the build plate (at the bottom of the domain), from where the heat diffuses through the structure. This creates a continuous temperature distribution within the structure. The heat source has a constant temperature of 1. At a location in the structure further away from the heat source, its temperature approaches 0. The time field, ascending from the build plate, is defined as $\boldsymbol{t} = \mathbf{1} - \boldsymbol{T}$.

2.3.2. HEAT EQUATION

To obtain a monotonic temperature field, we construct the following heat equation,

$$\nabla \cdot (\chi \nabla T) - \alpha_{\mathrm{T}} T = 0. \tag{2.9}$$

Here ∇ is the vector differential operator. This partial differential equation represents steady-state heat conduction within a heterogeneous medium, featuring spatially-varying thermal diffusivity $\chi(x, y)$, and a drain term $\alpha_{\mathrm{T}} T$, where α_{T} denotes a constant drain rate. The introduction of the drain term serves a crucial purpose. In the absence of this term, achieving a steady-state temperature distribution with spatial variation would necessitate employing an inhomogeneous Dirichlet boundary condition. However, when dealing with a structure that evolves during space-time

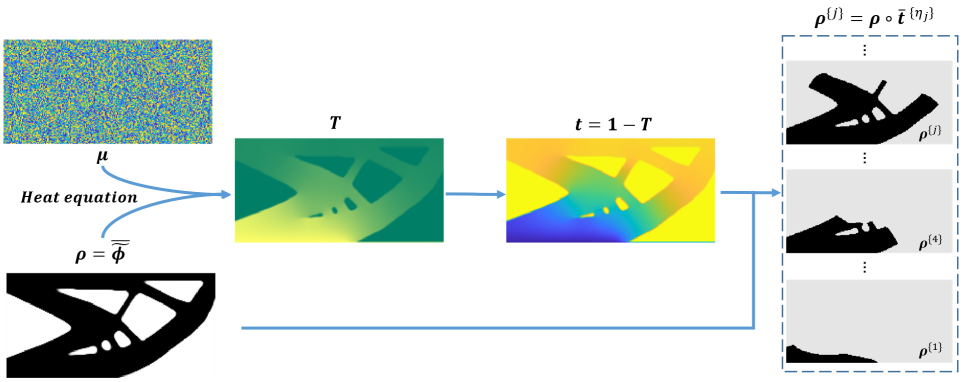

Figure 2.4.: The workflow of deriving a series of intermediate structures $\boldsymbol{\rho}^{\{j\}}$ from the thermal diffusivity field $\boldsymbol{\mu}$ and density field $\boldsymbol{\rho}$.

topology optimization, there is no clear rationale for determining the ideal location of a heat sink. An alternative approach to achieve a spatially-varying temperature distribution is to resort to transient heat conduction, and calculate the temperature distribution at a specific time [36, 197].

The heat equation is subject to the following boundary conditions: At the boundary adjacent to the build plate Γ_0, the temperature is constant, $T\big|_{\Gamma_0} = 1$. Other boundary segments of the structure are thermally insulated, $(\nabla T \cdot \vec{n})\big|_{\Gamma \setminus \Gamma_0} = 0$. Here ∇T represents the spatial gradient of the temperature field, and $\vec{n}$ denotes the normal direction on the boundary of the structure.

The solution of the heat equation, and the corresponding time field together with fabrication sequences, are illustrated in Fig. 2.5. In this example the thermal diffusivity field $\chi(x, y)$ is homogeneous. The temperature field and, consequently, the fabrication sequence are determined by the thermal diffusivity field. To allow the optimization of the fabrication sequence, the thermal diffusivity field is related to design variables $\boldsymbol{\mu}$, augmented by the unitless pseudo-density $\boldsymbol{\rho}$,

$$\boldsymbol{\chi} = \boldsymbol{\rho}\boldsymbol{\mu}. \tag{2.10}$$

The multiplication by the pseudo-density field constrains heat conduction within the structural layout, excluding void regions from the fabrication sequence planning. Additionally, this allows pseudo-densities to take intermediate values during the optimization process, thereby facilitating gradient-based numerical optimization.

We note interesting similarities and large differences to the filters based on Helmholtz-type partial differential equations (PDEs) [89]. In our formulation, the optimization variables (thermal diffusivity) in the PDE and the solution of the PDE (virtual temperature) have different physical interpretations. The desirable characteristic of the PDE is to attain a monotonic scalar field. In contrast, in the PDE filter [89], the optimization variables and the solution both represent density fields. The intention behind it is to get a smoothed scalar field, avoiding checkerboard patterns.

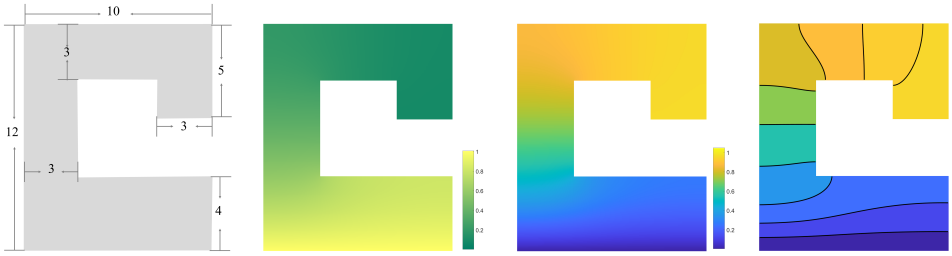

(a) Component (b) Temperature field (c) Time field (d) Sequence

Figure 2.5.: Heat conduction on a given component (a). The start points are the nodes on the bottom boundary. The generated virtual temperature field by solving Equation (2.11) is shown in (c). The light yellow indicates the largest temperature, and the dark blue indicates the smallest virtual temperature. The corresponding time field is shown in (c). The sequence generated with the time field shown in (d) which is composed of 10 layers.

We discretize Eq. 2.9 using the finite element method, resulting in a linear form,

$$\boldsymbol{K}_{\mathrm{T}}\boldsymbol{T} = \boldsymbol{b}, \tag{2.11}$$

where $\boldsymbol{T}$ is the nodal temperature vector. $\boldsymbol{b}$ is the thermal load vector corresponding to the boundary condition. $\boldsymbol{K}_{\mathrm{T}}$ is the global system matrix:

$$\boldsymbol{K}_{\mathrm{T}} = \sum_e \boldsymbol{K}_{\mathrm{T}}^e + \sum_e \boldsymbol{K}_{\mathrm{C}}^e. \tag{2.12}$$

Here the symbol $\sum$ stands for matrix assembly. The first element matrix corresponds to the thermal diffusivity. It is derived from the shape functions N_i and N_j by using the variational principle:

$$\boldsymbol{K}_{\mathrm{T}}^e = \int_{\Omega_e} \chi_e \left(\frac{\partial N_i}{\partial x}\frac{\partial N_j}{\partial x} + \frac{\partial N_i}{\partial y}\frac{\partial N_j}{\partial y} \right) d\Omega. \tag{2.13}$$

The second element matrix corresponds to the drain term:

$$\boldsymbol{K}_{\mathrm{C}}^e = \int_{\Omega_e} \alpha_{\mathrm{T}} N_i N_j \, d\Omega. \tag{2.14}$$

In our implementation, instead of calculating a consistent matrix $\boldsymbol{K}_{\mathrm{C}}^e$ from the shape functions using Eq. 2.14, we adopt a lumped matrix for simplicity, assuming that the drainage is lumped at the nodes.

The nodal temperature distribution from solving Eq. 2.11 is transformed into an elemental temperature field using bi-linear interpolation. Afterwards, the time field is computed by $\boldsymbol{t} = \mathbf{1} - \boldsymbol{T}$.

PARAMETER ANALYSIS

The constant drain rate α_{T} is a key parameter in the heat equation. Alongside the thermal diffusivity $\boldsymbol{\chi}$, this parameter plays a significant role in determining the

temperature distribution. To be able to generate layers of comparable size, the temperature distribution shall be smoothly varying between 0 and 1. Fig. 2.6 shows that a too small or large drain rate results in layers with significant variations in size. The domain is homogeneous in terms of thermal diffusivity $\boldsymbol{\chi}$, taking a value of 0.1. The heat source, with a constant temperature of 1, is placed on the bottom of the domain. If the drain rate is large, the temperature rapidly decreases to 0, as shown in Fig. 2.6(d). After the transformation $\boldsymbol{t} = \mathbf{1} - \boldsymbol{T}$, and with uniformly sampled thresholds $\tau_j = \frac{j}{N}$, the layers are squeezed to the bottom. Reversely, a small drain rate also leads to uneven layers, see Fig. 2.6(b). The segmentation in Fig. 2.6(c) is more uniform, providing a good starting point for the optimization of the thermal diffusivity field towards the desired segmentation of the domain into layers of equal size. To ensure numerical convergence, the thermal diffusivity variable $\boldsymbol{\mu}$ is constrained within the range of 0 to 1, matching the range of the density variable $\boldsymbol{\phi}$.

The temperature distribution is also affected by the size of the design domain. We introduce a size-independent parameter to help choose an appropriate drain rate. This parameter, denoted as β, relates the drain rate (α_T) to the characteristic length of the design domain (l_c),

$$\alpha_\mathrm{T} = \beta / l_c^2. \tag{2.15}$$

The unit of the drain rate is $\mathtt{m}^{-2}$, while the unit of the length is $\mathtt{m}$. Thus β is non-dimensional. We choose the longest path of heat diffusion in the design domain as its characteristic length.

In Fig. 2.6(e) we compare the temperature distribution under five different β values. When $\beta = 1$, the resulting temperature smoothly decreases from 1 on the left, to close to 0 on the right. From numerical tests we observed good convergence in the optimization of $\boldsymbol{\mu}$ and $\boldsymbol{\phi}$ with $\beta \in [0.1, 1]$. Slight derivation from this range does not lead to dramatic convergence issues. It is robust for different domain sizes and volume fractions. In the results section, $\beta = 0.1$ is consistently used for all examples.

2.3.3. FORMULATION OF SPACE-TIME TOPOLOGY OPTIMIZATION

To summarize, the space-time topology optimization using the heat equation is generically formulated as follows.

$$\underset{\boldsymbol{\phi},\boldsymbol{\mu}}{\text{minimize}}: \quad f = f_0(\boldsymbol{\rho}) + \sum_{j=1}^{N} w_j f_j(\boldsymbol{\rho}^{\{j\}}), \tag{2.16}$$

$$\text{subject to}: \quad \boldsymbol{K}(\boldsymbol{\rho})\boldsymbol{U} = \boldsymbol{F}, \tag{2.17}$$

$$\boldsymbol{K}^{\{j\}}(\boldsymbol{\rho}^{\{j\}})\boldsymbol{U}^{\{j\}} = \boldsymbol{F}^{\{j\}}, \quad j = 1, ..., N, \tag{2.18}$$

$$\boldsymbol{K}_\mathrm{T}(\boldsymbol{\phi},\boldsymbol{\mu})\boldsymbol{T} = \boldsymbol{b}, \tag{2.19}$$

$$g_0(\boldsymbol{\rho}) = \sum \rho_e v_e - V_0 \leq 0, \tag{2.20}$$

$$g_j(\boldsymbol{\rho}^{\{j\}}) = \sum \rho_e^{\{j\}} v_e - \frac{j}{N} V_0 \leq 0, \quad j = 1, ..., N, \tag{2.21}$$

$$0 \leq \phi_e \leq 1, \forall e \in \mathcal{M}, \tag{2.22}$$

$$0 \leq \mu_e \leq 1, \forall e \in \mathcal{M}. \tag{2.23}$$

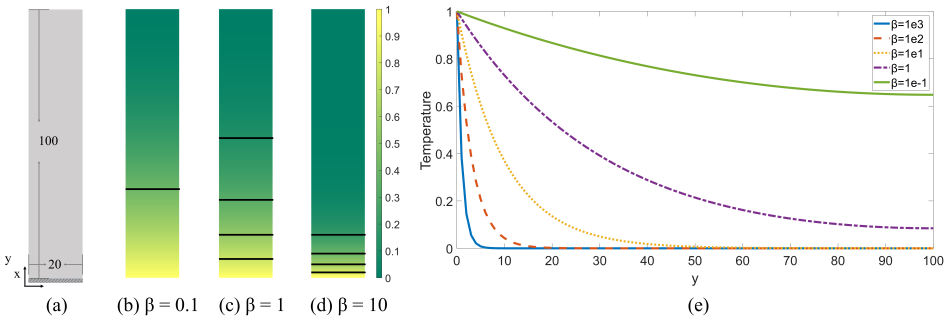

Figure 2.6.: The influence of the drain rate on the temperature distribution. (a) A rectangular component with a homogeneous thermal diffusivity. The virtual heat source with a fixed temperature of 1 is located at the bottom of the domain. (b, c, d) Virtual temperature distributions with $\beta = 0.1$, 1, and 10, respectively. The black lines represent the iso-contours of the temperature fields at temperature values of 0.2, 0.4, 0.6, and 0.8, which are intended to segment the component into 5 layers of comparable size. (e) Temperature distributions along a vertical line in the middle of the component, with five different β values.

The objective function f is composed of two parts. f_0 accounts for the performance of the final overall structure, while f_j is related to each intermediate structure during the fabrication process. The different objectives are balanced by the weighting factors w_j. The overall structure and intermediate structures all have their governing mechanical equation, i.e., Eq. 2.17 and Eq. 2.18, respectively. These mechanical equations are independent of each other, and thus can be solved in parallel. $\boldsymbol{K}$ and $\boldsymbol{U}$ are the global stiffness matrix and displacement vector corresponding to the overall structure, respectively, and $\boldsymbol{F}$ is the external force. The global stiffness matrix $\boldsymbol{K}^{\{j\}}$ of intermediate structures is determined by both the density variables ϕ and the diffusivity variables μ. The load vector $\boldsymbol{F}^{\{j\}}$ may also be dependent on these variables, e.g., process-dependent thermomechanical loads. Eq. 2.19 is the heat equation for obtaining a monotonic temperature field, as introduced in the previous subsection. The overall material usage is constrained in Eq. 2.20, while an even amount of material for each intermediate structure is described by Eq. 2.21 to ensure a constant fabrication speed.

Here, we present the general formulation of space-time topology optimization. For a more in-depth exploration of objective and constraint functions in specific application scenarios, such as structural compliance and thermal-induced distortion during fabrication, readers can refer to [168, 169]. When considering the entire density field as fixed, the optimization model described above simplifies into the formulation outlined in Section 2.2.2, focusing solely on sequence optimization.

We solve the optimization problem using the method of moving asymptotes (MMA) [153]. MMA is a gradient-based optimization method commonly used to solve large-scale, non-linear programming problems, particularly those arising from topology optimization. Its core concept involves transforming a complex, non-linear

optimization problem into a series of simpler, convex sub-problems that are easier to solve. In each iteration, MMA approximates the original nonlinear objective function and constraints with convex, separable functions, using dynamically adjusted asymptotes to ensure stability and convergence.

The general procedure for the calculation of the sensitivity / gradient is consistent with those described in [168, 169]. The primary distinction arises from the fact that the time field is no longer a direct design variable; it functions as an implicit variable dependent on both density ϕ and diffusivity μ. An adjoint analysis step is needed, as can be found in the appendix A.1.

2.4. RESULTS AND DISCUSSION

In this section, we first demonstrate that the effectiveness of the proposed method is independent of the initialization of the optimization variables, in contrast to prior formulations with explicit constraints (Section 2.4.1). We then evaluate our method for different application scenarios, including the minimization of gravity-induced distortion of intermediate structures during construction (Section 2.4.2), and minimization of thermal-induced distortion of fixed structural layout (Section 2.4.3) and by concurrent optimization of the structural layout and fabrication sequence (Section 2.4.4). Lastly, we test the proposed method for space-time topology optimization of 3D structures (Section 2.4.5). In all experiments, the Young's modulus was fixed at 1.0, and the Poisson's ratio was fixed at 0.3. Unless stated otherwise, in all 2D tests, we set 20 layers and a volume fraction of 0.6. The method was implemented in Matlab.

2.4.1. VALIDATION OF AVOIDING LOCAL MINIMA

The first example is intended to validate that our new formulation avoids the appearance of local minima in the time field. The test is performed on a cantilever beam, as illustrated in Fig. 2.7. The design domain is discretized into a regular quadrilateral mesh with the resolution of 210×140. The objective is to reduce the compliance of the entire component, under a load on the top-right corner. Process-dependent loads on intermediate structures are not considered in this test, by setting w_j in Eq. 2.16 to zero. To test the robustness of the new formulation, we run space-time topology optimization with different initializations of the optimization variables. We study in particular different initializations of the thermal diffusivity field $\boldsymbol{\mu}$. For the density-related field $\boldsymbol{\phi}$, we initialize it with a uniform density of the target volume fraction.

Figure 2.8 compares the results obtained using the original formulation [168] and the proposed new formulation, under different initializations. All results were generated with 500 optimization iterations. The three initializations are shown in the first column, from top to bottom, random, monotonic, and uniform. The second and third columns visualize the optimized time field and corresponding fabrication sequence, respectively, obtained using the original formulation where the optimization variables are the time field [168]. Under random as well as uniform initialization of the time field, the optimized time fields exhibit multiple local minima

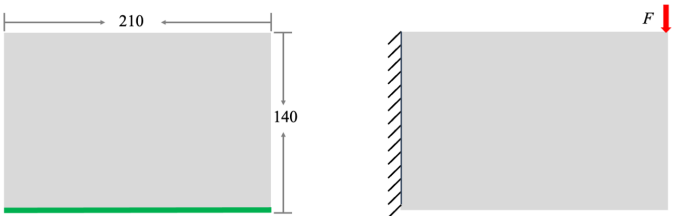

Figure 2.7.: Illustration of the problem setup. Left: the build plate (green) is placed at the bottom of the design domain, meaning the structure is to be constructed from the bottom upwards. Right: the boundary condition of the structure in its intended use scenario.

and maximum. Only the monotonic initialization results in a clear fabrication sequence. The last two columns visualize the optimized results with the proposed regularization. Here, regardless of the initialization of the thermal diffusivity field $\boldsymbol{\mu}$, the optimized time fields are monotonic. The time values increase, within the shape of the optimized structural designs, from the bottom which is prescribed as the build plate, to the up boundary of the domain. The areas outside of the optimized structural designs take a time value of 1, i.e., the upper bound of time values. The monotonic increase of the time field is also clearly visible from the optimized sequence shown on the right-hand side. In all tests, the compliance values are comparable. This is because the time field in this example is only used to segment the evolving structural layout into layers of equal areas, and no sequence-dependent loads are applied.

Fig. 2.9 plots the convergence curves of the objective function (left) and volume constraint per layer (right), corresponding to the optimization with a uniform thermal diffusivity field. The optimization stabilizes after about 200 iterations. A continuation is applied to the projection parameter β_t in Eq. 2.3. From these curves, we can see that the objective function converges well and all volume constraints are satisfied. Fig. 2.10(left) shows the history of the difference in the objective function between two successive iterations. After about 200 iterations, the difference becomes smaller than $\epsilon = 0.001$. Fig. 2.10(right) plots the maximum change in the two sets of optimization variables during the design update in each iteration. A move limit of 0.05 was prescribed for both the density variable ϕ and thermal diffusivity variable μ. After 200 iterations the maximum change in ϕ drops from the move limit of 0.05 to less than 0.005 and then stabilizes.

2.4.2. SPACE-TIME TOPOLOGY OPTIMIZATION UNDER GRAVITY LOADS

Our next example is the concurrent optimization of the structural design and fabrication sequence under gravity loads, a problem that has been studied in Ref. [168]. During fabrication, the self-weight of the intermediate structure may result in large deflection. The weight of the intermediate structure increases as the fabrication progresses, and it is dependent on the fabrication sequence. In this example, the objective function consists of two parts. The first part is the compliance

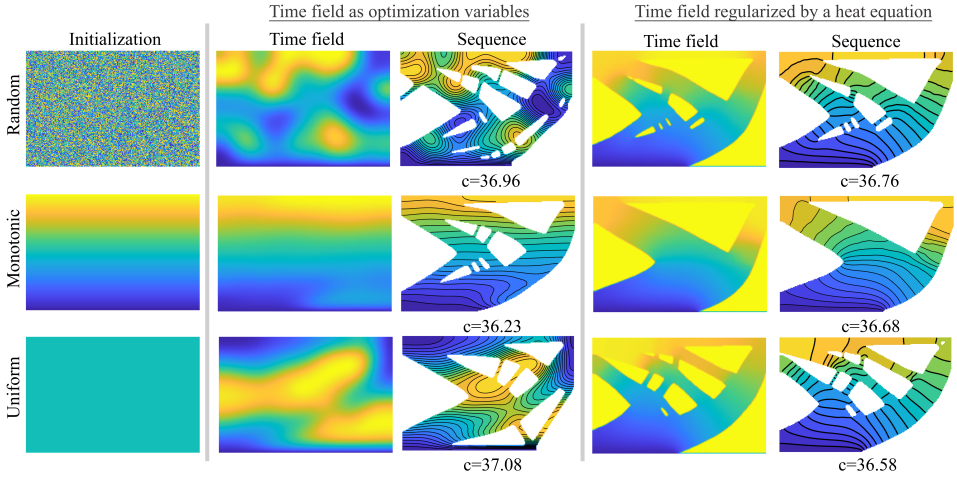

Figure 2.8.: Comparison of space-time topology optimization with the time field as optimization variables [168] and using the proposed regularization. The three different initializations are, from top to bottom, random, monotonic, and uniform. When using the time field as optimization variables, the time field is initialized, while in our proposed method, the initialization is applied to the thermal diffusivity field $\boldsymbol{\mu}$. Using the proposed regularization, the optimized time field is monotonic, regardless of the initial values.

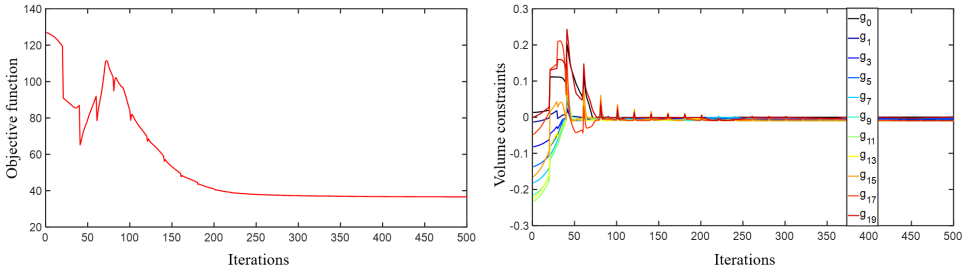

Figure 2.9.: The convergence curves of space-time optimization with regularization. Left: the objective function. Right: the per-layer volume constraints.

of the final structure, under the boundary condition as illustrated in Fig. 2.7(right). The second part is the sum of the compliance values of intermediate structures under self-weight. These two parts are integrated with a weighting factor α in Eq. 2.16. We note that the boundary condition for simulating the effects of gravity on the intermediate structure is different than that for simulating the load-bearing capacity of the complete structure.

Fig. 2.11 shows the optimization results with five different weighting factors. From left to right, 0.0, 0.1, 2.0, 5.0 and 10.0. The first row shows the optimized time fields. The second row shows the optimized structure as well as the fabrication sequence

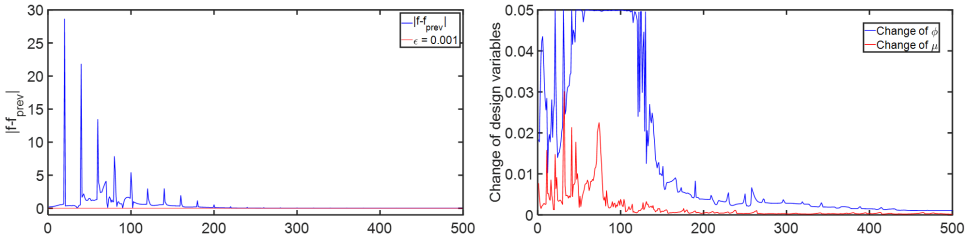

Figure 2.10.: The history of the difference in the objective function between two successive iterations (left), and the maximum change in the optimization variables during the design update of each iteration (right).

according to the time field. In all five cases, the fabrication sequence starts from the bottom of the domain where the build plate is located, and gradually moves upwards. Comparing the five results from left to right, as the weighting factor for intermediate structures increases, the optimized structure exhibits a progressively larger contact region with the build plate and concentrates more material in its lower part.

With this example, we compare the results of concurrent optimization of the structural layout and fabrication sequence with those from a sequential optimization approach. The sequential approach involves first designing the structural layout using classic topology optimization and then optimizing the fabrication sequence. Fig. 2.12(a) shows the structural layout designed with classic topology optimization, using the design domain and boundary conditions shown in Fig. 2.7(right). Subsequently, we optimize the sequence for this fixed geometry, minimizing the sum of the compliances of intermediate structures induced by gravity. The optimized sequence is shown in Fig. 2.12(b). For comparison, the structural layout and fabrication sequence obtained by the concurrent optimization method shown in Fig. 2.11 (with the weighting factor set as $w_j = 0.1$) is included in Fig. 2.12(c). Fig. 2.12(d) compares the compliance of each intermediate structure from both methods. For all 20 intermediate structures, the compliance of the concurrent optimization is consistently less than that of the sequential optimization. For example, at the last stage of fabrication, the gravity-induced compliance is 2.688 versus 0.753, a reduction of 71.99%. This significant reduction in compliance during fabrication is achieved with only a slight increase in the compliance of the total structure under its intended use scenario, with values of 36.04 for sequential optimization and 37.06 for concurrent optimization. This comparison demonstrates the benefits of concurrent optimization of the structural layout and fabrication sequence.

2.4.3. FABRICATION SEQUENCE OPTIMIZATION FOR MINIMIZING THERMAL-INDUCED DISTORTION

In the third set of numerical experiments, we validate our method in fabrication sequence optimization for minimizing the distortion induced by process-dependent

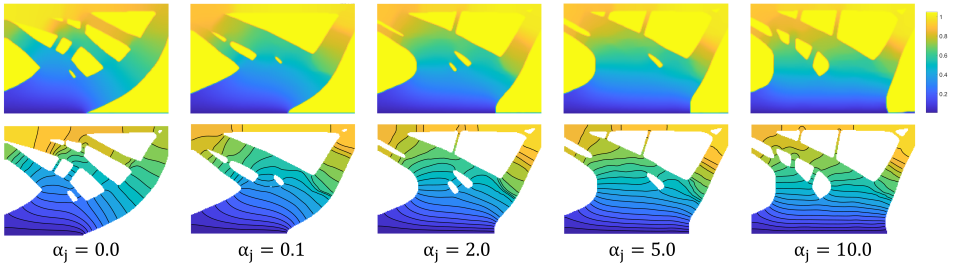

Figure 2.11.: Space-time topology optimization with gravity loads on intermediate structures. From left to right, the weighting factor for intermediate structures increases from 0.0 to 10.0. Top: the optimized time fields. Bottom: optimized structural layouts with the corresponding fabrication sequence.

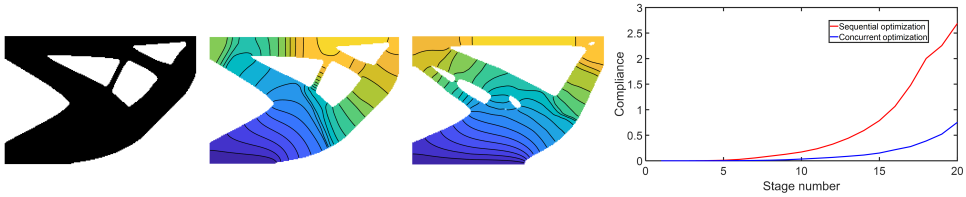

Figure 2.12.: Comparison of results from concurrent optimization (c) and sequential optimization. Sequential optimization involves first designing the structural layout using classic topology optimization (a) and then optimizing the fabrication sequence (b). The compliances of intermediate structures from both methods are shown in (d).

thermomechanical loads. Manufacturing-induced distortion is a critical challenge in metal additive manufacturing. It is caused by the intense energy input and large temperature gradients that occur during fabrication process, which lead to uneven thermal expansion and contraction within the material. In a previous work [169], the time field was directly optimized to minimize the distortion accumulation during manufacturing. As shown in Fig. 2.3, the feasibility of the optimized sequence depends on the initial values of the time field.

We test the proposed regularization on fabrication sequence optimization for three components, shown in Fig. 2.13. The green line at the bottom of each component indicates the build plate. The objective is to minimize thermal-induced distortion. In (a) the distortion is represented by the flatness of the blue edge, measured by the relative vertical displacements of nodes on the edge. In (b) the distortion is represented by the flatness of a horizontal and a vertical edge, both indicated by blue lines. In (c) the distortion is represented by the relative vertical displacements of two nodes on the top edge, indicated by blue dots. The distortion due to process-dependent thermomechanical loads is simulated using the inherent strain method, which will be explained in detail in the following chapter.

The optimized results are visualized in Fig. 2.14. From left to right, the optimized time field, corresponding fabrication sequence, and resulting distortion. The optimized time field of each component shows a continuous increase from the bottom of the domain to an edge that is furthest. This continuous change can also be observed in the optimized fabrication sequence. In all three examples, the measured distortion values are very small. From the enlarged figures on the right, it can be seen that the intended flatness of the edges is effectively achieved.

2.4.4. CONCURRENT STRUCTURE AND SEQUENCE OPTIMIZATION WITH CONSTRAINTS ON THERMAL-INDUCED DISTORTION

To further demonstrate the effectiveness of the proposed method, we concurrently optimize the structural layout and fabrication sequence. The test was performed on the design domains shown in Fig. 2.13(a) and (c). The objective is to minimize the compliance of the final structure under the boundary condition as illustrated. The optimization is subject to a bound on the thermal-induced distortion. The measurement of distortion follows the previous subsection. The target volume fractions of the two components are 0.5 and 0.6, respectively.

Fig. 2.15 visualizes the optimized structural layouts, time fields, fabrication sequences, and manufacturing-induced distortions. Despite the complexity of the optimized geometries, the time fields remain continuous throughout the solid regions. The absence of local optima in the time fields highlights the effectiveness of the proposed method.

2.4.5. SPACE-TIME TOPOLOGY OPTIMIZATION OF 3D STRUCTURES

The proposed regularization method is also tested on space-time topology optimization of 3D structures. The design domain and boundary condition are illustrated in Fig. 2.16(a). The left side of the domain is fixed, while a distributed load is applied on the top-right edge. The objective is to minimize compliance under this boundary condition. This is subject to a constraint on thermal-induced distortion,

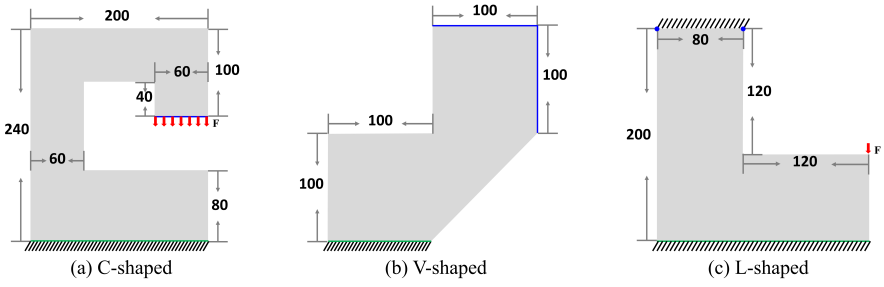

(a) C-shaped (b) V-shaped (c) L-shaped

Figure 2.13.: Illustration of the three components used in fabrication sequence optimization. The build plate (green) is located at the bottom of each domain. The objective is to minimize the thermal-induced distortion, measured on the geometric features marked in blue.

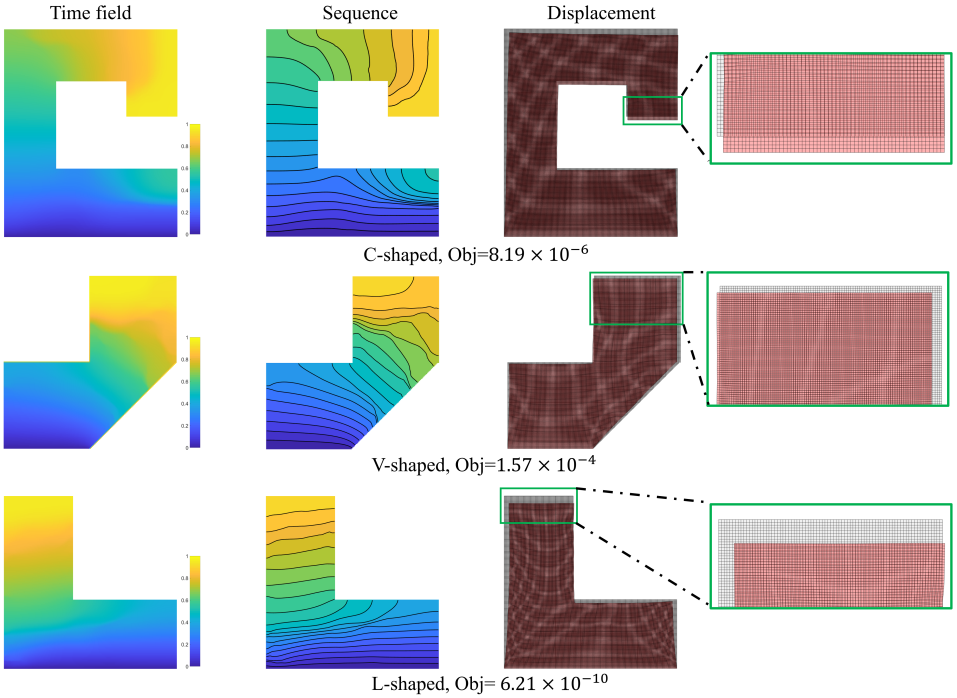

Figure 2.14.: Results of fabrication sequence optimization for distortion minimization. From left to right: the optimized time field, fabrication sequence, and simulated displacement field.

which is represented by the flatness of the edge where the external load is applied, i.e., the relative displacement of nodes on this edge along the x- and z-axis due to process-dependent thermomechanical loads. The constraint on thermal-induced distortion is set as

$$g_{\mathrm{d}} = \frac{1}{n(\mathscr{I})} \sum_{i \in \mathscr{I}} ((x_i - \bar{x})^2 + (z_i - \bar{z})^2) - 0.01 \leq 0.0, \tag{2.24}$$

where $\mathscr{I}$ is the set of nodes on the edge of interest. $n(\mathscr{I})$ is the number of nodes in this set. x_i and z_i and are the displacement of the i-th node in the x- and z axis, respectively. $\bar{x}$ and $\bar{z}$ are the average of displacements in the x- and z axis, respectively. The build plate is situated at the bottom of the domain, meaning the construction of the structure will proceed from the bottom up. The design domain is discretized into hexahedral finite elements with the resolution of $60 \times 20 \times 30$. The volume fraction is 0.2, and the number of layers is 10.

The optimized time field is shown in Fig. 2.16(b), while the optimized structure under thermal-induced distortion is visualized in (c). The flatness of the target edge is clearly visible. Also shown in (c) are the segmented layers, indicated by the varying colors. A simulation of the fabrication sequence is shown in (d). Additionally,

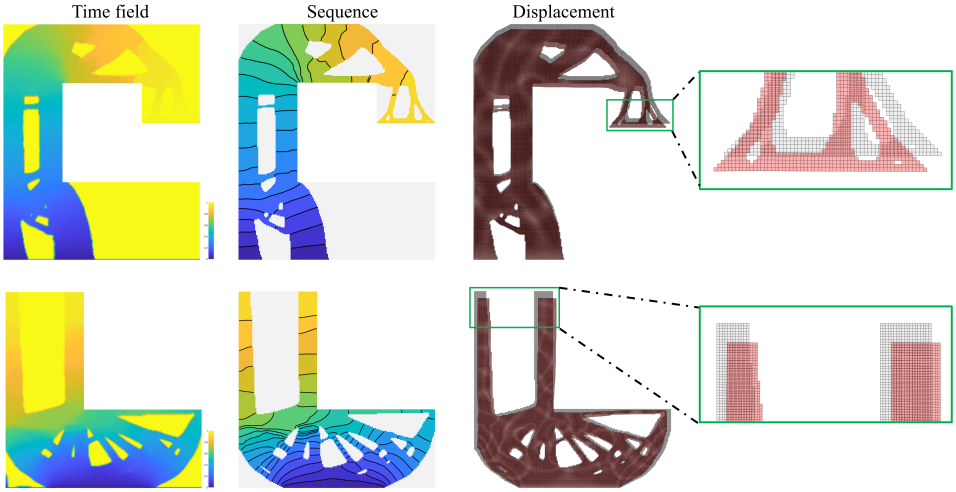

Figure 2.15.: Results of space-time topology optimization under constraints on thermal-induced distortion. From left to right: the optimized time field, fabrication sequence, and simulated displacement field.

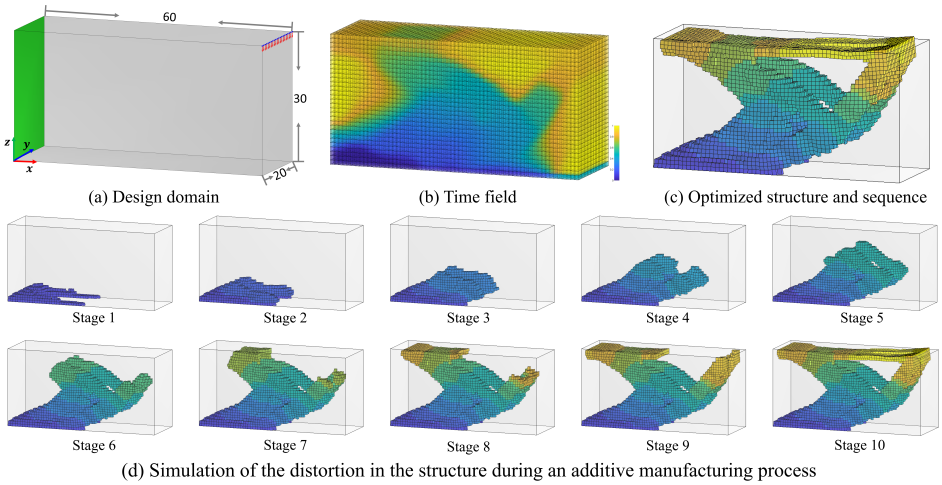

Figure 2.16.: Space-time topology optimization of a 3D structure. (a) The design domain and boundary conditions. (b) The optimized time field. (c) Simulation of the distortion in the optimized structural layout with the corresponding fabrication sequence. (d) Simulation of intermediate structures during the fabrication process.

Fig. 2.17 shows the convergence curves of the objective function and the constraint on thermal-induced distortion. The optimization stabilizes after about 250 iterations.

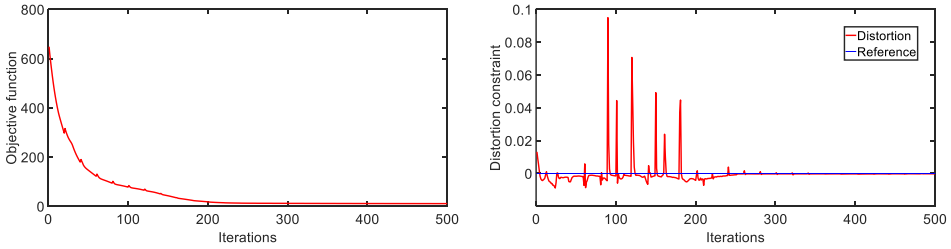

Figure 2.17.: The convergence curves of the objective function (left) and the distortion constraint (right) of the 3D example in Fig. 2.16. The blue reference line indicates that the distortion constraint function is approaching zero.

2.5. CONCLUSIONS

In this chapter, we present a novel method for regularizing the time field in space-time topology optimization. Instead of directly treating the time field as optimization variables, we employ a static heat equation with a drain term to derive a monotonic pseudo-temperature field. We then consider spatially varying thermal diffusivity in the heat equation as optimization variables. This approach effectively prevents local minima from appearing in the optimized time field, regardless of the initial values used in optimization. This approach is easily extendable to deal with 3D components. We demonstrate its effectiveness in additive manufacturing scenarios, which involve process-dependent loads such as gravity and thermomechanical loads on intermediate structures.

A monotonically progressing time field is fundamental for ensuring the viability of the interpreted fabrication sequence. This work thus lays a solid foundation for further advancements in space-time optimization for multi-axis additive manufacturing. As part of our future work, we are exploring methods to regularize the thickness of curved layers. While multi-axis additive manufacturing facilitates curved layers, approaching nearly uniform thickness remains a desirable goal.

3

LAYER GEOMETRY CONTROL IN FABRICATION SEQUENCE OPTIMIZATION

Multi-axis additive manufacturing enables dynamic adjustments in build direction, opening new possibilities for manufacturing complex structures. To explore its flexibility, curved slicing algorithms have been developed. These algorithms typically focus on geometric aspects such as surface quality and collision avoidance. However, the physical implications of fabrication sequences, including residual stresses and distortions, are often overlooked. The space-time optimization framework has been proposed for fabrication sequence optimization to minimize manufacturing-induced structural distortion. This framework parameterizes the fabrication sequence using a pseudo-time field, with layers being segmented using the isosurfaces of the scalar field. Despite its promise, the layers produced by the optimization framework often exhibit significant geometry variations, rendering them impractical for manufacturing. To address this issue, this chapter introduces a layer geometry control scheme to improve the thickness uniformity within each layer. It also ensures that the thicknesses of all layers remain within feasible limits. In addition, the curvatures of the layer boundaries are controlled in order to mitigate concave shapes that are prone to collision. The scheme evaluates the layer thickness based on the gradient of the pseudo-time field, and the local curvature is calculated using the Hessian matrix. Numerical results have demonstrated that the proposed method improves layer geometry uniformity, demonstrating its effectiveness in optimizing for multi-axis additive manufacturing.

Parts of this chapter is in preparation to be submitted to a journal.

3.1. INTRODUCTION

BY adding material layer upon layer, additive manufacturing offers great flexibility for producing components with complex geometries, many of which are impossible or cost-prohibitive with traditional manufacturing. Its integration with robotic arms has increased the manufacturing flexibility even further, which opens up the possibility of depositing material along curved layers by continuously varying the orientation of the end effector in relation to the baseplate. Such multi-axis additive manufacturing systems have been developed to print with both polymers and metals: material extrusion for polymers [38, 198] and wire arc additive manufacturing (WAAM) for metals [44, 135, 171].

Slicing [71, 114, 188] is a crucial step in additive manufacturing. It refers to the process of converting the digital model into a series of 2D layers that the printer can sequentially build up to create the physical object. In conventional additive manufacturing using planar layers, the printing direction is constrained by the orientation of the component. In contrast, multi-axis additive manufacturing enables curved printing [54, 55, 137, 185, 202], where structures can be sliced along free-form surfaces. Curved slicing allows for localized adjustment of the printing direction, providing greater flexibility in the fabrication process. This capability has significantly transformed the way structures can be manufactured.

A variety of slicing algorithms have been developed to segment the designed part into curved layers. These algorithms often use a scalar field to represent the fabrication sequence [168]. The scalar field is typically optimized by incorporating manufacturing requirements such as support-free and collision-free constraints [38], mechanical reinforcement through anisotropic material strength [55], or balancing multiple fabrication objectives simultaneously [97, 200]. To achieve a continuous fabrication sequence, the scalar field can also be derived implicitly from the geodesic distance [189], or by mimicking a virtual physical process such as heat transfer [141, 170] and wave propagation [158–160].

However, the above research primarily focuses on creating curved layers that meet geometric constraints, while the physical consequences of the resulting fabrication sequences are overlooked. In additive manufacturing, the sequence in which layers are deposited, commonly referred to as the fabrication sequence, plays a critical role in determining the manufacturing quality [7, 67, 117]. For example, studies have shown that the accumulation of thermal-induced distortion during manufacturing is significantly affected by the fabrication sequence [169].

To explicitly address the influence of fabrication sequencing, a space-time optimization framework [168, 170, 193] has been proposed. In this framework, the fabrication sequence is encoded as a pseudo-time field, allowing a continuous and adaptive representation of layer division. This pseudo-time field can be coupled with a pseudo-density field that defines the structural layout, enabling the extraction and analysis of intermediate structures throughout manufacturing. By modeling both spatial and temporal aspects of manufacturing, this framework provides a powerful tool to evaluate and optimize the entire manufacturing process. In this chapter, we focus on a pure fabrication sequence optimization under the space-time topology optimization framework by fixing the structural layout for simplicity.

However, a critical challenge of the original space-time optimization framework lies in the manufacturability of the resulting layer geometry. As can be seen in Fig. 3.1(a), the resulting layers exhibit irregular variations in layer thicknesses both within individual layers and across different layers. Although some variation in the layer thickness is necessary to create curved layers, excessive irregularities pose serious manufacturing challenges. For polymer-based additive manufacturing, the adaptation of the layer thickness can be implemented by controlling the feed rate of material extrusion [54, 149]. However, for metal applications such as WAAM, dynamically modifying process parameters to adjust layer thickness requires advanced control systems [3, 46, 85, 99, 116, 163, 184, 203] and adds significant complexity. Therefore, it is generally preferable for each layer to maintain a relatively uniform thickness within the capabilities of the manufacturing system [124].

In response to these manufacturability challenges, this chapter introduces a layer geometry control scheme to improve layer geometric consistency within the space-time optimization framework. The proposed approach consists of two key components. First, a layer thickness control method is developed to limit variations and promote uniform thickness across and within layers, as shown in Fig 3.1(b). Building on this, a curvature control method is introduced to enforce the convexity of layer boundaries to avoid collision, further enhancing geometric regularity (see Fig. 3.1(c)). These objectives are embedded into the regularized optimization framework from the previous chapter through the addition of dedicated objective terms and geometric constraints.

The proposed method is applicable to generating curved layers for both FDM and WAAM. In this study, we choose WAAM as the target application to investigate a key trade-off: whether the ability to reduce thermal-induced distortion through fabrication sequence planning is compromised by the introduction of layer geometry control. To simulate the process-induced distortion efficiently, the inherent strain method [119, 129, 140, 157] is adopted as a simplified process simulation model. This approach captures the essential thermo-mechanical behavior by prescribing inelastic strains that are incrementally activated layer by layer, thereby condensing the complex thermal history into a computationally tractable form.

This chapter is organized as follows. Section 3.2 provides a detailed explanation

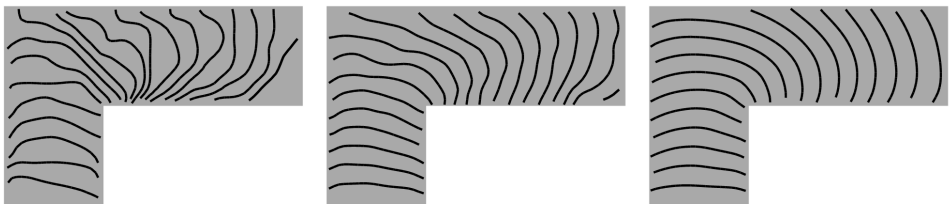

Figure 3.1.: Fabrication sequence optimization for minimizing thermal-induced distortion. (a) Without any layer geometry control. (b) With layer thickness control. (c) With layer thickness control and curvature control.

of the proposed method. In Section 3.3, we demonstrate the effectiveness of the proposed method using 2D and 3D examples. Finally, Section 3.4 summarizes the conclusions and outlines the directions for future work.

3.2. METHODOLOGY

In this section, we begin by describing the parameterization of the fabrication sequence using a pseudo-time field. On this basis, we introduce a new set of uniformity objective functions and layer thickness constraint functions to control layer geometry. We then provide a detailed explanation of the simplified process simulation model, specifically the inherent strain method. Finally, the space-time optimization framework with integrated layer geometry control is established.

3.2.1. PARAMETRIZATION OF FABRICATION SEQUENCE OPTIMIZATION

In space-time topology optimization, the fabrication sequence is paramterized using a scalar field, referred to as the pseudo-time field (or simply, time field). This time field is defined over a finite element discretization of the component, with each element assigned a scalar value t_e, representing the order in which it is fabricated. The time values vary continuously between $[0.0, 1.0]$, with smaller values indicating elements that materialize earlier in the manufacturing process. The concept of the pseudo-time field for encoding fabrication sequences was initially proposed in space-time topology optimization, which concurrently optimizes the structural design and fabrication sequence [168, 170, 180]. Fabrication sequence optimization can be achieved by assuming a fixed structural design in space-time topology optimization [169].

A series of intermediate structures, corresponding to the layer-by-layer manufacturing process, is derived from the time field. We denote the intermediate structure that has been built up to the time point τ by $\boldsymbol{\rho}^{\{\tau\}}$:

$$\rho_e^{\{\tau\}} = \begin{cases} 1.0, & \text{if } t_e \leq \tau, \\ 0.0, & \text{otherwise.} \end{cases} \tag{3.1}$$

Elements with time values smaller than τ have been manufactured and are thus assigned a value of 1.0, while the other elements have not yet been manufactured and are indicated by 0.0. Since this binary classification is not differentiable and does not comply with gradient-based optimization, a smoothed Heaviside function is adopted:

$$\rho_e^{\{\tau\}} = 1 - \frac{\tanh\big(\beta_t \tau\big) + \tanh\big(\beta_t (t_e - \tau)\big)}{\tanh\big(\beta_t \tau\big) + \tanh\big(\beta_t (1 - \tau)\big)}, \tag{3.2}$$

where β_t determines the sharpness of the Heaviside function. The smoothed Heaviside projection introduces grey values (between 0.0 and 1.0) in intermediate structures. These grey values are analogous to those in density-based topology optimization. To steer the grey values towards either 0.0 or 1.0, we apply a continuation scheme by increasing the projection parameter β_t every 50 iterations in optimization.

From the series of intermediate structures, the layers are extracted by calculating the difference between two successive intermediate structures. Suppose the fabrication consists of N layers, and assume an evenly-spaced time points, $\tau_j = \frac{j}{N}$. The j-th layer corresponds to the time interval $[\tau_{j-1}, \tau_j]$, and is calculated by

$$\boldsymbol{\eta}^{\{j\}} = \boldsymbol{\rho}^{\{\tau_j\}} - \boldsymbol{\rho}^{\{\tau_{j-1}\}}. \tag{3.3}$$

The first and last layers are treated slightly differently. The structure at $\tau_0 = 0$ is fully empty ($\boldsymbol{\rho}^{\{0\}} = \mathbf{0}$), and the structure at $\tau_N = 1$ is fully solid ($\boldsymbol{\rho}^{\{1\}} = \mathbf{1}$); the smoothed Heaviside function is not applied to $\tau = 0$ or 1.

TIME FIELD REGULARIZATION

To reflect realistic fabrication sequences, the pseudo-time field must satisfy certain fundamental requirements. First, the time field should be spatially continuous; otherwise, the manufacturing process becomes overly discrete and impractical to implement. Additionally, the time field should be free of local minima, as these represent dangling parts during manufacturing, which would require support structures.

In order to ensure continuity while avoiding local minima on the time field, a regularization method has been introduced in chapter 2. Instead of being directly used as the optimization variables, the time field is obtained from a virtual heat diffusion process:

$$\nabla(\boldsymbol{\mu}\nabla\boldsymbol{T}) - \alpha_{\mathrm{T}}\boldsymbol{T} = 0, \tag{3.4}$$

here $\boldsymbol{\mu}$ is a spatially varying heat diffusivity field. $\boldsymbol{T}$ is a virtual temperature field. ∇ is the vector differential operator, and α_{T} denotes a constant drain rate. When solving the equation, the boundary of the component adjacent to the baseplate is set to a fixed temperature of $T = 1$, while the other boundaries of the component are zero-Neumann boundaries. The time field $\boldsymbol{t}$ is derived from the virtual temperature field $\boldsymbol{T}$ by $\boldsymbol{t} = 1 - \boldsymbol{T}$. By using the element-wise heat diffusivities $\boldsymbol{\mu}$ as optimization variables, the time field $\boldsymbol{t}$ is optimized indirectly. In order to obtain a spatially smoother time field, an averaging-based filtering scheme [17, 23] is adopted for the heat diffusivity:

$$\tilde{\mu}_e = \frac{\sum_{i\in\mathbb{N}_e} H(\boldsymbol{x}_i)\,\mu_i}{\sum_{i\in\mathbb{N}_e} H(\boldsymbol{x}_i)}, \tag{3.5}$$

where $\mathbb{N}_e$ is the neighborhood set of element e within a given radius R. The weighting function $H(\boldsymbol{x}_i)$ is defined by a linearly decaying function measured by the distance between elements:

$$H(\boldsymbol{x}_i) = R - \|\boldsymbol{x}_i - \boldsymbol{x}_e\|. \tag{3.6}$$

The filtered heat diffusivity $\tilde{\mu}_e$ will be used in Eq. 3.4, replacing μ_e. This filtering procedure smoothes the heat diffusivity field, leading to a smoother time field. This is beneficial for obtaining a more uniform gradient of the time field in this research, as will be discussed in the following sections.

Fig. 3.2 illustrates the workflow of fabrication sequence optimization. The geometry (a) is discretized into a finite element model (b), enabling the definition

of element-wise variables. The design variable μ represents a spatially varying heat diffusivity field (c). Solving Eq. 3.4 yields the temperature field, which is then transformed into a time field (d) that encodes slicing information (e). After slicing the structure into layers, a layer-wise process simulation is performed to evaluate process-dependent properties such as distortion (f).

3.2.2. LAYER GEOMETRY CONTROL METHOD

The time field derived from the above heat equation is continuous and free from local minima. However, as can be seen in Fig. 3.1(a), the isolines of the time field are highly irregular and curved with significant fluctuations, making the layers quite nonuniform in geometry. The thickness within each single layer varies significantly, and there are substantial differences in the average thickness between layers. Moreover, the non-smooth layers with sharply inward curves (concavity) can easily cause collision during manufacturing, whereas outward layer boundaries (convexity) are generally preferred for smoother and more continuous fabrication. In this section, a novel method is proposed to reduce the variations of layer geometry in the fabrication sequence optimization framework.

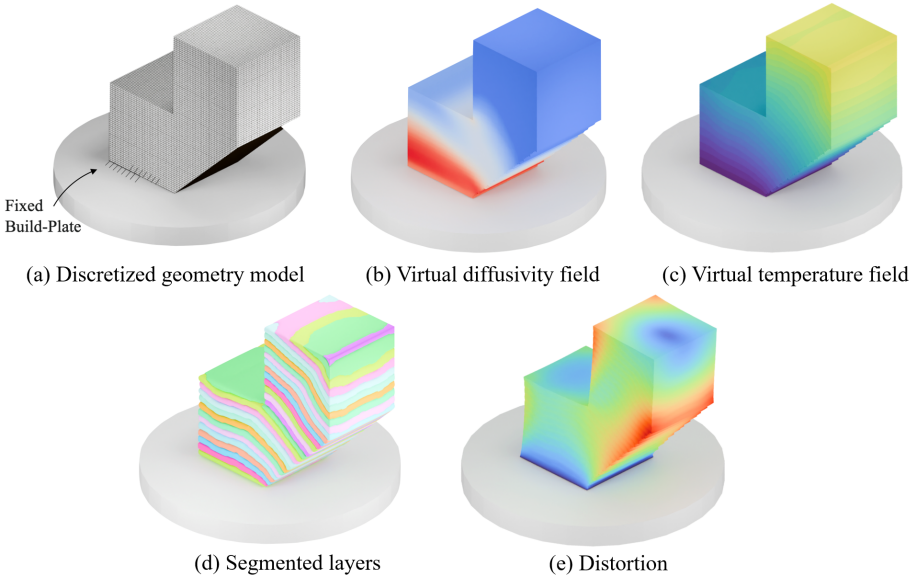

Figure 3.2.: Workflow of fabrication sequence optimization. (a) The geometry component to be sliced, discretized using finite elements in preparation for element-wise variable definition. (b) Element-wise defined heat diffusivities, acting as optimization variables. (c) The temperature field solved from Eq. 3.4, its complement is the time field. (d) Slicing the component using the isosurfaces of the time field, indicating the fabrication sequence. (e) The manufacturing-induced structural distortion, influenced by the fabrication sequence planning.

THICKNESS UNIFORMITY INSIDE EACH LAYER

In most additive manufacturing techniques, dynamically adjusting layer thickness during continuous layer deposition is challenging. However, for free-form curved slicing on components with flat edges, slight variations in layer thickness are needed to achieve effective curvature formation. Therefore, it is crucial to carefully maintain a relatively uniform layer thickness within each layer in slicing. While computing the exact thickness at each point of a free-form layer is a complicated task, the time field in space-time optimization offers a straightforward way to approximate layer thickness by analyzing its gradient.

On a structured mesh, the gradient of the time field can be calculated using the shape function,

$$\begin{aligned}\nabla t_e &= \left[\frac{\partial t}{\partial x}\Big|_e, \frac{\partial t}{\partial y}\Big|_e, \frac{\partial t}{\partial z}\Big|_e\right]^\top \\ &= \left[\sum_{i\in e}\frac{\partial N_i}{\partial x}\,t_i, \sum_{i\in e}\frac{\partial N_i}{\partial y}\,t_i, \sum_{i\in e}\frac{\partial N_i}{\partial z}\,t_i\right]^\top,\end{aligned} \tag{3.7}$$

where $\frac{\partial N_i}{\partial x}$ and $\frac{\partial N_i}{\partial y}$ are the spatial derivative of the shape functions evaluated at the centroid of element e. i is the node belonging to element e, and t_i is the nodal time value.

The gradient field's magnitude represents the local progression rate of the scalar time field, which is related to the spacing between consecutive layer boundaries. The magnitude of the gradient is computed using the Euclidean norm:

$$|\nabla t_e| = \sqrt{\left(\frac{\partial t}{\partial x}\Big|_e\right)^2 + \left(\frac{\partial t}{\partial y}\Big|_e\right)^2 + \left(\frac{\partial t}{\partial z}\Big|_e\right)^2}. \tag{3.8}$$

Similar magnitudes of the gradients over the length of the layer will result in similar thicknesses. To control the thickness uniformity of each single layer, the following formulation is incorporated into the objective function to be minimized:

$$f_{\text{geo}} = \sum_{j=1}^{N}\sum_{e}\eta_e^{\{j\}}\left(|\nabla t_e| - \overline{|\nabla t|}^{\{j\}}\right)^2. \tag{3.9}$$

This objective function resembles the variance function commonly used in statistics. $\eta_e^{\{j\}}$ is the density value of element e in the j-th layer as in Eq. 3.3. By reducing the variance of the gradient magnitudes within the layers, the variation in thickness within each layer is reduced. Here $\overline{|\nabla t|}^{\{j\}}$ is the average of the gradient magnitudes within the j-th layer, being calculated as:

$$\overline{|\nabla t|}^{\{j\}} = \frac{\sum_e \eta_e^{\{j\}}|\nabla t_e|}{\sum_e \eta_e^{\{j\}}}. \tag{3.10}$$

A lower bound $\epsilon_{\min} = 1\times 10^{-5}$ is added to $\eta_e^{\{j\}}$ to avoid singularity when calculating the average gradient magnitude.

THICKNESS UNIFORMITY ACROSS LAYERS

The above objective function is applied to improve the geometric uniformity inside each single layer. However, the geometric uniformity between layers are not ensured yet. It is possible that the geometric dimensions between different layers vary from each other. This requires the printer to adjust its process parameters every time a new layer is deposited, which is indeed applicable. However, the possible layer thickness for a certain additive manufacturing process should be within a certain limit $[d_{\min}, d_{\max}]$, in order to ensure a consistent manufacturing quality.

Based on the uniform layer thickness controlled by Eq.3.9, the thickness of the j-th layer can be approximated using:

$$d_j \approx \frac{\Delta\tau}{\overline{|\nabla t|}^{\{j\}}} = \frac{\tau_j - \tau_{j-1}}{\overline{|\nabla t|}^{\{j\}}}, \tag{3.11}$$

$\Delta\tau = \tau_j - \tau_{j-1}$ is the interval of time points. The quantified layer thickness d_j should be restricted to the permissible limit according to the choice of manufacturing techniques and process parameters:

$$d_{\min} \le d_j \le d_{\max}. \tag{3.12}$$

It is important to note that d_j does not always serve as an accurate approximation of the actual layer thickness, as demonstrated later in Section 3.3.1. Nevertheless, these constraints can offer an effective and efficient approach for layer thickness control within the space-time optimization framework.

CONTROL CURVATURE OF LAYER BOUNDARIES

The layer thickness control methods discussed above do not ensure well-defined layer boundaries. As illustrated in Fig. 3.1(b), some boundaries exhibit concave shapes, curving inward towards the previously manufactured part. Such concavities increase the risk of collisions between the print head and the existing structure. Moreover, they require abrupt changes in printing direction, which can lead to inconsistent material deposition and the formation of local defects. In this section, we introduce a curvature control method to prompt the formation of convex layer boundaries in the fabrication sequence optimization framework.

The curvature of a scalar field can be calculated locally according to the following formulation [62]:

$$\kappa_e = \frac{\nabla t_e^\top \boldsymbol{H}_e^* \nabla t_e}{|\nabla t_e|^3}, \tag{3.13}$$

$\boldsymbol{H}_e^*$ is the adjoint of the Hessian matrix that contains the second derivative information:

$$\boldsymbol{H}_e^* = \begin{bmatrix} \nabla^2 t_{xx} & -\nabla^2 t_{xy} \\ -\nabla^2 t_{yx} & \nabla^2 t_{yy} \end{bmatrix}_e = \begin{bmatrix} \frac{\partial^2 t}{\partial x^2}\big|_e & -\frac{\partial^2 t}{\partial x \partial y}\big|_e \\ -\frac{\partial^2 t}{\partial y \partial x}\big|_e & \frac{\partial^2 t}{\partial y^2}\big|_e \end{bmatrix}. \tag{3.14}$$

Convex regions, where the isoline curves outward, are identified by a positive curvature $\kappa_e > 0$, whereas concave regions, where the isoline curves inward, are characterized by a negative curvature $\kappa_e < 0$.

For C^0-continuous elements, where second derivatives are not directly available, a finite difference scheme can be used to approximate them. Specifically, the gradient (first derivative) computed at the element centroid is first extrapolated to the nodes. Then, the second derivatives within each element are approximated based on these nodal gradient values.

On this basis, we introduce another objective function to penalize concave curvatures of the time field:

$$f_{\text{curve}} = \sum_e \log\left(1 + e^{-P_0 \kappa_e}\right), \tag{3.15}$$

where coefficient P_0 determines the steepness of the penalization and should be set to a moderate value, such as $P_0 = 10$, to prevent numerical overflow. Concavity with negative curvature κ_e is thus penalized in a tunable and differentiable way.

3.2.3. SIMPLIFIED MANUFACTURING PROCESS SIMULATION

In this research, the main objective of fabrication sequence optimization is to minimize the thermal-induced distortion during the additive manufacturing process. To achieve this, the entire manufacturing process should be simulated layer by layer to calculate the accumulation of the total distortion. The inherent strain method is chosen as a simplified process simulation model because of its computational efficiency and its success in similar applications in the literature [16, 26, 113].

In the inherent strain method, the mechanical effects resulting from the complex manufacturing process of thermal cycles and phase transformations are simplified as an inelastic strain field that remains in material. Taking a single element as an example, a strain tensor is assigned to it after its deposition, denoted as: $\boldsymbol{\varepsilon}_0^* = [\epsilon_{xx}, \epsilon_{yy}, \epsilon_{xy}, \gamma_{xy}, \gamma_{yz}, \gamma_{zx}]^\mathsf{T}$. An equivalent nodal force acting upon the nodes of the element can be calculated as:

$$\boldsymbol{F}_e = \boldsymbol{D}^\mathsf{T} \boldsymbol{C} \boldsymbol{\varepsilon}_0^*, \tag{3.16}$$

where $\boldsymbol{D}$ is the strain–displacement relation matrix, and $\boldsymbol{C}$ denotes the elasticity matrix.

A simple illustration of the inherent strain method is shown in Fig. 3.3. It operates at the part scale, assuming that each individual layer is deposited in a single step. Supposing the whole structure is sliced into N layers for additive manufacturing, the accumulation of the thermal-induced distortion is obtained by conducting a set of N linear mechanical analyses formulated as:

$$\boldsymbol{K}^{\{j\}} \boldsymbol{\Delta U}^{\{j\}} = \boldsymbol{F}^{\{j\}}, \quad j = 1, \ldots, N, \tag{3.17}$$

where $\boldsymbol{\Delta U}^{\{j\}}$ is the nodal displacement increment vector associated with the addition of the j-th layer. $\boldsymbol{K}^{\{j\}}$ is the stiffness matrix of the intermediate structure with j layers already manufactured. $\boldsymbol{F}^{\{j\}}$ is the force vector assembled from the equivalent nodal forces of the inherent strains of elements in the j-th layer. According to the linear assumption [119], the total residual distortion $\boldsymbol{U}_{\text{thermal}}$ after finishing the whole

manufacturing process is the summation of all the layer-by-layer distortion $\Delta \boldsymbol{U}^{\{j\}}$:

$$\boldsymbol{U}_{\text{thermal}} = \sum_{j} \Delta \boldsymbol{U}^{\{j\}}. \tag{3.18}$$

Due to the smoothed Heaviside projection used to segment the time field in Eq.3.2, some elements have grey values because they do not fully belong to one specific layer yet. To assemble the stiffness matrix $\boldsymbol{K}^{\{j\}}$, the idea of Solid Isotropic Material with Penalization (SIMP) model from topology optimization is adopted. For calculation, the element stiffness matrix of these grey elements is scaled according to their grey values through:

$$\boldsymbol{K}_e^{\{j\}}(\rho_e^{\{\tau_j\}}) = \left(E_{\min} + (E_0 - E_{\min})\rho_e^{\{\tau_j\}^p}\right)\boldsymbol{K}_0, \tag{3.19}$$

where $\boldsymbol{K}_0$ is the base element stiffness matrix for solid element. p is a penalization factor, typically set as 3 to increase the stiffness contrast between solid and grey elements.

Similarly, the forcing vector $\boldsymbol{F}^{\{j\}}$ associated with the j-th layer deposition is assembled from each element's equivalent nodal force vector:

$$\boldsymbol{F}^{\{j\}} = \sum_{e} \eta_e^{\{j\}^p} \boldsymbol{F}_e. \tag{3.20}$$

A penalization term p is also needed to reduce the effect coming from grey elements at each layer.

3.2.4. OPTIMIZATION FRAMEWORK FOR FABRICATION SEQUENCE PLANNING WITH LAYER THICKNESS CONTROL

The main objective of our research is to minimize the thermal-induced distortion through fabrication sequence planning. This is achieved by defining an objective

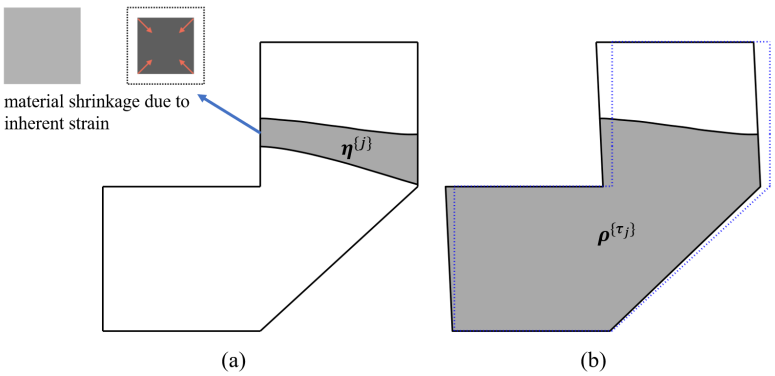

Figure 3.3.: Illustration of the inherent strain method. (a) The inherent strain is applied to the j-th layer upon deposition. (b) The application of inherent strain causes an increment in structural distortion.

function f_{dis} that quantifies the magnitude of local or global structural distortion. For a global measurement, the thermal-induced compliance can be used:

$$f_{\text{dis}} = c_{\text{thermal}} = \boldsymbol{U}_{\text{thermal}}^{\text{T}} \boldsymbol{K} \boldsymbol{U}_{\text{thermal}}, \tag{3.21}$$

where $\boldsymbol{K}$ is the overall stiffness matrix. The physical meaning of the thermal-induced compliance c_{thermal} is the total elastic strain energy needed to distort the whole structure into the current deformation shape.

It is also possible to minimize the distortion of specific nodes by defining a sparse matrix $\boldsymbol{Q}$. $\boldsymbol{Q}$ is symmetric, with only diagonal entries corresponding to the selected nodes set to 1. The objective function is written as:

$$f_{\text{dis}} = \boldsymbol{U}_{\text{thermal}}^{\text{T}} \boldsymbol{Q} \boldsymbol{U}_{\text{thermal}}. \tag{3.22}$$

In summary, the fabrication sequence optimization with layer thickness constraints is formulated as follows:

$$\underset{\boldsymbol{\mu}}{\text{Minimize:}} \quad f_0 = w_1 f_{\text{dis}} + w_2 f_{\text{geo}} + w_3 f_{\text{curve}} \tag{3.23}$$

$$\text{Subject to:} \quad \boldsymbol{K}^{\{j\}} \Delta \boldsymbol{U}^{\{j\}} = \boldsymbol{F}^{\{j\}}, \quad j = 1, 2, ..., N, \tag{3.24}$$

$$\boldsymbol{K}_{\text{T}} \boldsymbol{T} = \boldsymbol{b}, \tag{3.25}$$

$$g_j^{\text{geo1}} = d_j - d_{\max} \leq 0, \quad j = 1, 2, ..., N, \tag{3.26}$$

$$g_j^{\text{geo2}} = d_{\min} - d_j \leq 0, \quad j = 1, 2, ..., N, \tag{3.27}$$

$$\mu_{min} \leq \mu_e \leq 1. \tag{3.28}$$

The total objective function f_0 contains three parts with their individual weight coefficient: w_1 for the process related thermal-induced distortion f_{dis}, w_2 for the thickness uniformity f_{geo}, and w_3 for the curvature control f_{curve}. Since these three objectives may differ by orders of magnitude, we scale them to a value of 10 using their values from the first iteration. Eq. 3.25 is the discretized form of the heat equation in Eq. 3.4. $\mu_{min} = 0.001$ is the lower bound of the heat diffusivity to avoid singularity.

In the current formulation, there is no constraint on the volume of individual layers, leading to varying amounts of material across layers. With a constant material deposition speed, the manufacturing time for each layer will differ. Consequently, the time points associated with the iso-values of the pseudo-time field do not linearly related to the actual manufacturing time.

The optimization problem can be solved using a gradient-based numerical method, specifically the Method of Moving Asymptotes (MMA) [153]. The sensitivity analysis of the functions related to layer thickness uniformity is included in the appendix A.2.

3.3. NUMERICAL EXAMPLES

In this section, we verify the feasibility of the proposed method using numerical examples. We perform the fabrication sequence optimization on two 2D components with different geometries. The proposed method is also validated for 3D cases by taking advantage of high-performance computing based on PETSc [2, 8].

3.3.1. A 2D COMPONENT WITH OVERHANG REGION

The first example is a 2D component with a 45° overhang region, as shown in Fig. 3.4(a). The component is fully fixed at the bottom during manufacturing, and the fabrication process starts from the bottom baseplate. The height of the component is 100 mm in total, and the target layer thickness is 2 mm. The layer thickness is allowed to be varied between 1.6 mm and 2.4 mm. The optimization starts with an initial maximum of 50 layers. In this analysis, we aim to minimize the overall structural distortion by using the thermal-induced compliance as the objective function. The inherent strain value used is: $\boldsymbol{\epsilon}_0^* = [\epsilon_{xx}, \epsilon_{yy}, \epsilon_{xy}]^{\mathrm{T}} = [-0.00375, -0.00375, 0]^{\mathrm{T}}$.

We first make a comparison between space-time optimization with and without layer thickness control, while the curvature control method is switched off. As can be seen in Fig. 3.4(b), without integrating layer thickness control into the fabrication sequence optimization, the resulting layer division becomes disorganized. Certain regions have stacked layers, while others necessitate a substantial increase in layer thickness. Although each layer contains the same material volume, the lack of layer geometric uniformity poses challenges for manufacturing. In contrast, fabrication sequence optimization with layer thickness control can give out a rather smooth time field, as shown in Fig. 3.4(c). The isolines of the time field slice the structure

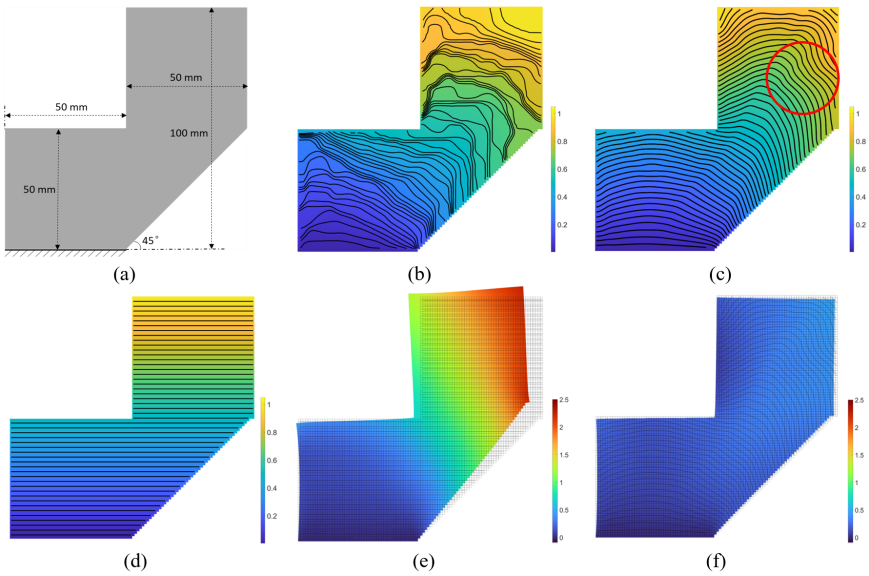

Figure 3.4.: Fabrication sequence optimization for a 2D component. (a) The sizes of the 2D component. (b) The optimized time field without any layer geometry control, its isolines segment the component into layers. (c) The optimized time field with layer thickness control, the layers are more uniform. (d) The trivial fabrication sequence with planar layers, serves as a reference. (e) The total structural distortion accumulated during the whole manufacturing process using planar layers. (f) The total structural distortion of the optimized curved fabrication.

into layers with improved layer thickness uniformity. While the thickness within each layer is more consistent, slight variations are still allowed to enable the formation of curved layers.

Moreover, the optimizer has the flexibility to reduce the number of layers when appropriate. With no constraints on the volume of each layer, the optimizer can adjust the amount of layers by allowing certain layers to diminish. The final result in Fig. 3.4(c) consists of only 49 layers as the volume of the 50-th layer is zero.

In order to quantitatively assess the effectiveness of the method, we introduce a geometric measurement of the layer thickness. It involves picking up a series of sampling points on each layer boundary. At each sampling point on the current layer boundary, the geometric layer thickness is calculated by finding the shortest distance to the points on the subsequent layer boundary. In order to minimize errors caused by the length differences between the adjacent two layer boundaries, the shorter one is always taken as the reference. Although the geometric layer thickness is not entirely accurate on its own, it offers an independent measurement distinct from the approximated layer thickness derived using the gradient as in Eq. 3.11.

As can be seen in Figure 3.5 (a), the approximated layer thickness of each layer stays within the range between 1.6 mm and 2.4 mm, confirming that all constraints are satisfied at the end of the optimization. Overall, the geometric layer thicknesses are consistent with the approximated ones. However, some discrepancies mainly arise in the final few layers, where the length of each subsequent layer is considerably shorter than the previous one. This amplifies the error caused by excluding domain boundaries in the calculation of geometric layer thickness. Besides, Figure 3.5 (b) presents histograms of point-wise geometric layer thicknesses for the 10th, 20th, 30th, and 40th layers. It shows that the geometric layer thicknesses are primarily concentrated within [1.6 mm, 2.4 mm] in most cases. Some deviations in the thickness distribution indicate the presence of local variations in layer thickness.

In addition, structural distortion induced by manufacturing is significantly

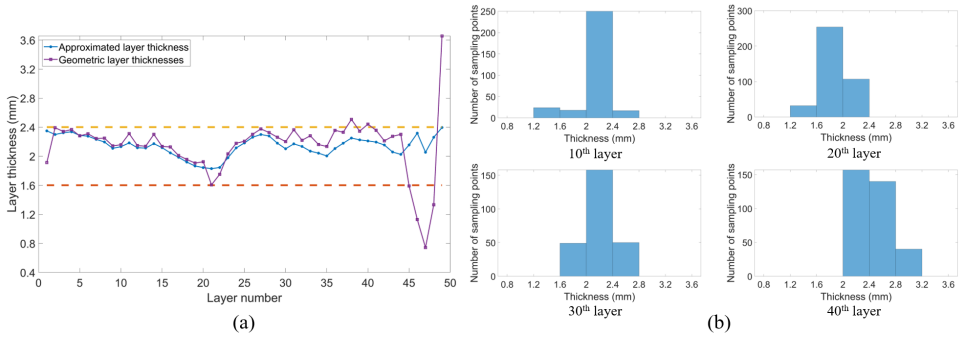

Figure 3.5.: Statistics of layer thickness for the result shown in Fig. 3.4(c). (a) Comparison between the geometric layer thicknesses and the approximated layer thicknesses. (b) Distribution of geometric layer thickness data for the 10th, 20th, 30th, and 40th layers.

minimized through fabrication sequencing planning. As can be seen in Fig. 3.4(d-f), compared to the fabrication sequence using planar layers, the accumulation of structural distortion can be greatly suppressed by adopting the optimized curved layers. As listed in Table 3.1, the thermal-induced compliance corresponding to the planar fabrication sequence is 1.910×10^5 mJ, while the thermal-induced compliance is reduced to 6.661×10^4 mJ by using the optimized curved layers. This finding remains consistent when shifting from a differential layer representation (Eq. 3.2) to a binary description (Eq. 3.1), which provides more accurate process simulation results.

INCORPORATING CURVATURE CONTROL METHOD

Although the layer thickness control method improves the uniformity of layer thickness, it does not guarantee their curvature shape. For example, the regions marked with red circles in Fig. 3.4(c) are concave shapes, which may cause manufacturing difficulties. By switching on the curvature control method, convex layers are promoted, as shown in Fig. 3.6(a).

Fig. 3.6(b) and (c) compare their curvature distributions, showing that the addition of curvature control effectively suppresses negative curvature values in the time field, which correspond to layer concavities. With curvature control, the minimum curvature increases from -0.569 to -0.222. These remaining negative values are primarily concentrated near the corners of the V-shaped component in the final layers, likely due to boundary effects.

Another interesting observation is to compare the thermal-induced distortion for sequence optimization with and without layer gemoetry control. As can be seen in Table 3.1, their thermal-induced compliances do not differ much under the binary layer description. The design flexibility to minimize thermal-induced distortion is not reduced by enforcing uniform layer thicknesses and curvature constraints.

PARAMETER STUDY OF THE WEIGHT COEFFICIENTS

Next, we examine how the ratio of the three weight coefficients in the objective – w_1 (thermal-induced distortion), w_2 (thickness uniformity) and w_3 (curvature control) affect the results. We perform a parameter sweep by fixing $w_1 = 1$ while varying

Table 3.1.: Structural distortion with different fabrication sequences

Sequences \ Compliance	Differential	Binary
Planar layers (reference)	1.910×10^5 mJ	1.556×10^5 mJ
Without layer geometry control	5.797×10^4 mJ	5.822×10^4 mJ
With layer thickness control	6.661×10^4 mJ	6.080×10^4 mJ
With layer thickness and curvature control	6.377×10^4 mJ	5.931×10^4 mJ
Refine from 10 to 50 layers	7.749×10^4 mJ	6.833×10^4 mJ

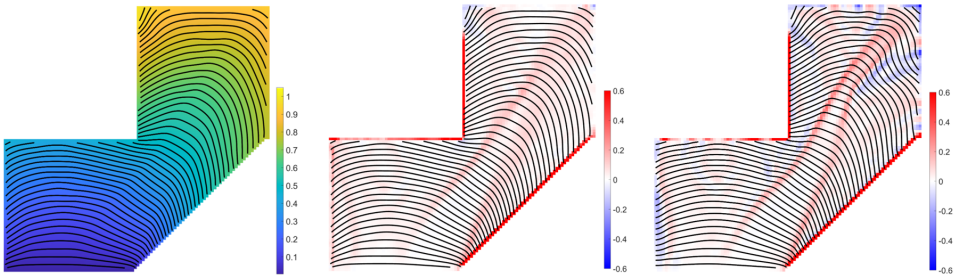

(a) (b) (c)

Figure 3.6.: Comparison of curvature distribution. (a) The optimized time field with layer thickness control and curvature control, layers are more convex. (b) The local curvature distribution of the result optimized with curvature control. (c) The local curvature distribution of the result optimized without curvature control.

w_2 and w_3 from 1 to 8. Fig. 3.7 presents the results obtained using different sets of weight coefficients, including their thermal-induced compliances, average layer thickness variances, and minimum curvatures.

As can be seen from these surface graphs, increasing the weight of thickness uniformity objectives w_2 results in more uniform layers, albeit at the expense of higher thermal-induced compliance. The positive aspect is that, even with the most uniform layer geometry, thermal-induced compliance remains significantly better than that of planar layers. This underscores the feasibility and importance of optimizing the fabrication sequence. Conversely, increasing the weight of curvature control w_3 has a smaller impact on the thermal-induced distortion and thickness uniformity but increases the minimum curvature value of the time field, helping to reduce concavities.

OPTIMIZATION USING FEWER LAYERS

Given that the obtained time field and its gradient are highly uniform, the time field progresses monotonically from one layer boundary to the next. This suggests that the structure can be sliced into even more layers directly from the current time field

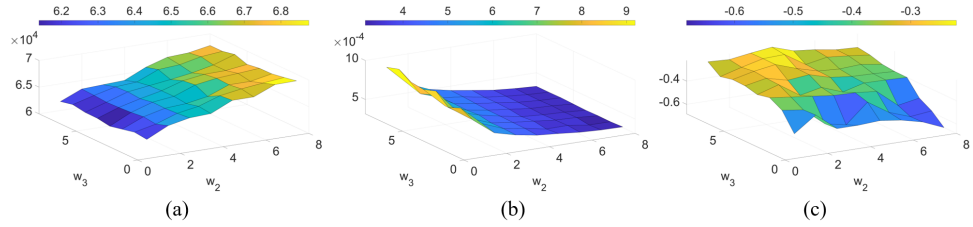

(a) (b) (c)

Figure 3.7.: Results obtained with varied weight coefficients w_2 and w_3. (a) Thermal-induced compliance. (b) Average thickness variance. (c) Minimum curvature.

while maintaining uniform layer thicknesses.

To validate this, we first do a sequence optimization on the same component as in Section 3.3.1 but with only 10 layers. The optimized time field is shown in Fig. 3.8, demonstrating good uniformity. On this basis, we can refine the number of layers/isolines on the same time field as a post-processing step. As shown in Fig. 3.8, the refined layers remain highly uniform, indicating that the optimization yields a consistent pseudo-time field.

We further compare its layer thickness statistics with the result optimized using 50 layers in Fig. 3.6(a). As shown in the left of Fig. 3.9, most of the approximated and geometric layer thicknesses fall within the target range in both cases. The right of Fig. 3.9 demonstrated the variances of layer thicknesses within each layer. In general, the result optimized with 10 layers exhibits less variation, suggesting improved thickness uniformity. The reason is that the reduced amount of layers in the optimization increases the weight of each layer in the thickness uniformity objective, and this uniformity is maintained during refinement. Additionally, reducing the number of constraints simplifies the optimization problem, allowing the optimizer to more easily locate better local optima.

However, as listed in Table 3.1, the thermal-induced distortion for the fabrication sequence obtained from layer refinement is noticeably larger. With fewer layers

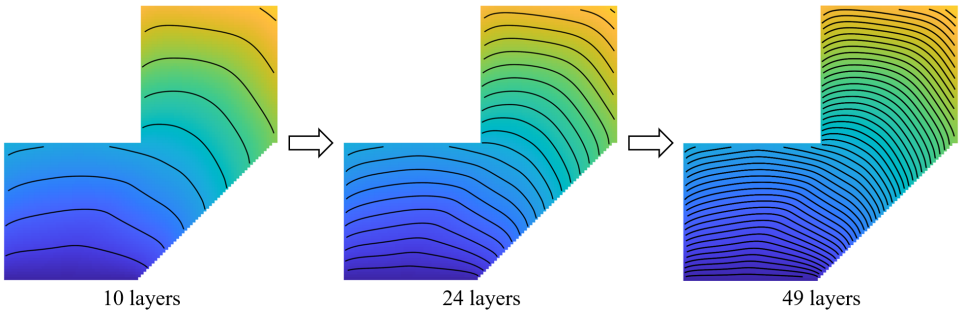

Figure 3.8.: Layer refinement in a post-processing step, the time field is initially optimized with 10 layers and subsequently segmented to 24 and 49 layers.

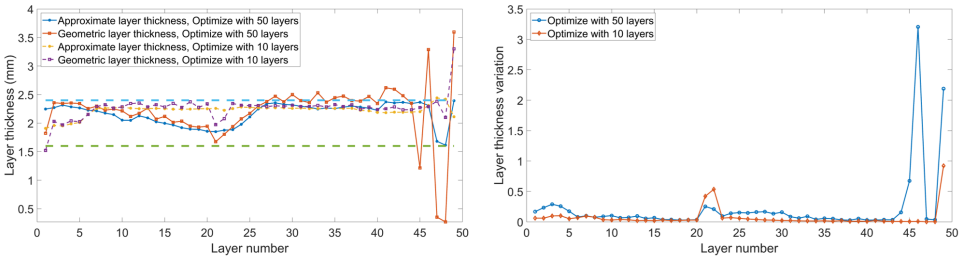

Figure 3.9.: Statistics of layer thickness for optimization using different numbers of layers. Left: average layer thicknesses. Right: thickness variation within each layer.

considered in the optimization, the thermal-induced compliance is increased. This is due to the coarser optimization granularity resulting from the reduced number of layers. In addition, the improved uniformity of layer thickness restricts the flexibility to further reduce the distortion.

The above observations suggest that the proposed method can serve as a decomposition approach by initially using a reduced number of layers in the optimization process. Once the optimized coarse-grained fabrication sequence is determined, the slicing procedure can be refined in a post-processing step.

3.3.2. A TOPOLOGY OPTIMIZED COMPONENT

We then validate the method on a topology-optimized component, as shown in Fig. 3.10(a). The structure is optimized for static compliance under a single load case applied on the right side. The structural layout is used as the prefixed component for fabrication sequence optimization. The component is optimized using 20 layers and then sliced into around 80 layers in post-processing. All three objectives are included in the optimization. The inherent strain value used is the same as that in the above section: $\boldsymbol{\epsilon}_0^* = \left[\epsilon_{xx}, \epsilon_{yy}, \epsilon_{xy}\right]^{\mathrm{T}} = [-0.00375, -0.00375, 0]^{\mathrm{T}}$.

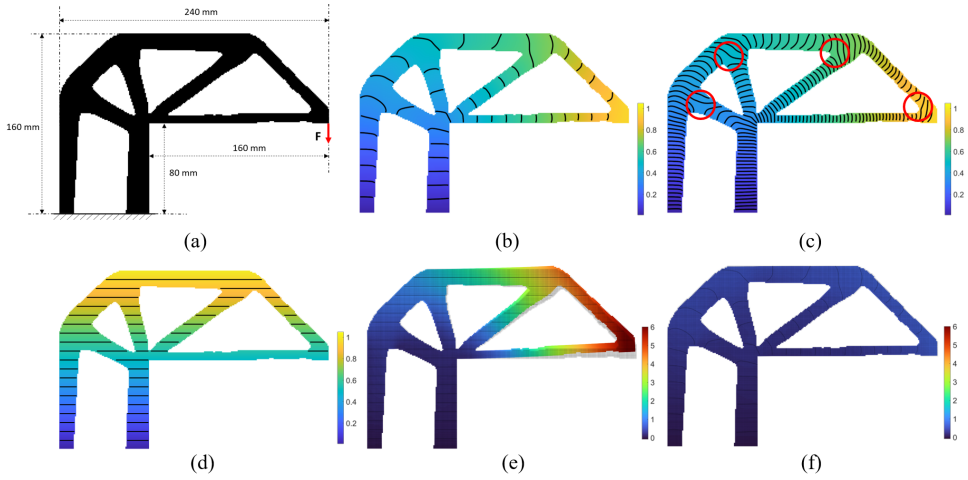

Figure 3.10.: Fabrication sequence optimization for a topology optimized structure. (a) The structural layout and sizes of the component. (b) The optimized time field, its isolines segment the component into 20 layers. (c) Segment the time field into 80 layers in a postprocessing step. (d) The trivial fabrication sequence with 20 planar layers, serves as a reference. (e) The total structural distortion accumulated during the whole manufacturing process using planar layers. (f) The total structural distortion accumulated during the whole manufacturing process using the optimized curved layers.

As can be seen from Fig. 3.10(b) and (c), the proposed layer geometry control scheme consistently achieves layers with uniform thickness, even when applied to structures with highly complex topologies. This demonstrates the robustness

and adaptability of the method in handling geometrically intricate components, maintaining its effectiveness across a wide range of configurations.

However, it should be noted that some concavities still appear in the time field despite the use of the curvature control method. As highlighted by the red circles in Fig. 3.10(c), these concavities typically form at intersections where multiple branching features intersect. In such regions, isolines originating from different branches tend to bend inward towards each other, resulting in a saddle-shaped region. To preserve uniform layer thickness, the succeeding isoline must also take on a concave profile, conforming to the local geometric constraints.

In comparison with a planar slicing pattern as in Fig. 3.10(d), the optimized curved layers contribute to minimizing the accumulation of structural distortion during manufacturing, as shown in Fig. 3.10(e-f). The thermal-induced compliance of the planar slicing pattern is significantly worse than that of the optimized result. Using the optimized curved slicing reduces the thermal-induced compliance from 2.281×10^5 mJ to 8.526×10^4 mJ.

3.3.3. 3D COMPONENT WITH OVERHANG REGION

The 3D structure with the overhang region is an extrusion of the 2D component in Section 3.3.1. As shown in Fig. 3.11(a), the component is also fully fixed at the bottom during manufacturing, and the fabrication process starts from the bottom baseplate. The dimension of the component is $2 \times 1 \times 2$ in the x, y, z direction, and is discretized with $80 \times 40 \times 80$ elements. The target layer thickness is set to 0.05, and is allowed to be varied between 0.045 and 0.055. The prescribed number of layers is set to a maximum of 40. In this analysis, we emphasize on minimizing the structural distortion of the top-right edge of the structural layout, as shown in acquamarine in Fig. 3.11(a). The nodal distortion measurement in Eq. 3.22 is used as the objective function. The inherent strain value used is: $\boldsymbol{\varepsilon}_0^* = \{-0.01, -0.01, -0.01, 0.0, 0.0, 0.0\}^{\mathrm{T}}$. To accelerate computations, the optimization framework is implemented using C++ based on the PETSc library for parallel computing.

The optimized time field and the corresponding slicing result are shown in Fig. 3.11(b) and (c). The final optimized solution consists of a total of 39 layers. The thickness of each layer is constrained within specified upper and lower limits, allowing minimal variations within layers to achieve curved layer shapes. The layers close to the geometry boundary are less uniform due to the boundary effect introduced by the zero Neumann boundary condition in the heat equation. In this 3D case, only the layer thickness control method is currently implemented, while the curvature control method has not yet been integrated.

In addition, the effectiveness of the proposed fabrication sequence optimization in reducing process-induced structural distortion is clearly illustrated in Fig. 3.11(d) and (e). Compared to conventional planar layer fabrication, the optimized curved-layer fabrication sequence decreases the distortion objective by two orders of magnitude from 7.0×10^{-1} to 2.0×10^{-3}.

Finally, a detailed overview of 10 manufacturing stages extracted from the optimized fabrication sequence is shown in Fig. 3.12. These snapshots provide insight into the progressive buildup of the entire structure.

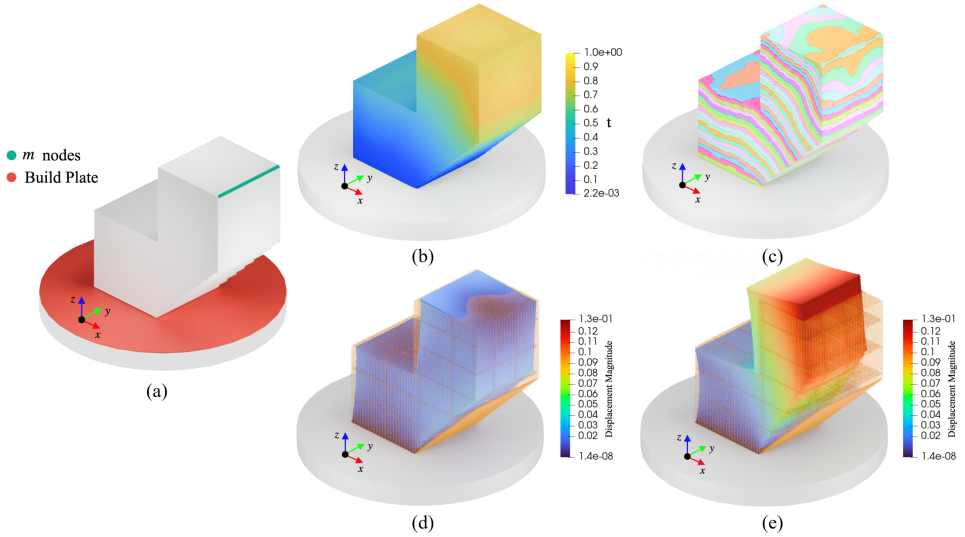

Figure 3.11.: Fabrication sequence optimization for the 3D structure with overhang. (a) The structural layout of the component, with the base plate indicated in red, and the nodes considered for the distortion objective indicated in aquamarine color. (b) The optimized time field. (c) The optimized fabrication sequence extracted from the optimized time field. Structural deformation due to manufacturing effect, with the orange grid representing the undeformed shape: (d) Manufacturing using the optimized fabrication sequence. (e) Manufacturing using 40 planar layers, for comparison.

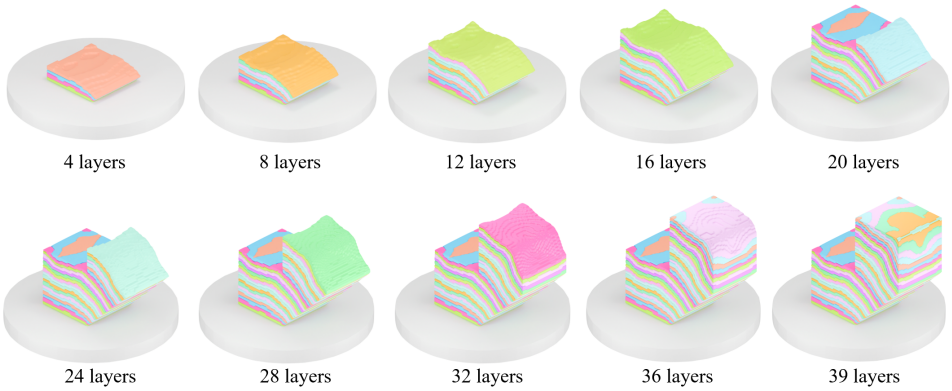

Figure 3.12.: The optimized curved layer fabrication process for the 3D component, with only 10 manufacturing stages shown for simplicity.

3.4. CONCLUSION

In this research, we develop a layer geometry control scheme for fabrication sequence planning within the space-time optimization framework. The proposed method has been validated through both 2D and 3D numerical examples, demonstrating its effectiveness and applicability. The obtained layers achieve improved uniformity, which is essential for the additive manufacturing process. The design flexibility of fabrication sequence planning is preserved, as the optimizer can adjust layer thickness within permissible limits, with minor variations inside each layer remaining acceptable. The optimization framework has proven effective in minimizing manufacturing-induced structural distortion by arranging the slicing pattern rationally.

The layer thickness control method enhances the uniformity of the pseudo-time field within the optimization framework. A post-processing step can be employed to generate additional layers beyond those predefined in optimization, while still maintaining uniform layer thicknesses. This approach allows for a reduced number of layers during the optimization process for computational efficiency, followed by a finer slicing procedure in the post-processing step to produce the actual layers required for manufacturing.

Furthermore, the method provides flexibility to balance competing objectives by tuning the weight coefficients in the objective function. This allows users to trade off between minimizing thermal-induced distortion and enhancing layer thickness uniformity based on specific manufacturing requirements. For techniques that allow greater variation in layer thickness, the optimization framework can exploit this flexibility to reduce distortion. Conversely, for additive manufacturing processes with stringent requirements on layer thickness uniformity, the method can be adapted to include stricter constraints, ensuring uniform layers while maintaining its effectiveness.

4

RESIDUAL STRESS-CONSTRAINED SPACE-TIME TOPOLOGY OPTIMIZATION

Residual stresses and distortions are major barriers to the broader adoption of wire arc additive manufacturing. These issues are coupled and arise due to large thermal gradients and phase transformations during the directed energy deposition process. Mitigating distortions may lead to substantial residual stresses, causing cracks in the fabricated components. In this chapter, we propose a novel method to reduce both residual stresses and distortions by optimizing the fabrication sequence. This approach explores the use of non-planar layers, leveraging the increased manufacturing flexibility provided by robotic arms. Additionally, our method allows for the concurrent optimization of the structural layout and corresponding fabrication sequence. We employ the inherent strain method as a simplified process simulation model to predict residual stresses and distortions. Local residual stresses are aggregated using a p-norm function, which is integrated into distortion minimization as a constraint. Through numerical examples, we demonstrate that the optimized non-planar fabrication strategies can effectively reduce both residual stresses and distortions.

Parts of this chapter have been published in *Computer Methods in Applied Mechanics and Engineering*. **440**, 117913 (2025) authored by Kai Wu, Fred van Keulen and Jun Wu, under the title *Residual Stress-constrained Space–time Topology Optimization for Multi-axis Additive Manufacturing.*

4.1. INTRODUCTION

ADDITIVE manufacturing has advanced rapidly in the past two decades. An important recent advancement is the introduction of robotic arms for 3D printing, which enables the production of large parts. In contrast to a fixed build orientation in Cartesian-type 3D printing, robotic arms provide rotational motion, further increasing manufacturing flexibility. By continuously adjusting the build orientation, robotic systems enable the deposition of material along non-planar layers, offering the possibility to avoid supports and improve manufacturing quality. These robotic systems have been employed for printing with both polymers and metals—using material extrusion for polymers [38, 198] and directed energy deposition techniques like wire arc additive manufacturing (WAAM) for metals [44, 106, 171]. WAAM, also known as wire arc directed energy deposition (WA-DED) [34, 120], combines traditional welding methods with modern additive manufacturing principles. It typically uses an electric arc as the heat source to melt a metal wire and deposit it layer by layer to build 3D components. It offers a cost-effective and efficient solution for producing large, customized metal parts, often with complex geometries that are impractical to achieve with conventional manufacturing.

However, the adoption of WAAM in critical industries is hindered by several challenges, particularly residual stresses and distortions [27, 172, 181]. As a directed energy deposition process, WAAM involves high energy input, large thermal gradients, multiple phase transformations, and repeated heating and cooling cycles. These factors result in significant residual stresses and distortions in the fabricated components. The residual stresses can lead to cracking [28] and large deflections during fabrication as well as upon unclamping [135]. Consequently, residual stresses compromise the reliability of the parts, while distortions often render them unusable without extensive and costly post-processing.

From a manufacturing perspective, various strategies have been employed to mitigate residual stresses. These include adjusting process parameters such as scanning speed, cooling rate, and welding mode [71], as well as implementing in situ temperature control to reduce temperature gradients [135]. Additionally, post-process treatments such as annealing and rolling [53, 63, 69, 142] are also commonly used. However, these measures often require significant upgrades to the entire system, which can be impractical due to the large scale of the parts and the constraints of existing manufacturing setups.

Residual stresses are closely related to the structural design. Design guidelines to avoid excessive distortions and residual stresses have been proposed for relatively simple geometries [106, 109, 124]. For complex continuum structures, structural optimization has been pursued to address these issues, primarily for Cartesian-type 3D printing based on powder beds. Allaire and Jakabčin [5] proposed a thermo-elastic model to predict the accumulation of residual stress and distortion, and integrated it into shape and topology optimization. Similarly, Misiun et al. [113] minimized thermal-induced distortion through structural optimization to avoid recoater collisions and build failures, adopting an inherent strain method for process simulation. Furthermore, Xu et al. [190] included constraints on residual stresses in topology optimization. Besides structural optimization, residual stresses can be

mitigated through support structure optimization [32, 33, 201]. Bruggi et al. [20] concurrently optimized the structural layout and constant build orientation to design lightweight structures, accounting for the material anisotropy in WAAM [21, 84, 180].

In this chapter, we propose optimizing the fabrication sequence to mitigate residual stresses and distortions in multi-axis additive manufacturing. In traditional Cartesian-based 3D printing, the layers are planar, and they are determined by a fixed build orientation. In multi-axis additive manufacturing, however, the rotational motion allows to deposit material along curved layers. By fabrication sequence in multi-axis additive manufacturing, we refer to a decomposition of the component into curved layers with varying orientations that are fabricated one upon another. It thus can be viewed as curved slicing, which, however, has been typically treated as a geometric problem, focusing on generating smoothly varying layers that the robotic arms can execute without collisions [38, 42, 43, 46]. In curved slicing, the material anisotropy due to curved layers has been taken into account [200]. However, the critical impact of curved fabrication sequences on residual stresses is an open research question, with optimization largely unexplored. This challenge requires simulating the additive manufacturing process and its underlying physics. Research from the related field of robotic welding has shown that the joining sequence significantly impacts residual stresses and distortions [10, 173]. Building on these insights, Wang et al. [169] demonstrated numerically that fabrication sequence optimization provides a viable and effective way to minimize thermally induced distortions. However, the reduction of distortions may be accompanied by increased residual stresses, making it a critical next step to limit residual stresses in fabrication sequence optimization.

While the fabrication sequence for residual stresses in the context of multi-axis printing has not been studied, it is worth mentioning a few papers that deal with scanning path optimization in Cartesian-based 3D printing. Chen et al. [26] proposed a scanning path optimization method based on level-set functions. The material anisotropy from the 2D scanning path is explored to reduce residual stresses. Boissier et al. [15] proposed scanning path optimization based on shape optimization theory, incorporating the simulation of the manufacturing process to minimize overheating and thus avoid excessive thermally induced residual stresses. This was later integrated with structural optimization to concurrently optimize the shape and the 2D scanning path [16].

Our method for reducing residual stresses and thermal-induced distortions is based on space-time topology optimization [168, 170]. Its core idea is to represent curved layers using isolines of a scalar field. This scalar field, which is optimized in an iterative process, defines the pseudo-time at which each spatial point is materialized. From the pseudo-time field, a series of intermediate structures can be derived, representing the additively fabrication process. This optimization focuses on analyzing the residual stresses and distortions that arise from the intermediate structures. This pseudo-time field can also be optimized concurrently with the structural layout, represented by a pseudo-density field as in conventional density-based topology optimization. In this concurrent optimization, structural performance is considered alongside residual stresses and distortions.

A key element in the optimization is to predict residual stresses efficiently. The inherent strain method has gained popularity as a simplified process model to predict distortions and residual stresses [98, 119, 129, 140, 157]. The inherent strain method simplifies the complex thermo-mechanical interactions as an inelastic inherent strain field, which can be calibrated from experimental tests. It is an attractive alternative to high-fidelity methods for its computational efficiency. This is particularly useful for optimization problems that require repeated process simulations. For simplicity, in this research, we assume that the inherent strain field is homogeneous and isotropic and its value does not change with respect to different fabrication sequences. These assumptions serve the purpose of demonstrating the effectiveness of the presented workflow. We expect more accurate process models [47, 48, 107, 118] can be integrated as well, albeit with the trade-off of more demanding computation. After obtaining the accumulation of residual stress layer by layer from the inherent strain method, we formulate the residual stresses as a constraint function in the optimization framework.

To incorporate residual stresses into optimization, we refer to general approaches dealing with stress constraints in topology optimization. Topology optimization with stress constraints has been extensively studied over the past decades, leading to the development of effective solutions for overcoming key challenges. The first challenge is the local nature of stress, resulting in a large number of constraints. A typical approach to managing a large number of local constraints is to aggregate them into a single global constraint using either p-norm or p-mean [50] or Kreisselmeier-Steinhauser function [194]. An alternative to this is based on augmented Lagrangian formulations [37, 196], which transform the original constrained optimization problem into a sequence of unconstrained subproblems. The second challenge is the 'singularity' problem: the feasible solution space of a stress-constrained problem contains degenerate subspaces with a lower dimension. This makes it difficult to find the global optimum using gradient-based algorithms. Relaxation of the stress constraints using ϵ-relaxation [29] or qp-approach [19, 91] has proven effective in alleviating this problem. In addition, Verbart et al. [164] has demonstrated that aggregating the local constraints using a lower bound aggregation function also effectively relaxes the feasible space. In this research, we build on these established methods for dealing with the local residual stresses. Specifically, local residual stresses are relaxed using the qp-approach and then aggregated into a global constraint using the p-norm function.

The remainder of this chapter is organized as follows. Section 4.2 elaborates the mathematical model of the proposed method in detail. Section 4.3 validates the effectiveness of the proposed method with a series of numerical examples. Lastly, Section 4.4 summarizes the key findings and conclusions.

4.2. METHODOLOGY

In the methodology section, we first introduce the basis of space-time topology optimization, where the fabrication sequence is optimized, optionally together with the structural layout. We then present the evaluation of residual stresses and

distortions in additive manufacturing, using an inherent strain method. Building on these key ingredients, we formulate a constraint function to restrict the maximum residual stress. Finally, we elaborate on the formulation of space-time topology optimization incorporating the residual stress constraint.

4.2.1. SPACE-TIME PARAMETERIZATION

In space-time topology optimization, the 3D printing sequence for fabricating a component is optimized simultaneously with the component's structural design. The fabrication sequence is represented by a scalar field, referred to as the pseudo-time field (or simply time field), which is defined over a finite element discretization of the component. This element-wise representation is analogous to density-based topology optimization, where each element is assigned a pseudo-density value. However, unlike the ideal binary density values ($\rho_e \in \{0,1\}$) that indicate whether an element is solid or void, the time field is continuous ($t_e \in [0.0, 1.0]$), with smaller time values corresponding to elements materializing earlier in the manufacturing process.

From the density and time fields, one can derive a series of intermediate structures during fabrication. This is essential for simulating the additive manufacturing process and the physics involved in fabrication. Fig. 4.1 illustrates the calculation of intermediate structures. Fig. 4.1(a) shows the density field, representing the structural design of a component, while Fig. 4.1(d) illustrates a continuous time field, whose isolines represent the fabrication sequence. An intermediate structure from this fabrication sequence is shown in Fig. 4.1(e). Fig. 4.1(b)-(c) represent intermediate steps for computing the time field, and will be explained shortly. At a time point τ, elements with time values smaller than τ have been fabricated, while elements with time values larger than τ have not. The intermediate structure at time point τ, denoted by $\boldsymbol{\rho}^{\{\tau\}}$, thus consists of

$$\rho_e^{\{\tau\}} = \begin{cases} \rho_e, & \text{if } t_e \leq \tau, \\ 0, & \text{otherwise.} \end{cases} \tag{4.1}$$

To facilitate gradient-based optimization, this conditional equation is replaced by an element-wise multiplication of the density field and a modified time field,

$$\rho_e^{\{\tau\}} = \rho_e \tilde{t}_e^{\{\tau\}}. \tag{4.2}$$

Specifically, the time field is modified by converting time values smaller than the threshold value τ to 1, and conversely, time values larger than τ to 0. This is implemented using a smoothed Heaviside function,

$$\tilde{t}_e^{\{\tau\}} = 1 - \frac{\tanh\big(\beta_t \tau\big) + \tanh\big(\beta_t (t_e - \tau)\big)}{\tanh\big(\beta_t \tau\big) + \tanh\big(\beta_t (1 - \tau)\big)}, \tag{4.3}$$

where β_t determines the sharpness of the step function. A continuation scheme is applied to β_t during optimization. It starts with a low value for reduced nonlinearity and gradually increases to achieve distinct layer segmentation by the end of the

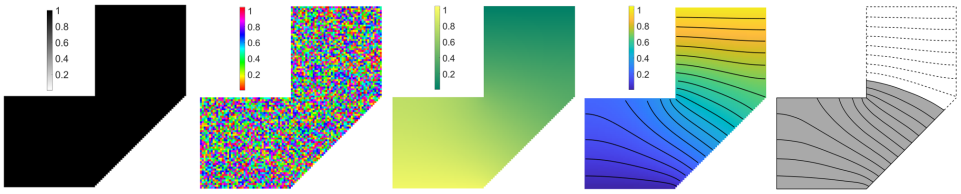

Figure 4.1.: Illustration of representations in space-time topology optimization. (a) The structural layout, represented by a density field $\boldsymbol{\rho}$. (b) A pseudo thermal diffusivity field, serving as optimization variables. For illustration purposes only, a random thermal diffusivity field is shown here. (c) The temperature field $\boldsymbol{T}$ obtained by solving the heat equation. (d) The time field $\boldsymbol{t}$ obtained from the temperature field using $\boldsymbol{t} = \mathbf{1} - \boldsymbol{T}$. Its isolines partition the component into 20 layers. (e) The 12-th intermediate structure during the manufacturing process, i.e., 12 layers have been manufactured and 8 layers are yet to be manufactured.

optimization process. Later in the results section, we compare simulation results using the differential formulation (Eq. 4.2) and binary classification (Eq. 4.1).

To simulate the additive manufacturing process, a series of intermediate structures is computed. Let the fabrication of the component consist of N layers, where N is specified by the user. The component is divided by time points that are evenly spaced over the interval $[0,1]$, $\tau_j = \frac{j}{N}$, where $j = 0,1,...,N$. We use $\boldsymbol{\rho}^{\{j\}}$ to indicate the j-th intermediate structure, i.e., corresponding to the time point τ_j. For example, the intermediate structure shown in Fig. 4.1(e) is $\boldsymbol{\rho}^{\{12\}}$, where the total number of layers is $N = 20$. The intermediate structure $\boldsymbol{\rho}^{\{j\}}$ for $j = 1,...,N-1$ is calculated using Eq. 4.2, while $\boldsymbol{\rho}^{\{0\}} = \mathbf{0}$, and $\boldsymbol{\rho}^{\{N\}} = \boldsymbol{\rho}$.

It is worth noting that instead of directly optimizing the time field and thus the fabrication sequence, it is solved through a partial differential equation (PDE), where the coefficients in the equation are optimization variables, as discussed in chapter 2. This approach avoids discontinuities in the time field that could arise from direct optimization. Specifically, this PDE describes the heat diffusion from the baseplate where the fabrication starts. The element-wise thermal diffusivity (μ) determines the temperature distribution (T),

$$\nabla(\boldsymbol{\rho}\boldsymbol{\mu}\nabla\boldsymbol{T}) - \alpha_{\mathrm{T}}\boldsymbol{T} = 0. \tag{4.4}$$

Here ∇ is the vector differential operator. α_{T} denotes a constant drain rate. The boundary of the component adjacent to the baseplate is set as the heat source with a constant temperature of $T = 1$, while the other boundaries of the component are insulted. This heat equation is introduced to obtain a scalar field that monotonically varies from the baseplate toward the distant boundary of the component. It should not be confused with the thermal process in metal additive manufacturing. The heat equation takes into account the evolving structural layout during iterative optimization by including the density field $\boldsymbol{\rho}$. The optimization variables $\boldsymbol{\mu}$ are restricted between 0 and 1. The constant drain term is selected such that the

temperature field smoothly varies from 1 to 0. After solving the heat equation, the temperature field is transformed by:

$$\boldsymbol{t} = \mathbf{1} - \boldsymbol{T}, \tag{4.5}$$

to obtain a pseudo-time field $\boldsymbol{t}$. By this transformation, elements adjacent to the baseplate, with a constant temperature of $T = 1$, are assigned $t = 0$, correctly serving as the starting point of fabrication.

4.2.2. RESIDUAL STRESSES CALCULATION USING THE INHERENT STRAIN METHOD

The inherent strain method is a computationally efficient approach to predict deformations and residual stresses in metal components produced by additive manufacturing. It simplifies the complex thermo-mechanical phenomena in additive manufacturing by decoupling the thermal and mechanical problems, focusing on deformation without performing a full thermal analysis. For computational efficiency, the inherent strain method is often applied layer by layer by assigning inherent strain values to each newly deposited layer, and predicting the deformation of the component due to the equivalent mechanical load acting on this layer.

In this study, we adopt the assumptions of geometric and material linearity to ensure computational efficiency in calculating the mechanical response. While nonlinear analysis could improve simulation accuracy under significant residual stresses and distortions, we find it computationally prohibitive for optimization purposes. The premise of our approach is that by optimization we will reduce residual stresses and distortions to a level where linearity assumptions remain valid. As pointed out by Munro et al. [119], under the linearity assumptions, the total deformations and residual stresses of the entire component are the superposition of all increments due to the deposition of each layer.

$$\boldsymbol{U}_{\text{thermal}} = \sum_j \Delta \boldsymbol{U}^{\{j\}}, \tag{4.6}$$

$$\boldsymbol{\sigma} = \sum_j \Delta \boldsymbol{\sigma}^{\{j\}}. \tag{4.7}$$

Here the superscript $\{j\}$ indicates the increment in the displacement or residual stress due to the deposition of the $j-$th layer. We explain the calculation of the increments in the following.

In space-time topology optimization, a newly added layer is identified by the difference between two consecutive intermediate structures,

$$\boldsymbol{\eta}^{\{j\}} = \boldsymbol{\rho}^{\{j\}} - \boldsymbol{\rho}^{\{j-1\}},\ j = 1, 2, ..., N. \tag{4.8}$$

By activating the inherent strain in each new layer, the incremental deformation and residual stress on the intermediate structure can be calculated. This is illustrated in Fig. 4.2. Fig. 4.2(a) shows an intermediate structure $\boldsymbol{\rho}^{\{j-1\}}$, with $j-1$ layers already manufactured. The intermediate structure is already deformed due to previous

manufacturing steps. Fig. 4.2(b) highlights the deposition of a new layer. The inherent strain of this new layer is then activated, creating equivalent nodal forces on each element within this new layer,

$$\boldsymbol{F}_e = \int_{\Omega_e} \boldsymbol{B}^\top \boldsymbol{D}\boldsymbol{\varepsilon}^* d\Omega_e, \tag{4.9}$$

where $\boldsymbol{B}$ is the strain-displacement matrix, $\boldsymbol{D}$ is the constitutive matrix, $\boldsymbol{\varepsilon}^*$ is the inherent strain vector. In this study, we use an isotropic inherent strain to simplify the analysis by disregarding directional effects resulting from fabrication sequences. This approach ensures that the inherent strain field is independent of fabrication sequences, providing a consistent basis for comparing the effects of different sequences. While anisotropic inherent strain could be integrated into the framework—by deriving local material deposition orientation from the gradient of the time field—we focus on the role of fabrication sequence in this work, leaving the exploration of anisotropic effects as a natural extension for future studies.

The nodal forces on each element are then assembled to obtain a global force vector for the entire component,

$$\boldsymbol{F}^{\{j\}} = \sum_e \eta_e^{\{j\}p} \boldsymbol{F}_e, \tag{4.10}$$

where $\sum_e$ represents the assembly over all elements. Note that the forces are scaled by a factor that depends on the new layer $\boldsymbol{\eta}$. This is because in space-time topology optimization, the structural layout, represented by the density field, is optimized along with the sequence optimization. To account for this, the density distribution is factored in as a scaling factor with a penalization p, in line with the power law relation between the stiffness and density in SIMP (Solid Isotropic Material with Penalization) [11]. This power law reduces the equivalent forces from elements with

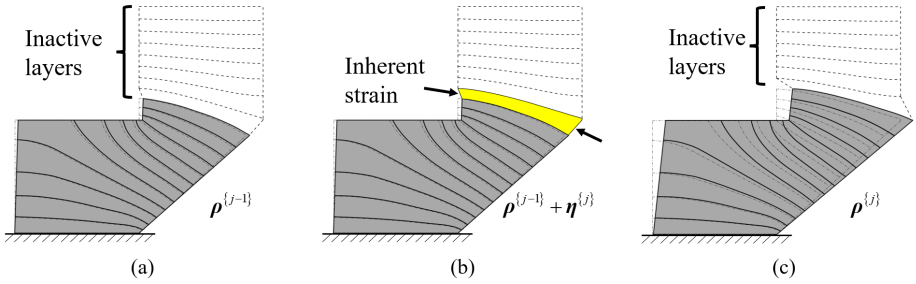

Figure 4.2.: Illustration of the inherent strain method in space-time topology optimization. (a) The 12-th intermediate structure, with deformation resulting from manufacturing the first 12 layers. (b) When the 13-th layer is deposited, the inherent strain field on this new layer is activated from its stress-free state. (c) The activation of the strain field on this new layer results in further deformation of the current intermediate structure. The inactive layers that haven't been manufactured yet stay undeformed.

intermediate densities that appear in the optimization process before convergence. In this research, we choose $p = 3$.

The incremental displacement of the entire domain induced by the inherent strain of the j-th layer is calculated by solving the linear elastic equation,

$$\boldsymbol{K}^{\{j\}} \Delta \boldsymbol{U}^{\{j\}} = \boldsymbol{F}^{\{j\}}. \tag{4.11}$$

Consequently, the residual stress corresponding to this displacement is calculated by

$$\Delta \boldsymbol{\sigma}_e{}^{\{j\}} = \rho_e^{\{j\}p} \boldsymbol{D}\boldsymbol{B} \Delta \boldsymbol{U}_e{}^{\{j\}} - \eta_e^{\{j\}p} \boldsymbol{D}\boldsymbol{\varepsilon}^*. \tag{4.12}$$

The residual stress consists of two parts. The first corresponds to the stress associated with the deformation induced by the new layer. It affects the intermediate structure $\boldsymbol{\rho}^{\{j\}}$. The second accounts for the release of the inherent stain. It mainly concerns the new layer $\boldsymbol{\eta}^{\{j\}}$.

It should be noted that the layers that have not been produced yet are also included in the analysis for calculating the distortion. Elements in the inactive layers are assigned a small density or Young's modulus to avoid the stiffness matrix from becoming singular. During manufacturing, each new layer is added in a stress-free state. To account for this stress-free initial state of a new layer, the first part in the residual stress (Eq. 4.12) is scaled by the density, with a power law relation in consistency with that for the inherent strain.

The above formulations are applied to simulate the component and fabrication sequence illustrated in Fig. 4.1. Fig. 4.3 shows the accumulated deformations and residual stresses in a series of intermediate structures. To enhance visibility, a scaling factor is applied to exaggerate the displacements. Individual elements in the intermediate structures are colored by their von Mises residual stress. Significant residual stresses are observed at the bottom of the component, particularly on both sides, where it is attached to the baseplate. Additionally, a smaller stress concentration is noticeable around the right-angled corner in the middle of the component.

4.2.3. RESIDUAL STRESS CONSTRAINT

We formulate residual stresses in a constraint in space-time topology optimization. Specifically, we consider the residual stress distribution after the entire component has been fabricated in this research. As our simulation results will show later, the residual stress during the manufacturing process will not significantly exceeds the final residual stress value. For future work, it also makes sense to further include layer-wise residual stresses constraints.

We follow established methods for handling the 'singularity' and large number of stress constraints in topology optimization. 'Singularity' refers to the situation where the global optimum is located in a lower dimensional subspace within the solution space, and cannot be reached using gradient-based optimization [29]. To cope with this problem, the idea is to relax the stress definition and thus the solution space. In our work, we adopt the qp-relaxation [19, 91]:

$$\hat{\boldsymbol{\sigma}} = \boldsymbol{\rho}^q \boldsymbol{\sigma}, \tag{4.13}$$

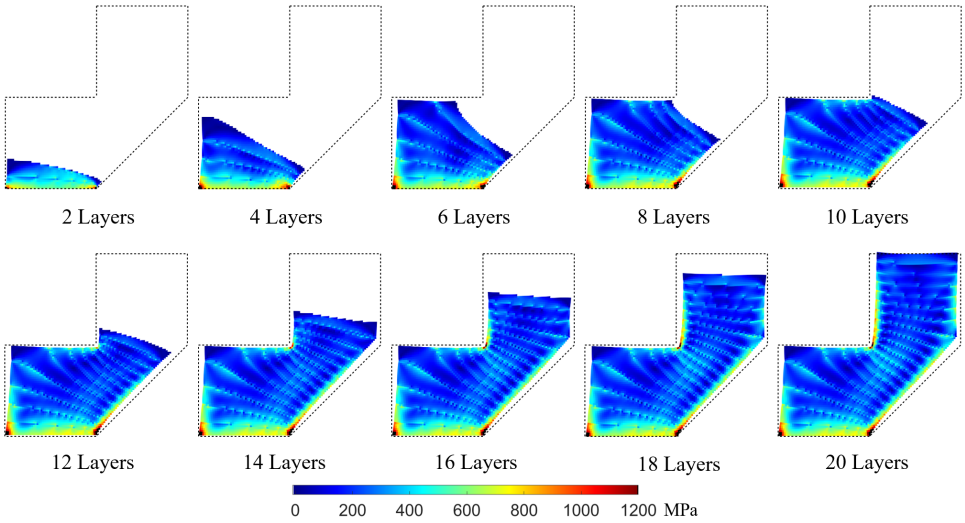

Figure 4.3.: Simulation of the layer-based manufacturing process, with the accumulation of residual stresses and distortions.

where $\hat{\boldsymbol{\sigma}}$ is the relaxed stress. $\boldsymbol{\sigma}$ is the residual stress as calculated from Eq. 4.7. q is a relaxation parameter, and is set as $q = 0.5$.

We use the von Mises stress as the yielding criterion. For general plane stress condition, the von Mises stress ($\hat{\sigma}_{\mathrm{vM},e}$) is evaluated at each element

$$\hat{\sigma}_{\mathrm{vM},e} = \sqrt{\hat{\sigma}_{11,e}^2 + \hat{\sigma}_{22,e}^2 + 3\hat{\sigma}_{12,e}^2 - \hat{\sigma}_{11,e}\hat{\sigma}_{22,e}}, \tag{4.14}$$

where $\hat{\sigma}_{11,e}, \hat{\sigma}_{22,e}, \hat{\sigma}_{12,e}$ are components of the relaxed stress tensor. This equation is rewritten in matrix format to simplify sensitivity analysis:

$$\hat{\sigma}_{\mathrm{vM},e} = \left(\hat{\boldsymbol{\sigma}}_e^{\mathrm{T}} \boldsymbol{V} \hat{\boldsymbol{\sigma}}_e\right)^{1/2}, \tag{4.15}$$

where $\hat{\boldsymbol{\sigma}}_e$ is the vectorized residual stress tensor of element e, and matrix $\boldsymbol{V}$ is defined as:

$$\boldsymbol{V} = \begin{bmatrix} 1 & -1/2 & 0 \\ -1/2 & 1 & 0 \\ 0 & 0 & 3 \end{bmatrix}. \tag{4.16}$$

Stress is a local measure and thus a constraint on stress shall be applied to each element. To reduce the large number of stress constraints, we use the p-norm to aggregate the residual stresses into one single global value $\sigma_{\mathrm{vM,P}}$:

$$\sigma_{\mathrm{vM,P}} = \left(\sum_e \hat{\sigma}_{\mathrm{vM},e}^P\right)^{\frac{1}{P}} \leq \sigma_{\mathrm{lim}}, \tag{4.17}$$

where P is the aggregation parameter. σ_{lim} is the stress limit, e.g., the yield stress of the material. A large P value leads to a more accurate approximation of the

maximum stress. However, it also implies a high nonlinearity. In this research, we choose $P = 10$ as a trade-off between ensuring adequate smoothness for good performance of the optimization algorithm and an adequate approximation.

To improve the approximation accuracy between the maximum stress and the p-norm, we adopt the normalization procedure as suggested by Le et al. [91]. A normalization parameter A^I is defined as follows,

$$A^I = \alpha \frac{\max \hat{\sigma}_{\mathrm{vM},e}}{\sigma_{\mathrm{vM,P}}} + (1-\alpha) A^{I-1}, \tag{4.18}$$

where α is a control parameter, chosen as 0.5 in this research. The parameter A^I, with the superscript indicating the I-th iteration, is updated at every iteration, partially using the information from the last iteration $(I-1)$. The constraint on the normalized residual stress is written as

$$g_s = A^I \sigma_{\mathrm{vM,P}} - \sigma_{\mathrm{lim}} \leq 0. \tag{4.19}$$

We note that A^I is non-differentiable and treated as a constant in each iteration. As the optimization advances, the changes in the design between successive iterations diminish. As a result, the normalization parameter A^I tends to stabilize.

4.2.4. RESIDUAL STRESS-CONSTRAINED SPACE-TIME TOPOLOGY OPTIMIZATION

The constraint on residual stresses is incorporated into two optimization settings. In the first setting, only the fabrication sequence is optimized, while the structural layout of the component remains fixed. This is typical in the manufacturing industry, where component designs are provided externally. In the second setting, both the structural layout and the fabrication sequence are optimized simultaneously. This approach reflects a more integrated design and fabrication process, offering greater design flexibility.

SEQUENCE OPTIMIZATION

The fabrication sequence optimization is formulated as follows, where $\boldsymbol{\mu}$ is the only set of design variables:

$$\underset{\boldsymbol{\mu}}{\text{Minimize:}} \quad f_0 = \omega_1 c_{\mathrm{thermal}} + \omega_2 f_{\mathrm{geo}} \tag{4.20}$$

$$\text{Subject to:} \quad \boldsymbol{K}^{\{j\}} \Delta \boldsymbol{U}^{\{j\}} = \boldsymbol{F}^{\{j\}}, \quad j = 1, 2, ..., N, \tag{4.21}$$

$$\boldsymbol{K}_{\mathrm{T}} \boldsymbol{T} = \boldsymbol{b}, \tag{4.22}$$

$$g_j = \sum \rho_e^{\{j\}} v_e - \frac{j}{N} V_0 \leq 0, \quad j = 1, 2, ..., N, \tag{4.23}$$

$$g_s = A^I \sigma_{\mathrm{vM,P}} - \sigma_{\mathrm{lim}} \leq 0, \tag{4.24}$$

$$0 \leq \mu_e \leq 1. \tag{4.25}$$

The objective function comprises two terms, scaled by weight coefficients ω_1 and ω_2. The first term evaluates the deformation of the component caused by

the successive release of layer-wise inherent strains. For demonstration purposes, we take inspiration from the static compliance used in conventional compliance minimization problems, and define this term as:

$$c_{\text{thermal}} = \boldsymbol{U}_{\text{thermal}}^{\mathrm{T}} \boldsymbol{K} \boldsymbol{U}_{\text{thermal}}, \tag{4.26}$$

where $\boldsymbol{K}$ is the stiffness matrix of the complete component. $\boldsymbol{U}_{\text{thermal}}$ is the accumulated displacement vector as defined in Eq. 4.6. This measure accounts for the deformation of all elements, and thus can be viewed as a global metric. Alternative distortion measures, such as the flatness of edges or surfaces that are important for assembly, can also be employed [169, 170].

The second term in the objective function concerns variations in the layer geometry. The layers in the optimized fabrication sequence are typically curved, with a large variation of height (or thickness) within each layer. The large variation is less favorable from a manufacturing perspective. The term f_{geo} measures variations in each layer, by

$$f_{\text{geo}} = \sum_{j=1}^{N} \sum_{e} \eta_e^{\{j\}p} \left(|\nabla t_e| - \overline{|\nabla t|}^{\{j\}} \right)^2, \tag{4.27}$$

where $|\nabla t_e|$ is the magnitude of the gradient of the time field at an element, and $\overline{|\nabla t|}^{\{j\}}$ is the averaged magnitude of gradients within the j-th layer, i.e.,

$$\overline{|\nabla t|}^{\{j\}} = \frac{\sum_e \eta_e^{\{j\}p} |\nabla t_e|}{\sum_e \eta_e^{\{j\}p}}. \tag{4.28}$$

It should be noted that f_{geo} does not guarantee a uniform layer thickness. In fact, variations in layer thickness offer the flexibility needed to form non-planar curved layers.

The optimization problem is subject to two sets of PDEs, both of which are discretized using finite element methods. Eq. 4.21 analyzes the incremental displacement of the intermediate structure under the equivalent load of inherent strains in each newly deposited layer. The number of such equations corresponds to the number of layers being analyzed, which constitutes the primary computational bottleneck. Eq. 4.22 is the discretized version of the virtual heat equation (Eq. 4.4). In addition to the PDE constraints, g_j is the volume constraint for each layer, assuming a constant manufacturing speed — the same amount of material volume is processed at each time interval. V_0 is the total material volume. g_s is the global residual stress constraint as discussed in Section 4.2.3.

CONCURRENT OPTIMIZATION OF STRUCTURAL LAYOUT AND FABRICATION SEQUENCE

In the concurrent optimization setting, the structural layout is optimized as well. Here we consider design optimization of lightweight load-bearing structures. The structural performance and total material consumption are added to the formulation

as constraints.

$$\text{Subject to:} \quad \boldsymbol{K}\boldsymbol{U} = \boldsymbol{F}, \tag{4.29}$$

$$g_c = \boldsymbol{U}^{\mathrm{T}}\boldsymbol{K}\boldsymbol{U} - c_{\mathrm{lim}} \leq 0, \tag{4.30}$$

$$g_0 = \sum \rho_e v_e - V_0 \leq 0, \tag{4.31}$$

$$0 \leq \phi_e \leq 1. \tag{4.32}$$

Eq. 4.29 is the static equilibrium equation for the complete structure under external loads in its service condition. g_c sets an upper bound for the mechanical compliance, c_{lim}. Alternatively, this constraint can also be added into the objective function, with an additional weight coefficient. Lastly, g_0 is the global volume constraint, which limits the total amount of material used for the entire structure.

It should be noted that the pseudo-density field, $\boldsymbol{\rho}$, is not directly treated as design variables. Instead, we adopt the three-field approach commonly used in density-based topology optimization [166]. The design variables are represented by the design field $\boldsymbol{\phi}$, which is then smoothed through a convolution filter to obtain a filtered field, $\tilde{\boldsymbol{\phi}}$. This filtering prevents the occurrence of checkerboard patterns in the optimized structure. The filtered field $\tilde{\boldsymbol{\phi}}$ is subsequently transformed using a smoothed Heaviside function to promote a black-and-white design. This yields the pseudo-density field $\boldsymbol{\rho} = \bar{\tilde{\boldsymbol{\phi}}}$, which is used in the structural analysis that follows. For details about the transformations of optimization variables, readers are referred to chapter 2.

Both optimization problems are solved using gradient-based methods, specifically the method of moving asymptotes (MMA) [153]. A detailed sensitivity analysis for the residual stress constraint is provided in the appendix A.3.

4.3. NUMERICAL EXAMPLES

In this section, we validate the proposed method using multiple numerical examples. We start with fabrication sequence optimization on an L-shaped component (Section 4.3.1) and a bracket (Section 4.3.2). Following that, we extend to simultaneous optimization of the structural layout and fabrication sequence, allowing for more flexibility (Section 4.3.3). The material used in these examples is titanium, with Young's modulus $E = 110\,\mathrm{GPa}$ and Poisson's ratio $\nu = 0.3$. The residual stress limit is set as $\sigma_{\mathrm{lim}} = 1200\,\mathrm{MPa}$, while the inherent strain value is $\boldsymbol{\epsilon}_0^* = \left[\epsilon_{xx}, \epsilon_{yy}, \epsilon_{xy}\right]^{\mathrm{T}} = [-0.00375, -0.00375, 0]^{\mathrm{T}}$, unless otherwise specified. The method is implemented in MATLAB, and the code has not been specifically optimized for computational efficiency. All simulations were executed on a single CPU core of a workstation equipped with an Intel Xeon E-2630v4 processor and 256 GB of RAM.

4.3.1. FABRICATION SEQUENCE OPTIMIZATION FOR A V-SHAPED COMPONENT

The first example for fabrication sequence optimization is a V-shaped component, shown in Fig. 4.4(a). The resolution of the background mesh is 100×100 elements.

The baseplate for fabrication is located at the bottom of the component. In the manufacturing process simulation, the component is fixed at the bottom. The prescribed number of layers is 40. On average, each iteration in the optimization process takes 275.2 seconds.

Fig. 4.4(top) presents simulation results for the component manufactured using planar layers. Fig. 4.4(b) displays the von Mises stress distribution of the total residual stresses in the final structure. It reveals a maximum residual stress of $\sigma_{\max} = 2551.1\,\text{MPa}$, which is 112.6% above the limit. The corresponding structural distortion is shown in Fig. 4.4(c), with a total thermal-induced compliance of $1.565 \times 10^5\,\text{mJ}$. By comparison, the optimized fabrication sequence (Fig. 4.4, bottom) employs curved layers to mitigate these effects. The maximum residual stress is reduced to $\sigma_{\max} = 1200.4\,\text{MPa}$, numerically satisfying the stress constraint, while distortion decreases significantly to $8.327 \times 10^4\,\text{mJ}$, a 46.8% reduction in compliance compared to the planar case.

From the residual stress distributions, high residual stresses can be observed at the two ends of the bottom and around the right-angled corner in the middle (marked as P_1, P_2, and P_3 in Fig. 4.4(a)). The histories of residual stresses at

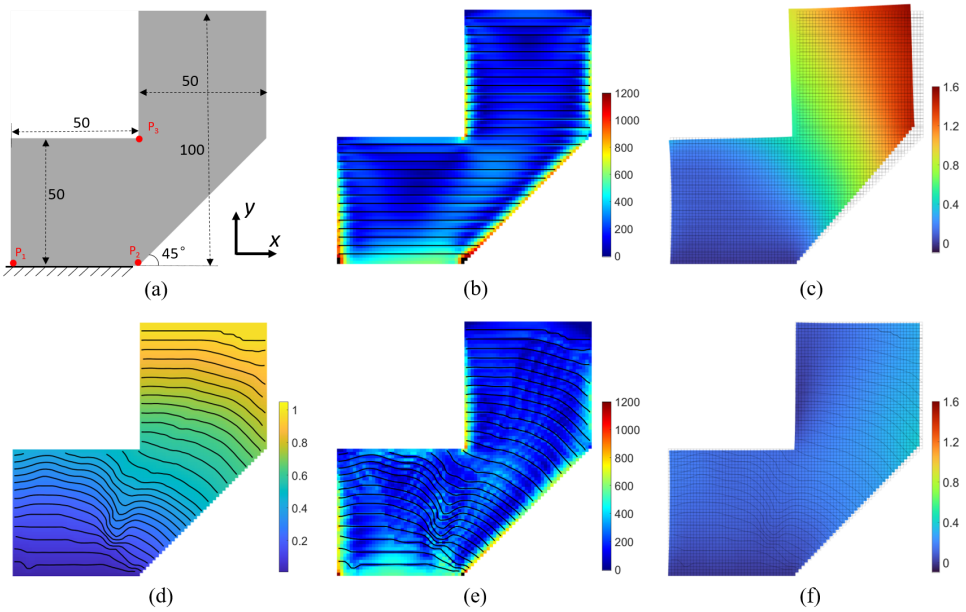

Figure 4.4.: Comparisons between planar and non-planar fabrication of a V-shaped component. (a) The dimensions of the V-shaped component. (b) The resulting residual stresses from planar fabrication. Elements with stresses exceeding the limit ($\sigma_{\text{lim}} = 1200\,\text{MPa}$) are colored in black. (c) The corresponding structural distortion. (d) The optimized time field. Its isolines segment the component into curved layers. (e, f): Using curved fabrication, the resulting residual stresses (e) and distortion (f).

these three locations are plotted in Fig. 4.5, with the horizontal axis indicating the increasing number of layers during the manufacturing process. The subfigure on the left represents fabrication with planar layers, while the one on the right shows fabrication with optimized curved layers. When the component is manufactured using planar layers, the residual stresses at Point 1 and Point 2 increase gradually, both exceeding the stress limit of 1200 MPa after 5 layers. The stress at Point 3 appears after 19 layers and stops increasing at around 940 MPa until the end of fabrication. In contrast, when manufactured using optimized fabrication sequences, the increases of residual stresses at Point 1 and Point 2 are suppressed. The residual stress at Point 1 remains below the stress limit, with a margin of 40 MPa. While the residual stress at Point 2 increases to slightly over the stress limit after 20 layers, it returns to the limit onwards. The stress at Point 3 appears after 21 layers and reaches around 750 MPa at the end of fabrication.

The above observations demonstrate the effectiveness of the residual stress constraint. We note that this constraint is applied to the residual stresses at the completion of fabrication (i.e., after 40 layers). During the manufacturing process, the maximum residual stress does not significantly exceed the limit, so the residual stress history is currently not included in the optimization. However, in principle, it could be included, though at the cost of increasing the number of residual stress constraints by considering the stresses of all intermediate structures.

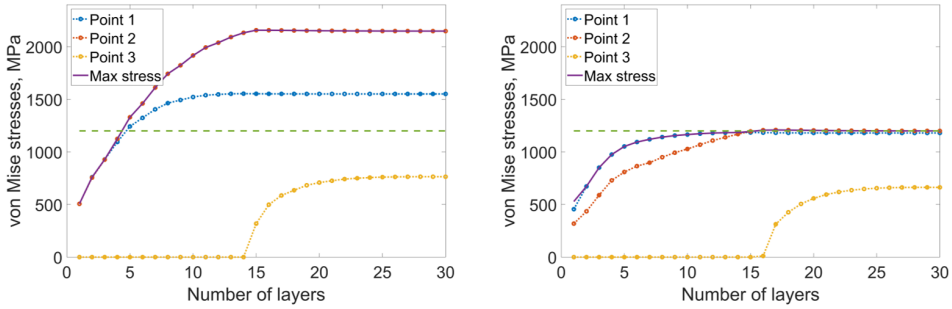

Figure 4.5.: The accumulation of residual stresses at three sampling points during the manufacturing process. Left: fabrication according to the planar layers. Right: fabrication according to the optimized curved layers shown in Fig. 4.4(b).

We further analyze the effects of approximating discrete manufacturing processes with a differential formulation that facilitates gradient-based optimization. To this end, we perform a post-optimization analysis of the optimized sequence, adopting the binary layer description defined in Eq. 4.1. The maximum residual stresses and thermal-induced compliances in the optimization and the post-analysis are summarized in Table 4.1. Specifically, for the optimized layers, post-analysis reveals an increase in the maximum residual stress from 1200.4 MPa to 1276.0 MPa, i.e., an increase of 6.30%. The thermal-induced compliance is increased from 8.327×10^4 mJ to 8.396×10^4 mJ, i.e., an increase of 0.83%. A similar trend is observed for the planar layers, which in the continuous formulation were defined by a height field, i.e.,

$t_e = \frac{y_e}{Y}$, where y_e is the y-coordinate of the element's centroid, and Y is the height of the component. The difference between the differential and binary layer descriptions comes from grey elements in the intermediate structures $\boldsymbol{\rho}^{\{j\}}$. The discrepancies are small, thanks to the continuation scheme for the projection parameter β_t in the smoothed Heaviside projection. To account for the unavoidable discrepancies due to the continuous approximation of a discrete manufacturing process, one could set a tighter residual stress limit in the constraint, i.e., reducing σ_{lim} to e.g., 1100 MPa.

Table 4.1.: Results of the L-shaped component with planar and curved fabrication.

		Optimization result with differential layers	
		Maximum stress	Thermal compliance
$N = 40$	Planar layers	2551.1 MPa	1.565×10^5 mJ
	Optimized curved layers	1200.4 MPa	8.327×10^4 mJ
		Post-analysis with binary layers	
		Maximum stress	Thermal compliance
$N = 40$	Planar layers	2709.3 MPa	1.435×10^5 mJ
	Optimized curved layers	1276.0 MPa	8.396×10^4 mJ

4.3.2. FABRICATION SEQUENCE OPTIMIZATION FOR A BRACKET

The second example is a bracket, shown in Fig. 4.6(a). The resolution of the background mesh is 200×88. During manufacturing, the component is fully fixed at the bottom, where the fabrication starts. Fig. 4.6(b) and (c) show the resulting residual stress and distortion, respectively, if the component is fabricated with 30 planar layers. The maximum residual stress in the final structure is $\sigma_{\text{max}} = 1950.5$ MPa, exceeding the stress limit by 62.54%. The thermal-induced compliance is 6.786×10^4 mJ. The bottom row of Fig. 4.6 shows, from left to right, the optimized curved layers, corresponding residual stress distribution, and distortion. The curved layers are optimized to minimize the thermal-induced compliance under a constraint on residual stresses. With the curved layers, the maximum residual stress is reduced to $\sigma_{\text{max}} = 1199.6$ MPa.

To help understand how the curved layers avoid high residual stresses, Fig. 4.7 presents the sequence of the first 8 layers. As observed in the first layer, the printing process begins from the two bottom corners. This approach is in contrast to a conventional planar first layer, which typically involves a longer, continuous deposition path. By shortening the deposition length at these critical regions, the curved-layer strategy effectively reduces residual stress accumulation, particularly at the left and right corners where stress concentration is more likely to occur.

It is noticed that while the residual stress is effectively constrained by the curved layers, the corresponding thermal-induced distortion increases by 7.38%, to 7.287×10^4 mJ. It is worth noting that the bracket is well-suited for planar fabrication

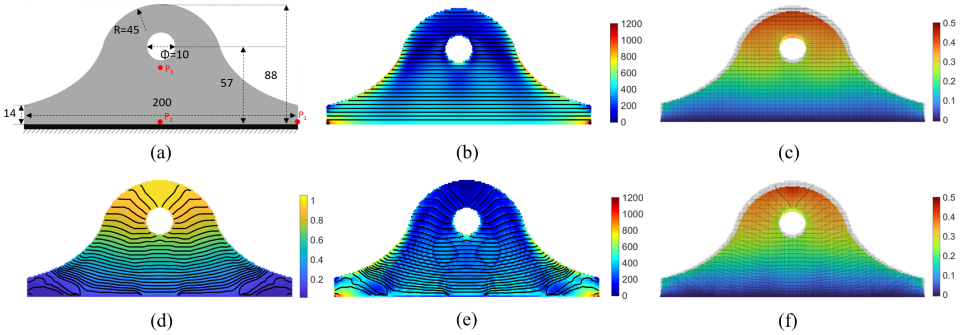

Figure 4.6.: Comparisons between planar and non-planar fabrication on a symmetric bracket, with 30 layers. (a) The geometry of the bracket. (b, c): Using planar fabrication, the resulting residual stresses (b) and distortion (c). (d) The optimized time field. Its isolines segment the component into curved layers. (e, f): Using curved fabrication, the resulting residual stresses (e) and distortion (f).

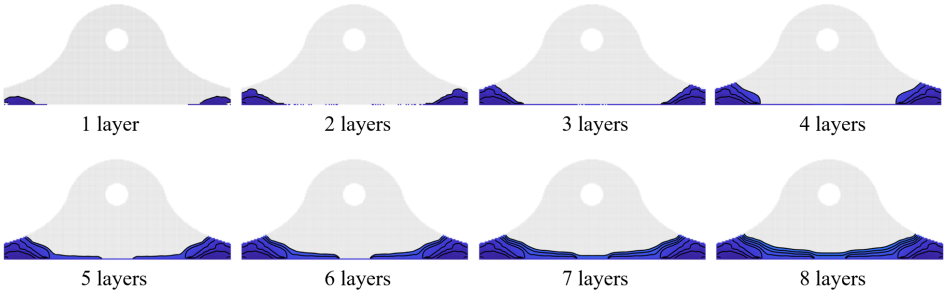

Figure 4.7.: Illustration of the first 8 layers in manufacturing the bracket according to the optimized fabrication sequence.

due to its symmetric geometry and the presence of only a minor overhang at the top of the inner ring. In planar fabrication, the bracket exhibits significantly less thermal distortion compared to the L-shaped component. This is because the symmetry of the brackets allows the distortion from the opposite sides to be canceled out. However, this suppression of distortion through symmetry results in high residual stresses that must be mitigated. Curved fabrication offers an effective solution to reduce these stresses.

The left subfigure of Fig. 4.8 plots the history of residual stresses at three critical points when the component is fabricated with the curved layers. The locations of these three points are marked in Fig 4.6(a). The residual stresses at all three points monotonically increase during manufacturing, with the point on the end at the bottom showing the highest residual stress. In addition, the convergence history of the objective function and the constraint functions are shown in the right subfigure of Fig. 4.8. All the constraint functions converge to zero, and the objective function converges stably. The initial time field is solved from a uniform heat conductivity

field, leading to a low objective value but significant violations of the constraints. As the constraints are gradually satisfied, the objective value increases. Notably, abrupt changes in the convergence curve occur every 50 iterations, which are due to the continuation scheme applied to the projection parameter β_t.

Table 4.2.: Results of the bracket with planar and curved fabrication.

		Optimization result with differential layers	
		Maximum stress	Thermal compliance
$N = 30$	Planar layers	1950.5 MPa	6.786×10^4 mJ
	Optimized curved layers	1199.6 MPa	7.287×10^4 mJ
$N = 10$	Planar layers	1649.3 MPa	5.313×10^4 mJ
	Optimized curved layers	1201.0 MPa	5.592×10^4 mJ
		Post-analysis with binary layers	
		Maximum stress	Thermal compliance
$N = 30$	Planar layers	1997.1 MPa	6.147×10^4 mJ
	Optimized curved layers	1250.8 MPa	7.119×10^4 mJ
$N = 10$	Planar layers	1655.6 MPa	5.097×10^4 mJ
	Optimized curved layers	1251.5 MPa	5.124×10^4 mJ

To investigate the influence of the number of layers, we also optimized the fabrication sequence with a reduced number of layers, i.e., from 30 to 10. Consequently, the average computation time per iteration is reduced from 228 s to 84 s, achieving a 2.7-fold speedup, which aligns with the three-fold reduction in the number of mechanical analyses. The simulation results of the planar layers and the optimized curved layers are shown in the top and bottom rows of Fig. 4.9, respectively. The maximum residual stress and thermal-induced compliance are

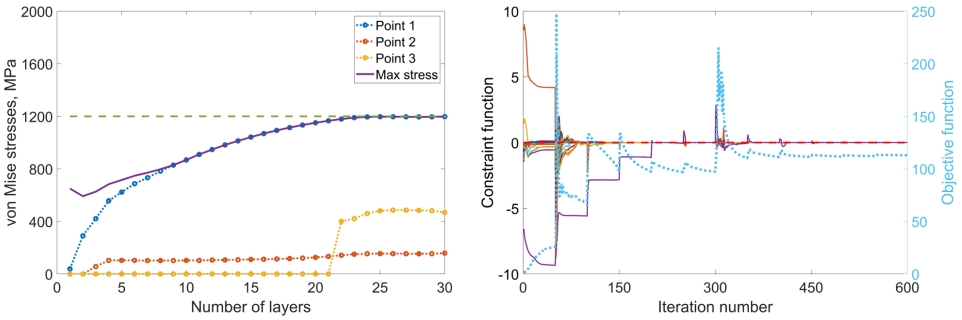

Figure 4.8.: Data analysis for the bracket component. Left: the accumulation of residual stresses at three sampling points during manufacturing. Right: convergence of the objective function (dotted line in light blue) and the constraint functions.

summarized in Table 4.2. With 10 planar layers, both the maximum residual stress and the thermal-induced compliance were reduced, in comparison to 30 planar layers. The optimized curved fabrication, with 10 layers, is again effective in restricting the maximum residual stress. However, when the number of layer divisions decreases, the design freedom for fabrication sequence is restricted. The entire bottom edge has to be built within the first single layer, as there are only 10 layers in total. The appropriate number of layers shall be chosen based on the experimental setup, particularly considering the layer thickness.

4.3.3. CONCURRENT STRUCTURAL AND SEQUENCE OPTIMIZATION FOR THE L-SHAPED COMPONENT

In the last example, we validate the concurrent optimization of the structural layout and the fabrication sequence, and compare it with a decoupled sequential optimization strategy. The design domain is defined by the L-shaped component shown in Fig. 4.10(a). The domain is discretized using a grid of 180×120 elements. In structural optimization, the material volume ratio is restricted to 0.5, and an external force is applied on the top right corner. As the total amount of material is reduced by half, less energy is introduced into the structure during fabrication, and thus small residual stresses and distortions. To demonstrate the effectiveness of the optimization, we doubled the inherent strain value in order to amplify the resulting residual stresses: $\boldsymbol{\epsilon}_0^* = \left[\epsilon_{xx}, \epsilon_{yy}, \epsilon_{xy}\right]^{\mathrm{T}} = [-0.0075, -0.0075, 0]^{\mathrm{T}}$. In the manufacturing process simulation, the component is fixed at the bottom, consistent with its intended application condition. The total number of layers is prescribed to 20. The average computation time per iteration is 240 s.

Figure 4.10 (b) shows the structural layout obtained from space-time topology optimization. As a reference, the layout from the standard topology optimization (i.e., no consideration of the manufacturing process) is shown in Fig. 4.10(c). Both

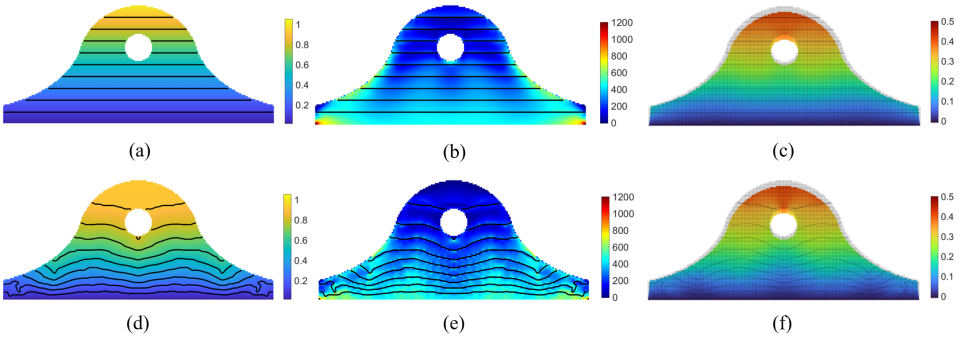

Figure 4.9.: Comparisons between planar and non-planar fabrication on a symmetric bracket, with 10 layers. (a) The planar layers. (b, c): Using planar fabrication, the resulting residual stresses (b) and distortion (c). (d) The optimized time field. Its isolines segment the component into curved layers. (e, f): Using curved fabrication, the resulting residual stresses (e) and distortion (f).

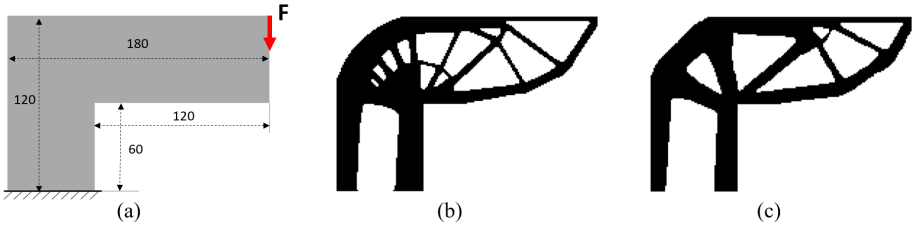

Figure 4.10.: Structural optimization of the L-shaped component. (a) The design domain and boundary condition of the L-shaped component. (b) The optimized structure when the structural layout and fabrication sequence are simultaneously optimized. (c) The optimized structure from standard topology optimization.

optimizations lead to clear structural layouts. The external boundaries of both designs are quite similar; however, the internal structures resulting from standard topology optimization are noticeably less complex, despite the use of the same filtering radius for the density field. In standard topology optimization, the objective is to minimize compliance, which is reduced 2170.4 mJ in this case. Taking this value as a reference, the compliance limit is set to 2200.0 mJ in space-time topology optimization, in which compliance is treated as a constraint (Eq. 4.30). This constraint function is numerically satisfied in the optimization process, leading to a compliance of 2202.8 mJ.

The corresponding fabrication sequence optimized from space-time topology optimization is shown in Fig. 4.11(g). For comparison, two planar fabrication sequences for the same structural layout are included: horizontal layers (a), and layers inclined at 45° (f). The residual stress distributions for all three sequences (horizontal, inclined, and optimized) are shown in the middle column of each row, while thermal-induced distortions are illustrated on the right. As summarized in Table 4.3, both horizontal and inclined layers result in the maximum stress above the limit, while by the optimized curved layers the maximum is reduced to 1211.1 MPa. Converting the grey values in the differentiable layer formulation to binary layers, the maximum residual stresses are 1352.3 MPa, 1410.9 MPa and 1189.0 MPa for the three fabrication sequences respectively. The optimized sequence reduces the maximum residual stress by more than 12%. More pronouncedly, the thermal-induced distortion is reduced from 5.207×10^5 mJ to 2.168×10^5 mJ, a reduction of 58.36%.

An additional comparison is conducted using the structural layout from the standard topology optimization, as shown in Fig. 4.10(c). The first two rows show results for horizontal and inclined layers (45°). The bottom row shows the outcome of applying fabrication sequence optimization to the topology-optimized structure–performed sequentially after the structural optimization rather than concurrently. Compared to planar manufacturing strategies, the optimized fabrication sequence effectively reduces both the maximum residual stress and the thermal-induced distortion, aligning with the trends observed in earlier examples. This highlights the importance of considering sequence planning even after structural design.

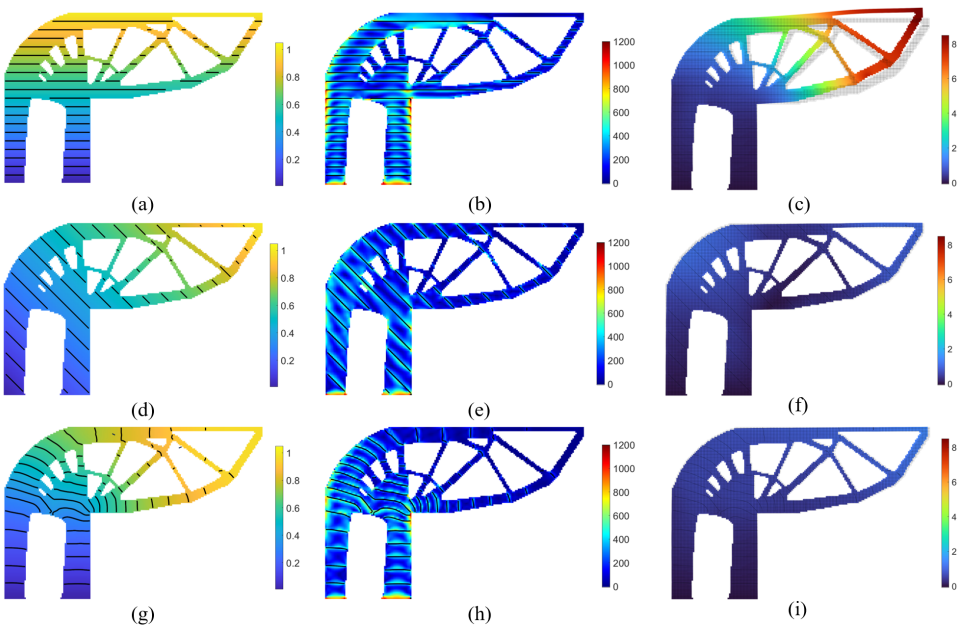

Figure 4.11.: The simultaneously optimized structure (Fig. 4.10(b)) and sequence are compared to the same structure but with planar layers. (a) The horizontal planar layers. (b, c): Using horizontal layers, the resulting residual stresses (b) and distortion (c). (d, e, f): The inclined layers and corresponding stresses and distortion. (g, h, i) Curved layers from the simultaneously optimized time field, and the corresponding stresses and distortion.

An interesting observation arises from comparing the sequential optimization (Fig. 4.12, bottom) with the concurrent optimization (Fig. 4.11, bottom). The numerical values for these two scenarios, summarized in Table 4.3, differ only marginally, which was somewhat unexpected but not entirely surprising. This can be attributed to the large number of variables involved in sequence optimization, which results in a vast solution space even when the structure is fixed. Additionally, the search within the even larger solution space in concurrent structural and sequence optimization is mathematically more complicated. Furthermore, structural and fabrication sequence optimizations have distinct objectives, which are integrated into the concurrent optimization in a mixed approach—structural compliance in a constraint, while distortion is part of the objective.

Lastly, the convergence history in the concurrent optimization for the L-shaped beam is plotted in Fig. 4.13. To illustrate the design evolution during optimization, the structural layouts at the 100-th, 200-th, 300-th, 400-th iterations are shown. The structural layout gradually converges to a clear black-and-white design after about 300 iterations. All constraint functions approach zero. Although the objective function exhibits fluctuations due to the parameter continuation strategy discussed earlier, it shows an overall decreasing trend.

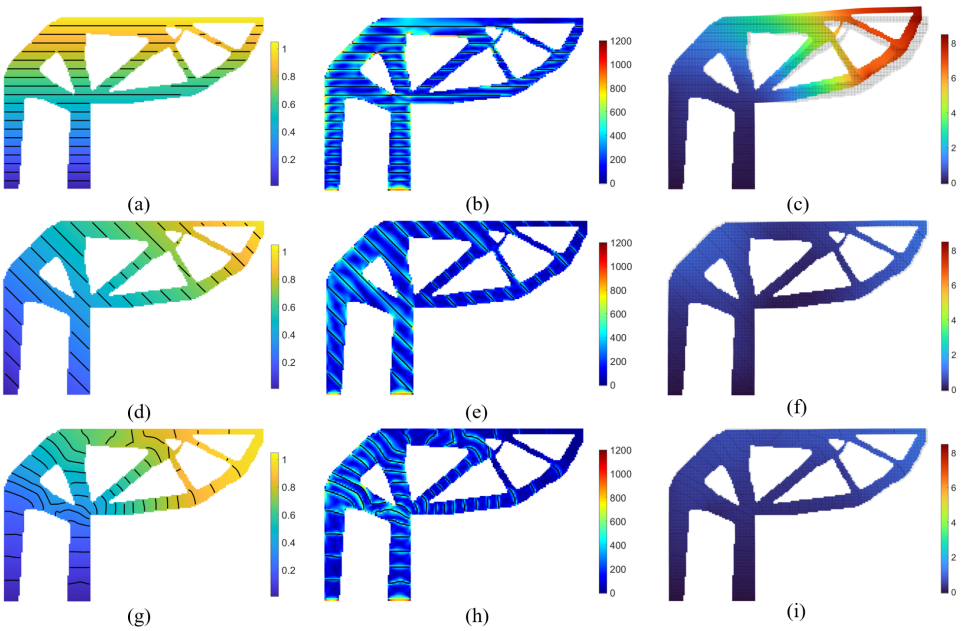

Figure 4.12.: Comparisons between horizontal (top), inclined (middle), and curved layers (bottom), tested on the structure from standard topology optimization (Fig. 4.10(c)). From left to right: layers, residual stresses, and distortions.

The layer-by-layer manufacturing process of the optimized L-shaped component is displayed in Fig. 4.14.

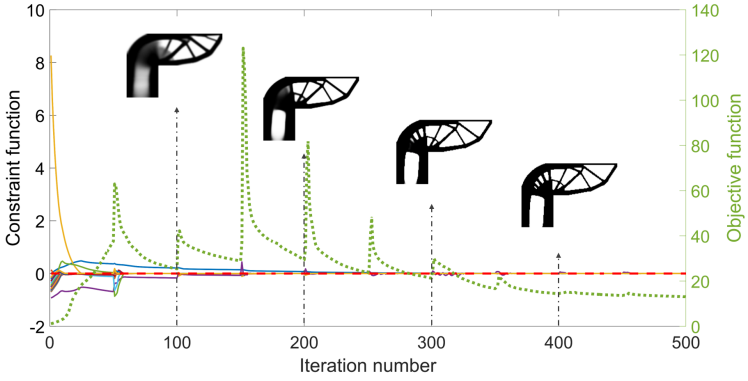

Figure 4.13.: Convergence of the objective and constraint functions in simultaneous optimization of the structural layout and fabrication sequence. The evolving structural layouts at the 100-th, 200-th, 300-th, 400-th iterations are included.

Table 4.3.: Results of the L-shape component with different structural layouts and fabrication sequences, $N = 20$

	Compliance	fabrication sequence	Maximum stress	
			Differential	Binary
Simultaneous optimization	2202.8 mJ	Horizontal layers	1324.7 MPa	1352.3 MPa
		Inclined layers	1308.4 MPa	1410.9 MPa
		Curved layers	1211.1 MPa	1189.0 MPa
Sequential optimization	2170.4 mJ	Horizontal layers	1369.2 MPa	1410.6 MPa
		Inclined layers	1263.1 MPa	1359.5 MPa
		Curved layers	1200.1 MPa	1200.8 MPa

	fabrication sequence	Thermal compliance	
		Differential	Binary
Simultaneous optimization	Horizontal layers	5.819×10^5 mJ	5.207×10^5 mJ
	Inclined layers	3.204×10^5 mJ	2.794×10^5 mJ
	Curved layers	2.284×10^5 mJ	2.168×10^5 mJ
Sequential optimization	Horizontal layers	6.041×10^5 mJ	5.422×10^5 mJ
	Inclined layers	2.831×10^5 mJ	2.592×10^5 mJ
	Curved layers	2.139×10^5 mJ	1.957×10^5 mJ

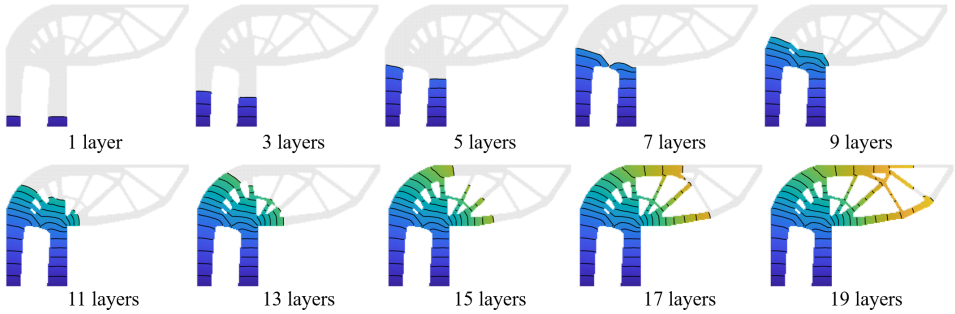

Figure 4.14.: Illustration of the fabrication process of the optimized structure with curved layers. For simplicity, only odd-numbered layers are included.

4.4. CONCLUSION

This chapter introduces a novel method for reducing residual stresses in wire arc additive manufacturing. Our method optimizes the fabrication sequence, represented as isolines of a pseudo-time field. The optimization integrates residual stresses as a constraint while minimizing thermally induced distortions. The resulting sequences are predominantly curved, with smoothly varying orientations. Compared to traditional planar layers, the optimized curved layers significantly reduce distortion and effectively control excessive residual stresses. Additionally, the method allows

for simultaneous optimization of both the fabrication sequence and the structural layout, offering valuable insights into how these factors influence residual stresses.

This work introduces fabrication sequence optimization as a new approach for enhancing the quality of WAAM and opens up several avenues for future exploration. Firstly, the inherent strain model could be replaced with high-fidelity process models to enhance the accuracy of residual stress and distortion predictions. Additionally, application-specific criteria (such as the Tsai–Wu failure criterion instead of von Mises stresses, or distortion metrics targeting critical geometric features like the flatness of assembly surfaces) could refine optimization outcomes. Furthermore, future work could explore tailoring the residual stress distribution, to improve the component strength under in-service mechanical loads. Last but not least, a key next step is the transition from numerical simulations to experimental validation, which is critical for industrial adoption. While the numerical results demonstrate considerable promise, practical realization through robotic systems for curved layer fabrication presents new challenges. For instance, while layers with varying thickness can be achieved by adjusting manufacturing process parameters, manufacturing practice favors curved layers with minimal thickness variation to ensure consistent print quality. Furthermore, the varying process parameters need to be incorporated into the process model. By addressing these challenges, this framework holds the potential to advance WAAM as a robust and reliable technology, enabling innovative applications across industries.

5

SPACE-TIME TOPOLOGY OPTIMIZATION FOR ANISOTROPIC MATERIALS

Wire and Arc Additive Manufacturing (WAAM) has great potential for efficiently producing large metallic components. However, like other additive manufacturing techniques, materials processed by WAAM exhibit anisotropic properties. Assuming isotropic material properties in design optimization thus leads to less efficient material utilization. Instead of viewing WAAM-induced material anisotropy as a limitation, we consider it an opportunity to improve structural performance. This requires the integration of process planning into structural design. In this chapter, we propose a novel method to utilize material anisotropy to enhance the performance of structures both during fabrication and in their use. Our approach is based on space-time topology optimization, which simultaneously optimizes the structural layout and the fabrication sequence. To model material anisotropy in space-time topology optimization, we derive the material deposition direction from the gradient of the pseudo-time field, which encodes the fabrication sequence. Numerical results demonstrate that leveraging material anisotropy effectively improves the performance of intermediate structures during fabrication as well as the overall structure.

Parts of this chapter have been published in *International Journal of Mechanical Sciences* **284**, 109712 (2024) authored by Kai Wu, Weiming Wang, Fred van Keulen and Jun Wu, under the title *Space-time Topology Optimization for Anisotropic Materials in Wire and Arc Additive Manufacturing.*

5.1. INTRODUCTION

TOPOLOGY optimization is essential in structural design for additive manufacturing. By topology optimization, structural design is transformed into an optimization problem of determining the optimal material distribution to maximize structural performance, such as creating lightweight structures with high load-bearing capacity [146, 161]. It has been widely applied across engineering disciplines, including aerospace, automotive, civil and biomechanical engineering. Additive manufacturing, also known as 3D printing, fabricates components layer-upon-layer from digital models. In the manufacturing process, the material is added precisely where needed, allowing for complex geometries, customization, and reduced waste compared to traditional manufacturing methods [183]. The design freedom provided by topology optimization complements the manufacturing flexibility of additive manufacturing, allowing for the creation of components with exceptional performance [151, 162]. However, the complex geometries resulting from topology optimization often pose production challenges, even with advanced additive manufacturing techniques. Consequently, integrating additive manufacturing constraints into structural design optimization has been a key research area over the past decade. Important issues that have been addressed include overhang limitation [86, 87, 158], local overheating [133], support structures [81, 177], and residual stresses [5, 190]. We refer to the review articles [9, 100, 207] for a comprehensive overview of developments in topology optimization for additive manufacturing.

Beyond structural design, the manufacturing process itself greatly influences the quality of additively produced components. For example, in wire and arc additive manufacturing (WAAM) [3, 71, 171], substantial distortion may occur during fabrication and after cutting off from the build plate. An essential aspect of manufacturing process planning is the fabrication sequence, which dictates the layer-by-layer construction of the structure. In traditional 2.5D printing, where each layer is planar and parallel to each other, the layer-wise sequence is uniquely defined by the orientation of the structure on the build plate. Topology optimization, combined with build orientation optimization for 2.5D printing, has been explored in several studies [20, 25, 88, 96, 125, 165]. However, advancements in multi-axis printing using robotic arms, capable of rotational and translational movements, allow for material deposition along non-planar layers [38, 55, 75, 155]. This capability expands the solution space for fabrication sequence planning. Optimizing the fabrication sequence can significantly enhance the quality of fabricated components. For instance, it reduces structural distortions caused by high temperature gradients and phase transitions in WAAM [169].

Fabrication sequences are typically planned after the structure has been designed, leading to insufficient consideration of the manufacturing process during the design phase. This disconnect results in discrepancies between digital designs and their physical counterparts. Recent studies aim to close this gap by integrating manufacturing process planning into structural design optimization [7, 22]. Achieving optimal structural performance necessitates a holistic approach that concurrently optimizes both the structural layout and the fabrication sequence [16, 168].

Known as space-time topology optimization [168], it introduces a pseudo-time field alongside the pseudo-density field used in conventional topology optimization. The pseudo-time field encodes the fabrication sequence, facilitating the planning of the sequence as the structural layout evolves during optimization. The isolines of the pseudo-time field divide the structural layout into an ordered sequence of curved layers, enabling the analysis of intermediate structures that emerge during the manufacturing process.

Previous implementations of the space-time topology optimization framework have generally assumed isotropic material properties. However, in additive manufacturing, material properties such as elastic modulus, tensile strength, and yield strength are significantly influenced by the manufacturing process, leading to anisotropic behavior [14, 66, 74, 78, 80, 93, 172, 199, 208]. Assuming isotropic material properties in design optimization thus leads to suboptimal performance [79, 94, 134, 143, 182]. In WAAM, material anisotropy is particularly prevalent in components fabricated from materials like austenitic stainless steel [83] and Ti-6Al-4V [115], primarily due to rapid and uneven solidification during manufacturing [83]. It is therefore important to take material anisotropy into account when designing for WAAM [111, 132].

In this chapter, we propose a novel method to utilize material anisotropy to enhance the performance of structures both during fabrication and in their use. By considering the effects of material anisotropy in the concurrent optimization of structural design and process planning, we aim to reduce the gap between digital designs and their physical counterparts, ultimately enhancing the quality of produced components.

The consideration of material anisotropy in structural topology optimization dates back to the 1980s. Early research was driven by the anisotropic properties of laminated and fiber-reinforced composites [131, 150, 154, 204, 205]. Pedersen [126, 127] established that the optimal orientations of orthotropic materials for maximizing structural stiffness align with the principal stress directions. This foundation led to stress-based methods [30, 40, 52, 55, 61, 138, 152] where the material reinforcement direction is derived from principal stress directions. For structures subjected to multiple load cases, the arrangement of local material orientation is treated as an optimization problem, with material orientation defined as either a discrete or continuous variable, represented using the polar angle [72, 73] or a vector in the Cartesian coordinate system [92, 122]. This approach has been integrated with topology optimization to simultaneously optimize structural layout and material orientation [72, 73, 92, 122, 139]. However, these methods are not directly applicable to design for additive manufacturing, as they either derive material orientation from stress fields or treat local material orientation as independent optimization variables. The resulting optimized anisotropic material orientation may not be achievable through an additive manufacturing process.

Recent studies have incorporated material anisotropy in structural optimization for additive manufacturing, coupling material orientation with structural design based on material deposition toolpaths in manufacturing processes. Level-set-based topology optimization [161] is particularly well-suited for this purpose, where iso-value level set contours are interpreted as deposition toolpaths, with material orientations

aligned accordingly [26, 56, 103, 191]. While this typically results in toolpaths that are quasi-parallel to the optimized shape's boundary, it does not allow for more complex patterns, such as zig-zag toolpaths. Vibhas et al.[111] proposed a method to optimize structural design for WAAM by integrating material anisotropy, with deposition toolpaths manually derived from the optimized orientation in a post-processing step. Automated extraction of toolpaths from specialized topology optimization methods has also been explored, such as the phase-field de-homogenization approach [70] and the streamline algorithm [51]. However, it is important to note that in both these methods and others, the toolpaths are static and do not determine the printing order. Our work differs by specifically analyzing the printing order of toolpaths, an investigation made possible through space-time topology optimization [168–170].

In space-time topology optimization, the fabrication sequence is represented by a pseudo-time field, and it is optimized concurrently with the pseudo-density field representing the structural layout. To integrate material anisotropy into space-time topology optimization, a differentiable relationship between material anisotropy and the fabrication sequence should be established. In this chapter, we will illustrate that the anisotropic material orientation can be implicitly derived from the pseudo-time field. Furthermore, the printing order can also be derived from the pseudo-time field, allowing us to predict its consequence on printing quality. This research demonstrates the feasibility and benefits of incorporating manufacturing-induced material anisotropy in space-time topology optimization.

The remainder of the chapter is organized as follows. Section 5.2 details the mathematical model underlying our method. Section 5.3 presents a series of numerical examples, validating the effectiveness of the proposed method. Lastly, Section 5.4 summarizes the key findings and contributions.

5.2. METHOD

In this section, we first introduce the parameterization of the structural layout and fabrication sequence, specifically the space-time parameterization using pseudo-density and pseudo-time fields (Section 5.2.1). Next, we discuss the anisotropic material model, emphasizing the relationship between material anisotropy and the pseudo-time field (Section 5.2.2). The computational steps involved in space-time topology optimization are detailed in Section 5.2.3. Finally, Section 5.2.3 presents the mathematical model for space-time topology optimization with anisotropic materials, along with the pseudo-code summarizing the solution process.

5.2.1. SPACE-TIME PARAMETERIZATION

Here we review the parameterization for space-time topology optimization, which forms the foundation of our current work. In space-time optimization, both the structural layout and the corresponding fabrication sequence are optimized concurrently. The structural layout is represented using a pseudo-density field $\boldsymbol{\rho}$, as in classic density-based topology optimization. Simultaneously, the fabrication sequence is encoded through a pseudo-time field $\boldsymbol{t}$. For simplicity, the pseudo-density and pseudo-time fields are referred to as density and time fields, respectively.

These fields are defined in the domain of the 2D or 3D component.

Applying the same discretization to both density and time fields, each element is assigned two variables, ρ_e and t_e. In a discrete setup, the density ρ_e assumes values of either 0 or 1, where $\rho_e = 0$ indicates void and $\rho_e = 1$ represents solid material. To avoid solving a binary optimization problem, this binary design variable is relaxed, allowing densities to take intermediate values. Correspondingly, the elastic modulus associated with intermediate density values is determined by a commonly used material interpolation model, i.e., SIMP (Solid Isotropic Material with Penalization).

Unlike the intended binary representation of the density field, the time variable t_e assumes continuous values between 0 and 1. A higher time value indicates that an element is to be built later in the manufacturing process. Specifically, a time value of 0 denotes the beginning of manufacturing, while 1 indicates that the element is produced at the very end of the manufacturing process.

As illustrated in Fig. 5.1, from the continuous time field, a series of intermediate structures is derived. Fig. 5.1(a) shows the structural layout, represented by a density field. Fig. 5.1(b) visualizes the time field on the structure using a colormap. The isolines of the time field partition the component into a series of layers. The iso-values are $\tau_j = \frac{j}{N}, j = 0, 1, ..., N$, with N being the prescribed number of layers. The elements with a time value belonging to the interval $[\tau_{j-1}, \tau_j]$, $j = 1, ..., N$, are part of the j-th layer. Fig. 5.1(c) and (d) illustrate the intermediate structure at two consecutive stages during the manufacturing process. The intermediate structure at time τ is composed of elements with a time value equal to or less than τ. Elements with a time value larger than τ have not been produced and thus are assigned a density value of zero,

$$\rho_e^{\{\tau\}} = \begin{cases} \rho_e, & \text{if } t_e \leq \tau, \\ 0, & \text{otherwise.} \end{cases} \tag{5.1}$$

To facilitate gradient-based optimization, this conditional equation is approximated using a smoothed Heaviside function,

$$\rho_e^{\{\tau\}} = \rho_e \bar{t}_e^{\{\tau\}}, \tag{5.2}$$

with

$$\bar{t}_e^{\{\tau\}} = 1 - \frac{\tanh\big(\beta_t \tau\big) + \tanh\big(\beta_t (t_e - \tau)\big)}{\tanh\big(\beta_t \tau\big) + \tanh\big(\beta_t (1 - \tau)\big)}. \tag{5.3}$$

Here, β_t determines the sharpness of the step function. This function converts, in a differentiable manner, a time value smaller than the threshold value τ to 1, and, conversely, a time value larger than τ to 0.

5.2.2. MATERIAL ANISOTROPY

From the time field that encodes the fabrication sequence, the direction of material deposition can be derived accordingly. In this subsection, we present the computation of local material deposition directions, followed by the constitutive model of anisotropic material in space-time topology optimization.

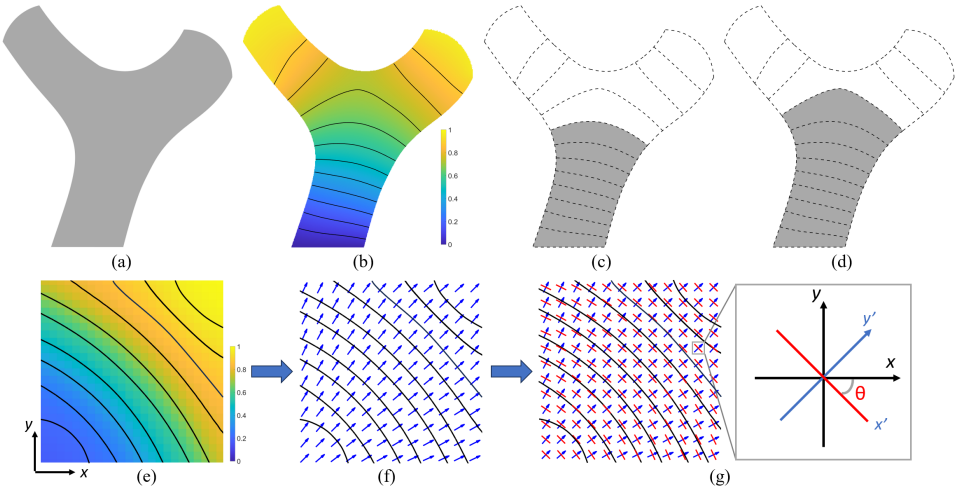

Figure 5.1.: Illustration of space-time parameterization and the orthogonal relationship between the gradient of the time field and the local material orientation. Top row: (a) A structural layout, represented by a density field. (b) The structure color-coded by a time field, with the isolines partitioning the structure into 12 layers. (c,d) Two successive intermediate structures during fabrication, in which 8 or 9 layers have been produced. Bottom row: (e) The time field in a rectangular domain. (f) The normalized gradient (blue arrow) of the time field. (g) The local material deposition direction (red) is perpendicular to the gradient vector element-wise. The local material orientation is denoted by angle θ.

The direction of material deposition correlates with the gradient of the time field, as depicted in the bottom row of Fig. 5.1. Shown in Fig. 5.1(e) is the time field, visualized by a colormap, along with the isolines, which segment this component into curved layers. In Fig. 5.1(f), the gradient of the time field (blue arrow) is visualized, while Fig. 5.1(g) additionally displays the tangent of the time field, which defines the material deposition direction (red line). Although the tangent direction is a vector, we do not differentiate whether the material is deposited along the positive or negative direction of the vector, as this has little influence on material anisotropy. We represent the local material deposition direction using the angle formed between the tangent of the time field and the horizontal axis. As shown in Fig. 5.1(g), the $x-y$ axes are the global reference axes pointing in horizontal and vertical directions. The local material axes $x'-y'$ are aligned with the local material deposition direction, represented by angle θ, which is confined within the range of $-90°$ to $90°$.

The local material deposition direction is orthogonal to the gradient of the time field (∇t),

$$\nabla t\big|_e \cdot \vec{\boldsymbol{\theta}}_e = 0, \tag{5.4}$$

where $\nabla t\big|_e$ is the gradient vector of the time field on element e, and $\vec{\boldsymbol{\theta}}_e = [\cos\theta_e, \sin\theta_e]^\top$ is the vector form of the local material deposition direction θ_e. On a structured mesh, the gradient of the time field can be computed by making

use of the shape functions,

$$\nabla t\big|_e = \left[\sum_{i\in e}\frac{\partial N_i}{\partial x}\,t_i, \sum_{i\in e}\frac{\partial N_i}{\partial y}\,t_i\right]^\top, \tag{5.5}$$

where $\frac{\partial N_i}{\partial x}$ and $\frac{\partial N_i}{\partial y}$ are the spatial derivative of the shape functions evaluated at the centroid of element e. i is a node of element e, and t_i is the nodal time value. The local material deposition direction, restricted to the range of $[-90°, 90°]$, is calculated by

$$\theta_e = \arctan\left(-\frac{\sum_{i\in e}\frac{\partial N_i}{\partial x}\,t_i}{\sum_{i\in e}\frac{\partial N_i}{\partial y}\,t_i}\right). \tag{5.6}$$

The generalized Hooke's law of an orthotropic material can be found in the appendix B. After obtaining the local material deposition direction θ, the elasticity tensor $\boldsymbol{D}$ in the global reference axes $(x-y)$ is related to $\boldsymbol{D}_0$ in the local material axes $(x'-y')$ by a transformation [111]:

$$\boldsymbol{D}(\theta) = \boldsymbol{R}^\top(\theta)\,\boldsymbol{D}_0\boldsymbol{R}(\theta), \tag{5.7}$$

the transformation matrix is

$$\boldsymbol{R}(\theta) = \begin{bmatrix} \cos^2\theta & \sin^2\theta & \sin\theta\cos\theta \\ \sin^2\theta & \cos^2\theta & -\sin\theta\cos\theta \\ -2\sin\theta\cos\theta & 2\sin\theta\cos\theta & \cos^2\theta-\sin^2\theta \end{bmatrix}. \tag{5.8}$$

Eq. 5.7 describes the elasticity tensor for a solid element ($\rho_e = 1$) with anisotropic material. For elements with an intermediate density ($\rho_e \in [0.0, 1.0]$), we apply the SIMP interpolation scheme to anisotropic material,

$$\begin{aligned}\boldsymbol{D}_e(\rho_e,\theta_e) &= \boldsymbol{R}^\top(\theta_e)\,\boldsymbol{D}_0\left(\rho_e\right)\boldsymbol{R}(\theta_e) \\ &= \left[\epsilon + (1-\epsilon)\rho_e^p\right]\boldsymbol{R}^\top(\theta_e)\,\boldsymbol{D}_0\boldsymbol{R}(\theta_e),\end{aligned} \tag{5.9}$$

where ϵ is a very small stiffness assigned to void elements to prevent the stiffness matrix from becoming singular. p is a penalization of intermediate densities to promote a black-and-white design (typically $p = 3$).

MATERIAL ANISOTROPY IN WAAM

Materials processed by metal additive manufacturing exhibit distinctive anisotropic behavior. Here we focus on stainless steel, one of the most common materials used in WAAM. Fig. 5.2(a) illustrates a thin-walled structure manufactured layer-by-layer using WAAM. The material behavior is measured on samples taken in three directions: along the horizontal layer ($\alpha = 0°$), perpendicular to the layer ($\alpha = 90°$), and with an angle of 45°. According to the experimental data reported by Kyvelou et al. [83], the Young's modulus (slope of the curves) of these samples is different, revealing the anisotropic elasticity. Specifically, the Young's modulus along the layer ($\alpha = 0°$) is very close to that perpendicular to the layer ($\alpha = 90°$); 143.3 GPa

and 139.6 GPa, respectively. In contrast, with a Young's modulus of 219.5 GPa, the samples along the 45° direction are significantly stiffer. We note that this anisotropic material behavior differs from the anisotropy in material extrusion 3D printing or fiber-reinforced 3D printing [51], where the material is often stiffest in the deposition direction.

Figure 5.2(b) and (c) visualize the modulus in reference axes for finite element analysis, when the material is deposited at different angles (θ). The plots in Fig. 5.2(b) correspond to the WAAM-produced stainless steel. Considering the nearly identical values of the Young's modulus along and perpendicular to the layer (143.3 GPa and 139.6 GPa, respectively), we simplify by setting E_x and E_y to the same value, $E_x = E_y = 141.45$ GPa, indicating a cubic orthotropic material. The Poisson's ratio in this context is $\nu_{xy} = \nu_{yx} = 0.30$. The shear modulus of this material reaches its peak when the material is deposited along the horizontal reference axis ($\theta = 0°$). The stiffest direction of this material appears at $\theta = \pm 45°$ with $E_{\pm 45°} = 219.50$ GPa, conforming to Fig. 5.2(b).

As a comparison, Fig. 5.2(c) plots the Young's modulus and shear modulus of a different material for various material deposition directions. At $\theta = 0°$, this material shares the same Young's modulus ($E = 141.45$ GPa) as with the material in Fig. 5.2(b). However, its shear modulus is minimal at $\theta = 0°$. This material is stiffer along (and perpendicular to) the deposition direction $\theta = 0°$ than along other directions. While such behavior differs from that observed in WAAM-processed metals, we employ it in our results section for a comparative study investigating the influence of material properties on fabrication sequence optimization.

By incorporating these two distinct types of anisotropic materials, we can enable a comparative analysis of how varying material properties affect the optimized fabrication sequences and resulting structural layouts. This investigation helps to

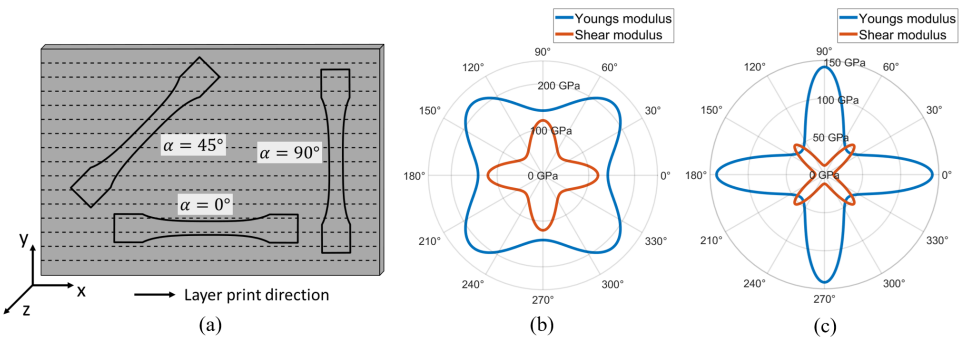

Figure 5.2.: Anisotropic elasticity in WAAM-processed material. (a) Test samples with different orientations relative to layer print direction. (b) Polar plot of Young's modulus and shear modulus measured in the horizontal axis when the WAAM-processed stainless steel is deposited at different angles (θ). The highest Young's modulus is achieved when the material is deposited at $\pm 45°$. (c) Polar plot of another cubic orthotropic material, whose highest Young's modulus is achieved along or perpendicular to the material deposition direction.

evaluate the sensitivity of the optimization framework to material anisotropy and offers valuable insights into the design considerations.

5.2.3. COMPUTATIONAL WORKFLOW

This section presents key steps in the computational workflow of space-time topology optimization, including the regularization of the time field (Section 5.2.3) and the filtering and projection procedures (Section 5.2.3).

Figure 5.3 depicts the computational workflow of space-time topology optimization, with the integration of the anisotropic material model. We employ the space-time optimization framework recently proposed by Wang et al. [170]. Rather than directly taking the time field as optimization variables, this framework introduces auxiliary variables $\boldsymbol{\mu}$ and a partial differential equation to implicitly define the time field, avoiding local minima that may appear when the time field is directly optimized. Specifically, as will be elaborated in Section 5.2.3, the time field $\boldsymbol{t}$ is computed by solving a heat equation, based on the density field $\boldsymbol{\rho}$ that represents the structural layout, and a thermal diffusivity field $\tilde{\boldsymbol{\mu}}$. The density and thermal diffusivity fields are filtered versions of optimization variables $\boldsymbol{\varphi}$ and $\boldsymbol{\mu}$, respectively. The filtering procedure is common in density-based topology optimization, and thus omitted in the illustration but will be explained in Section 5.2.3. From the time field, the material deposition direction is calculated, accordingly to Section 5.2.2. By combining the density and time fields, intermediate structures are computed, as introduced in Section 5.2.1. Afterward, the stiffness matrix of intermediate structures is calculated, taking the material anisotropy into account (Section 5.2.2). This is then used to analyze the response of intermediate structures. Based on the response functions, as well as the sensitivities, the optimization variables are updated.

REGULARIZATION OF THE TIME FIELD

As discussed in Section 5.2.1, we use a time field to encode the fabrication sequence, with a larger time value indicating that the corresponding location is intended for fabrication at a later stage. Isolines of this scalar field divide the structural layout into curved layers. This parameterization of the fabrication process opens up a huge solution space. However, the sequence represented by the isolines does not guarantee manufacturability. Ensuring fabrication continuity is crucial among the manufacturability constraints: material should only be deposited on already produced parts or directly onto the build plate. This requires the time field to be free of local minima.

To address this issue, a regularization method based on a heat equation has been proposed in chapter 2. Assuming a virtual heat source (with a constant temperature of 1) at the build plate, this creates a virtual temperature field that gradually decreases. The temperature field ($\boldsymbol{T}$) is continuous and free of local maxima. Its inverse is interpreted as the time field,

$$\boldsymbol{t} = \mathbf{1} - \boldsymbol{T}. \tag{5.10}$$

It is important to note that the virtual heat source is introduced solely to generate a

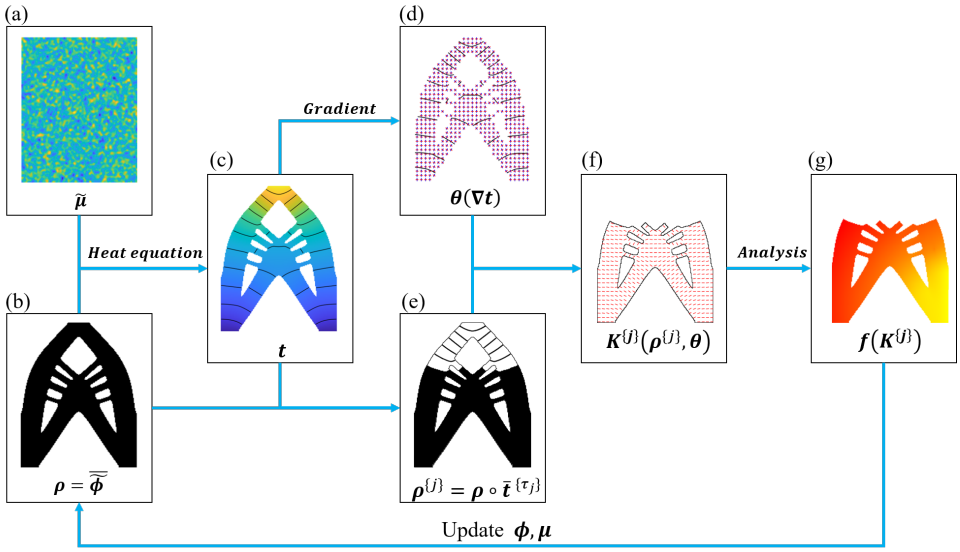

Figure 5.3.: Workflow of space-time topology optimization considering material anisotropy. (a) The heat diffusivity field. (b) The physical density field. (c) The pseudo-time field obtained from solving the heat equation Eq. 5.11. (d) Material orientation field obtained through the orthogonal relationship as in Eq. 5.4. (e) The j-th intermediate structure represented as in Eq. 5.2. (f) The mechanical properties of the intermediate structure. (g) The mechanical analysis of the intermediate structure.

continuous scalar field and should not be mistaken for the actual thermomechanical processes involved in additive manufacturing.

The virtual temperature field is determined by locally varying thermal diffusivity ($\boldsymbol{\mu}$) across the domain, treated as optimization variables to steer the fabrication sequence. It is further coupled with the density field to reflect the influence of the structural layout. The heat equation takes the form of

$$\nabla(\rho\tilde{\mu}\nabla T) - \alpha_T T = 0. \tag{5.11}$$

Here ∇ is the vector differential operator. ρ is the density, obtained from the design variable $\phi \in [0.0, 1.0]$. $\tilde{\mu}$ represents the pseudo thermal diffusivity. It is obtained from a new set of optimization variables $\mu \in [0.0, 1.0]$. α_T denotes a constant drain rate.

Using the finite element method, the heat equation is discretized into a linear form,

$$\boldsymbol{K}_T\left(\boldsymbol{\rho}, \tilde{\boldsymbol{\mu}}\right)\boldsymbol{T} = \boldsymbol{b}, \tag{5.12}$$

where $\boldsymbol{K}_T$ is the thermal stiffness matrix. $\boldsymbol{T}$ denotes the nodal temperature vector. $\boldsymbol{b}$ represents the thermal load vector specifying the virtual heat source, corresponding to the region where manufacturing is prescribed to start. Bi-linear interpolation is used to obtain the temperature field on the elements.

The thermal stiffness matrix consists of two parts,

$$\begin{aligned} \boldsymbol{K}_{\mathrm{T}}^{e}\left(\rho,\tilde{\mu}\right) = &\int_{\Omega_e} \rho_e \tilde{\mu}_e \left(\frac{\partial N_i}{\partial x}\frac{\partial N_j}{\partial x} + \frac{\partial N_i}{\partial y}\frac{\partial N_j}{\partial y} \right) d\Omega_e \\ &+ \int_{\Omega_e} \alpha_{\mathrm{T}} N_i N_j d\Omega_e. \end{aligned} \tag{5.13}$$

The first part corresponds to the thermal diffusivity, while the second part represents the drain term. N_i and N_j are the shape functions.

FILTERING AND PROJECTION

Filtering of the design variables is important in density-based topology optimization to avoid checkerboard problems for low-order elements [144]. We use the convolution filter as introduced in [17, 23] for the density field:

$$\tilde{\phi}_e = \frac{\sum_{i\in\mathbb{N}_e} H(\boldsymbol{x}_i)\,\phi_i}{\sum_{i\in\mathbb{N}_e} H(\boldsymbol{x}_i)}, \tag{5.14}$$

where $\mathbb{N}_e$ is the neighborhood set of element e, including elements whose distance to element e is less than a given radius R_e. $\boldsymbol{x}_i$ denotes the centroid of element i. The weighting factor of an element linearly decreases according to its distance to $\boldsymbol{x}_e$,

$$H(\boldsymbol{x}_i) = R_e - \|\boldsymbol{x}_i - \boldsymbol{x}_e\|. \tag{5.15}$$

The filtering is followed by a projection to promote a black-and-white design. We use the tanh function [145, 166]:

$$\rho_e = \bar{\tilde{\phi}}_e = \frac{\tanh\left(\beta_d \eta\right) + \tanh\left(\beta_d(\tilde{\phi}_e - \eta)\right)}{\tanh\left(\beta_d \eta\right) + \tanh\left(\beta_d(1-\eta)\right)}. \tag{5.16}$$

This function projects values larger than η to one, and those less than η to zero. η is set to 0.5. The parameter β_d controls the sharpness of projection. A continuous is applied in optimization; the optimization starts with a small β_d and gradually increases it after a fixed number of iterations. The obtained physical density $\boldsymbol{\rho}$ is used in the structural analysis and the heat equation Eq. 5.11.

Filtering is also necessary for the second set of optimization variables, μ. We use the same filtering technique as for the density field, but note that the filter radius and weighting functions for ρ and μ are not necessarily the same:

$$\tilde{\mu}_e = \frac{\sum_{i\in\mathbb{N}_e} H(\boldsymbol{x}_i)\,\mu_i}{\sum_{i\in\mathbb{N}_e} H(\boldsymbol{x}_i)}. \tag{5.17}$$

The filtering of the thermal diffusivity field is important to increase the smoothness of the time field, which contributes to the smoothness of the local material orientation.

SPACE-TIME TOPOLOGY OPTIMIZATION FOR ANISOTROPIC MATERIAL

In space-time topology optimization, the objective includes performance measures of both intermediate structures during fabrication and the final structure. It should be noted that the intermediate structures and the final structure can have different boundary conditions and load cases. The boundary conditions of the intermediate structures correspond to the manufacturing process, whereas the boundary conditions for the final structure relate to its intended use scenario. The optimization problem is formulated as follows:

$$\min_{\boldsymbol{\phi},\boldsymbol{\mu}} \quad f_0 = c_0 + \sum_{j=1}^{N} w_j c_j, \tag{5.18}$$

$$\text{s.t.} \quad \boldsymbol{K}\left(\boldsymbol{\rho},\boldsymbol{\theta}\right)\boldsymbol{U} = \boldsymbol{F}, \tag{5.19}$$

$$\boldsymbol{K}^{\{j\}}\left(\boldsymbol{\rho}^{\{j\}},\boldsymbol{\theta}\right)\boldsymbol{U}^{\{j\}} = \boldsymbol{G}^{\{j\}}, \quad j = 1,2,...,N, \tag{5.20}$$

$$g_0 = \sum \rho_e v_e \leq V_0, \tag{5.21}$$

$$g_j = \sum \rho_e^{\{j\}} v_e \leq \frac{j}{N} V_0, \quad j = 1,2,...,N, \tag{5.22}$$

$$0 \leq \phi_e \leq 1, \tag{5.23}$$

$$0 \leq \mu_e \leq 1, \tag{5.24}$$

where N is the prescribed number of layers or intermediate structures. $c_0 = \boldsymbol{U}^\top \boldsymbol{K}\boldsymbol{U}$ is the compliance of the final structure, and $c_j = \left(\boldsymbol{U}^{\{j\}}\right)^\top \boldsymbol{K}^{\{j\}}\boldsymbol{U}^{\{j\}}$ is the compliance of the j-th intermediate structure. The compliances are weighted by w_j.

Eq. 5.19 and 5.20 describe the governing equations of the final structure and intermediate structures, respectively. $\boldsymbol{F}$ is the external load for the final structure. $\boldsymbol{G}^{\{j\}}$ is the load applied on the j-th intermediate structure, such as the structure's self-weight, the weight of the robotic arm, or thermal-induced loads. The stiffness matrices of intermediate structures are a function of $\boldsymbol{\rho}^{\{j\}}$ and $\boldsymbol{\theta}$. $\boldsymbol{\rho}^{\{j\}}$ is the material distribution of the j-th intermediate structure, corresponding to the time point τ_j. It is obtained by re-writing Eq. 5.2 in a vector form, $\boldsymbol{\rho}^{\{j\}} = \boldsymbol{\rho} \circ \bar{\boldsymbol{t}}^{\{\tau_j\}}$, with $\circ$ denoting the Hadamard product of two vectors. $\boldsymbol{\theta}$ is derived from the time field (Eq. 5.6).

Eq. 5.21 and Eq. 5.22 prescribe the volume of the entire structure and intermediate structures, respectively. V_0 is the total material budget, and v_e is the volume of each element. Assuming a constant material deposition rate, the volume increase per layer is constant, i.e., $\frac{1}{N}V_0$.

The optimization includes two sets of variables, each ranging between 0.0 and 1.0. By fixing the density field and excluding it from the design update, the formulation is simplified to optimize only the fabrication sequence.

We solve the optimization problem by using the method of moving asymptotes (MMA) [153]. The sensitivity analysis is detailed in the appendix A.4. Algorithm 1 details the optimization process. The optimization stopping criteria is either the design change Δ is smaller than a certain value, e.g., $\epsilon_{\text{lim}} = 1e-5$ or the number of total iterations reaches the maximum iteration step It_{max}.

Algorithm 1 Space-time topology optimization for anisotropic materials

Input: Total material volume V_0 and number of layers N
Output: Optimized density field $\boldsymbol{\rho}$ and time field $\boldsymbol{t}$

Design variables initialization $\boldsymbol{\phi} = \boldsymbol{\phi}_0, \boldsymbol{\mu} = \boldsymbol{\mu}_0$
Iteration index $itr = 0$
Design change $\Delta = 1.0$
Projection parameters $\beta_t = 10.0, \beta_d = 1.0$
while $\Delta \geq \epsilon_{\text{lim}}$ and $itr \leq \text{It}_{\text{max}}$ **do**
    $itr = itr + 1$
    $\boldsymbol{\rho} = \bar{\tilde{\boldsymbol{\phi}}} \leftarrow \tilde{\boldsymbol{\phi}} \leftarrow \boldsymbol{\phi}$ via Eq. 5.14 and Eq. 5.16
    $\tilde{\boldsymbol{\mu}} \leftarrow \boldsymbol{\mu}$ via Eq. 5.17
    $\boldsymbol{K}_{\text{T}} \leftarrow \boldsymbol{\rho}, \tilde{\boldsymbol{\mu}}$ via Eq. 5.13
    $\boldsymbol{t} = 1 - \boldsymbol{T}$ via solving Eq. 5.12
    $\nabla \boldsymbol{t} \leftarrow \boldsymbol{t}$ via Eq. 5.5
    $\boldsymbol{\theta} \leftarrow \nabla \boldsymbol{t}$ via Eq. 5.4
    $\boldsymbol{K} \leftarrow \boldsymbol{\rho}, \boldsymbol{\theta}$ via Eq. 5.9
    $\boldsymbol{U} \leftarrow \boldsymbol{K}$ via solving Eq. 5.19
    $c_0 \leftarrow \boldsymbol{K}, \boldsymbol{U}$
    $\frac{\partial c_0}{\partial \boldsymbol{\phi}}, \frac{\partial c_0}{\partial \boldsymbol{\mu}}$ as formulated in Appendix A.4.
    for $j = 1$ **to** N **do**
        $\boldsymbol{\rho}^{\{j\}} \leftarrow \boldsymbol{\rho}, \boldsymbol{t}$ via Eq. 5.2
        $\boldsymbol{K}^{\{j\}} \leftarrow \boldsymbol{\rho}^{\{j\}}, \boldsymbol{\theta}$ via Eq. 5.9
        $\boldsymbol{U}^{\{j\}} \leftarrow \boldsymbol{K}^{\{j\}}$ via solving Eq. 5.20
        $c_j \leftarrow \boldsymbol{K}^{\{j\}}, \boldsymbol{U}^{\{j\}}$
        $\frac{\partial c_j}{\partial \boldsymbol{\phi}}, \frac{\partial c_j}{\partial \boldsymbol{\mu}}$ as formulated in Appendix A.4.
    end for
    $\boldsymbol{\phi}, \boldsymbol{\mu} \leftarrow \frac{\partial c_0}{\partial \boldsymbol{\phi}}, \frac{\partial c_0}{\partial \boldsymbol{\mu}}, \frac{\partial c_j}{\partial \boldsymbol{\phi}}, \frac{\partial c_j}{\partial \boldsymbol{\mu}}$ via MMA solver
    $\Delta = \max_{\forall e} \left(| \phi_e^{itr} - \phi_e^{itr-1} |, | \mu_e^{itr} - \mu_e^{itr-1} | \right)$
    if $\text{mod}\ (itr, 50) = 0$ **then**
        $\beta_t = \beta_t + 10.0$
        $\beta_d = \beta_d \times 2$
    end if
end while

5.3. NUMERICAL EXAMPLES

In this section, we validate the proposed method through multiple numerical examples. We start by comparing the fabrication sequences optimized with different types of material anisotropy, using a simple geometry (Section 5.3.1), followed by fabrication sequence optimization of a mechanical component (Section 5.3.2). We then proceed to validate the effects of material anisotropy in space-time topology optimization, considering the self-weight of intermediate structures (Section 5.3.3) and the weight of a mobile robotic platform on intermediate structures (Section 5.3.4). All examples are in 2D and under the plane stress condition. Each optimization involves 600 iterations.

5.3.1. ANISOTROPIC MATERIALS

To investigate the effects of material anisotropy on design optimization, we consider two simple load cases where a rectangular shape is under pure tension or shear stress, as illustrated in Fig. 5.4(a) and Fig. 5.5(a), respectively. We optimize the fabrication sequence to produce this rectangular shape, i.e., the density field is kept constant and excluded from optimization, while the time field is to be

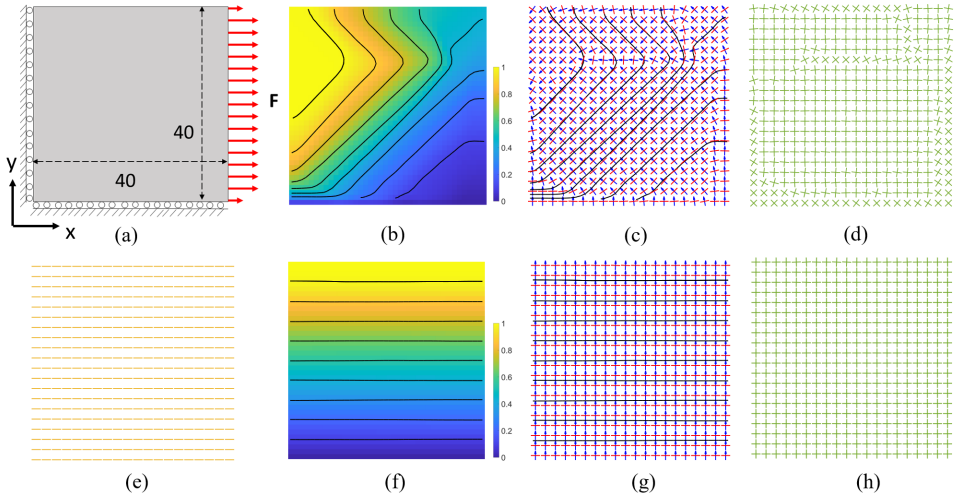

Figure 5.4.: Comparison of optimized fabrication sequences for anisotropic materials with high-shear and low-shear modulus, tested for uniaxial tension condition. (a) A rectangular component under uniaxial tension. (e) The optimal orientation of the stiffest direction of the material (major principal stress direction) is horizontal. For anisotropic materials with high-shear modulus: (b) The optimized time field with isolines, representing the optimized fabrication sequence, (c) The gradient direction of the time field (blue arrows) and the corresponding material orientation (red lines), (d) The two orthogonal stiffest directions of the anisotropic material. In the same order, (f-h) depict the results for anisotropic materials with low-shear modulus.

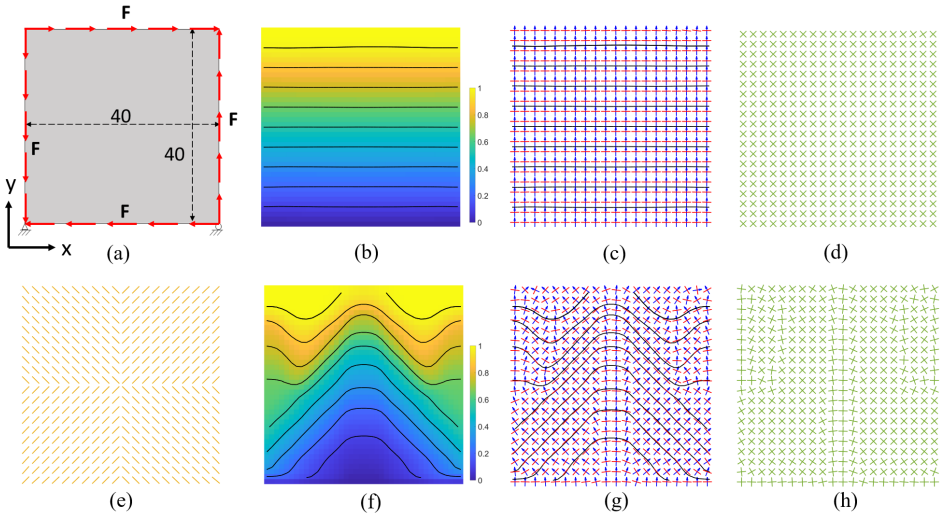

Figure 5.5.: Comparison of optimized fabrication sequences for anisotropic materials with high-shear and low-shear modulus, tested for pure shear stress condition. (a) A rectangular component under pure shear stress. (e) The optimal orientation of the stiffest direction of the material (major principal stress direction) is at $\pm 45°$ to the x-axis. For anisotropic materials with high-shear modulus: (b) The optimized time field with isolines, representing the optimized fabrication sequence, (c) The gradient direction of the time field (blue arrows) and the corresponding material orientation (red lines), (d) The two orthogonal stiffest directions of the anisotropic material. In the same order, (f-h) depict the results for anisotropic materials with low-shear modulus.

optimized. The objective is to minimize the compliance of the shape as it is fully fabricated. No performance characteristics of intermediate structures are included in the objective. The compliance of the entire shape depends on the orientation of the anisotropic material, which is governed by the fabrication sequence. The fabrication is prescribed to start from the bottom of the domain, and finish with 10 layers. The domain is discretized into a regular grid of 40 by 40 finite elements.

We test sequence optimization with two anisotropic materials, as previously introduced in Section 5.2.2 and illustrated in Fig. 5.2. The material properties are summarized in Table 5.1. Material-1 has a high shear modulus. Its stiffest direction is at 45° to the layer orientation, i.e., $\theta = \pm 45°$. In contrast, the shear modulus of Material-2 is low. Its stiffest direction is along and perpendicular to the layer, i.e., $\theta = 0°$ and $\theta = 90°$.

In the uniaxial tension case (Fig. 5.4), the major principal stress is horizontal, shown in (e). The fabrication sequences, optimized with Material-1 and Material-2, are shown in the first row (b, c, d) and second row (f, g, h), respectively. With the high-shear material, the layers are oriented at $\pm 45°$ to the x-axis (b, c). In contrast, with the low-shear material, the layers are horizontal (f, g). However, with both

Table 5.1.: Material properties of two anisotropic materials. The unit of elastic modules is GPa.

	E_x	E_y	G_{xy}	ν_{xy}
Material-1	141.45	141.45	120.10	0.3
Material-2	141.45	141.45	12.01	0.3

materials, the stiffest material direction is primarily along the x- and y-axis (d, h), in agreement with the major principal stress direction (e).

An alignment of the stiffest material direction to the major principal stress is also observed in the case of pure shear stress (Fig. 5.5). In the first row, corresponding to the high-shear material, the optimized layers are horizontal (b, c), resulting in the stiffest material direction at $\pm 45°$ to the x-axis (d). In the second row, with the low-shear material, the optimized layers are curved, and mostly at $\pm 45°$ to the x-axis (f, g), leading to the stiffest material direction at $\pm 45°$ to the x-axis (h).

5

5.3.2. FABRICATION SEQUENCE OPTIMIZATION

The third example of fabrication sequence optimization is a bracket shown in Fig. 5.6. The bracket is clamped at its bottom, on the left and right. It has two alternating loads on its inner circle, pointing upwards and downwards. The objective is to minimize the compliance of the component subject to both loading conditions. Similar to previous examples, the fabrication is prescribed to start from the bottom. The prescribed number of layers is 20.

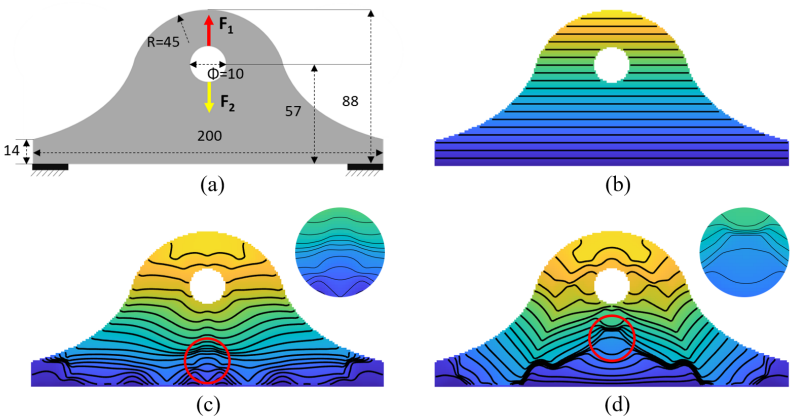

Figure 5.6.: Fabrication sequence optimization for a bracket. (a) The bracket and boundary conditions for its intended use scenario. (b) Planar fabrication process as a reference. (c, d) Optimized time field and isolines, representing the optimized fabrication sequence, obtained using the anisotropic material with (c) high-shear modulus, Material-1 and (d) with low-shear modulus, Material-2.

The optimized fabrication sequence using Material-1 is shown in Fig. 5.6(c). It is symmetric due to the symmetric boundary conditions and structural layout. For comparison, the planar fabrication sequence is illustrated in Fig. 5.6(b). The component manufactured using planar layers has the compliances of $c_1 = 98.85$ and $c_2 = 92.59$ for the two loads, while according to the optimized fabrication sequence in Fig. 5.6(c) it has the compliances of $c_1 = 91.75$ and $c_2 = 88.61$. The smaller compliances confirm that by optimizing the fabrication sequence, the mechanical capabilities of the final structure can be enhanced through the effective utilization of material anisotropy.

We note that the improvement in structural performance through fabrication sequence optimization depends on the extent of material anisotropy. When repeating the fabrication sequence optimization with Material-2, the improvement in structural performance compared to planar layers is more significant. The optimized sequence is illustrated in Fig. 5.6(d). In most areas, the layer orientation differs from that of Material-1 by $\pm 45°$. The component manufactured using planar layers with Material-2 has compliances of $c_1 = 321.0$ and $c_2 = 336.1$ for the two loads. In contrast, the component produced with the optimized fabrication sequence shown in Fig. 5.6(d) has compliances of $c_1 = 163.6$ and $c_2 = 154.2$. This optimization reduces the sum of compliances by 51.64%.

Material-2 has its stiffest direction aligned with the material deposition direction. For single-load cases, arranging the material along the principal stress distribution results in a stiff structure. For two load cases, aligning the material direction according to the principal stress of one load case improves the stiffness for that specific load but leaves the performance under the other load unoptimized. In this example, aligning the material deposition direction with the principal stress direction of the first load case, $\boldsymbol{F}_1$, results in structural compliances of $c_1 = 142.9$ and $c_2 = 195.3$. Conversely, using the principal stress directions of the second load case, $\boldsymbol{F}_2$, yields compliances of $c_1 = 197.9$ and $c_2 = 137.6$. The sums of these compliances are 6.42% and 5.57% higher, respectively, than those achieved with the optimized sequence considering both loads simultaneously.

The examples above have demonstrated that the optimized fabrication sequence is influenced by the anisotropic characteristics of the material. In the following section, we will continue with the high-shear material model (Material-1), which corresponds to WAAM-processed austenitic stainless steel.

5.3.3. SPACE-TIME OPTIMIZATION FOR SELF-WEIGHT

After demonstrating the impact of fabrication sequence on material anisotropy and, consequently, on structural performance, we proceed to showcase the importance of incorporating material anisotropy in space-time topology optimization. The structural layout and fabrication sequence will collectively exploit the anisotropic characteristics of material stiffness.

This example concerns a vertically oriented beam, as shown in Fig. 5.7(a). The rectangular design domain is discretized into 100×400 finite elements. The objective is to minimize the compliance of the entire structure in its intended use scenario (c_0) and the compliance of intermediate structures during fabrication ($\sum c_j$). In

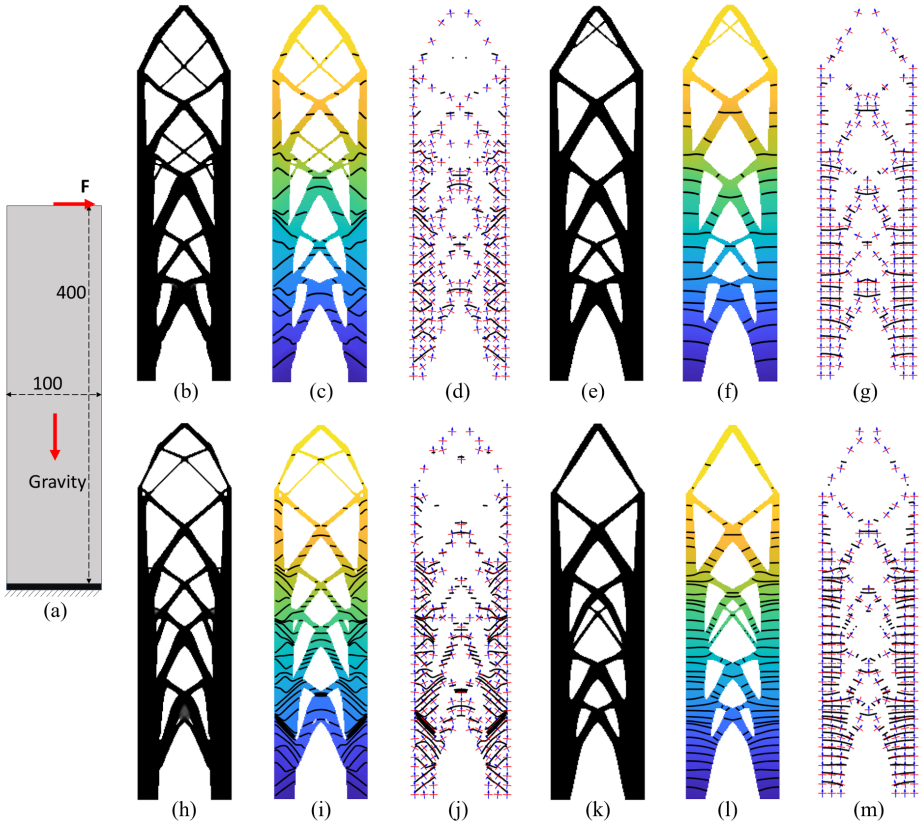

Figure 5.7.: Space-time topology optimization of a vertical beam. (a) Design domain of a vertical beam, consider the self-weight of the structure during fabrication, and an external load ($\boldsymbol{F}$) on the fully fabricated structure. The optimization is performed in four different setups. Top row (b-g): $N = 20$, with anisotropic material (b, c, d) and isotropic material (e, f, g). Bottom row (h-m): $N = 40$, with anisotropic material (h, i, j) and isotropic material (k, l, m). For each setup, from left to right: Optimized structural layout, optimized structure color-coded by the optimized time field, and gradient directions and the corresponding material orientations.

the use scenario, i.e., after the beam has been fully fabricated, it is fixed at its bottom and supports a horizontal load at its top. The fabrication process starts from the bottom, assuming the bottom of the beam is fixed on a horizontal baseplate. Throughout fabrication, the intermediate structure supports the gravitational load of its own weight. This load is dependent on both the structural layout and fabrication sequence. The total weight of the structure equals the magnitude of the external force $\boldsymbol{F}$ applied during its use scenario.

Some key parameters for optimization are outlined below: The entire structure is segmented into $N = 20$ or 40 layers for manufacturing. The weight coefficients

assigned to compliances of intermediate structures in the objective function are set to $w_j = 1/N$. The volume fraction of the entire structure is fixed at 0.5. The filter radius for the density and heat conductivity fields is set to 3 times the length of a single element. The material property corresponding to the WAAM-produced stainless steel (Material-1) is utilized.

The optimized results with $N = 20$ layers are visualized in Fig. 5.7(b-d). Fig. 5.7(b) shows the optimized structural layout, represented by the physical density field. In Fig. 5.7(c), the structural layout is color-coded according to the time field, illustrating the fabrication sequence. The isolines of the time field, indicated by the black lines, outline the boundaries of layers. The layers are sequentially stacked from the bottom. In Fig. 5.7(d), the gradient direction of the optimized time field and the material orientation are depicted, which are orthogonal. The material orientations are observed to generally align with the layer boundaries, as in all examples.

Table 5.2.: Mechanical performances of a vertically oriented beam, considering the self-weight of intermediate structures.

		Optimization result		
	Compliances (scaled)	c_0	$\sum c_j$	$f_0 = c_0 + \sum w_j c_j$
$N = 20$	Optimized with anisotropic material	98.76	1.00	98.81
	Optimized with isotropic material	138.55	1.21	138.62
$N = 40$	Optimized with anisotropic material	99.82	1.68	99.86
	Optimized with isotropic material	140.52	2.14	140.57
		Analysis with anisotropic material		
	Compliances (scaled)	c_0	$\sum c_j$	$c_0 + \sum w_j c_j$
$N = 20$	Optimized with anisotropic material	98.76	1.00	98.81
	Optimized with isotropic material	134.19	1.19	134.25
$N = 40$	Optimized with anisotropic material	99.82	1.68	99.86
	Optimized with isotropic material	134.48	2.09	134.54

The compliance of the final structure under the external force is $c_0 = 1825.85$, and the sum of compliances of intermediate structures under their own weight is $\sum c_j = 18.49$. For an easy comparison to variations later on, we scale these values by dividing $\sum c_j$, leading to $c_0 = 98.76$ and $\sum c_j = 1.00$. The same scaling factor is applied to other designs in this section. As a comparison, if the optimized structure is to be manufactured using planar layers, the compliances become $c_0 = 131.62$ and $\sum c_j = 1.31$. Both are larger in comparison to the design with optimized curved layers and material orientations. This confirms the advantage of optimizing the fabrication sequences along with the structural design using space-time topology optimization.

In a further comparative study, we optimize the beam using an isotropic material to reveal the differences in structural layout and fabrication sequence with and without material anisotropy. The property of the isotropic material is set as: $E_x = 141.45\,\text{GPa}, E_y = 141.45\,\text{GPa}, \nu_{xy} = 0.30, G_{xy} = E_x/2(1+\nu) = 54.40\,\text{GPa}$. The

orientation of the isotropic material has no effect on structural performance. The optimized results are shown in Fig. 5.7(e-g). The optimized structural layout displayed in Fig. 5.7(e) is rather similar to that in Fig. 5.7(b), while the optimized fabrication sequences differ more. The whole structure's compliance is $c_0 = 138.55$, and the sum of intermediate structures' compliances is $\sum c_j = 1.21$. For a fair comparison, we conduct a post-analysis on the optimized structural layout and sequence, using the anisotropic material in replacement of the isotropic one. The results are summarized in Table 5.2. The compliances resulting from the optimization using the anisotropic material are 26.54% smaller than those using the isotropic material. Both the compliance of the final structure and that of intermediate structures are improved when material anisotropy is included in optimization.

The same conclusion holds when the structure and sequence are optimized with 40 layers. The optimized results using anisotropic and isotropic materials are shown in the second row in Fig. 5.7, and their corresponding structural performances are included in Table 5.2. Compared to the results obtained with $N = 20$, the optimization with $N = 40$ layers results in slightly increased compliances. This increase can be attributed to the more stringent constraints introduced by the finer granularity of the fabrication sequence.

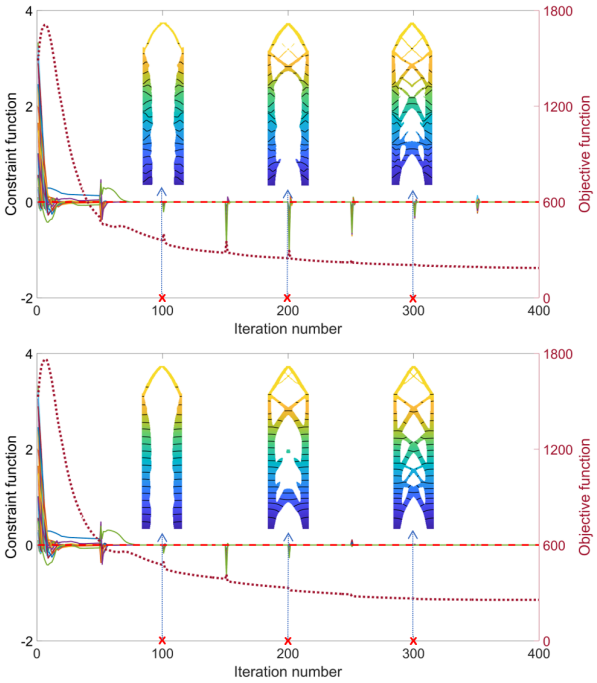

Figure 5.8.: Convergence curves of the objective function and constraints. Top: for the design optimized using anisotropic material shown in Fig. 5.7(c). Bottom: the design optimized using isotropic material shown in Fig. 5.7(f).

In addition, Fig. 5.8 shows convergence curves of the objective function and constraint functions corresponding to the results in Fig. 5.7(c) and (f). In both scenarios, the objective function (red dotted line) stably decreases, and all the constraint functions converge to zero. The slight discontinuities in the curves, which occur every 50 iterations, are due to the continuation scheme of the projection parameters β_t and β_d. The designs at the 100-th, 200-th, and 300-th iteration are included in the figures. Both scenarios show comparable convergence, with the isotropic scenario converging somewhat faster, suggesting added complexity introduced by the anisotropic material. The objective function with the anisotropic material converges to a smaller value than with the isotropic material.

5.3.4. SPACE-TIME OPTIMIZATION FOR A MOBILE ROBOT

Our last example is the construction of a large cantilever beam using a mobile robotic platform, inspired by an artistic illustration from MX3D. The artistic illustration and the simplified model for space-time optimization are shown in Fig. 5.9(a,b). Similar to the previous example, the objective is to minimize the compliance of the entire structure (c_0) and compliance of intermediate structures ($\sum c_j$). However, for intermediate structures, rather than the self-weight of the structure, we consider the weight of the mobile robot. The full structure is anchored on the left and supports an external load on the right ($\boldsymbol{F} = 5000\,\mathrm{N}$). The fabrication is prescribed to start from the clamped edge on the left. During fabrication, the intermediate structure need to provide support to the mobile robotic platform, which moves from left to right. It is assumed that the robot moves at a constant speed and its weight is also constant ($\boldsymbol{G} = 1000\,\mathrm{N}$). At the i-th stage in fabrication, the robot is located at a distance of $\frac{i-1}{N} L_x$ to the left edge, where N is the number of stages and $L_x = 160$ represents the length of the domain. The key optimization parameters remain the same as in the previous example.

The results optimized using both the anisotropic and isotropic material are shown in Fig. 5.9. As can be seen from (c,f), the optimized structural layouts using the two different materials are quite similar. Although the overhang feature in the top right of the domain might not seem intuitive, it is created to support the last location of the robotic platform during the fabrication process. On the other hand, the fabrication sequences differ for the two types of materials. For example, in regions of the structure primarily subjected to tension (marked by the red box), the layer shapes differ notably between the two. With the anisotropic material, the layers are more curved, strategically aligned to exploit the material's stiffer directions. In contrast, for the isotropic material, the layers remain nearly planar, as there is no directional stiffness to influence the sequence design.

Comparisons of mechanical performances between the results optimized using anisotropic and isotropic materials are included in Table 5.3. The compliance values are scaled for clarity. The overall performance, measured as $c_0 + \sum w_j c_j$, of the result optimized using the anisotropic material is smaller, which again confirms the benefit of incorporating manufacturing-induced material anisotropy into space-time topology optimization. This performance gain is primarily due to the improved performance of the entire structure (100.00 vs 125.28).

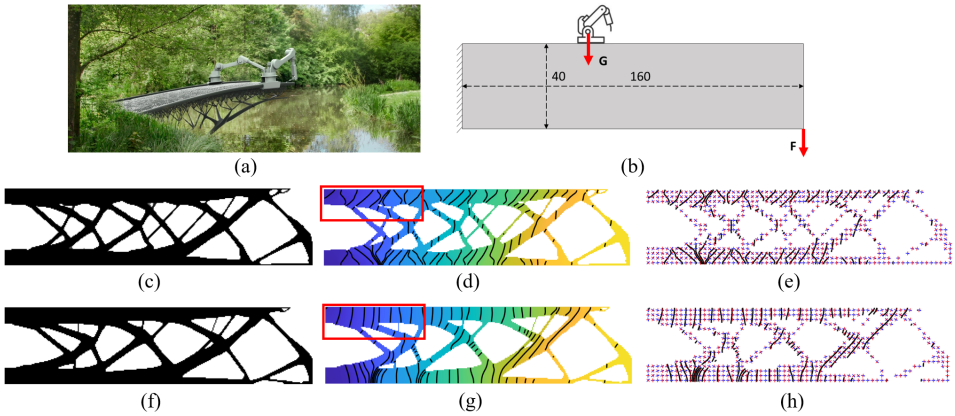

Figure 5.9.: Space-time topology optimization of a cantilever beam. (a) Artistic illustration of building a bridge with a robot moving on top of it (Courtesy MX3D). The bridge under construction shall support the mobile robotic platform at all intermediate stages. (b) Simplified design domain of the cantilever bridge, consider the weight of a robotic platform during fabrication, and an external load ($\boldsymbol{F}$) on the fully fabricated structure. (c-h) The optimization results for anisotropic material (c-e) and isotropic material (f-h). From left to right: Optimized structural layout (c,f), optimized structure color-coded by the optimized time field (d,g), gradient directions and the corresponding material orientations (e,h).

Table 5.3.: Mechanical performances of a cantilever beam, considering the weight of a mobile robot on intermediate structures.

		Optimization result		
	Compliances (scaled)	c_0	$\sum c_j$	$f_0 = c_0 + \sum w_j c_j$
$N = 30$	Optimized with anisotropic material	100.00	57.22	101.97
	Optimized with isotropic material	134.58	72.22	137.07
		Analysis with anisotropic material		
	Compliances (scaled)	c_0	$\sum c_j$	$c_0 + \sum w_j c_j$
$N = 30$	Optimized with anisotropic material	100.00	57.22	101.97
	Optimized with isotropic material	125.28	64.92	127.52

Figure 5.10 shows the manufacturing process according to the optimized fabrication sequence in Fig. 5.9(d). The positions where the mobile robot is located during manufacturing are marked in red bricks on the top boundary. It is evident that the evolving intermediate structure not only forms the final geometry but also serves as a functional support platform for the mobile robot throughout the process. This highlights the importance of combining structural design and sequence planning.

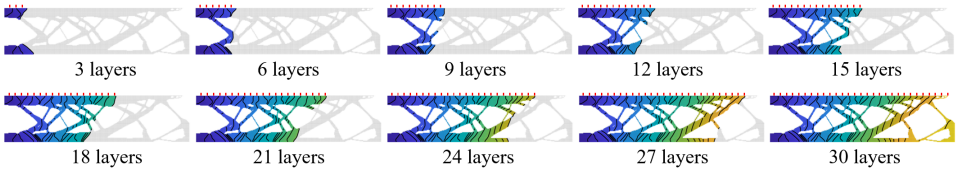

Figure 5.10.: Illustration of the manufacturing process according to the optimized fabrication sequence in Fig. 5.9(d), the locations of the robotic platform on the top of the domain are marked in red bricks.

5.4. CONCLUSIONS AND FUTURE WORK

In this chapter, we have introduced a space-time topology optimization method that accounts for elastic anisotropy in WAAM-processed material. We utilize a pseudo-density field to represent the structural layout and a pseudo-time field to encode the fabrication sequence. The orientation of anisotropic materials is determined from the pseudo-time field, with the local material deposition direction orthogonal to the gradient of the time field. Our numerical study focuses on anisotropic stiffness, and we anticipate that extending this approach to consider anisotropic strength is feasible since the anisotropic direction has already been derived from the optimization variables.

Our results prove the possibility and benefits of incorporating material anisotropy into structural design and process planning. Firstly, by examples of fabrication sequence optimization, we have shown that leveraging elastic anisotropy can enhance mechanical performance. Unlike planar fabrication sequences in conventional 2.5D printing, optimized fabrication sequences align material deposition orientations to take advantage of the stiffer direction of materials. It was observed that the anisotropic characteristic (high-shear vs low-shear modulus) significantly influences the optimization results. Secondly, incorporating material anisotropy into space-time topology optimization also yields distinct structural layouts and fabrication sequences compared to those based on isotropic materials. Leveraging material anisotropy proves to be an effective approach to enhancing the performance of intermediate structures as well as the overall structure.

The work presented in this chapter provides a strong foundation for exploring the full potential of robot-assisted additive manufacturing. However, further advancements are necessary to achieve experimental validation of the innovative fabrication sequences proposed. One of the primary challenges lies in accurately producing layers with significant thickness variations, even when utilizing multi-axis printing. To address this, it is essential to limit these variations within the computational design method and implement adaptive adjustments to process parameters during manufacturing, to account for the impact of the curved fabrication on the geometry of layer beads. Additionally, incorporating advanced models of the WAAM process, including factors such as metal transfer modes and intermediate cooling processes, would enhance the accuracy of predictions regarding mechanical properties and manufacturing precision. However, this approach

demands intensive computational resources, as performance predictions are required at each iteration of the optimization process. Lastly, our current method is primarily for the manufacturing of thin-walled structures. Extending this approach to bulkier 3D components will necessitate the development of toolpath planning within each layer. These aspects represent our ongoing research efforts, which are part of the broader and exciting direction initiated by this study.

6

CONCLUSIONS AND OUTLOOK

This chapter presents a comprehensive summary of the key findings and conclusions derived from the PhD research. It also provides a reflective discussion on potential avenues for future work, highlighting opportunities for further exploration and development based on the results of this study.

6.1. CONCLUSIONS

The conclusions of each chapter have been presented in detail individually. Here, we summarize the general conclusions and contributions of the dissertation by answering the main research questions outlined in Section 1.2:

- *What are the flaws and limitations of the original space-time topology optimization? How to get rid of them efficiently in the numerical algorithm?*

Manufacturability is the primary concern in space-time topology optimization, as the method is intended to serve multi-axis additive manufacturing. However, the original method encounters two key challenges in this regard. First, local minima can appear in the generated time field, leading to unrealistic fabrication sequences in which isolated parts are produced without support from earlier layers. Second, the resulting layers often exhibit non-uniform geometric dimensions, which complicates the manufacturing by necessitating frequent and impractical adjustments to processing parameters. These issues result in designs that are not readily applicable to manufacturing.

The local minima problem is addressed in **Chapter** 2, where a novel regularization method for space-time topology optimization is proposed. The time field is regularized by using a PDE equation that resembles a heat transfer process. A monotonically progressing time field can thus be obtained. This approach effectively prevents local minima from appearing in the optimized time field, regardless of the initial values of the time field used in optimization. This work lays a solid foundation for further advancements in space-time optimization for multi-axis additive manufacturing.

On this basis, a layer geometry control scheme is further developed for fabrication sequence planning within the space-time optimization framework in **Chapter** 3. This scheme makes use of the gradient of the time field to approximate the layer thickness and its uniformity. The obtained layers achieve greater geometric uniformity, which is essential for the additive manufacturing process. More importantly, the design flexibility of fabrication sequence planning is still maintained, as the optimizer can adjust layer thickness within allowable limits on a layer-by-layer basis. Additionally, this research promotes convex layer shapes to reduce the risk of collisions during fabrication.

- *Is it possible to reduce residual stress and thermal distortion simultaneously in WAAM through fabrication sequence planning? Does the concurrent optimization of structural layout and fabrication sequence outperform a decoupled sequential optimization strategy?*

The feasibility of mitigating residual stresses and distortion through fabrication sequence planning has been validated in **Chapter** 4. However, the effectiveness of the optimization approach depends on the structure itself and its boundary conditions during manufacturing. In some cases, simultaneously mitigating residual stresses and thermal-induced distortions is challenging. This difficulty arises because the release of accumulated stresses can itself cause deformation or distortion in the part.

Furthermore, our method allows for simultaneous optimization of both the fabrication sequence and the structural layout. The structural layout obtained from space-time topology optimization differs from that produced by standard topology optimization. In

space-time optimization, the fabrication sequence and the structural layout are intrinsically aligned with each other, effectively reducing residual stress and thermal-induced distortion caused by the manufacturing process.

However, space-time topology optimization does not always outperform a decoupled strategy, where the structural layout and fabrication sequence are optimized separately in a sequential manner. The limitation arises from the inherent complexity of fully exploring the expanded design space that space-time topology optimization introduces. It requires the optimizer to manage two different sets of design variables simultaneously. This increases computational burden and makes it more challenging to effectively navigate the design space, often leading to suboptimal solutions compared to the decoupled approach. Overcoming these challenges will require advancements in optimization algorithms and computational strategies to better handle the coupled nature of the design variables.

- *How can space-time topology optimization account for process-induced material anisotropy? What are the advantages does this offer?*

In **Chapter** 5, we demonstrate the feasibility of incorporating manufacturing-induced material anisotropy into the space-time topology optimization framework. Given that material anisotropy is inherently related to the manufacturing process, the orientation of anisotropic materials can be directly derived from the pseudo-time field, with the local material deposition direction orthogonal to the gradient of the time field. Numerical results demonstrate the possibility and benefits of incorporating material anisotropy into structural design and process planning. Leveraging material anisotropy proves to be an effective approach to enhancing the performance of intermediate structures as well as the overall structure.

6.2. OUTLOOK

The space-time topology optimization framework in this dissertation is developed on the basis of several foundational assumptions, some of which can be overly idealized for practical manufacturing applications. Nevertheless, despite these limitations, the framework offers exciting opportunities for innovation and further investigation. This study lays a promising groundwork that can motivate the manufacturing industry to explore and potentially capitalize on novel multi-axis additive manufacturing techniques. There is considerable potential for future research, including but not limited to the following directions:

EXPANDING THE SCOPE OF PROCESS PLANNING

Fabrication sequence planning is just one important aspect of process planning. Other topics, including tool path planning and selection of process parameters, are also important to be considered. For example, layer slicing and toolpath planning could be optimized together to minimize residual stress for WAAM: slicing offers coarse-grained insights into layer-wise heat generation and stress accumulation, while toolpath planning provides fine-grained details inside each layer. The potential of mitigating residual stress through process planning can be fully realized by integrating both aspects.

However, toolpath planning on curved planar surfaces itself is a challenging topic, particularly in terms of collision avoidance and the selection of appropriate deposition strategies. Although the space-time optimization framework offers a promising direction by embedding sequence planning into structural design, its current formulation requires further expansion to incorporate additional aspects of process planning. Effectively bridging these process planning elements is crucial for achieving truly manufacturable 3D designs in multi-axis additive manufacturing.

HIGH-FIDELITY PROCESS SIMULATION

In this dissertation, residual stress and thermal-induced distortion are calculated using the inherent strain method without accounting for the interactions between fabrication sequences, manufacturing parameters, and thermo-mechanical loads. The inherent strain values are predefined, which may oversimplify the process and fail to capture the actual material response, particularly in the context of multi-axis additive manufacturing. Notably, process parameters should be dynamically adjusted during the process to generate curved layers, which in turn affect thermal input, temperature history, and the accumulation of residual stresses. As a result, the inherent strain method requires appropriate calibration to address these complexities.

For future work, adopting high-fidelity simulation models will be insightful to gain a comprehensive understanding of the manufacturing process, which spans multiple lengths and time scales. For instance, the current approach relies on linear elastic analysis and does not account for material plasticity. Incorporating plastic deformation would enable more accurate prediction of stress accumulation. However, the use of high-fidelity models comes with a trade-off, as it substantially increases computational demands. Additionally, the integration of such models into the space-time topology optimization framework requires further exploration to ensure compatibility and feasibility.

COMPUTATIONAL EFFICIENCY

Space-time topology optimization involves intensive computation. The main reason is that each intermediate structure during manufacturing is analyzed to supervise the entire manufacturing process. The number of intermediate manufacturing steps to be analyzed thus determines the number of system equations to be solved. For large-scale structures with fine-granularity layer division, this results in a substantial computational burden for the equation solver. As discussed above, the computational demands will increase even further if a more precise process simulation model is integrated into the optimization to enhance the accuracy of process predictions. Moreover, the current gradient-based optimization solver adopted in the framework needs to update the density field and the time field simultaneously, requiring more inner iterations for convergence and increasing computation time.

Although a parallel computing platform based on PETSc has been developed in this research, additional acceleration techniques could potentially be integrated to further improve computational efficiency. For instance, under the assumption of linearity, intermediate structures could theoretically be solved in parallel. However, this can cause a load imbalance issue in parallel computing, as the sparsity of stiffness matrices varies between different intermediate structures.

Aside from handling the computational complexity by adopting more efficient programming languages or computing architectures, the computational efficiency could also be improved by reformulating the problem itself. In our current approach, the density field and the time field are defined on the same scale, using the same discretization mesh. However, this uniform resolution is not always efficient. For instance, when constructing a large-scale structure with many detailed features, a high-resolution mesh is required to define the density field accurately for fine geometric representation. While distinguishing the fabrication sequence of every small feature can be unnecessary, as their influence on the overall structure is minimal. In such cases, defining the time field on a coarser scale or mesh reduces the computational effort by narrowing the solution space. Conversely, when a simpler geometry with few detailed features is preferred but a detailed layer division is essential to capture precise manufacturing sequences for material chunks, defining the time field at a finer resolution than the density field becomes beneficial. The above strategy, referred to as multi-resolution space-time topology optimization, adapts the resolution of the density and time fields to the specific requirements of the problem, is beneficial for improving computational efficiency.

EXPERIMENTAL VALIDATION

Last but not least, while the theoretical foundation of space-time topology optimization is well established, experimental validation remains a crucial next step, especially for WAAM. For initial testing of curved-layer implementation, polymer-based multi-axis techniques, such as FDM, offer a more accessible and straightforward path. Multi-axis FDM systems are already available, though further improvements in manufacturing accuracy are still needed. While the space-time optimization framework can be adapted to generate curved layers in FDM, some of its primary objectives should be re-evaluated, such as thermal effects. This is because polymers generally undergo less thermal distortion and residual stress than metals.

On the other hand, implementing curved-layer fabrication in WAAM presents significantly more complex challenges. Unlike polymer-based processes, the WAAM process involves the deposition of molten metal under intense heat input, accompanied by rapid melting and solidification cycles, as well as dynamic molten material flow. These conditions create complex thermo-mechanical interactions, making it particularly difficult to maintain precise deposition along predefined curved paths. To address these challenges, a highly responsive and adaptive manufacturing system is required that can perform real-time monitoring and control of the process parameters.

Ultimately, a successful demonstration of the production of optimized structures with curved layers, particularly in real industrial environments, would be a major milestone. Any discrepancies observed between simulation and fabrication will provide critical insights into practical limitations and guide future refinements to the current optimization framework. Close collaboration with industry partners will be essential to translate theoretical advances into real-world applications, driving a wave of innovation in additive manufacturing.

REFERENCES

[1] N. Aage, E. Andreassen, B. S. Lazarov, and O. Sigmund. "Giga-voxel computational morphogenesis for structural design". In: *Nature* 550.7674 (2017), pp. 84–86. DOI: 10.1038/nature23911.

[2] N. Aage, E. Andreassen, and B. S. Lazarov. "Topology optimization using PETSc: An easy-to-use, fully parallel, open source topology optimization framework". In: *Structural and Multidisciplinary Optimization* 51.3 (2015), pp. 565–572. DOI: 10.1007/s00158-014-1157-0.

[3] T. Abe and H. Sasahara. "Layer geometry control for the fabrication of lattice structures by wire and arc additive manufacturing". In: *Additive Manufacturing* 28 (2019), pp. 639–648. DOI: 10.1016/j.addma.2019.06.010.

[4] G. Allaire, C. Dapogny, R. Estevez, A. Faure, and G. Michailidis. "Structural optimization under overhang constraints imposed by additive manufacturing technologies". In: *Journal of Computational Physics* 351 (2017), pp. 295–328. DOI: 10.1016/j.jcp.2017.09.041.

[5] G. Allaire and L. Jakabčin. "Taking into account thermal residual stresses in topology optimization of structures built by additive manufacturing". In: *Mathematical Models and Methods in Applied Sciences* 28.12 (2018), pp. 2313–2366. DOI: 10.1142/s0218202518500501.

[6] G. Allaire, F. Jouve, and A.-M. Toader. "Structural optimization using sensitivity analysis and a level-set method". In: *Journal of Computational Physics* 194.1 (2004), pp. 363–393. DOI: 10.1016/j.jcp.2003.09.032.

[7] O. Amir and Y. Mass. "Topology optimization for staged construction". In: *Structural and Multidisciplinary Optimization* 57.4 (Apr. 2018), pp. 1679–1694. DOI: 10.1007/s00158-017-1837-7.

[8] S. Balay, S. Abhyankar, M. F. Adams, S. Benson, J. Brown, P. Brune, K. Buschelman, E. Constantinescu, L. Dalcin, A. Dener, V. Eijkhout, J. Faibussowitsch, W. D. Gropp, V. Hapla, T. Isaac, P. Jolivet, D. Karpeev, D. Kaushik, M. G. Knepley, F. Kong, S. Kruger, D. A. May, L. C. McInnes, R. T. Mills, L. Mitchell, T. Munson, J. E. Roman, K. Rupp, P. Sanan, J. Sarich, B. F. Smith, H. Suh, S. Zampini, H. Zhang, H. Zhang, and J. Zhang. *PETSc/TAO Users Manual*. Tech. rep. ANL-21/39 - Revision 3.22. Argonne National Laboratory, 2024. DOI: 10.2172/2205494.

[9] M. Bayat, O. Zinovieva, F. Ferrari, C. Ayas, M. Langelaar, J. Spangenberg, R. Salajeghe, K. Poulios, S. Mohanty, O. Sigmund, *et al.* "Holistic computational design within additive manufacturing through topology optimization combined with multiphysics multi-scale materials and process modelling". In: *Progress in Materials Science* 138 (2023), p. 101129. DOI: 10.1016/j.pmatsci.2023.101129.

[10] V. Beik, H. Marzbani, and R. Jazar. “Welding sequence optimisation in the automotive industry: A review”. In: *Proceedings of the Institution of Mechanical Engineers, Part C: Journal of Mechanical Engineering Science* 233.17 (2019), pp. 5945–5952. DOI: 10.1177/0954406219859909.

[11] M. P. Bendsøe and O. Sigmund. “Material interpolation schemes in topology optimization”. In: *Archive of Applied Mechanics (Ingenieur Archiv)* 69.9-10 (1999), pp. 635–654. DOI: 10.1007/s004190050248.

[12] M. P. Bendsøe and N. Kikuchi. “Generating optimal topologies in structural design using a homogenization method”. In: *Computer methods in applied mechanics and engineering* 71.2 (1988), pp. 197–224. DOI: 10.1016/0045-7825(88)90086-2.

[13] M. P. Bendsøe and O. Sigmund. *Topology optimization: theory, methods, and applications*. Springer Science & Business Media, 2013. DOI: 10.1007/978-3-662-05086-6.

[14] M. Bi, P. Tran, L. Xia, G. Ma, and Y. M. Xie. “Topology optimization for 3D concrete printing with various manufacturing constraints”. In: *Additive Manufacturing* 57 (2022), p. 102982. DOI: 10.1016/j.addma.2022.102982.

[15] M. Boissier, G. Allaire, and C. Tournier. “Additive manufacturing scanning paths optimization using shape optimization tools”. In: *Structural and Multidisciplinary Optimization* 61.6 (2020), pp. 2437–2466. DOI: 10.1007/s00158-020-02614-3.

[16] M. Boissier, G. Allaire, and C. Tournier. “Concurrent Shape Optimization of the Part and Scanning Path for Powder Bed Fusion Additive Manufacturing”. In: *SIAM Journal on Control and Optimization* 61.2 (2023), pp. 697–722. DOI: 10.1137/21M1461976.

[17] B. Bourdin. “Filters in topology optimization”. In: *International Journal for Numerical Methods in Engineering* 50.9 (2001), pp. 2143–2158. DOI: 10.1002/nme.116.

[18] D. Brackett, I. Ashcroft, and R. Hague. “Topology optimization for additive manufacturing”. In: *2011 International Solid Freeform Fabrication Symposium*. University of Texas at Austin. 2011. DOI: 10.26153/tsw/15300.

[19] M. Bruggi. “On an alternative approach to stress constraints relaxation in topology optimization”. In: *Structural and Multidisciplinary Optimization* 36.2 (2008), pp. 125–141. DOI: 10.1007/s00158-007-0203-6.

[20] M. Bruggi, V. Laghi, and T. Trombetti. “Simultaneous design of the topology and the build orientation of Wire-and-Arc Additively Manufactured structural elements”. In: *Computers & Structures* 242 (2021), p. 106370. DOI: 10.1016/j.compstruc.2020.106370.

[21] M. Bruggi, V. Laghi, and T. Trombetti. “Optimal Design of Wire-and-Arc Additively Manufactured I-Beams for Prescribed Deflection”. In: *Computer Assisted Methods in Engineering and Science* (2022). DOI: 10.24423/cames.469.

[22] M. Bruggi, N. Parolini, F. Regazzoni, and M. Verani. “Topology optimization with a time-integral cost functional”. In: *Finite Elements in Analysis and Design* 140 (2018), pp. 11–22. DOI: 10.1016/j.finel.2017.10.011.

[23] T. E. Bruns and D. A. Tortorelli. “Topology optimization of non-linear elastic structures and compliant mechanisms”. In: *Computer methods in applied mechanics and engineering* 190.26-27 (2001), pp. 3443–3459. URL: https://hdl.handle.net/2142/83749.

[24] C. Cambon, I. Bendaoud, S. Rouquette, and F. Soulié. “A WAAM benchmark: From process parameters to thermal effects on weld pool shape, microstructure and residual stresses”. In: *Materials Today Communications* 33 (2022), p. 104235. DOI: 10.1016/j.mtcomm.2022.104235.

[25] A. Chandrasekhar, T. Kumar, and K. Suresh. “Build optimization of fiber-reinforced additively manufactured components”. In: *Structural and Multidisciplinary Optimization* 61.1 (2020), pp. 77–90. DOI: 10.1007/s00158-019-02346-z.

[26] Q. Chen, J. Liu, X. Liang, and A. C. To. “A level-set based continuous scanning path optimization method for reducing residual stress and deformation in metal additive manufacturing”. In: *Computer Methods in Applied Mechanics and Engineering* 360 (2020), p. 112719. DOI: 10.1016/j.cma.2019.112719.

[27] S.-g. Chen, H.-j. Gao, Y.-d. Zhang, Q. Wu, Z.-h. Gao, and X. Zhou. “Review on residual stresses in metal additive manufacturing: formation mechanisms, parameter dependencies, prediction and control approaches”. In: *Journal of Materials Research and Technology* 17 (2022), pp. 2950–2974. DOI: 10.1016/j.jmrt.2022.02.054.

[28] S. Chen, M. Xu, T. Yuan, X. Jiang, H. Zhang, and X. Zheng. “Thermal–microstructural analysis of the mechanism of liquation cracks in wire-arc additive manufacturing of Al–Zn–Mg–Cu alloy”. In: *Journal of Materials Research and Technology* 16 (2022), pp. 1260–1271. DOI: 10.1016/j.jmrt.2021.12.016.

[29] G. D. Cheng and X. Guo. “ε-relaxed approach in structural topology optimization”. In: *Structural Optimization* 13.4 (1997), pp. 258–266. DOI: 10.1007/bf01197454.

[30] H. C. Cheng, N. Kikuchi, and Z. D. Ma. “An improved approach for determining the optimal orientation of orthotropic material”. In: *Structural Optimization* 8.2-3 (1994), pp. 101–112. DOI: 10.1007/bf01743305.

[31] L. Cheng, J. Bai, and A. C. To. “Functionally graded lattice structure topology optimization for the design of additive manufactured components with stress constraints”. In: *Computer Methods in Applied Mechanics and Engineering* 344 (2019), pp. 334–359. DOI: 10.1016/j.cma.2018.10.010.

[32] L. Cheng, X. Liang, J. Bai, Q. Chen, J. Lemon, and A. To. “On utilizing topology optimization to design support structure to prevent residual stress induced build failure in laser powder bed metal additive manufacturing”. In: *Additive Manufacturing* 27 (2019), pp. 290–304. DOI: 10.1016/j.addma.2019.03.001.

[33] L. Cheng and A. To. “Part-scale build orientation optimization for minimizing residual stress and support volume for metal additive manufacturing: Theory and experimental validation”. In: *Computer-Aided Design* 113 (2019), pp. 1–23. DOI: 10.1016/j.cad.2019.03.004.

[34] S. C. A. Costello, C. R. Cunningham, F. Xu, A. Shokrani, V. Dhokia, and S. T. Newman. “The state-of-the-art of wire arc directed energy deposition (WA-DED) as an additive manufacturing process for large metallic component manufacture”. In: *International Journal of Computer Integrated Manufacturing* 36.3 (2023), pp. 469–510. DOI: 10.1080/0951192x.2022.2162597.

[35] D. Coupek, J. Friedrich, D. Battran, and O. Riedel. “Reduction of Support Structures and Building Time by Optimized Path Planning Algorithms in Multi-axis Additive Manufacturing”. In: *Procedia CIRP* 67 (2018), pp. 221–226. DOI: 10.1016/j.procir.2017.12.203.

[36] K. Crane, C. Weischedel, and M. Wardetzky. “Geodesics in Heat: A New Approach to Computing Distance Based on Heat Flow”. In: *Acm Transactions on Graphics* 32.5 (2013), pp. 13–15. DOI: 10.1145/2516971.2516977.

[37] G. A. Da Silva, N. Aage, A. T. Beck, and O. Sigmund. “Three-dimensional manufacturing tolerant topology optimization with hundreds of millions of local stress constraints”. In: *International Journal for Numerical Methods in Engineering* 122.2 (2021), pp. 548–578. DOI: 10.1002/nme.6548.

[38] C. Dai, C. C. L. Wang, C. Wu, S. Lefebvre, G. Fang, and Y.-J. Liu. “Support-free Volume Printing by Multi-axis Motion”. In: *ACM Transactions on Graphics (TOG)* 37.4 (July 2018), 134:1–134:14. DOI: 10.1145/3197517.3201342.

[39] C. Dapogny, R. Estevez, A. Faure, and G. Michailidis. “Shape and topology optimization considering anisotropic features induced by additive manufacturing processes”. In: *Computer Methods in Applied Mechanics and Engineering* 344 (2019), pp. 626–665. DOI: 10.1016/j.cma.2018.09.036.

[40] A. R. Díaz and M. P. Bendsøe. “Shape optimization of structures for multiple loading conditions using a homogenization method”. In: *Structural Optimization* 4.1 (1992), pp. 17–22. DOI: 10.1007/bf01894077.

[41] D. Ding. “Process planning for robotic wire ARC additive manufacturing”. Thesis. 2015. DOI: https://ro.uow.edu.au/theses/4613.

[42] D. Ding, Z. Pan, D. Cuiuri, and H. Li. “A tool-path generation strategy for wire and arc additive manufacturing”. In: *The International Journal of Advanced Manufacturing Technology* 73.1-4 (2014), pp. 173–183. DOI: 10.1007/s00170-014-5808-5.

[43] D. Ding, Z. Pan, D. Cuiuri, and H. Li. “A practical path planning methodology for wire and arc additive manufacturing of thin-walled structures”. In: *Robotics and Computer-Integrated Manufacturing* 34 (2015), pp. 8–19. DOI: 10.1016/j.rcim.2015.01.003.

[44] D. Ding, Z. Pan, D. Cuiuri, and H. Li. "Wire-feed additive manufacturing of metal components: technologies, developments and future interests". In: *The International Journal of Advanced Manufacturing Technology* 81.1-4 (2015), pp. 465–481. DOI: 10.1007/s00170-015-7077-3.

[45] D. Ding, Z. Pan, D. Cuiuri, H. Li, N. Larkin, and S. van Duin. "Automatic multi-direction slicing algorithms for wire based additive manufacturing". In: *Robotics and Computer-Integrated Manufacturing* 37 (2016), pp. 139–150. DOI: 10.1016/j.rcim.2015.09.002.

[46] D. Ding, Z. Pan, D. Cuiuri, H. Li, S. van Duin, and N. Larkin. "Bead modelling and implementation of adaptive MAT path in wire and arc additive manufacturing". In: *Robotics and Computer-Integrated Manufacturing* 39 (2016), pp. 32–42. DOI: 10.1016/j.rcim.2015.12.004.

[47] J. Ding, P. Colegrove, J. Mehnen, S. Ganguly, P. M. Sequeira Almeida, F. Wang, and S. Williams. "Thermo-mechanical analysis of Wire and Arc Additive Layer Manufacturing process on large multi-layer parts". In: *Computational Materials Science* (2011). DOI: 10.1016/j.commatsci.2011.06.023.

[48] J. Ding, P. Colegrove, J. Mehnen, S. Williams, F. Wang, and P. S. Almeida. "A computationally efficient finite element model of wire and arc additive manufacture". In: *The International Journal of Advanced Manufacturing Technology* 70.1-4 (2013), pp. 227–236. DOI: 10.1007/s00170-013-5261-x.

[49] A. Donoso, E. Aranda, and D. Ruiz. "A new approach based on spectral graph theory to avoiding enclosed holes in topology optimization". In: *Computer Methods in Applied Mechanics and Engineering* 393 (2022), p. 114769. DOI: 10.1016/j.cma.2022.114769.

[50] P. Duysinx and O. Sigmund. "New developments in handling stress constraints in optimal material distribution". In: *7th AIAA/USAF/NASA/ISSMO Symposium on Multidisciplinary Analysis and Optimization*. 1998. DOI: 10.2514/6.1998-4906.

[51] M. Eckrich, P. A. Arrabiyeh, A. M. Dlugaj, and D. May. "Structural topology optimization and path planning for composites manufactured by fiber placement technologies". In: *Composite Structures* 289 (2022), p. 115488. DOI: 10.1016/j.compstruct.2022.115488.

[52] M. Eckrich, P. A. Arrabiyeh, A. M. Dlugaj, and D. May. "An anisotropic topology optimization procedure for continuous fiber reinforced polymer structures with biaxial fiber layout for improved intersection point design". In: *Composite Structures* 337 (2024), p. 118064. DOI: 10.1016/j.compstruct.2024.118064.

[53] J. W. Elmer, K. Fisher, G. Gibbs, J. Sengthay, and D. Urabe. "Post-build thermo-mechanical processing of wire arc additively manufactured stainless steel for improved mechanical properties and reduction of crystallographic texture". In: *Additive Manufacturing* 50 (2022), p. 102573. DOI: 10.1016/j.addma.2021.102573.

[54] J. Etienne, N. Ray, D. Panozzo, S. Hornus, C. C. L. Wang, J. Martínez, S. McMains, M. Alexa, B. Wyvill, and S. Lefebvre. "CurviSlicer: slightly curved slicing for 3-axis printers". In: *ACM Trans. Graph.* 38.4 (2019), Article 81. DOI: 10.1145/3306346.3323022.

[55] G. Fang, T. Zhang, S. Zhong, X. Chen, Z. Zhong, and C. C. L. Wang. "Reinforced FDM: multi-axis filament alignment with controlled anisotropic strength". In: *ACM Transactions on Graphics* 39.6 (2020), pp. 1–15. DOI: 10.1145/3414685.3417834.

[56] F. Fernandez, W. S. Compel, J. P. Lewicki, and D. A. Tortorelli. "Optimal design of fiber reinforced composite structures and their direct ink write fabrication". In: *Computer Methods in Applied Mechanics and Engineering* 353 (2019), pp. 277–307. DOI: 10.1016/j.cma.2019.05.010.

[57] E. Fernández, C. Ayas, M. Langelaar, and P. Duysinx. "Topology optimisation for large-scale additive manufacturing: generating designs tailored to the deposition nozzle size". In: *Virtual and Physical Prototyping* 16.2 (2021), pp. 196–220. DOI: 10.1080/17452759.2021.1914893.

[58] E. Fernández, K.-k. Yang, S. Koppen, P. Alarcón, S. Bauduin, and P. Duysinx. "Imposing minimum and maximum member size, minimum cavity size, and minimum separation distance between solid members in topology optimization". In: *Computer Methods in Applied Mechanics and Engineering* 368 (2020), p. 113157. DOI: 10.1016/j.cma.2020.113157.

[59] L. Gardner, P. Kyvelou, G. Herbert, and C. Buchanan. "Testing and initial verification of the world's first metal 3D printed bridge". In: *Journal of Constructional Steel Research* 172 (2020), p. 106233. DOI: 10.1016/j.jcsr.2020.106233.

[60] A. T. Gaynor and J. K. Guest. "Topology optimization considering overhang constraints: Eliminating sacrificial support material in additive manufacturing through design". In: *Structural and Multidisciplinary Optimization* 54.5 (2016), pp. 1157–1172. DOI: 10.1007/s00158-016-1551-x.

[61] H. C. Gea and J. H. Luo. "On the stress-based and strain-based methods for predicting optimal orientation of orthotropic materials". In: *Structural and Multidisciplinary Optimization* 26.3-4 (2004), pp. 229–234. DOI: 10.1007/s00158-003-0348-x.

[62] R. Goldman. "Curvature formulas for implicit curves and surfaces". In: *Computer Aided Geometric Design* 22.7 (2005), pp. 632–658. DOI: https://doi.org/10.1016/j.cagd.2005.06.005.

[63] V. Gornyakov, J. Ding, Y. Sun, and S. Williams. "Understanding and designing post-build rolling for mitigation of residual stress and distortion in wire arc additively manufactured components". In: *Materials & Design* 213 (2022), p. 110335. DOI: 10.1016/j.matdes.2021.110335.

[64] S. Graziosi, J. Wu, Z. Doubrovski, N. Meisel, M. Schütz, and T. Stankovic. "Advancing design for Additive Manufacturing Education: A focus on computational skills and competencies". In: *ETH Learning and Teaching Journal* 4.1 (2023), pp. 5–21. DOI: 10.16906/lt-eth.v4i1.220.

[65] X. Guo, W. Zhang, and W. Zhong. “Doing Topology Optimization Explicitly and Geometrically—A New Moving Morphable Components Based Framework”. In: *Journal of Applied Mechanics* 81.8 (2014), p. 081009. DOI: 10.1115/1.4027609.

[66] T. Hassel and T. Carstensen. “Properties and anisotropy behaviour of a nickel base alloy material produced by robot-based wire and arc additive manufacturing”. In: *Welding in the World* 64.11 (2020), pp. 1921–1931. DOI: 10.1007/s40194-020-00971-7.

[67] G. A. Haveroth, C. J. Thore, M. R. Correa, R. F. Ausas, S. Jakobsson, J. A. Cuminato, and A. Klarbring. “Topology optimization including a model of the layer-by-layer additive manufacturing process”. In: *Computer Methods in Applied Mechanics and Engineering* 398 (2022), p. 115203. DOI: 10.1016/j.cma.2022.115203.

[68] K. Hildebrand, B. Bickel, and M. Alexa. “Orthogonal slicing for additive manufacturing”. In: *Computers & Graphics* 37.6 (2013), pp. 669–675. DOI: 10.1016/j.cag.2013.05.011.

[69] J. R. Hönnige, P. A. Colegrove, S. Ganguly, E. Eimer, S. Kabra, and S. Williams. “Control of residual stress and distortion in aluminium wire + arc additive manufacture with rolling”. In: *Additive Manufacturing* 22 (2018), pp. 775–783. DOI: 10.1016/j.addma.2018.06.015.

[70] N. Ichihara and M. Ueda. “3D-printed high-toughness composite structures by anisotropic topology optimization”. In: *Composites Part B: Engineering* 253 (2023), p. 110572. DOI: 10.1016/j.compositesb.2023.110572.

[71] D. Jafari, T. H. J. Vaneker, and I. Gibson. “Wire and arc additive manufacturing: Opportunities and challenges to control the quality and accuracy of manufactured parts”. In: *Materials and Design* (2021), p. 109471. DOI: 10.1016/j.matdes.2021.109471.

[72] D. R. Jantos, K. Hackl, and P. Junker. “Topology optimization with anisotropic materials, including a filter to smooth fiber pathways”. In: *Structural and Multidisciplinary Optimization* 61.5 (2020), pp. 2135–2154. DOI: 10.1007/s00158-019-02461-x.

[73] D. Jiang, R. Hoglund, and D. Smith. “Continuous Fiber Angle Topology Optimization for Polymer Composite Deposition Additive Manufacturing Applications”. In: *Fibers* 7.2 (2019), p. 14. DOI: 10.3390/fib7020014.

[74] D. Jiang and D. E. Smith. “Anisotropic mechanical properties of oriented carbon fiber filled polymer composites produced with fused filament fabrication”. In: *Additive Manufacturing* 18 (2017), pp. 84–94. DOI: 10.1016/j.addma.2017.08.006.

[75] Z. Kallai, M. Dammann, and T. Schueppstuhl. “Operation and experimental evaluation of a 12-axis robot-based setup used for 3D-printing”. In: *ISR 2020; 52th International Symposium on Robotics*. 2020, pp. 1–9.

[76] M. Kerschbaumer, G. Ernst, and P. O’Leary. “Tool path generation for 3D laser cladding using adaptive slicing technology”. In: Laser Institute of America, 2005, p. 604. DOI: 10.2351/1.5060506.

[77] M. Kick, D. R. Jantos, and P. Junker. “Thermodynamic topology optimization for sequential additive manufacturing including structural self-weight”. In: *Civil Engineering Design* 4.5-6 (2022), pp. 162–173. DOI: 10.1002/cend.202200007.

[78] Y. Kok, X. P. Tan, P. Wang, M. L. S. Nai, N. H. Loh, E. Liu, and S. B. Tor. “Anisotropy and heterogeneity of microstructure and mechanical properties in metal additive manufacturing: A critical review”. In: *Materials and Design* 139 (2018), pp. 565–586. DOI: 10.1016/j.matdes.2017.11.021.

[79] R. D. Kundu and X. S. Zhang. “Additive manufacturing of stiff and strong structures by leveraging printing-induced strength anisotropy in topology optimization”. In: *Additive Manufacturing* 75 (2023), p. 103730. DOI: 10.1016/j.addma.2023.103730.

[80] K. Kunze, T. Etter, J. Grässlin, and V. Shklover. “Texture, anisotropy in microstructure and mechanical properties of IN738LC alloy processed by selective laser melting (SLM)”. In: *Materials Science and Engineering: A* 620 (2015), pp. 213–222. DOI: 10.1016/j.msea.2014.10.003.

[81] Y.-H. Kuo, C.-C. Cheng, Y.-S. Lin, and C.-H. San. “Support structure design in additive manufacturing based on topology optimization”. In: *Structural and Multidisciplinary Optimization* 57.1 (2018), pp. 183–195. DOI: 10.1007/s00158-017-1743-z.

[82] P. Kyvelou, C. Buchanan, and L. Gardner. “Numerical simulation and evaluation of the world’s first metal additively manufactured bridge”. In: *Structures* 42 (2022), pp. 405–416. DOI: 10.1016/j.istruc.2022.06.012.

[83] P. Kyvelou, H. Slack, D. Daskalaki Mountanou, M. A. Wadee, T. B. Britton, C. Buchanan, and L. Gardner. “Mechanical and microstructural testing of wire and arc additively manufactured sheet material”. In: *Materials and Design* 192 (2020), p. 108675. DOI: 10.1016/j.matdes.2020.108675.

[84] V. Laghi, M. Palermo, M. Bruggi, G. Gasparini, and T. Trombetti. “Blended structural optimization for wire-and-arc additively manufactured beams”. In: *Progress in Additive Manufacturing* 8.3 (2023), pp. 381–392. DOI: 10.1007/s40964-022-00335-1.

[85] F. Lambiase, S. I. Scipioni, and A. Paoletti. “Accurate prediction of the bead geometry in wire arc additive manufacturing process”. In: *The International Journal of Advanced Manufacturing Technology* (2022). DOI: 10.1007/s00170-021-08588-w.

[86] M. Langelaar. “Topology optimization of 3D self-supporting structures for additive manufacturing”. In: *Additive Manufacturing* 12 (2016), pp. 60–70. DOI: 10.1016/j.addma.2016.06.010.

[87] M. Langelaar. “An additive manufacturing filter for topology optimization of print-ready designs”. In: *Structural and multidisciplinary optimization* 55.3 (2017), pp. 871–883. DOI: 10.1007/s00158-016-1522-2.

[88] M. Langelaar. “Combined optimization of part topology, support structure layout and build orientation for additive manufacturing”. In: *Structural and Multidisciplinary Optimization* 57.5 (2018), pp. 1985–2004. DOI: 10.1007/s00158-017-1877-z.

[89] B. S. Lazarov and O. Sigmund. “Filters in topology optimization based on Helmholtz-type differential equations”. In: *International Journal for Numerical Methods in Engineering* 86.6 (2011), pp. 765–781. DOI: 10.1002/nme.3072.

[90] B. S. Lazarov, F. Wang, and O. Sigmund. “Length scale and manufacturability in density-based topology optimization”. In: *Archive of Applied Mechanics* 86.1-2 (2016), pp. 189–218. DOI: 10.1007/s00419-015-1106-4.

[91] C. Le, J. Norato, T. Bruns, C. Ha, and D. Tortorelli. “Stress-based topology optimization for continua”. In: *Structural and Multidisciplinary Optimization* 41.4 (2010), pp. 605–620. DOI: 10.1007/s00158-009-0440-y.

[92] J. Lee, D. Kim, T. Nomura, E. M. Dede, and J. Yoo. “Topology optimization for continuous and discrete orientation design of functionally graded fiber-reinforced composite structures”. In: *Composite Structures* 201 (2018), pp. 217–233. DOI: 10.1016/j.compstruct.2018.06.020.

[93] L. Li, Q. Sun, C. Bellehumeur, and P. Gu. “Composite Modeling and Analysis for Fabrication of FDM Prototypes with Locally Controlled Properties”. In: *Journal of Manufacturing Processes* 4.2 (2002), pp. 129–141. DOI: 10.1016/S1526-6125(02)70139-4.

[94] P. Li, J. Yvonnet, and Y. Wu. “Improved fracture resistance of 3D-printed elasto-plastic structures with respect to their topology and orientation of deposited layers”. In: *International Journal of Mechanical Sciences* 220 (2022), p. 107147. DOI: 10.1016/j.ijmecsci.2022.107147.

[95] Q. Li, W. Chen, S. Liu, and L. Tong. “Structural topology optimization considering connectivity constraint”. In: *Structural and Multidisciplinary Optimization* 54.4 (2016), pp. 971–984. DOI: 10.1007/s00158-016-1459-5.

[96] S. Li, S. Yuan, J. Zhu, C. Wang, J. Li, and W. Zhang. “Additive manufacturing-driven design optimization: Building direction and structural topology”. In: *Additive Manufacturing* 36 (2020), p. 101406. DOI: 10.1016/j.addma.2020.101406.

[97] Y. Li, D. He, S. Yuan, K. Tang, and J. Zhu. “Vector field-based curved layer slicing and path planning for multi-axis printing”. In: *Robotics and Computer-Integrated Manufacturing* 77 (2022), p. 102362. DOI: 10.1016/j.rcim.2022.102362.

[98] X. Liang, Q. Chen, L. Cheng, D. Hayduke, and A. C. To. “Modified inherent strain method for efficient prediction of residual deformation in direct metal laser sintered components”. In: *Computational Mechanics* 64.6 (2019), pp. 1719–1733. DOI: 10.1007/s00466-019-01748-6.

[99] J. Liu, Y. Xu, Y. Ge, Z. Hou, and S. Chen. “Wire and arc additive manufacturing of metal components: a review of recent research developments”. In: *The International Journal of Advanced Manufacturing Technology* 111.1-2 (2020), pp. 149–198. DOI: 10.1007/s00170-020-05966-8.

[100] J. Liu, A. T. Gaynor, S. Chen, Z. Kang, K. Suresh, A. Takezawa, L. Li, J. Kato, J. Tang, C. C. Wang, *et al.* "Current and future trends in topology optimization for additive manufacturing". In: *Structural and Multidisciplinary Optimization* 57.6 (2018), pp. 2457–2483. DOI: 10.1007/s00158-018-1994-3.

[101] J. Liu and Y. Ma. "A survey of manufacturing oriented topology optimization methods". In: *Advances in Engineering Software* 100 (2016), pp. 161–175. DOI: 10.1016/j.advengsoft.2016.07.017.

[102] J. Liu and A. C. To. "Deposition path planning-integrated structural topology optimization for 3D additive manufacturing subject to self-support constraint". In: *Computer-Aided Design* 91 (2017), pp. 27–45. DOI: 10.1016/j.cad.2017.05.003.

[103] J. Liu and H. Yu. "Concurrent deposition path planning and structural topology optimization for additive manufacturing". In: *Rapid Prototyping Journal* 23.5 (2017), pp. 930–942. DOI: 10.1108/RPJ-05-2016-0087.

[104] S. Liu, Q. Li, W. Chen, L. Tong, and G. Cheng. "An identification method for enclosed voids restriction in manufacturability design for additive manufacturing structures". In: *Frontiers of Mechanical Engineering* 10.2 (2015), pp. 126–137. DOI: 10.1007/s11465-015-0340-3.

[105] Y. Liu, M. Zhou, C. Wei, and Z. Lin. "Topology optimization of self-supporting infill structures". In: *Structural and Multidisciplinary Optimization* 63.5 (2021), pp. 2289–2304. DOI: 10.1007/s00158-020-02805-y.

[106] H. Lockett, J. Ding, S. Williams, and F. Martina. "Design for Wire+ Arc Additive Manufacture: design rules and build orientation selection". In: *Journal of Engineering Design* 28.7-9 (2017), pp. 568–598. DOI: 10.1080/09544828.2017.1365826.

[107] A. Lundbäck and L.-E. Lindgren. "Modelling of metal deposition". In: *Finite Elements in Analysis and Design* 47.10 (2011), pp. 1169–1177. DOI: 10.1016/j.finel.2011.05.005.

[108] Y. Luo, O. Sigmund, Q. Li, and S. Liu. "Additive manufacturing oriented topology optimization of structures with self-supported enclosed voids". In: *Computer Methods in Applied Mechanics and Engineering* 372 (2020), p. 113385. DOI: 10.1016/j.cma.2020.113385.

[109] J. Mehnen, J. Ding, H. Lockett, and P. Kazanas. "Design study for wire and arc additive manufacture". In: *International Journal of Product Development* 19.1/2/3 (2014), p. 2. DOI: 10.1504/ijpd.2014.060028.

[110] T. Miki and T. Yamada. "Topology optimization considering the distortion in additive manufacturing". In: *Finite Elements in Analysis and Design* 193 (2021), p. 103558. DOI: 10.1016/j.finel.2021.103558.

[111] V. Mishra, C. Ayas, M. Langelaar, and F. Keulen. "Simultaneous Topology and Deposition Direction Optimization for Wire and Arc Additive Manufacturing". In: *Manufacturing Letters* 31 (2021), pp. 45–51. DOI: 10.1016/j.mfglet.2021.05.011.

[112] V. Mishra, C. Ayas, and M. Langelaar. “Design for material properties of additively manufactured metals using topology optimization”. In: *Materials & Design* 235 (2023), p. 112388. DOI: 10.1016/j.matdes.2023.112388.

[113] G. Misiun, E. van de Ven, M. Langelaar, H. Geijselaers, F. van Keulen, T. van den Boogaard, and C. Ayas. “Topology Optimization for additive manufacturing with distortion constraints”. In: *Computer Methods in Applied Mechanics and Engineering* 386 (2021), p. 114095. DOI: 10.1016/j.cma.2021.114095.

[114] P. Mohan Pandey, N. Venkata Reddy, and S. G. Dhande. “Slicing procedures in layered manufacturing: a review”. In: *Rapid Prototyping Journal* 9.5 (2003), pp. 274–288. DOI: 10.1108/13552540310502185.

[115] S. H. Mok, G. Bi, J. Folkes, I. Pashby, and J. Segal. “Deposition of Ti–6Al–4V using a high power diode laser and wire, Part II: Investigation on the mechanical properties”. In: *Surface and Coatings Technology* 202.19 (2008), pp. 4613–4619. DOI: 10.1016/j.surfcoat.2008.03.028.

[116] H. Mu, J. Polden, Y. Li, F. He, C. Xia, and Z. Pan. “Layer-by-layer model-based adaptive control for wire arc additive manufacturing of thin-wall structures”. In: *Journal of Intelligent Manufacturing* 33.4 (2022), pp. 1165–1180. DOI: 10.1007/s10845-022-01920-5.

[117] M. Mughal, R. Mufti, and H. Fawad. “The mechanical effects of deposition patterns in welding-based layered manufacturing”. In: *Proceedings of the Institution of Mechanical Engineers, Part B: Journal of Engineering Manufacture* 221.10 (2007), pp. 1499–1509. DOI: 10.1243/09544054JEM783.

[118] T. Mukherjee, W. Zhang, and T. DebRoy. “An improved prediction of residual stresses and distortion in additive manufacturing”. In: *Computational Materials Science* 126 (2017), pp. 360–372. DOI: 10.1016/j.commatsci.2016.10.003.

[119] D. Munro, C. Ayas, M. Langelaar, and F. Van Keulen. “On process-step parallel computability and linear superposition of mechanical responses in additive manufacturing process simulation”. In: *Additive Manufacturing* 28 (2019), pp. 738–749. DOI: 10.1016/j.addma.2019.06.023.

[120] A. P. Nagalingam, M. Shamir, E. B. Tureyen, A. R. C. Sharman, O. Poyraz, E. Yasa, and J. Hughes. “Recent progress in wire-arc and wire-laser directed energy deposition (DED) of titanium and aluminium alloys”. In: *The International Journal of Advanced Manufacturing Technology* (2025). DOI: 10.1007/s00170-024-14967-w.

[121] A. Nazir, O. Gokcekaya, K. Md Masum Billah, O. Ertugrul, J. Jiang, J. Sun, and S. Hussain. “Multi-material additive manufacturing: A systematic review of design, properties, applications, challenges, and 3D printing of materials and cellular metamaterials”. In: *Materials & Design* 226 (2023), p. 111661. DOI: 10.1016/j.matdes.2023.111661.

[122] T. Nomura, E. M. Dede, J. Lee, S. Yamasaki, T. Matsumori, A. Kawamoto, and N. Kikuchi. “General topology optimization method with continuous and discrete orientation design using isoparametric projection”. In: *International Journal for Numerical Methods in Engineering* 101.8 (2015), pp. 571–605. DOI: 10.1002/nme.4799.

[123] J. A. Norato, B. K. Bell, and D. A. Tortorelli. “A geometry projection method for continuum-based topology optimization with discrete elements”. In: *Computer Methods in Applied Mechanics and Engineering* 293 (2015), pp. 306–327. DOI: 10.1016/j.cma.2015.05.005.

[124] J. Norrish, J. Polden, and I. Richardson. “A review of wire arc additive manufacturing: development, principles, process physics, implementation and current status”. In: *Journal of Physics D: Applied Physics* 54.47 (2021), p. 473001. DOI: 10.1088/1361-6463/ac1e4a.

[125] A. M. Olesen, S. M. Hermansen, and E. Lund. “Simultaneous optimization of topology and print orientation for transversely isotropic fatigue”. In: *Structural and Multidisciplinary Optimization* 64.3 (2021), pp. 1041–1062. DOI: 10.1007/s00158-021-02995-z.

[126] P. Pedersen. “On optimal orientation of orthotropic materials”. In: *Structural Optimization* 1.2 (1989), pp. 101–106. DOI: 10.1007/bf01637666.

[127] P. Pedersen. “Bounds on elastic energy in solids of orthotropic materials”. In: *Structural Optimization* 2.1 (1990), pp. 55–63. DOI: 10.1007/bf01743521.

[128] J. Pellens, G. Lombaert, M. Michiels, T. Craeghs, and M. Schevenels. “Topology optimization of support structure layout in metal-based additive manufacturing accounting for thermal deformations”. In: *Structural and Multidisciplinary Optimization* 61.6 (2020), pp. 2291–2303. DOI: 10.1007/s00158-020-02512-8.

[129] V. Ploshikhin, A. Prihodovsky, A. Ilin, and C. Heimerdinger. “Advanced numerical method for fast prediction of welding distortions of large aircraft structures”. In: *International Journal of Microstructure and Materials Properties* 5.4-5 (2010), pp. 423–435. DOI: 10.1504/IJMMP.2010.037619.

[130] X. Qian. “Undercut and overhang angle control in topology optimization: A density gradient based integral approach”. In: *International Journal for Numerical Methods in Engineering* 111.3 (2017), pp. 247–272. DOI: 10.1002/nme.5461.

[131] Z. Qiu, Q. Li, Y. Luo, and S. Liu. “Concurrent topology and fiber orientation optimization method for fiber-reinforced composites based on composite additive manufacturing”. In: *Computer Methods in Applied Mechanics and Engineering* 395 (2022), p. 114962. DOI: 10.1016/j.cma.2022.114962.

[132] C. Ramonell and R. Chacón. “On the topological optimization of horizontal links in eccentrically braced frames”. In: *Journal of Constructional Steel Research* 185 (2021), p. 106887. DOI: 10.1016/j.jcsr.2021.106887.

[133] R. Ranjan, C. Ayas, M. Langelaar, and F. V. Keulen. “Controlling local overheating in topology optimization for additive manufacturing”. In: *Structural and Multidisciplinary Optimization* 65.6 (2022). DOI: 10.1007/s00158-022-03258-1.

[134] N. Ray and I. Y. Kim. “Fiber reinforced additive manufacturing: structurally motivated print orientation and sequential topology optimization of anisotropic material”. In: *Rapid Prototyping Journal* 30.2 (2024), pp. 305–322. DOI: 10.1108/rpj-08-2023-0276.

[135] T. A. Rodrigues, V. Duarte, R. Miranda, T. G. Santos, and J. Oliveira. “Current Status and Perspectives on Wire and Arc Additive Manufacturing (WAAM)”. In: *Materials* 12.7 (2019), p. 1121. DOI: 10.3390/ma12071121.

[136] S. Rosso, F. Uriati, L. Grigolato, R. Meneghello, G. Concheri, and G. Savio. “An Optimization Workflow in Design for Additive Manufacturing”. In: *Applied Sciences* 11.6 (2021), p. 2572. DOI: 10.3390/app11062572.

[137] J. Ruan, T. E. Sparks, A. Panackal, F. W. Liou, K. Eiamsa-Ard, K. Slattery, H.-N. Chou, and M. Kinsella. “Automated Slicing for a Multiaxis Metal Deposition System”. In: *Journal of Manufacturing Science and Engineering* 129.2 (2007), pp. 303–310. DOI: 10.1115/1.2673492.

[138] A. A. Safonov. “3D topology optimization of continuous fiber-reinforced structures via natural evolution method”. In: *Composite Structures* 215 (2019), pp. 289–297. DOI: 10.1016/j.compstruct.2019.02.063.

[139] M.-P. Schmidt, L. Couret, C. Gout, and C. B. W. Pedersen. “Structural topology optimization with smoothly varying fiber orientations”. In: *Structural and Multidisciplinary Optimization* 62.6 (2020), pp. 3105–3126. DOI: 10.1007/s00158-020-02657-6.

[140] I. Setien, M. Chiumenti, S. van der Veen, M. San Sebastian, F. Garciandía, and A. Echeverría. “Empirical methodology to determine inherent strains in additive manufacturing”. In: *Computers and Mathematics with Applications* 78.7 (2019), pp. 2282–2295. DOI: 10.1016/j.camwa.2018.05.015.

[141] Y. Shan, D. Gan, and H. Mao. “Curved Layer Slicing based on Isothermal Surface”. In: *Procedia Manufacturing* 53 (2021), pp. 484–491. DOI: 10.1016/j.promfg.2021.06.081.

[142] H. Shen, J. Lin, Z. Zhou, and B. Liu. “Effect of induction heat treatment on residual stress distribution of components fabricated by wire arc additive manufacturing”. In: *Journal of Manufacturing Processes* 75 (2022), pp. 331–345. DOI: 10.1016/j.jmapro.2022.01.018.

[143] Y. Shi, Y. Huang, and I. Y. Kim. “Multi-material topology optimization considering both isotropy and anisotropy with fibre orientation optimization”. In: *Engineering Optimization* (2024), pp. 1–25. DOI: 10.1080/0305215x.2024.2358922.

[144] O. Sigmund and J. Petersson. “Numerical instabilities in topology optimization: A survey on procedures dealing with checkerboards, mesh-dependencies and local minima”. In: *Structural Optimization* 16.1 (1998), pp. 68–75. DOI: 10.1007/bf01214002.

[145] O. Sigmund. “Morphology-based black and white filters for topology optimization”. In: *Structural and Multidisciplinary Optimization* 33.4-5 (2007), pp. 401–424. DOI: 10.1007/s00158-006-0087-x.

[146] O. Sigmund and K. Maute. “Topology optimization approaches: A comparative review”. In: *Structural and Multidisciplinary Optimization* 48.6 (2013), pp. 1031–1055. DOI: 10.1007/s00158-013-0978-6.

[147] O. Sigmund and S. Torquato. “Design of materials with extreme thermal expansion using a three-phase topology optimization method”. In: *Journal of the Mechanics and Physics of Solids* 45.6 (1997), pp. 1037–1067. DOI: 10.1016/S0022-5096(96)00114-7.

[148] P. Singh and D. Dutta. “Multi-Direction Slicing for Layered Manufacturing”. In: *Journal of Computing and Information Science in Engineering* 1.2 (2001), pp. 129–142. DOI: 10.1115/1.1375816.

[149] H.-C. Song, N. Ray, D. Sokolov, and S. Lefebvre. “Anti-aliasing for fused filament deposition”. In: *Computer-Aided Design* 89 (2017), pp. 25–34. DOI: 10.1016/j.cad.2017.04.001.

[150] S. N. Sørensen and E. Lund. “Topology and thickness optimization of laminated composites including manufacturing constraints”. In: *Structural and Multidisciplinary Optimization* 48.2 (2013), pp. 249–265. DOI: 10.1007/s00158-013-0904-y.

[151] A. Suárez, F. Veiga, T. Bhujangrao, and E. Aldalur. “Study of the Mechanical Behavior of Topologically Optimized Arc Wire Direct Energy Deposition Aerospace Fixtures”. In: *Journal of Materials Engineering and Performance* (2022). DOI: 10.1007/s11665-022-06702-x.

[152] K. Suzuki and N. Kikuchi. “A homogenization method for shape and topology optimization”. In: *Computer Methods in Applied Mechanics and Engineering* 93.3 (1991), pp. 291–318. DOI: 10.1016/0045-7825(91)90245-2.

[153] K. Svanberg. “The method of moving asymptotes—a new method for structural optimization”. In: *International journal for numerical methods in engineering* 24.2 (1987), pp. 359–373. DOI: 10.1002/nme.1620240207.

[154] B. Szederkenyi, N. K. Kovacs, and T. Czigany. “A comprehensive review of fiber–reinforced topology optimization for advanced polymer composites produced by automated manufacturing”. In: *Advanced Industrial and Engineering Polymer Research* (2024). DOI: 10.1016/j.aiepr.2024.05.002.

[155] P. Tang, X. Zhao, H. Shi, B. Hu, J. Ding, B. Yang, and W. Xu. “A review of multi-axis additive manufacturing: Potential, opportunity and challenge”. In: *Additive Manufacturing* 83 (2024), p. 104075. DOI: 10.1016/j.addma.2024.104075.

[156] M. K. Thompson, G. Moroni, T. Vaneker, G. Fadel, R. I. Campbell, I. Gibson, A. Bernard, J. Schulz, P. Graf, B. Ahuja, and F. Martina. “Design for Additive Manufacturing: Trends, opportunities, considerations, and constraints”. In: *CIRP Annals* 65.2 (2016), pp. 737–760. DOI: 10.1016/j.cirp.2016.05.004.

[157] Y. Ueda, H. Murakawa, K. Nakacho, and N. X. Ma. “Establishment of computational welding mechanics”. In: *Welding and Surfacing Reviews* 8.1 (1997), pp. 265–299. URL: https://www.scopus.com/inward/record.uri?eid=2-s2.0-8544232814&partnerID=40&md5=1eee6e96a8edb87dbd358a3418bf7b4d.

[158] E. Van De Ven, R. Maas, C. Ayas, M. Langelaar, and F. Van Keulen. "Continuous front propagation-based overhang control for topology optimization with additive manufacturing". In: *Structural and Multidisciplinary Optimization* 57.5 (2018), pp. 2075–2091. DOI: 10.1007/s00158-017-1880-4.

[159] E. Van De Ven, R. Maas, C. Ayas, M. Langelaar, and F. Van Keulen. "Overhang control based on front propagation in 3D topology optimization for additive manufacturing". In: *Computer Methods in Applied Mechanics and Engineering* 369 (2020), p. 113169. DOI: 10.1016/j.cma.2020.113169.

[160] E. Van De Ven, R. Maas, C. Ayas, M. Langelaar, and F. Van Keulen. "Overhang control in topology optimization: a comparison of continuous front propagation-based and discrete layer-by-layer overhang control". In: *Structural and Multidisciplinary Optimization* (2021). DOI: 10.1007/s00158-021-02887-2.

[161] N. P. Van Dijk, K. Maute, M. Langelaar, and F. Van Keulen. "Level-set methods for structural topology optimization: a review". In: *Structural and Multidisciplinary Optimization* 48.3 (2013), pp. 437–472. DOI: 10.1007/s00158-013-0912-y.

[162] F. Veiga, A. Suárez, E. Aldalur, I. Goenaga, and J. Amondarain. "Wire Arc Additive Manufacturing Process for Topologically Optimized Aeronautical Fixtures". In: *3D Print Addit Manuf* 10.1 (2023), pp. 23–33. DOI: 10.1089/3dp.2021.0008.

[163] K. Venkata Rao, S. Parimi, L. Suvarna Raju, and G. Suresh. "Modelling and optimization of weld bead geometry in robotic gas metal arc-based additive manufacturing using machine learning, finite-element modelling and graph theory and matrix approach". In: *Soft Computing* (2022). DOI: 10.1007/s00500-022-06749-x.

[164] A. Verbart, M. Langelaar, and F. v. Keulen. "A unified aggregation and relaxation approach for stress-constrained topology optimization". In: *Structural and Multidisciplinary Optimization* 55.2 (2016), pp. 663–679. DOI: 10.1007/s00158-016-1524-0.

[165] C. Wang and X. Qian. "Simultaneous optimization of build orientation and topology for additive manufacturing". In: *Additive Manufacturing* 34 (2020), p. 101246. DOI: 10.1016/j.addma.2020.101246.

[166] F. Wang, B. S. Lazarov, and O. Sigmund. "On projection methods, convergence and robust formulations in topology optimization". In: *Structural and Multidisciplinary Optimization* 43.6 (2011), pp. 767–784. DOI: 10.1007/s00158-010-0602-y.

[167] M. Y. Wang, X. Wang, and D. Guo. "A level set method for structural topology optimization". In: *Computer Methods in Applied Mechanics and Engineering* 192.1 (2003), pp. 227–246. DOI: 10.1016/S0045-7825(02)00559-5.

[168] W. Wang, D. Munro, C. C. Wang, F. van Keulen, and J. Wu. "Space-time topology optimization for additive manufacturing". In: *Structural and Multidisciplinary Optimization* 61.1 (2020), pp. 1–18. DOI: 10.1007/s00158-019-02420-6.

[169] W. Wang, F. van Keulen, and J. Wu. “Fabrication Sequence Optimization for Minimizing Distortion in Multi-Axis Additive Manufacturing”. In: *Computer Methods in Applied Mechanics and Engineering* 406 (2023), p. 115899. DOI: 10.1016/j.cma.2023.115899.

[170] W. Wang, K. Wu, F. van Keulen, and J. Wu. “Regularization in space–time topology optimization for additive manufacturing”. In: *Computer Methods in Applied Mechanics and Engineering* 431 (2024), p. 117202. DOI: 10.1016/j.cma.2024.117202.

[171] S. W. Williams, F. Martina, A. C. Addison, J. Ding, G. Pardal, and P. Colegrove. “Wire + Arc Additive Manufacturing”. In: *Materials Science and Technology* 32.7 (2016), pp. 641–647. DOI: 10.1179/1743284715Y.0000000073.

[172] B. Wu, Z. Pan, D. Ding, D. Cuiuri, H. Li, J. Xu, and J. Norrish. “A review of the wire arc additive manufacturing of metals: properties, defects and quality improvement”. In: *Journal of Manufacturing Processes* 35 (2018), pp. 127–139. DOI: 10.1016/j.jmapro.2018.08.001.

[173] C. Wu, C. Wang, and J.-W. Kim. “Welding sequence optimization to reduce welding distortion based on coupled artificial neural network and swarm intelligence algorithm”. In: *Engineering Applications of Artificial Intelligence* 114 (2022), p. 105142. DOI: 10.1016/j.engappai.2022.105142.

[174] J. Wu, N. Aage, R. Westermann, and O. Sigmund. “Infill Optimization for Additive Manufacturing—Approaching Bone-Like Porous Structures”. In: *IEEE Transactions on Visualization and Computer Graphics* 24.2 (2018), pp. 1127–1140. DOI: 10.1109/tvcg.2017.2655523.

[175] J. Wu, A. Clausen, and O. Sigmund. “Minimum compliance topology optimization of shell–infill composites for additive manufacturing”. In: *Computer Methods in Applied Mechanics and Engineering* 326 (2017), pp. 358–375. DOI: 10.1016/j.cma.2017.08.018.

[176] J. Wu, O. Sigmund, and J. P. Groen. “Topology optimization of multi-scale structures: a review”. In: *Structural and Multidisciplinary Optimization* (2021). DOI: 10.1007/s00158-021-02881-8.

[177] J. Wu, C. C. L. Wang, X. Zhang, and R. Westermann. “Self-supporting rhombic infill structures for additive manufacturing”. In: *Computer-Aided Design* 80 (2016), pp. 32–42. DOI: 10.1016/j.cad.2016.07.006.

[178] K. Wu, O. Sigmund, and J. Du. “Design of metamaterial mechanisms using robust topology optimization and variable linking scheme”. In: *Structural and Multidisciplinary Optimization* (2021). DOI: 10.1007/s00158-020-02791-1.

[179] K. Wu, F. van Keulen, and J. Wu. “Residual stress-constrained space–time topology optimization for multi-axis additive manufacturing”. In: *Computer Methods in Applied Mechanics and Engineering* 440 (2025), p. 117913. DOI: 10.1016/j.cma.2025.117913.

[180] K. Wu, W. Wang, F. van Keulen, and J. Wu. “Space–time topology optimization for anisotropic materials in wire and arc additive manufacturing”. In: *International Journal of Mechanical Sciences* 284 (2024), p. 109712. DOI: 10.1016/j.ijmecsci.2024.109712.

[181] Q. Wu, T. Mukherjee, A. De, and T. DebRoy. “Residual stresses in wire-arc additive manufacturing – Hierarchy of influential variables”. In: *Additive Manufacturing* 35 (2020), p. 101355. DOI: 10.1016/j.addma.2020.101355.

[182] Y. Wu and L. Yang. “Modeling and analysis of material anisotropy-topology effects of 3D cellular structures fabricated by powder bed fusion additive manufacturing”. In: *International Journal of Mechanical Sciences* 197 (2021), p. 106325. DOI: 10.1016/j.ijmecsci.2021.106325.

[183] Y. Wu, J. Fang, C. Wu, C. Li, G. Sun, and Q. Li. “Additively manufactured materials and structures: A state-of-the-art review on their mechanical characteristics and energy absorption”. In: *International Journal of Mechanical Sciences* 246 (2023), p. 108102. DOI: 10.1016/j.ijmecsci.2023.108102.

[184] C. Xia, Z. Pan, J. Polden, H. Li, Y. Xu, S. Chen, and Y. Zhang. “A review on wire arc additive manufacturing: Monitoring, control and a framework of automated system”. In: *Journal of Manufacturing Systems* 57 (2020), pp. 31–45. DOI: 10.1016/j.jmsy.2020.08.008.

[185] X. Xiao and S. Joshi. “Process planning for five-axis support free additive manufacturing”. In: *Additive Manufacturing* 36 (2020), p. 101569. DOI: 10.1016/j.addma.2020.101569.

[186] Y. M. Xie and G. P. Steven. “A simple evolutionary procedure for structural optimization”. In: *Computers & Structures* 49.5 (1993), pp. 885–896. DOI: 10.1016/0045-7949(93)90035-c.

[187] F. Xu, V. Dhokia, P. Colegrove, A. McAndrew, S. Williams, A. Henstridge, and S. T. Newman. “Realisation of a multi-sensor framework for process monitoring of the wire arc additive manufacturing in producing Ti-6Al-4V parts”. In: *International Journal of Computer Integrated Manufacturing* 31.8 (2018), pp. 785–798. DOI: 10.1080/0951192x.2018.1466395.

[188] J. Xu, X. Gu, D. Ding, Z. Pan, and K. Chen. “A review of slicing methods for directed energy deposition based additive manufacturing”. In: *Rapid Prototyping Journal* 24.6 (2018), pp. 1012–1025. DOI: 10.1108/rpj-10-2017-0196.

[189] K. Xu, Y. Li, L. Chen, and K. Tang. “Curved layer based process planning for multi-axis volume printing of freeform parts”. In: *Computer-Aided Design* 114 (2019), pp. 51–63. DOI: 10.1016/j.cad.2019.05.007.

[190] S. Xu, J. Liu, and Y. Ma. “Residual stress constrained self-support topology optimization for metal additive manufacturing”. In: *Computer Methods in Applied Mechanics and Engineering* 389 (2022), p. 114380. DOI: 10.1016/j.cma.2021.114380.

[191] Y. Xu, Z. Feng, Y. Gao, C. Wu, J. Fang, G. Sun, N. Qiu, G. P. Steven, and Q. Li. "Topology optimization for additive manufacturing of CFRP structures". In: *International Journal of Mechanical Sciences* 269 (2024), p. 108967. DOI: 10.1016/j.ijmecsci.2024.108967.

[192] Y. Xu, Y. Gao, C. Wu, J. Fang, G. Sun, G. P. Steven, and Q. Li. "Concurrent optimization of topological configuration and continuous fiber path for composite structures — A unified level set approach". In: *Computer Methods in Applied Mechanics and Engineering* 399 (2022), p. 115350. DOI: 10.1016/j.cma.2022.115350.

[193] L. Yang, W. Wang, Y. Ji, C. Zhu, and C. C. L. Wang. "Space–time isogeometric topology optimization with additive manufacturing constraints". In: *Computer Methods in Applied Mechanics and Engineering* 441 (2025), p. 117976. DOI: https://doi.org/10.1016/j.cma.2025.117976.

[194] R. J. Yang and C. J. Chen. "Stress-based topology optimization". In: *Structural Optimization* 12.2-3 (1996), pp. 98–105. DOI: 10.1007/bf01196941.

[195] T. Zegard and G. H. Paulino. "Bridging topology optimization and additive manufacturing". In: *Structural and Multidisciplinary Optimization* 53.1 (2016), pp. 175–192. DOI: 10.1007/s00158-015-1274-4.

[196] X. Zhai, F. Chen, and J. Wu. "Alternating optimization of design and stress for stress-constrained topology optimization". In: *Structural and Multidisciplinary Optimization* (2021). DOI: 10.1007/s00158-021-02985-1.

[197] X. Zhai, W. Wang, F. Chen, and J. Wu. "Topology optimization of differentiable microstructures". In: *Computer Methods in Applied Mechanics and Engineering* 418 (2024), p. 116530. DOI: 10.1016/j.cma.2023.116530.

[198] K. Zhang, W. Zhang, and X. Ding. "Multi-axis additive manufacturing process for continuous fibre reinforced composite parts". In: *Procedia CIRP* 85 (2019), pp. 114–120. DOI: 10.1016/j.procir.2019.09.022.

[199] P. Zhang, J. Liu, and A. C. To. "Role of anisotropic properties on topology optimization of additive manufactured load bearing structures". In: *Scripta Materialia* 135 (2017), pp. 148–152. DOI: 10.1016/j.scriptamat.2016.10.021.

[200] T. Zhang, G. Fang, Y. Huang, N. Dutta, S. Lefebvre, Z. M. Kilic, and C. C. Wang. "S3-slicer: A general slicing framework for multi-axis 3D printing". In: *ACM Transactions on Graphics (TOG)* 41.6 (2022), pp. 1–15. DOI: 10.1145/3550454.3555516.

[201] Z.-D. Zhang, O. Ibhadode, U. Ali, C. F. Dibia, P. Rahnama, A. Bonakdar, and E. Toyserkani. "Topology optimization parallel-computing framework based on the inherent strain method for support structure design in laser powder-bed fusion additive manufacturing". In: *International Journal of Mechanics and Materials in Design* 16.4 (2020), pp. 897–923. DOI: 10.1007/s10999-020-09494-x.

[202] G. Zhao, G. Ma, J. Feng, and W. Xiao. "Nonplanar slicing and path generation methods for robotic additive manufacturing". In: *The International Journal of Advanced Manufacturing Technology* 96.9-12 (2018), pp. 3149–3159. DOI: 10.1007/s00170-018-1772-9.

[203] Y. Zhao, F. Li, S. Chen, and Z. Lu. “Unit block–based process planning strategy of WAAM for complex shell–shaped component”. In: *The International Journal of Advanced Manufacturing Technology* 104.9-12 (2019), pp. 3915–3927. DOI: 10.1007/s00170-019-04141-y.

[204] K. Zhou and X. Li. “Topology optimization for minimum compliance under multiple loads based on continuous distribution of members”. In: *Structural and Multidisciplinary Optimization* 37.1 (2008), pp. 49–56. DOI: 10.1007/s00158-007-0214-3.

[205] K. Zhou and X. Li. “Topology optimization of structures under multiple load cases using a fiber-reinforced composite material model”. In: *Computational Mechanics* 38.2 (2006), pp. 163–170. DOI: 10.1007/s00466-005-0735-9.

[206] Z. Zhou, H. Shen, J. Lin, B. Liu, and X. Sheng. “Continuous tool-path planning for optimizing thermo-mechanical properties in wire-arc additive manufacturing: An evolutional method”. In: *Journal of Manufacturing Processes* 83 (2022), pp. 354–373. DOI: 10.1016/j.jmapro.2022.09.009.

[207] J. Zhu, H. Zhou, C. Wang, L. Zhou, S. Yuan, and W. Zhang. “A review of topology optimization for additive manufacturing: Status and challenges”. In: *Chinese Journal of Aeronautics* 34.1 (2021), pp. 91–110. DOI: 10.1016/j.cja.2020.09.020.

[208] J. Zou and X. Xia. “Topology optimization for additive manufacturing with strength constraints considering anisotropy”. In: *Journal of Computational Design and Engineering* 10.2 (2023), pp. 892–904. DOI: 10.1093/jcde/qwad028.

A

SENSITIVITY ANALYSIS

A.1. SENSITIVITY ANALYSIS FOR CHAPTER 2

The general procedure for sensitivity calculation is consistent with those outlined in [168, 169]. Here we focus on the primary distinction that arises from the fact that the time field is no longer a direct design variable; rather, it functions as an implicit variable dependent on both density ϕ and diffusivity μ.

Sensitivity w.r.t design variable $\boldsymbol{\mu}$ Take the objective function f_j as an example, the sensitivity is calculated using the adjoint method by adding an augmented Lagrangian term:

$$f_j = f_j + \boldsymbol{\lambda}^\top (\boldsymbol{K}_\mathrm{T}\boldsymbol{T} - \boldsymbol{b}), \tag{A.1}$$

where $\boldsymbol{\lambda}$ is the Lagrangian multiplier. Without loss of generality, if f_j has no explicit component of the diffusivity design variable μ_e, the derivative of f_j with respect to μ_e is given by:

$$\frac{\partial f_j}{\partial \mu_e} = \sum_{i \in \mathcal{M}} \frac{\partial f_j}{\partial t_i}\frac{\partial t_i}{\partial \mu_e} + \boldsymbol{\lambda}^\top \left(\frac{\partial \boldsymbol{K}_\mathrm{T}}{\partial \mu_e}\boldsymbol{T} + \boldsymbol{K}_\mathrm{T}\frac{\partial \boldsymbol{T}}{\partial \mu_e} \right). \tag{A.2}$$

Rewrite the above equation in vector form while using the inverse relation between the time field and nodal temperature field $\boldsymbol{t} = \mathbf{1} - \boldsymbol{G}\boldsymbol{T}$, $\boldsymbol{G}$ is a sparse transformation matrix for converting nodal values to elemental values:

$$\begin{aligned} \frac{\partial f_j}{\partial \mu_e} &= -\left(\frac{\partial f_j}{\partial \boldsymbol{t}}\right)^\top \boldsymbol{G}\frac{\partial \boldsymbol{T}}{\partial \mu_e} + \boldsymbol{\lambda}^\top \left(\frac{\partial \boldsymbol{K}_\mathrm{T}}{\partial \mu_e}\boldsymbol{T} + \boldsymbol{K}_\mathrm{T}\frac{\partial \boldsymbol{T}}{\partial \mu_e} \right) \\ &= \left(-\left(\frac{\partial f_j}{\partial \boldsymbol{t}}\right)^\top \boldsymbol{G} + \boldsymbol{\lambda}^\top \boldsymbol{K}_\mathrm{T} \right) \frac{\partial \boldsymbol{T}}{\partial \mu_e} + \boldsymbol{\lambda}^\top \frac{\partial \boldsymbol{K}_\mathrm{T}}{\partial \mu_e}\boldsymbol{T}. \end{aligned} \tag{A.3}$$

To directly calculate the derivative of the temperature field with respect to the thermal diffusivity, the Lagrangian multiplier $\boldsymbol{\lambda}$ is chosen to eliminate the first term:

$$-\left(\frac{\partial f_j}{\partial \boldsymbol{t}}\right)^\top \boldsymbol{G} + \boldsymbol{\lambda}^\top \boldsymbol{K}_\mathrm{T} = 0. \tag{A.4}$$

A

The derivative of f_j regarding to μ_e can thus be rewritten as

$$\frac{\partial f_j}{\partial \mu_e} = \boldsymbol{\lambda}^\top \frac{\partial \boldsymbol{K}_\mathrm{T}}{\partial \mu_e} \boldsymbol{T}. \tag{A.5}$$

Lagrangian multiplier $\boldsymbol{\lambda}$ In order to solve for the Lagrangian multiplier in Eq. A.4, the derivative of f_j with respect to the time field $\boldsymbol{t}$ needs to be calculated. Since f_j is the function of $\boldsymbol{\rho}^{\{j\}}$, from the chain rule:

$$\frac{\partial f_j}{\partial t_e} = \frac{\partial f_j}{\partial \bar{t}_e} \frac{\partial \bar{t}_e}{\partial t_e}. \tag{A.6}$$

where $\partial \bar{t}_e / \partial t_e$ is calculated from the Heaviside projection of Eq. 2.3. In most of the cases, f_j contains terms related to $\boldsymbol{U}^{\{j\}}$, thus another adjoint analysis is needed:

$$\begin{aligned}
\frac{\partial f_j}{\partial \bar{t}_e} &= \frac{\partial f_j}{\partial \bar{t}_e} + \boldsymbol{\gamma}^\top \frac{\partial \left(\boldsymbol{K}^{\{j\}} \boldsymbol{U}^{\{j\}} - \boldsymbol{F}^{\{j\}} \right)}{\partial \bar{t}_e} \\
&= \frac{\partial f_j}{\partial \boldsymbol{U}^{\{j\}}} \frac{\partial \boldsymbol{U}^{\{j\}}}{\partial \bar{t}_e} + \boldsymbol{\gamma}^\top \left(\frac{\partial \boldsymbol{K}^{\{j\}}}{\partial \bar{t}_e} \boldsymbol{U}^{\{j\}} + \boldsymbol{K}^{\{j\}} \frac{\partial \boldsymbol{U}^{\{j\}}}{\partial \bar{t}_e} \right) \\
&= \left(\frac{\partial f_j}{\partial \boldsymbol{U}^{\{j\}}} + \boldsymbol{\gamma}^\top \boldsymbol{K}^{\{j\}} \right) \frac{\partial \boldsymbol{U}^{\{j\}}}{\partial \bar{t}_e} + \boldsymbol{\gamma}^\top \frac{\partial \boldsymbol{K}^{\{j\}}}{\partial \bar{t}_e} \boldsymbol{U}^{\{j\}}.
\end{aligned} \tag{A.7}$$

Here $\boldsymbol{\gamma}$ is the Lagrangian multiplier related to the mechanical equilibrium equation of intermediate structure, which is solved from:

$$\frac{\partial f_j}{\partial \boldsymbol{U}^{\{j\}}} + \boldsymbol{\gamma}^\top \boldsymbol{K}^{\{j\}} = 0. \tag{A.8}$$

The equation above simply assume that there is no explicit term about $\bar{t}_e$ in f_j, and the external loads $F^{\{j\}}$ is independent on the design $\boldsymbol{\rho}^{\{j\}}$. These are not necessary true, for example, design-dependent load like self-weight can also be considered by making slight modifications on the sensitivity analysis.

Sensitivity w.r.t design variable $\boldsymbol{\phi}$ The derivative of f_j with respect to the density design variable ϕ_e can be obtained using the chain rule, which aligns with the filtering and projection procedure:

$$\frac{\partial f_j}{\partial \phi_e} = \sum_{i \in \mathbb{N}_e} \frac{\mathrm{d} f_j}{\mathrm{d} \rho_i} \frac{\partial \rho_i}{\partial \tilde{\phi}_i} \frac{\partial \tilde{\phi}_i}{\partial \phi_e}. \tag{A.9}$$

The derivative of f_j regarding the physical density ρ_e is also calculated using the adjoint method. However, it should be noted that since the objective function has multiple components that contains ρ_e implicitly. As indicated in Eq. 2.10, the time field obtained from the heat equation is also dependent on the density field. We thus divide the sensitivity of f_j into two parts. The first part is independent of the time field $\boldsymbol{t}$, while the second part is related to the time field $\boldsymbol{t}$.

$$\frac{\mathrm{d}f_j}{\mathrm{d}\rho_e} = \frac{\partial f_j}{\partial \rho_e} + \sum_{i \in \mathcal{M}} \frac{\partial f_j}{\partial t_i} \frac{\partial t_i}{\partial \rho_e}. \tag{A.10}$$

Similar to Eq. A.3, the above equation is written into an augmented form:

$$\begin{aligned} \frac{\mathrm{d}f_j}{\mathrm{d}\rho_e} &= \frac{\partial f_j}{\partial \rho_e} - \left(\frac{\partial f_j}{\partial \boldsymbol{t}}\right)^\top \boldsymbol{G} \frac{\partial \boldsymbol{T}}{\partial \rho_e} + \boldsymbol{\lambda}^\top \left(\frac{\partial \boldsymbol{K}_\mathrm{T}}{\partial \rho_e} \boldsymbol{T} + \boldsymbol{K}_\mathrm{T} \frac{\partial \boldsymbol{T}}{\partial \rho_e}\right) \\ &= \frac{\partial f_j}{\partial \rho_e} + \left(-\left(\frac{\partial f_j}{\partial \boldsymbol{t}}\right)^\top \boldsymbol{G} + \boldsymbol{\lambda}^\top \boldsymbol{K}_\mathrm{T}\right) \frac{\partial \boldsymbol{T}}{\partial \rho_e} + \boldsymbol{\lambda}^\top \frac{\partial \boldsymbol{K}_\mathrm{T}}{\partial \rho_e} \boldsymbol{T}. \end{aligned} \tag{A.11}$$

By using the same Lagrangian multiplier as solved from Eq. A.4, the above equation is simplified into

$$\frac{\mathrm{d}f_j}{\mathrm{d}\rho_e} = \frac{\partial f_j}{\partial \rho_e} + \boldsymbol{\lambda}^\top \frac{\partial \boldsymbol{K}_\mathrm{T}}{\partial \rho_e} \boldsymbol{T}. \tag{A.12}$$

The first part is directly related to ϕ_e, and can also be calculated by using adjoint analysis:

$$\begin{aligned} \frac{\partial f_j}{\partial \rho_e} &= \frac{\partial f_j}{\partial \rho_e} + \boldsymbol{\gamma}^\top \frac{\partial \left(\boldsymbol{K}^{\{j\}} \boldsymbol{U}^{\{j\}} - \boldsymbol{F}^{\{j\}}\right)}{\partial \rho_e} \\ &= \left(\frac{\partial f_j}{\partial \boldsymbol{U}^{\{j\}}} + \boldsymbol{\gamma}^\top \boldsymbol{K}^{\{j\}}\right) \frac{\partial \boldsymbol{U}^{\{j\}}}{\partial \rho_e} + \boldsymbol{\gamma}^\top \frac{\partial \boldsymbol{K}^{\{j\}}}{\partial \rho_e} \boldsymbol{U}^{\{j\}} \\ &= \boldsymbol{\gamma}^\top \frac{\partial \boldsymbol{K}^{\{j\}}}{\partial \rho_e} \boldsymbol{U}^{\{j\}}. \end{aligned} \tag{A.13}$$

Here $\boldsymbol{\gamma}$ is same the Lagrangian multiplier as in Eq. A.8.

The sensitivity analysis of these volume constraint functions g_0 and g_j is a simpler version of the analysis above, as they only have explicit parts related to their corresponding $\boldsymbol{\rho}^{\{j\}}$.

A

A.2. SENSITIVITY ANALYSIS FOR CHAPTER 3

A.2.1. SENSITIVITY ANALYSIS FOR THE OBJECTIVE FUNCTION

The objective function f_{geo} is determined by the optimization variables $\boldsymbol{\mu}$ via an intermediate field $\boldsymbol{t}$ using a heat equation. The sensitivity of the objective function in relation to the filtered thermal diffusivity $\tilde{\boldsymbol{\mu}}$ can be calculated from a chain rule:

$$\frac{\partial f_{\text{geo}}}{\partial \tilde{\mu}_i} = \frac{\partial f_{\text{geo}}}{\partial \boldsymbol{t}} \frac{\partial \boldsymbol{t}}{\partial \tilde{\mu}_i}. \tag{A.14}$$

Directly calculating the sensitivities can be computationally expensive, an adjoint method is thus adopted based on the governing heat equation Eq. 3.25:

$$\begin{aligned}\frac{\partial f_{\text{geo}}}{\partial \tilde{\mu}_i} &= \frac{\partial f_{\text{geo}}}{\partial \boldsymbol{t}} \frac{\partial \boldsymbol{t}}{\partial \tilde{\mu}_i} + \boldsymbol{\lambda}^\top \left(\frac{\partial \boldsymbol{b}}{\partial \tilde{\mu}_i} - \frac{\partial \boldsymbol{K}_{\text{T}}}{\partial \tilde{\mu}_i} \boldsymbol{T} - \boldsymbol{K}_{\text{T}} \frac{\partial \boldsymbol{T}}{\partial \tilde{\mu}_i} \right), \\ &= -\left(\frac{\partial f_{\text{geo}}}{\partial \boldsymbol{t}} + \boldsymbol{\lambda}^\top \boldsymbol{K}_{\text{T}} \right) \frac{\partial \boldsymbol{T}}{\partial \tilde{\mu}_i} - \boldsymbol{\lambda}^\top \frac{\partial \boldsymbol{K}_{\text{T}}}{\partial \tilde{\mu}_i} \boldsymbol{T},\end{aligned} \tag{A.15}$$

where λ is the vector of Lagrange multiplier. By setting the Lagrange multiplier according to the equation:

$$\frac{\partial f_{\text{geo}}}{\partial \boldsymbol{t}} + \boldsymbol{\lambda}^\top \boldsymbol{K}_{\text{T}} = \boldsymbol{0}, \tag{A.16}$$

the sensitivity of the objective function is simplified to:

$$\frac{\partial f_{\text{geo}}}{\partial \tilde{\mu}_i} = -\boldsymbol{\lambda}^\top \frac{\partial \boldsymbol{K}_{\text{T}}}{\partial \tilde{\mu}_i} \boldsymbol{T}. \tag{A.17}$$

The sensitivity in relation to the original optimization variable μ is computed using the chain rule:

$$\frac{\partial f_{\text{geo}}}{\partial \mu_e} = \sum_{i \in \mathcal{N}_e} \frac{\partial f_{\text{geo}}}{\partial \tilde{\mu}_i} \frac{\partial \tilde{\mu}_i}{\partial \mu_e}. \tag{A.18}$$

Lagrangian multiplier $\boldsymbol{\lambda}$ To solve for Lagrange multiplier $\boldsymbol{\lambda}$ in Eq. A.15, the derivative of the objective function with respect to the nodal time field is needed:

$$\begin{aligned}\frac{\partial f_{geo}}{\partial \boldsymbol{t}} &= \sum_{j=1}^{N} \frac{\partial \sum_e \eta_e^{\{j\}^\kappa} \left(|\nabla t_e| - \overline{|\nabla t|}^{\{j\}} \right)^2}{\partial \boldsymbol{t}}, \\ &= \sum_{j=1}^{N} \sum_e [\frac{\partial \eta_e^{\{j\}^\kappa}}{\partial \boldsymbol{t}} \left(|\nabla t_e| - \overline{|\nabla t|}^{\{j\}} \right)^2 + 2 \eta_e^{\{j\}^\kappa} (|\nabla t_e| - \overline{|\nabla t|}^{\{j\}}) \left(\frac{\partial |\nabla t_e|}{\partial \boldsymbol{t}} - \frac{\partial \overline{|\nabla t|}^{\{j\}}}{\partial \boldsymbol{t}} \right)].\end{aligned} \tag{A.19}$$

The derivative of the gradient average $\overline{|\nabla t|}^{\{j\}}$ with respect to the nodal time field is:

$$\frac{\partial \overline{|\nabla t|}^{\{j\}}}{\partial \boldsymbol{t}} = \frac{\frac{\partial \sum_e \eta_e^{\{j\}^\kappa} |\nabla t_e|}{\partial \boldsymbol{t}} \left(\sum_e \eta_e^{\{j\}^\kappa} \right) - \left(\sum_e \eta_e^{\{j\}^\kappa} |\nabla t_e| \right) \frac{\partial \sum_e \eta_e^{\{j\}^\kappa}}{\partial \boldsymbol{t}}}{\sum_e \eta_e^{\{j\}^{\kappa 2}}}. \tag{A.20}$$

The derivative of the magnitude of the gradient $|\nabla t_e|$ with regard to t_j is derived from Eqn. 3.8, $\partial|\nabla t_e|/\partial t_j$ is non-zero only if node j belongs to element e:

$$\frac{\partial|\nabla t_e|}{\partial t_j} = \frac{\left(\sum_{i\in e}\frac{\partial N_i}{\partial x}t_i\right)\frac{\partial N_j}{\partial x} + \left(\sum_{i\in e}\frac{\partial N_i}{\partial y}t_i\right)\frac{\partial N_j}{\partial y} + \left(\sum_{i\in e}\frac{\partial N_i}{\partial z}t_i\right)\frac{\partial N_j}{\partial z}}{\sqrt{\left(\sum_{i\in e}\frac{\partial N_i}{\partial x}t_i\right)^2 + \left(\sum_{i\in e}\frac{\partial N_i}{\partial y}t_i\right)^2 + \left(\sum_{i\in e}\frac{\partial N_i}{\partial z}t_i\right)^2}}. \tag{A.21}$$

A.2.2. SENSITIVITY ANALYSIS FOR THE CURVATURE CONTROL OBJECTIVE FUNCTION

Similarly, the derivative of the curvature control objective f_{curve} with respect to the nodal time field can be derived from Eq.3.15:

$$\begin{aligned}\frac{\partial f_{\text{curve}}}{\partial \boldsymbol{t}} &= \sum_e \frac{\partial \log\left(1+e^{-P_0\kappa_e}\right)}{\partial \boldsymbol{t}},\\ &= \sum_e \frac{-P_0 e^{-P_0\kappa_e}}{\left(1+e^{-P_0\kappa_e}\right)}\frac{\partial \kappa_e}{\partial \boldsymbol{t}}.\end{aligned} \tag{A.22}$$

The derivative of the elemental curvature κ_e with respect to the nodal time field can be derived from Eq.3.13:

$$\begin{aligned}\frac{\partial \kappa_e}{\partial \boldsymbol{t}} &= \frac{\partial \frac{\nabla t_e^\top \boldsymbol{H}_e \nabla t_e}{|\nabla t_e|^3}}{\partial \boldsymbol{t}},\\ &= \frac{|\nabla t_e|^3 \frac{\partial \nabla t_e^\top \boldsymbol{H}_e \nabla t_e}{\partial \boldsymbol{t}} - 3|\nabla t_e|^2 \nabla t_e^\top \boldsymbol{H}_e \nabla t_e \frac{\partial|\nabla t_e|}{\partial \boldsymbol{t}}}{|\nabla t_e|^6},\end{aligned} \tag{A.23}$$

among which:

$$\frac{\partial \nabla t_e^\top \boldsymbol{H}_e \nabla t_e}{\partial \boldsymbol{t}} = 2\nabla t_e^\top \boldsymbol{H}_e \frac{\partial \nabla t_e}{\partial \boldsymbol{t}} + \nabla t_e^\top \frac{\partial \boldsymbol{H}_e}{\partial \boldsymbol{t}} \nabla t_e. \tag{A.24}$$

A.2.3. SENSITIVITY ANALYSIS FOR THE CONSTRAINT FUNCTIONS

Similarly, the sensitivity of the layer geometry constraint function in relation to the filtered thermal diffusivity $\tilde{\boldsymbol{\mu}}$ can be calculated from a chain rule:

$$\frac{\partial g_j^{\text{geo}}}{\partial \tilde{\mu}_i} = \frac{\partial g_j^{\text{geo}}}{\partial \boldsymbol{t}}\frac{\partial \boldsymbol{t}}{\partial \tilde{\mu}_i}. \tag{A.25}$$

By adopting adjoint method, the sensitivity can be written as:

$$\begin{aligned}\frac{\partial g_j^{\text{geo}}}{\partial \tilde{\mu}_i} &= \frac{\partial g_j^{\text{geo}}}{\partial \boldsymbol{t}}\frac{\partial \boldsymbol{t}}{\partial \tilde{\mu}_i} + \boldsymbol{\lambda}^\top\left(\frac{\partial \boldsymbol{b}}{\partial \tilde{\mu}_i} - \frac{\partial \boldsymbol{K}_{\text{T}}}{\partial \tilde{\mu}_i}\boldsymbol{T} - \boldsymbol{K}_{\text{T}}\frac{\partial \boldsymbol{T}}{\partial \tilde{\mu}_i}\right),\\ &= -\left(\frac{\partial g_j^{\text{geo}}}{\partial \boldsymbol{t}} + \boldsymbol{\lambda}^\top \boldsymbol{K}_{\text{T}}\right)\frac{\partial \boldsymbol{T}}{\partial \tilde{\mu}_i} - \boldsymbol{\lambda}^\top \frac{\partial \boldsymbol{K}_{\text{T}}}{\partial \tilde{\mu}_i}\boldsymbol{T}.\end{aligned} \tag{A.26}$$

By setting the Lagrange multiplier according to the equation:

$$\frac{\partial g_j^{\text{geo}}}{\partial \boldsymbol{t}} + \boldsymbol{\lambda}^\top \boldsymbol{K}_\text{T} = \boldsymbol{0}, \tag{A.27}$$

the sensitivity of is simplified to:

$$\frac{\partial g_j^{\text{geo}}}{\partial \tilde{\mu}_i} = -\boldsymbol{\lambda}^\top \frac{\partial \boldsymbol{K}_\text{T}}{\partial \tilde{\mu}_i} \boldsymbol{T}. \tag{A.28}$$

Lagrangian multiplier $\boldsymbol{\lambda}$ To solve for Lagrange multiplier $\boldsymbol{\lambda}$ in Eq. A.26, the derivative of the constraint function with respect to the nodal time field is needed:

$$\frac{\partial g_j^{\text{geo}}}{\partial \boldsymbol{t}} = \frac{\partial d_j}{\partial \boldsymbol{t}} = \frac{\partial \frac{\Delta\tau}{\overline{|\nabla t|}^{\{j\}}}}{\partial \boldsymbol{t}} = -\frac{\Delta\tau}{\overline{|\nabla t|}^{\{j\}2}} \frac{\partial \overline{|\nabla t|}^{\{j\}}}{\partial \boldsymbol{t}}. \tag{A.29}$$

The derivative of the gradient average $\overline{|\nabla t|}^{\{j\}}$ with respect to the nodal time field can be found in Eq. A.20.

A.3. SENSITIVITY ANALYSIS FOR CHAPTER 4

A.3.1. SENSITIVITY ANALYSIS OF THE RESIDUAL STRESS CONSTRAINT

The residual stress constraint g_s is determined by optimization variables $\boldsymbol{\phi}$ and $\boldsymbol{\mu}$ via two intermediate fields, the density field $\boldsymbol{\rho} = \bar{\tilde{\boldsymbol{\phi}}}$, and the time field $\boldsymbol{t}$:

$$g_s\left(\boldsymbol{\phi}, \boldsymbol{\mu}\right) = g_s\left(\boldsymbol{\rho}, \boldsymbol{t}(\boldsymbol{\rho}, \boldsymbol{\mu})\right). \tag{A.30}$$

The time field depends on both the density field $\boldsymbol{\rho}$ and the thermal diffusivity field $\boldsymbol{\mu}$ by solving the heat equation.

Sensitivity w.r.t design variable $\boldsymbol{\phi}$ The design field $\boldsymbol{\phi}$ is filtered and then projected to obtain the density field $\boldsymbol{\rho}$. According to the chain rule, we have

$$\frac{\partial g_s}{\partial \phi_e} = \sum_{i \in \mathcal{N}_e} \frac{\mathrm{d}g_s}{\mathrm{d}\rho_i} \frac{\partial \bar{\tilde{\phi}}_i}{\partial \tilde{\phi}_i} \frac{\partial \tilde{\phi}_i}{\partial \phi_e}. \tag{A.31}$$

The sensitivity regarding the filtering and projection operations is routine. We focus on the derivative of the constraint function g_s with respect to the density $\boldsymbol{\rho}$.

The residual stress constraint g_s contains $\boldsymbol{\rho}$ explicitly, as well as implicitly through the time field. The density field is involved in defining the time field using a heat equation. An adjoint analysis is thus performed:

$$\begin{aligned}
\frac{\mathrm{d}g_s}{\mathrm{d}\rho_i} &= \frac{\partial g_s}{\partial \rho_i} + \frac{\partial g_s}{\partial \boldsymbol{t}} \frac{\partial \boldsymbol{t}}{\partial \rho_i} + \boldsymbol{\lambda}_{\mathrm{T}}^{\top} \left(\frac{\partial \boldsymbol{b}}{\partial \rho_i} - \frac{\partial \boldsymbol{K}_{\mathrm{T}}}{\partial \rho_i} \boldsymbol{T} - \boldsymbol{K}_{\mathrm{T}} \frac{\partial \boldsymbol{T}}{\partial \rho_i} \right), \\
&= \frac{\partial g_s}{\partial \rho_i} - \frac{\partial g_s}{\partial \boldsymbol{t}} \frac{\partial \boldsymbol{T}}{\partial \rho_i} + \boldsymbol{\lambda}_{\mathrm{T}}^{\top} \left(-\frac{\partial \boldsymbol{K}_{\mathrm{T}}}{\partial \rho_i} \boldsymbol{T} - \boldsymbol{K}_{\mathrm{T}} \frac{\partial \boldsymbol{T}}{\partial \rho_i} \right), \\
&= \frac{\partial g_s}{\partial \rho_i} - \left(\frac{\partial g_s}{\partial \boldsymbol{t}} + \boldsymbol{\lambda}_{\mathrm{T}}^{\top} \boldsymbol{K}_{\mathrm{T}} \right) \frac{\partial \boldsymbol{T}}{\partial \rho_i} - \boldsymbol{\lambda}_{\mathrm{T}}^{\top} \frac{\partial \boldsymbol{K}_{\mathrm{T}}}{\partial \rho_i} \boldsymbol{T}.
\end{aligned} \tag{A.32}$$

The Lagrange multiplier $\boldsymbol{\lambda}_{\mathrm{T}}$ is solved from

$$\frac{\partial g_s}{\partial \boldsymbol{t}} + \boldsymbol{\lambda}_{\mathrm{T}}^{\top} \boldsymbol{K}_{\mathrm{T}} = \boldsymbol{0}. \tag{A.33}$$

The calculation of $\frac{\partial g_s}{\partial \boldsymbol{t}}$ will be presented shortly. With that, the sensitivity of the constraint function is simplified into

$$\frac{\mathrm{d}g_s}{\mathrm{d}\rho_i} = \frac{\partial g_s}{\partial \rho_i} - \boldsymbol{\lambda}_{\mathrm{T}}^{\top} \frac{\partial \boldsymbol{K}_{\mathrm{T}}}{\partial \rho_i} \boldsymbol{T}. \tag{A.34}$$

The residual stress contains the accumulation of $\Delta \boldsymbol{U}^{\{j\}}$, which is solved from the linear equation of each intermediate structure as in Eq. 4.21. A set of adjoint analyses is needed accordingly for the calculation of $\frac{\partial g_s}{\partial \rho_i}$:

$$g_s = g_s + \sum_j \boldsymbol{\lambda}^{\{j\}} \left(\boldsymbol{K}^{\{j\}} \Delta \boldsymbol{U}^{\{j\}} - \boldsymbol{F}^{\{j\}} \right). \tag{A.35}$$

A

Its derivative with respect to the density of the i-th element ρ_i is:

$$\frac{\partial g_s}{\partial \rho_i} = \frac{\partial g_s}{\partial \rho_i} + \sum_j \boldsymbol{\lambda}^{\{j\}} \left(\frac{\partial \boldsymbol{K}^{\{j\}}}{\partial \rho_i} \Delta \boldsymbol{U}^{\{j\}} + \boldsymbol{K}^{\{j\}} \frac{\partial \Delta \boldsymbol{U}^{\{j\}}}{\partial \rho_i} - \frac{\partial \boldsymbol{F}^{\{j\}}}{\partial \rho_i} \right). \tag{A.36}$$

Substituting g_s using Eq. 4.24 gives

$$\frac{\partial g_s}{\partial \rho_i} = A^I \left(\sum_e \hat{\sigma}_{\mathrm{vM},e}^P \right)^{\frac{1-P}{P}} \left(\sum_e \hat{\sigma}_{\mathrm{vM},e}^{P-1} \frac{\partial \hat{\sigma}_{\mathrm{vM},e}}{\partial \rho_i} \right), \tag{A.37}$$

where $\frac{\partial \hat{\sigma}_{\mathrm{vM},e}}{\partial \rho_i}$ is derived according to Eq. 4.15

$$\frac{\partial \hat{\sigma}_{\mathrm{vM},e}}{\partial \rho_i} = \frac{\hat{\boldsymbol{\sigma}}_e^{\mathrm{T}} \boldsymbol{V} \frac{\partial \hat{\boldsymbol{\sigma}}_e}{\partial \rho_i}}{\hat{\sigma}_{\mathrm{vM},e}}. \tag{A.38}$$

Here the relaxed stress $\hat{\boldsymbol{\sigma}}_e$ is calculated according to Eq. 4.13, and thus

$$\frac{\partial \hat{\boldsymbol{\sigma}}_e}{\partial \rho_i} = \frac{\partial \boldsymbol{\sigma}_e}{\partial \rho_i} \rho_e{}^q + \frac{\partial \rho_e^q}{\partial \rho_i} \boldsymbol{\sigma}_e. \tag{A.39}$$

The next key step is to calculate the derivative of the stress $\boldsymbol{\sigma}_e$ with respect to the density ρ_i, according to Eq.4.12 and Eq.4.7,

$$\begin{aligned} \frac{\partial \boldsymbol{\sigma}_e}{\partial \rho_i} &= \sum_j \frac{\partial \Delta \boldsymbol{\sigma}_e{}^{\{j\}}}{\partial \rho_i} \\ &= \sum_j \left(\boldsymbol{D}\boldsymbol{B} \frac{\partial \Delta \boldsymbol{U}_e^{\{j\}}}{\partial \rho_i} R_E(\rho_e^{\{j\}}) + \boldsymbol{D}\boldsymbol{B} \Delta \boldsymbol{U}_e^{\{j\}} \frac{\partial R_E(\boldsymbol{\rho}^{\{j\}})}{\partial \rho_i} - \boldsymbol{D}\boldsymbol{\varepsilon}^* \frac{\partial R_B(\eta_e^{\{j\}})}{\partial \rho_i} \right). \end{aligned} \tag{A.40}$$

By summarizing the above equations, Eq. A.36 can be rewritten:

$$\begin{aligned} \frac{\partial g_s}{\partial \rho_i} = & A^I \left(\sum_e \hat{\sigma}_{\mathrm{vM},e}^P \right)^{\frac{1-P}{P}} \sum_e \left[\hat{\boldsymbol{\sigma}}_{\mathrm{vM,e}}^{P-2} \cdot \left(\hat{\boldsymbol{\sigma}}_{\boldsymbol{e}}^{\mathrm{T}} \boldsymbol{V}\boldsymbol{D} \sum_j \left(\boldsymbol{B} \frac{\partial \Delta \boldsymbol{U}_e^{\{j\}}}{\partial \rho_i} R_E(\rho_e^{\{j\}}) + \boldsymbol{B} \Delta \boldsymbol{U}_e^{\{j\}} \frac{\partial R_E(\rho_e^{\{j\}})}{\partial \rho_i} \right. \right. \right. \\ & \left. \left. \left. - \boldsymbol{\varepsilon}^* \frac{\partial R_B(\eta_e^{\{j\}})}{\partial \rho_i} \right) \rho_e^q + \hat{\boldsymbol{\sigma}}_{\boldsymbol{e}}^{\mathrm{T}} \boldsymbol{V} \boldsymbol{\sigma}_e \frac{\partial \boldsymbol{\rho}_e^q}{\partial \rho_i} \right) \right] + \sum_j \boldsymbol{\lambda}^{\{j\}} \left(\frac{\partial \boldsymbol{K}^{\{j\}}}{\partial \rho_i} \Delta \boldsymbol{U}^{\{j\}} + \boldsymbol{K}^{\{j\}} \frac{\partial \Delta \boldsymbol{U}^{\{j\}}}{\partial \rho_i} - \frac{\partial \boldsymbol{F}^{\{j\}}}{\partial \rho_i} \right), \end{aligned} \tag{A.41}$$

$$\begin{aligned} = & A^I \left(\sum_e \hat{\sigma}_{\mathrm{vM},e}^P \right)^{\frac{1-P}{P}} \sum_j \sum_e \left[\hat{\boldsymbol{\sigma}}_{\mathrm{vM,e}}^{P-2} \rho_e^q \cdot \hat{\boldsymbol{\sigma}}_{\boldsymbol{e}}^{\mathrm{T}} \boldsymbol{V}\boldsymbol{D} \left(\boldsymbol{B} \frac{\partial \Delta \boldsymbol{U}_e^{\{j\}}}{\partial \rho_i} R_E(\rho_e^{\{j\}}) + \boldsymbol{B} \Delta \boldsymbol{U}_e^{\{j\}} \frac{\partial R_E(\rho_e^{\{j\}})}{\partial \rho_i} \right. \right. \\ & \left. \left. - \boldsymbol{\varepsilon}^* \frac{\partial R_B(\eta_e^{\{j\}})}{\partial \rho_i} \right) \right] + A^I \left(\sum_e \hat{\sigma}_{\mathrm{vM},e}^P \right)^{\frac{1-P}{P}} \sum_e \left(\hat{\boldsymbol{\sigma}}_{\mathrm{vM,e}}^{P-2} \hat{\boldsymbol{\sigma}}_{\boldsymbol{e}}^{\mathrm{T}} \boldsymbol{V} \boldsymbol{\sigma}_e \frac{\partial \boldsymbol{\rho}_e^q}{\partial \rho_i} \right) \\ & + \sum_j \boldsymbol{\lambda}^{\{j\}} \left(\frac{\partial \boldsymbol{K}^{\{j\}}}{\partial \rho_i} \Delta \boldsymbol{U}^{\{j\}} + \boldsymbol{K}^{\{j\}} \frac{\partial \Delta \boldsymbol{U}^{\{j\}}}{\partial \rho_i} - \frac{\partial \boldsymbol{F}^{\{j\}}}{\partial \rho_i} \right). \end{aligned} \tag{A.42}$$

There are N Lagrangian equations to be solved in total:

$$A^I\left(\sum_e \hat{\sigma}^P_{\mathrm{vM},e}\right)^{\frac{1-P}{P}}\left(\sum_e \hat{\boldsymbol{\sigma}}^{P-2}_{\mathrm{vM,e}}\rho_e^q R_E(\rho_e^{\{j\}})\cdot\hat{\boldsymbol{\sigma}}_{\boldsymbol{e}}^{\mathrm{T}}\boldsymbol{V}\boldsymbol{D}\boldsymbol{B}\right)+\boldsymbol{\lambda}^{\{j\}}\boldsymbol{K}^{\{j\}}=0. \tag{A.43}$$

After calculating the Lagrangian multipliers $\boldsymbol{\lambda}^{\{j\}}$, Eq. A.36 is further simplified,

$$\frac{\partial g_s}{\partial \rho_i}=A^I\left(\sum_e \hat{\sigma}^P_{\mathrm{vM},e}\right)^{\frac{1-P}{P}}\sum_j\sum_e\left[\hat{\boldsymbol{\sigma}}^{P-2}_{\mathrm{vM,e}}\rho_e^q\cdot\hat{\boldsymbol{\sigma}}_{\boldsymbol{e}}^{\mathrm{T}}\boldsymbol{V}\boldsymbol{D}\left(\boldsymbol{B}\Delta\boldsymbol{U}_e^{\{j\}}\frac{\partial R_E(\rho_e^{\{j\}})}{\partial\rho_i}-\boldsymbol{\varepsilon}^*\frac{\partial R_B(\eta_e^{\{j\}})}{\partial\rho_i}\right)\right] \tag{A.44}$$

$$+A^I\left(\sum_e \hat{\sigma}^P_{\mathrm{vM},e}\right)^{\frac{1-P}{P}}\sum_e\left(\hat{\boldsymbol{\sigma}}^{P-2}_{\mathrm{vM,e}}\hat{\boldsymbol{\sigma}}_{\boldsymbol{e}}^{\mathrm{T}}\boldsymbol{V}\boldsymbol{\sigma}_e\frac{\partial\boldsymbol{\rho}_e^q}{\partial\rho_i}\right)+\sum_j\boldsymbol{\lambda}^{\{j\}}\left(\frac{\partial\boldsymbol{K}^{\{j\}}}{\partial\rho_i}\Delta\boldsymbol{U}^{\{j\}}-\frac{\partial\boldsymbol{F}^{\{j\}}}{\partial\rho_i}\right). \tag{A.45}$$

Sensitivity w.r.t design variable $\boldsymbol{\mu}$ The sensitivity analysis of the pseudo heat diffusivity variable $\boldsymbol{\mu}$ is similar to that of the density field. An adjoint analysis is also needed for the heat equation,

$$\begin{aligned}\frac{\partial g_s}{\partial\mu_i}&=\frac{\partial g_s}{\partial\boldsymbol{t}}\frac{\partial\boldsymbol{t}}{\partial\mu_i}+\boldsymbol{\lambda}_{\mathrm{T}}^{\top}\left(\frac{\partial\boldsymbol{b}}{\partial\mu_i}-\frac{\partial\boldsymbol{K}_{\mathrm{T}}}{\partial\mu_i}\boldsymbol{T}-\boldsymbol{K}_{\mathrm{T}}\frac{\partial\boldsymbol{T}}{\partial\mu_i}\right),\\&=\left(\frac{\partial g_s}{\partial\boldsymbol{t}}+\boldsymbol{\lambda}_{\mathrm{T}}^{\top}\boldsymbol{K}_{\mathrm{T}}\right)\frac{\partial\boldsymbol{T}}{\partial\mu_i}-\boldsymbol{\lambda}_{\mathrm{T}}^{\top}\frac{\partial\boldsymbol{K}_{\mathrm{T}}}{\partial\mu_i}\boldsymbol{T}.\end{aligned} \tag{A.46}$$

The Lagrangian multiplier $\boldsymbol{\lambda}_{\mathrm{T}}$ is the same as that in Eq. A.32.

Lagrangian multiplier $\boldsymbol{\lambda}$ In order to solve for the Lagrangian multiplier $\boldsymbol{\lambda}_{\mathrm{T}}$ in Eq. A.32 and Eq. A.46. The derivative of the residual stress constraint with respect to the time field is needed. By substituting g_s using Eq. 4.24, we get

$$\frac{\partial g_s}{\partial t_i}=A^I\left(\sum_e \hat{\sigma}^P_{\mathrm{vM},e}\right)^{\frac{1-P}{P}}\sum_e\left[\hat{\sigma}^{P-2}_{\mathrm{vM},e}\cdot\hat{\boldsymbol{\sigma}}_e^{\mathrm{T}}\boldsymbol{V}\frac{\partial\boldsymbol{\sigma}_e}{\partial t_i}\rho_e{}^q\right], \tag{A.47}$$

$\frac{\partial\boldsymbol{\sigma}_e}{\partial t_i}$ is obtained according to Eq.4.12 and Eq.4.7,

$$\frac{\partial\boldsymbol{\sigma}_e}{\partial t_i}=\sum_j\left(\boldsymbol{D}\boldsymbol{B}\frac{\partial\Delta\boldsymbol{U}_e^{\{j\}}}{\partial t_i}R_E(\rho_e^{\{j\}})+\boldsymbol{D}\boldsymbol{B}\Delta\boldsymbol{U}_e^{\{j\}}\frac{\partial R_E(\boldsymbol{\rho}^{\{j\}})}{\partial t_i}-\boldsymbol{D}\boldsymbol{\varepsilon}^*\frac{\partial R_B(\eta_e^{\{j\}})}{\partial t_i}\right). \tag{A.48}$$

The sensitivity of the time field can also be rewritten in an augmented form:

$$\begin{aligned}\frac{\partial g_s}{\partial t_i}=&A^I\left(\sum_e \hat{\sigma}^P_{\mathrm{vM},e}\right)^{\frac{1-P}{P}}\sum_j\sum_e\left[\hat{\boldsymbol{\sigma}}^{P-2}_{\mathrm{vM,e}}\rho_e^q\cdot\hat{\boldsymbol{\sigma}}_{\boldsymbol{e}}^{\mathrm{T}}\boldsymbol{V}\boldsymbol{D}\left(\boldsymbol{B}\frac{\partial\Delta\boldsymbol{U}_e^{\{j\}}}{\partial t_i}R_E(\rho_e^{\{j\}})+\boldsymbol{B}\Delta\boldsymbol{U}_e^{\{j\}}\frac{\partial R_E(\rho_e^{\{j\}})}{\partial t_i}\right.\right.\\&\left.\left.-\boldsymbol{\varepsilon}^*\frac{\partial R_B(\eta_e^{\{j\}})}{\partial t_i}\right)\right]+\sum_j\boldsymbol{\lambda}^{\{j\}}\left(\frac{\partial\boldsymbol{K}^{\{j\}}}{\partial t_i}\Delta\boldsymbol{U}^{\{j\}}+\boldsymbol{K}^{\{j\}}\frac{\partial\Delta\boldsymbol{U}^{\{j\}}}{\partial t_i}-\frac{\partial\boldsymbol{F}^{\{j\}}}{\partial t_i}\right).\end{aligned} \tag{A.49}$$

A

Therefore, by using the same Lagrangian multipliers as in Eq. A.43, the above equation is simplified,

$$\frac{\partial g_s}{\partial t_i} = A^I \left(\sum_e \hat{\sigma}_{\mathrm{vM},e}^P\right)^{\frac{1-P}{P}} \sum_j \sum_e \left[\hat{\boldsymbol{\sigma}}_{\mathrm{vM,e}}^{P-2} \rho_e^q \cdot \hat{\boldsymbol{\sigma}}_{\boldsymbol{e}}^{\mathrm{T}} \boldsymbol{V}\boldsymbol{D}\left(\boldsymbol{B}\Delta\boldsymbol{U}_e^{\{j\}} \frac{\partial R_E(\rho_e^{\{j\}})}{\partial t_i} - \boldsymbol{\varepsilon}^* \frac{\partial R_B(\eta_e^{\{j\}})}{\partial t_i}\right)\right] + \sum_j \boldsymbol{\lambda}^{\{j\}} \left(\frac{\partial \boldsymbol{K}^{\{j\}}}{\partial t_i}\Delta\boldsymbol{U}^{\{j\}} - \frac{\partial \boldsymbol{F}^{\{j\}}}{\partial t_i}\right). \tag{A.50}$$

A.3.2. SENSITIVITY ANALYSIS OF THE OBJECTIVE FUNCTION

The objective function consists of two parts: the thermally induced distortion c_{thermal}, and variations in the layer geometry f_{geo}. The sensitivity analysis of the first part can be found in [170]. We here focus on the second part. Similar to the stress constraint, f_{geo} is also related to optimization variables $\boldsymbol{\phi}$ and $\boldsymbol{\mu}$ via the density field $\boldsymbol{\rho} = \bar{\tilde{\boldsymbol{\phi}}}$, and the time field $\boldsymbol{t}$.

Sensitivity w.r.t density $\boldsymbol{\rho}$ The sensitivity of f_{geo} in relation to density is

$$\begin{aligned}\frac{\mathrm{d}f_{\mathrm{geo}}}{\mathrm{d}\rho_i} &= \frac{\partial f_{\mathrm{geo}}}{\partial \rho_i} + \frac{\partial f_{\mathrm{geo}}}{\partial \boldsymbol{t}}\frac{\partial \boldsymbol{t}}{\partial \rho_i} + \boldsymbol{\lambda}^\top\left(\frac{\partial \boldsymbol{b}}{\partial \rho_i} - \frac{\partial \boldsymbol{K}_{\mathrm{T}}}{\partial \rho_i}\boldsymbol{T} - \boldsymbol{K}_{\mathrm{T}}\frac{\partial \boldsymbol{T}}{\partial \rho_i}\right), \\ &= \frac{\partial f_{\mathrm{geo}}}{\partial \rho_i} - \left(\frac{\partial f_{\mathrm{geo}}}{\partial \boldsymbol{t}} + \boldsymbol{\lambda}^\top \boldsymbol{K}_{\mathrm{T}}\right)\frac{\partial \boldsymbol{T}}{\partial \rho_i} - \boldsymbol{\lambda}^\top \frac{\partial \boldsymbol{K}_{\mathrm{T}}}{\partial \rho_i}\boldsymbol{T}.\end{aligned} \tag{A.51}$$

The calculation of the sensitivity of the objective function f_{geo} is also divided into two parts. The first part f_{geo} is explicitly related to the density field by treating the time field $\boldsymbol{t}$ as constant, while the second part f_{geo} is related to the density field through the time field. The mathematical formulations of f_{geo} and f_{geo} are the same as f_{geo}. With the formulation of f_{geo} in Eq. 4.27, the first part of the above equation is calculated as

$$\begin{aligned}\frac{\partial f_{\mathrm{geo}}}{\partial \rho_i} &= \sum_{j=1}^{N} \frac{\partial \sum_e \eta_e^{\{j\}p}\left(|\nabla t_e| - \overline{|\nabla t|}^{\{j\}}\right)^2}{\partial \rho_i}, \\ &= \sum_{j=1}^{N}\sum_e \left[\frac{\partial \eta_e^{\{j\}p}}{\partial \rho_i}\left(|\nabla t_e| - \overline{|\nabla t|}^{\{j\}}\right)^2 + 2\eta_e^{\{j\}p}\left(|\nabla t_e| - \overline{|\nabla t|}^{\{j\}}\right)\frac{\partial \overline{|\nabla t|}^{\{j\}}}{\partial \rho_i}\right].\end{aligned} \tag{A.52}$$

The derivative of the gradient average $\overline{|\nabla t|}^{\{j\}}$ with respect to the density ρ_i is derived from Eq. 4.28:

$$\frac{\partial \overline{|\nabla t|}^{\{j\}}}{\partial \rho_i} = \frac{\frac{\partial \sum_e \eta_e^{\{j\}p}|\nabla t_e|}{\partial \rho_i}\left(\sum_e \eta_e^{\{j\}p}\right) - \left(\sum_e \eta_e^{\{j\}p}|\nabla t_e|\right)\frac{\partial \sum_e \eta_e^{\{j\}p}}{\partial \rho_i}}{\sum_e \eta_e^{\{j\}p2}}. \tag{A.53}$$

Sensitivity w.r.t design variable $\boldsymbol{\mu}$ The sensitivity of f_{geo} in relation to the filtered thermal diffusivity $\boldsymbol{\mu}$ is calculated by using the adjoint analysis as well:

$$\begin{aligned}\frac{\partial f_{\text{geo}}}{\partial \mu_i} &= \frac{\partial f_{\text{geo}}}{\partial \boldsymbol{t}}\frac{\partial \boldsymbol{t}}{\partial \mu_i} + \boldsymbol{\lambda}^{\top}\left(\frac{\partial \boldsymbol{b}}{\partial \mu_i} - \frac{\partial \boldsymbol{K}_{\text{T}}}{\partial \mu_i}\boldsymbol{T} - \boldsymbol{K}_{\text{T}}\frac{\partial \boldsymbol{T}}{\partial \mu_i}\right),\\ &= -\left(\frac{\partial f_{\text{geo}}}{\partial \boldsymbol{t}} + \boldsymbol{\lambda}^{\top}\boldsymbol{K}_{\text{T}}\right)\frac{\partial \boldsymbol{T}}{\partial \mu_i} - \boldsymbol{\lambda}^{\top}\frac{\partial \boldsymbol{K}_{\text{T}}}{\partial \mu_i}\boldsymbol{T}.\end{aligned} \tag{A.54}$$

Lagrangian multiplier $\boldsymbol{\lambda}$ To solve for the Lagrange multiplier $\boldsymbol{\lambda}$, the derivative of f_{geo} with respect to the nodal time field is needed,

$$\begin{aligned}\frac{\partial f_{\text{geo}}}{\partial \boldsymbol{t}} &= \sum_{j=1}^{N}\frac{\partial \sum_e \eta_e^{\{j\}p}\left(|\nabla t_e| - \overline{|\nabla t|}^{\{j\}}\right)^2}{\partial \boldsymbol{t}},\\ &= \sum_{j=1}^{N}\sum_e [\frac{\partial \eta_e^{\{j\}p}}{\partial \boldsymbol{t}}\left(|\nabla t_e| - \overline{|\nabla t|}^{\{j\}}\right)^2 + 2\eta_e^{\{j\}p}(|\nabla t_e| - \overline{|\nabla t|}^{\{j\}})\left(\frac{\partial |\nabla t_e|}{\partial \boldsymbol{t}} - \frac{\partial \overline{|\nabla t|}^{\{j\}}}{\partial \boldsymbol{t}}\right)].\end{aligned} \tag{A.55}$$

Here the derivative of the gradient average $\overline{|\nabla t|}^{\{j\}}$ with respect to the nodal time field is given by

$$\frac{\partial \overline{|\nabla t|}^{\{j\}}}{\partial \boldsymbol{t}} = \frac{\frac{\partial \sum_e \eta_e^{\{j\}p}|\nabla t_e|}{\partial \boldsymbol{t}}\left(\sum_e \eta_e^{\{j\}p}\right) - \left(\sum_e \eta_e^{\{j\}p}|\nabla t_e|\right)\frac{\partial \sum_e \eta_e^{\{j\}p}}{\partial \boldsymbol{t}}}{\sum_e \eta_e^{\{j\}p2}}. \tag{A.56}$$

A

A.4. SENSITIVITY ANALYSIS FOR CHAPTER 5

We here focus on the sensitivity of the objective function related to the material anisotropy. The objective function is determined by optimization variables $\boldsymbol{\phi}$ and $\boldsymbol{\mu}$ via two intermediate fields, the density field $\boldsymbol{\rho} = \tilde{\bar{\boldsymbol{\phi}}}$, and the time field $\boldsymbol{t}$. The time field, according to Eq. 5.11, is determined by both the density field $\boldsymbol{\rho}$ and the thermal diffusivity field $\tilde{\boldsymbol{\mu}}$. Re-writing the objective function by

$$_0(\boldsymbol{\rho}, \tilde{\boldsymbol{\mu}}) = f_0(\boldsymbol{\rho}, \boldsymbol{t}(\boldsymbol{\rho}, \tilde{\boldsymbol{\mu}})), \tag{A.57}$$

the sensitivity of the objective function with respect to $\boldsymbol{\rho}$ and $\tilde{\boldsymbol{\mu}}$ are, respectively,

$$\frac{\partial_0}{\partial \rho_e} = \frac{\partial f_0}{\partial \rho_e} + \frac{\partial f_0}{\partial \boldsymbol{t}} \frac{\partial \boldsymbol{t}}{\partial \rho_e}, \tag{A.58}$$

and

$$\frac{\partial_0}{\partial \tilde{\mu}_e} = \frac{\partial f_0}{\partial \boldsymbol{t}} \frac{\partial \boldsymbol{t}}{\partial \tilde{\mu}_e}. \tag{A.59}$$

Sensitivity w.r.t design variable $\boldsymbol{\phi}$ The augmented form of the objective function is written as:

$$_0 = f_0 + \boldsymbol{\lambda}^\top (\boldsymbol{b} - \boldsymbol{K}_\mathrm{T} \boldsymbol{T}), \tag{A.60}$$

where λ is the vector of Lagrange multipliers. The sensitivity of the objective function in relation to the density is:

$$\begin{aligned}
\frac{\partial_0}{\partial \rho_e} &= \frac{\partial f_0}{\partial \rho_e} + \frac{\partial f_0}{\partial \boldsymbol{t}} \frac{\partial \boldsymbol{t}}{\partial \rho_e} + \boldsymbol{\lambda}^\top \left(\frac{\partial \boldsymbol{b}}{\partial \rho_e} - \frac{\partial \boldsymbol{K}_\mathrm{T}}{\partial \rho_e} \boldsymbol{T} - \boldsymbol{K}_\mathrm{T} \frac{\partial \boldsymbol{T}}{\partial \rho_e} \right), \\
&= \frac{\partial f_0}{\partial \rho_e} - \frac{\partial f_0}{\partial \boldsymbol{t}} \frac{\partial \boldsymbol{T}}{\partial \rho_e} + \boldsymbol{\lambda}^\top \left(- \frac{\partial \boldsymbol{K}_\mathrm{T}}{\partial \rho_e} \boldsymbol{T} - \boldsymbol{K}_\mathrm{T} \frac{\partial \boldsymbol{T}}{\partial \rho_e} \right), \\
&= \frac{\partial f_0}{\partial \rho_e} - \left(\frac{\partial f_0}{\partial \boldsymbol{t}} + \boldsymbol{\lambda}^\top \boldsymbol{K}_\mathrm{T} \right) \frac{\partial \boldsymbol{T}}{\partial \rho_e} - \boldsymbol{\lambda}^\top \frac{\partial \boldsymbol{K}_\mathrm{T}}{\partial \rho_e} \boldsymbol{T}.
\end{aligned} \tag{A.61}$$

By setting the Lagrange multiplier according to the equation:

$$\frac{\partial f_0}{\partial \boldsymbol{t}} + \boldsymbol{\lambda}^\top \boldsymbol{K}_\mathrm{T} = \boldsymbol{0}, \tag{A.62}$$

the sensitivity of the objective function is simplified to

$$\frac{\partial_0}{\partial \rho_e} = \frac{\partial f_0}{\partial \rho_e} - \boldsymbol{\lambda}^\top \frac{\partial \boldsymbol{K}_\mathrm{T}}{\partial \rho_e} \boldsymbol{T}. \tag{A.63}$$

Substantiating the objective function, $f_0 = c_0 + \sum_{j=1}^{N} w_j c_j$, the first part of the above equation is calculated as

$$\frac{\partial f_0}{\partial \rho_e} = \frac{\partial c_0}{\partial \rho_e} + \sum_{j=1}^{N} w_j \frac{\partial c_j}{\partial \rho_e}, \tag{A.64}$$

where the adjoint method should again be used, resulting in

$$\frac{\partial c_0}{\partial \rho_e} = \frac{\partial \boldsymbol{U}^\top \boldsymbol{K} \boldsymbol{U}}{\partial \rho_e} = -\boldsymbol{U}^\top \frac{\partial \boldsymbol{K}}{\partial \rho_e} \boldsymbol{U}, \tag{A.65}$$

and

$$\begin{aligned} \frac{\partial c_j}{\partial \rho_e} &= \frac{\partial \left(\boldsymbol{U}^{\{j\}}\right)^\top \boldsymbol{K}^{\{j\}} \boldsymbol{U}^{\{j\}}}{\partial \rho_e}, \\ &= 2\left(\boldsymbol{U}^{\{j\}}\right)^\top \frac{\partial \boldsymbol{G}^{\{j\}}}{\partial \rho_e} - \left(\boldsymbol{U}^{\{j\}}\right)^\top \frac{\partial \boldsymbol{K}^{\{j\}}}{\partial \rho_e} \boldsymbol{U}^{\{j\}}. \end{aligned} \tag{A.66}$$

Here the external load on intermediate structures $\boldsymbol{G}^{\{j\}}$ can be design dependent, e.g., self-weight.

Lastly, by using the chain rule, the sensitivity of the objective function in relation to the optimization variable ϕ can be computed using:

$$\frac{\partial_0}{\partial \phi_e} = \sum_{i \in \mathcal{N}_e} \frac{\partial_0}{\partial \rho_i} \frac{\partial \rho_i}{\partial \tilde{\phi}_i} \frac{\partial \tilde{\phi}_i}{\partial \phi_e}. \tag{A.67}$$

Sensitivity w.r.t design variable $\boldsymbol{\mu}$ The sensitivity of the objective function in relation to the thermal diffusivity $\tilde{\boldsymbol{\mu}}$ is calculated by using the adjoint method as well:

$$\begin{aligned} \frac{\partial_0}{\partial \tilde{\mu}_e} &= \frac{\partial f_0}{\partial \boldsymbol{t}} \frac{\partial \boldsymbol{t}}{\partial \tilde{\mu}_e} + \boldsymbol{\lambda}^\top \left(\frac{\partial \boldsymbol{b}}{\partial \tilde{\mu}_e} - \frac{\partial \boldsymbol{K}_\mathrm{T}}{\partial \tilde{\mu}_e} \boldsymbol{T} - \boldsymbol{K}_\mathrm{T} \frac{\partial \boldsymbol{T}}{\partial \tilde{\mu}_e} \right), \\ &= -\left(\frac{\partial f_0}{\partial \boldsymbol{t}} + \boldsymbol{\lambda}^\top \boldsymbol{K}_\mathrm{T} \right) \frac{\partial \boldsymbol{T}}{\partial \tilde{\mu}_e} - \boldsymbol{\lambda}^\top \frac{\partial \boldsymbol{K}_\mathrm{T}}{\partial \tilde{\mu}_e} \boldsymbol{T}. \end{aligned} \tag{A.68}$$

The sensitivity in relation to the original optimization variable μ is computed using the chain rule:

$$\frac{\partial_0}{\partial \mu_e} = \sum_{i \in \mathcal{N}_e} \frac{\partial f_0}{\partial \tilde{\mu}_i} \frac{\partial \tilde{\mu}_i}{\partial \mu_e}. \tag{A.69}$$

Lagrangian multiplier $\boldsymbol{\lambda}$ Eq. A.61 and Eq. A.68 have the same Lagrange multiplier $\boldsymbol{\lambda}$. To solve for $\boldsymbol{\lambda}$, we need the derivative of the objective function with regard to the nodal time field:

$$\frac{\partial f_0}{\partial t_i} = \frac{\partial c_0}{\partial t_i} + \sum_{j=1}^{N} w_j \frac{\partial c_j}{\partial t_i}. \tag{A.70}$$

Again by using the adjoint method we obtain:

$$\frac{\partial c_0}{\partial t_i} = \frac{\partial \boldsymbol{U}^\top \boldsymbol{K} \boldsymbol{U}}{\partial t_i} = \boldsymbol{U}^\top \frac{\partial \boldsymbol{K}}{\partial t_i} \boldsymbol{U} = \sum_e \boldsymbol{U}_e^\top \frac{\partial \boldsymbol{K}_e}{\partial t_i} \boldsymbol{U}_e, \tag{A.71}$$

$$\begin{aligned} \frac{\partial c_j}{\partial t_i} &= \frac{\partial \left(\boldsymbol{U}^{\{j\}}\right)^\top \boldsymbol{K}^{\{j\}} \boldsymbol{U}^{\{j\}}}{\partial t_i}, \\ &= 2\left(\boldsymbol{U}^{\{j\}}\right)^\top \frac{\partial \boldsymbol{G}^{\{j\}}}{\partial t_i} - \sum_e \left(\boldsymbol{U}_e^{\{j\}}\right)^\top \frac{\partial \boldsymbol{K}_e^{\{j\}}}{\partial t_i} \boldsymbol{U}_e^{\{j\}}. \end{aligned} \tag{A.72}$$

A

The derivative of the stiffness matrices in relation to t_i is obtained using Eq. 5.9:

$$\begin{aligned}\frac{\partial \boldsymbol{K}_e}{\partial t_i} = &\left[\varepsilon + (1-\varepsilon)\rho_e^p\right] \int_{\Omega_e} \left[\boldsymbol{B}^\top \frac{\partial \boldsymbol{R}^\top(\theta_e)}{\partial t_i} \boldsymbol{D}_0 \boldsymbol{R}(\theta_e)\, \boldsymbol{B} \right. \\ &\left. + \boldsymbol{B}^\top \boldsymbol{R}^\top(\theta_e)\, \boldsymbol{D}_0 \frac{\partial \boldsymbol{R}(\theta_e)}{\partial t_i} \boldsymbol{B} \right] d\Omega_e,\end{aligned} \tag{A.73}$$

$$\begin{aligned}\frac{\partial \boldsymbol{K}_e^{\{j\}}}{\partial t_i} = &(1-\varepsilon) \frac{\partial \left(\rho_e^{\{j\}}\right)^p}{\partial t_i} \int_{\Omega_e} \boldsymbol{B}^\top \boldsymbol{R}^\top(\theta_e)\, \boldsymbol{D}_0 \boldsymbol{R}(\theta_e)\, \boldsymbol{B}\, d\Omega_e \\ &+ \left[\varepsilon + (1-\varepsilon)\left(\rho_e^{\{j\}}\right)^p\right] \int_{\Omega_e} \left[\boldsymbol{B}^\top \frac{\partial \boldsymbol{R}^\top(\theta_e)}{\partial t_i} \boldsymbol{D}_0 \boldsymbol{R}(\theta_e)\, \boldsymbol{B} \right. \\ &\left. + \boldsymbol{B}^\top \boldsymbol{R}^\top(\theta_e)\, \boldsymbol{D}_0 \frac{\partial \boldsymbol{R}(\theta_e)}{\partial t_i} \boldsymbol{B} \right] d\Omega_e.\end{aligned} \tag{A.74}$$

The derivative of the rotation matrix $\boldsymbol{R}(\theta_e)$ with regard to t_i is calculated using the chain rule:

$$\frac{\partial \boldsymbol{R}(\theta_e)}{\partial t_i} = \frac{\partial \boldsymbol{R}(\theta_e)}{\partial \theta_e} \frac{\partial \theta_e}{\partial t_i}, \tag{A.75}$$

$\partial\theta_e/\partial t_i$ is non-zero only if node i belongs to element e. From Eq. 5.6 we get

$$\frac{\partial \theta_e}{\partial t_i} = \frac{\left(\sum_{j\in e} \frac{\partial N_j}{\partial y} t_j\right) \frac{\partial N_i}{\partial x} - \left(\sum_{j\in e} \frac{\partial N_j}{\partial x} t_j\right) \frac{\partial N_i}{\partial y}}{\left(\sum_{j\in e} \frac{\partial N_j}{\partial x} t_j\right)^2 + \left(\sum_{j\in e} \frac{\partial N_j}{\partial y} t_j\right)^2}. \tag{A.76}$$

B

GENERALIZED HOOKE'S LAW OF ORTHOTROPIC MATERIAL

The generalized Hooke's law of an orthotropic material in the Voigt notation is

$$\boldsymbol{\sigma}_0 = \boldsymbol{D}_0 \boldsymbol{\varepsilon}_0, \tag{B.1}$$

where $\boldsymbol{\varepsilon}_0$ and $\boldsymbol{\sigma}_0$ denote the stress and strain tensor, respectively. $\boldsymbol{D}_0$ represents the elasticity tensor. For plane stress problems with infinitesimal strain, and with the horizontal axis denoted as x and the vertical axis as y, the elasticity tensor is expressed as

$$\boldsymbol{D}_0 = \frac{1}{1-\nu_{xy}\nu_{yx}} \begin{bmatrix} E_x & \nu_{yx}E_x & 0 \\ \nu_{xy}E_y & E_y & 0 \\ 0 & 0 & G_{xy}(1-\nu_{xy}\nu_{yx}) \end{bmatrix}, \tag{B.2}$$

where E_x and E_y are the Young's modulus along the reference axes, and G_{xy} is the shear modulus. ν_{xy}, ν_{yx} are the Poisson's ratio, satisfying $\nu_{xy}E_y = \nu_{yx}E_x$.

ACKNOWLEDGEMENTS

My PhD journey has come to an end. It was not without struggle, but never without meaning. I faced challenges, grew through adversity, and remained true to the pursuit of knowledge. I am deeply grateful for this rare chapter in my life dedicated to science.

First of all, I would like to express my heartfelt gratitude to my promotors. Thank you, **Jun**, for being such a supportive supervisor. I have learned a lot from you, not only about conducting solid research but also about adhering to academic standards. I also cherish the warm memories of the times you invited me and my wife to your new house and shared dinners with your family. Thank you, **Fred**, for being my promotor. Your ability to think outside the box and offer high-level perspectives on research has been truly inspiring. Even after you became the dean of our faculty, despite your busy schedule, you have remained actively involved and continued to offer valuable guidance to keep the project on track.

I would also like to thank my co-author **Weiming**. You have provided invaluable support during the early stages of my PhD. I sincerely wish you all the best for your future academic career!

Hereby, I also want to express my gratitude to my former master's supervisor at Tsinghua University, **Jianbin Du**. Thank you for introducing me to the fascinating world of scientific research. Since then, it has been an amazing and enriching journey. I am also deeply grateful for your warm welcome and insightful advice when I returned to Tsinghua.

During my master's study, I luckily got the opportunity to have a short visit to the Technical University of Denmark (DTU), where I received guidance from **Ole Sigmund**. It was quite inspiring for me to learn how the leading scientists of our time approach research. Thank you for your encouragement every time we crossed paths in the past years.

I also sincerely thank the professors in the CDM group for their kind support over the past four years. Thank you **Matthijs** for hosting me in the CDM group and supporting me to attend academic conferences, the suggestions and feedbacks you gave me on our group meetings are quite insightful. Thank you **Can** for always providing valuable advice on our Vidi project meetings; it was a great experience working with you to supervise master students and discuss all aspects about design for additive manufacturing. Thanks **Hans** for our engaging conversations, you showed me the fancy projects you had been working on, which greatly extended my research horizon. Thanks **Alejandro** for inviting me to your academic writing session, where I greatly benefited. Thank you **Lise** for always being nice and supportive. I remember that you always sat in the audience and gave me applause when I gave my presentations at conferences. Thank you **Omid** for our pleasant discussions, and for offering help to reach out to researchers working on reinforcement learning. Thank you **Haluk** for our coffee chat, I am excited to see the machine learning innovations you will bring to the group.

I also would like to take this opportunity to thank Prof. **Charlie C.L. Wang**, Prof. **Ian Gibson**, and Prof. **Kaspar M.B. Jansen** for kindly serving as a member of my defense committee. I appreciate the time and effort you dedicated to reviewing my dissertation and offering insightful feedback. A special thanks to **Marcel Hermans** for our inspiring discussion on WAAM–your depth of experience and knowledge helped me avoid overly impractical ideas.

In addition, I would like to express my thanks to my master's students: **Mike**, **Budhaditya**, **Manabendra**, and **Riccardo**. By acting as your daily supervisor, I truly understand the old Chinese saying: To teach is to learn. I have learned a lot along the way you progressed. My PhD research could not be so enriched without your contributions. I would also like to thank **Tim** and **Adhiraj**–your valuable contributions to the advancement of manufacturing systems have greatly complemented our computational approach. It was wonderful to see those real printed outcomes from your projects.

I also want to thank my dear colleagues in the CDM group, it was nice to be accompanied by you guys during my PhD journey. **Arnoud**, thank you for your help with C++, PETSc and parallel computing. **Aditya**, it was great to have you as a fitness partner, let's keep our healthy lifestyle going. **Breno**, you are such a nice friend. A lot of fun activities would not be happening without you. **Casper**, your creativity and inspiring ideas always stood out. **Dirk**, thank you for your guidance on the inherent strain method. **Jian**, thank you for the delicious food and our engaging discussions at the EM symposium. **Lidan**, I wish you and your husband a pleasant life! **Maarten**, our talks on science and culture were truly enjoyable. **Marek**, your smile always brings good vibes and motivation. **Rajit**, it was great co-supervising the master's student with you. **Stijn**, I still remember the amazing karaoke night. **Surya**, thanks for reaching out for potential collaboration on machine learning. **Vibhas**, thank you for the many times of mutual support, I will always remember our late-night chat in Leeds about personal development. **Xander**, thank you for helping me with the Linux system and MPI issue. **Yoo-Seong**, I liked getting to know Korean culture from you. **Yong**, it was nice to play soccer and card games with you. **Yuheng**, thanks for the encouraging chats we had. **Yang**, thanks for always bringing energy and happiness to the office. And the others: **Serena**, **Guillermo**, **Sanne**, **Ana**, **Ludovica**, **Chintan**, **Paul**, **Sabiju**. A special thanks to **Joran** and **Nils** for being my paranymphs. I truly appreciated the fun moments we had together and wish you all the best with the rest of your PhD journeys.

I would also like to thank the other colleagues in the PME department for the enjoyable lunch breaks, coffee chats, and fun activities: **Lucas**, **Endre**, **Vivek**, **Ata**, **Ali**, **Paulina**, **Santiago**, **Aditya**, **Pierre**, **Domas**, **Marcin**, **Giorgos**, **Malte**, **Frederike**, **Hande**, **Inge**...

A heartfelt thank you to all my Chinese friends from PME, we've shared so many wonderful moments and gatherings together: **Zichao**, **Mingkai**, **Xinxin**, **Sifeng**, **Minxing**, **Binbin**, **Xiliang**, **Ze**, **Xuerong**, **Zhilin**, **Huihui**, **Hanqin**, **Ruibo**, **Xueying**, **Zhiwei**, **Xianfeng**, **Yuchen**, **Peiyu**, **Yuxuan**, **Zhichao**, **Rui**, **Yujiang**, **Chao**.

In addition, I would also like to extend my gratitude to a group of lovely friends I met over the past four years: **Xiaoyu**, **Jiao**, **Xueqing**, **Fenghua**, **Xinhe**, **Tianlong**, **Jing**, **Yingfu**, **Cai**, **Zhenzhen**, **Dinghao**, **Yifei**, **Ruipeng**, **Ziqing**, **Sihao**, **Xuerui**, **Wenxiu**, **Jihong**, **Yujie**, **Desong**, **Zhaochong**, **Xiaohuan**, **Sen**, **Wenyi**, **Guangze**, **Yukai**, **Qing**, **Xiaopeng**, **Hongpeng**, **Junhan**, **Jiaxiang**, **Kai**, **Kaidong**, **Heng**, **Xiaoya**, **Junpeng**...

I would like to express my deepest love and gratitude to my parents. You have supported every important decision I have made, never imposing pressure, but always offering patience, understanding, and trust. My father's perseverance, determination, and resilience have deeply inspired me, just as my mother's extraordinary strength and compassion have profoundly shaped my perspective on life. I hope to spend more time with you in the years to come.

I also want to express my sincere gratitude and affection to my parents-in-law. Your solid support for Jingyi and me as we pursue our PhDs abroad has meant so much to us. Your understanding and encouragement have given us comfort and confidence throughout this journey.

Finally, to my beloved wife, **Jingyi** – your love has been my light through the shadows. Your presence always brings me strength, calm, and clarity. We have shared our joys and thoughts, cared for each other, and grown side by side. I could not have completed this journey without your support. I am deeply grateful to have walked this path together with you.

Wu Kai
Delft, May 2025

CURRICULUM VITÆ

Kai WU

01-04-1995 Born in Jiangyan, Jiangsu, China.

EDUCATION

2010–2013 High School
Jiangyan High School of Jiangsu Province, China

2013–2017 BSc in Engineering
Harbin Institute of Technology, Harbin, China
Technische Universität München (Oct. 2016–Mar. 2017), Germany
Thesis: Dynamic analysis of a pneumatic spindle with magnetic levitation
Supervisor: Prof. Baojun Pang

2017–2020 MSc in Mechanics
Tsinghua University, Beijing, China
Thesis: Design of metamaterial mechanisms based on topology optimization
Supervisors: Dr. Jianbin Du & Prof. Ole Sigmund

2020–2024 PhD in Precision and Microsystems Engineering
Delft University of Technology, the Netherlands
Thesis: Space-time topology optimization for multi-axis additive manufacturing
Promotors: Dr. Jun Wu & Prof. Fred van Keulen

List of Publications

Journal

6. **K. Wu**, F. van Keulen, and J. Wu. "Residual stress-constrained space–time topology optimization for multi-axis additive manufacturing". In: *Computer Methods in Applied Mechanics and Engineering* **440** (2025), p. 117913. DOI: https://doi.org/10.1016/j.cma.2025.117913

5. **K. Wu**, W. Wang, F. van Keulen, and J. Wu. "Space–time topology optimization for anisotropic materials in wire and arc additive manufacturing". In: *International Journal of Mechanical Sciences* **284** (2024), p. 109712. DOI: https://doi.org/10.1016/j.ijmecsci.2024.109712

4. W. Wang, **K. Wu**, F. van Keulen, and J. Wu. "Regularization in space–time topology optimization for additive manufacturing". In: *Computer Methods in Applied Mechanics and Engineering* **431** (2024), p. 117202. DOI: https://doi.org/10.1016/j.cma.2024.117202

3. **K. Wu**, O. Sigmund, and J. Du. "Design of metamaterial mechanisms using robust topology optimization and variable linking scheme". In: *Structural and Multidisciplinary Optimization* **63** (2021), pp. 1975–1988. DOI: https://doi.org/10.1007/s00158-020-02791-1

2. **K. Wu**, R. Di Girolamo, M. Lansu, F. van Keulen, and J. Wu. "Controlling layer geometry in fabrication sequence optimization for multi-axis additive manufacturing". To be submitted

1. M. Nath Das, R. Ranjan, **K. Wu**, J. Wu, and C. Ayas. "A geometric approach for controlling local overheating in topology optimization for additive manufacturing". To be submitted

TU Delft

ISBN: 978-94-6510-665-6